D O C T O R A L T H E S I S

ENVIRONMENTAL SENSORS BASED ON GEOMETRICALLY MODIFIED MAGNETOELASTIC RESONATORS FUNCTIONALIZED WITH MOFS

PAULA GONZALEZ SAIZ

Supervisors:

MARÍA ISABEL ARRIORTUA

ANA CATARINA LOPES

November 2020

eman ta zabal zazu

Universidad del País Vasco

Euskal Herriko Unibertsitatea

Este trabajo de investigación para optar al Grado de Doctor por la Universidad del País Vasco (UPV/EHU) se ha realizado en colaboración entre la Fundación Basque Center for Materials, Applications and Nanostructures (BCMaterials) y el Departamento de Geología de la Facultad de Ciencia y Tecnología de la UPV/EHU.

- ***Bueno, creo que ya va siendo hora de concluir, ¿le gustaría añadir algo?***

\+ ***Mucho, pero la vida es corta…***

Naukas 2019 

Para Mami ♡

ACKNOWLEDGEMENTS

Esta tesis ha dado muchas vueltas (¡la ciencia!) así que estas son las únicas líneas que han estado claras desde el principio. Aunque nunca he estado 100% segura de sí las llegaría a escribir. Ha sido difícil llegar hasta aquí, una montaña rusa, pero parece que aquí estamos, el viaje ha llegado a su fin y no habría sido posible sin la ayuda de muchas personitas.

The first people I want to thank are my supervisors, both those on paper and those that do not appear in any document. Maribel, Catarina, Rober, muchísimas gracias por vuestra ayuda, por enseñarme tanto, por estar disponibles siempre que os he necesitado y por vuestra paciencia. No hubiera sido posible llegar hasta aquí sin vuestro apoyo y dedicación. Y gracias infinitas por los últimos meses de revisiones y papeleo, ¡lo hemos conseguido!.

Thanks to the Basque Center for Materials, Applications and Nanostructures (BCMaterials), which has been my home (really) during the last three year, for giving me the opportunity to do the thesis with a pre-doctoral fellowship. And thanks to all my colleagues here, for making this stage much better; por los nachos en el basquery, las comidas de tesis, las cenas de Navidad, las cañas en pozas, el café de las 10:30 o las sonrisas en el pasillo (aunque en los últimos meses la mascarilla os la ocultase). Gracias, a todos. Y en especial a las personas que también se embarcaron en esta aventura de la tesis el 1 Octubre de 2017, creo que son las personas menos de agradecimientos y felicitaciones y esas mierdas que conozco pero han sido muy importantes para mi estos 3 años. Cristian, Ander, David, gracias por dejarme descargar con vosotros las penas y alegrías de esta montaña rusa, parece que hemos llegado al final, doctores!!. Also to the people with whom I have worked closely: Ari, Andoni, Txema, Edu, Dani, Manu, Arkaitz, y demás compis, gracias por vuestros consejos de postdoc y vuestra disponibilidad! Al resto de predocs (que no saben en la que se han metido!). Y a todas las personas de administración, por volverles locos con los pedidos, las instalaciones, las solicitudes de compra y demás cosas y estar siempre dispuestos a ayudar. Eskerrik asko BCMaterials!

A la gente de la UPV, en especial a Jon, por enseñarme sobre magnetoelasticidad, por llevarme a Grecia y a Eslovaquia y por el lío con el papeleo estos últimos días y a Luis por la ayuda con

las medidas de EPR y el papeleo del doctorado. A los técnicos de los Servicios Generales (SGIker) por todas las medidas, en especial a Txesko por el MHSPM y por estar siempre dispuesto a resolver cualquier duda y a Iñaki por la ayuda con Labview y con el magnetismo. También a Tekniker (a Iban y a Jon) por la preparación de nuestros "geometrically modified resonators for improved mass sensitivities".

A todas las personas de Chile que hicieron que me sintiese como en casa. A Andreina por cuidarnos tanto y enseñarnos una nueva forma de trabajar. A Barbara por los buenos momentos en el labo, por lavar más de 100 frascos al día y por las jornadas interminables para acabar a tiempo. A Joseba por adoptarnos en el labo. A Maibe, Marce, Rodrigo, Jessica y demás personitas por las Chelas. Y a Chile en general por enseñarme tanto: ¡Hasta que la dignidad se haga costumbre!. Gracias también a Dimitris por dejarme colarme en su laboratorio en Grecia para descubrir su sistema de gases y darme la oportunidad de conocer Patras. Y hablando de viajar, a mis directores, al BC y a ciertas asociaciones (APS, IEEE, RSEQ…) por permitirme asistir a cursos y conferencias en distintos países que me han permitido, aprender un montón, conocer científicos de todo el mundo (¡¡incluso un par de premios nobel!!), viajar y, lo más importante, perder la vergüenza a hablar en público.

Y no puedo olvidarme de mis profes de Cantabria que me iniciaron en esto de la investigación y me ayudaron a elegir este camino. En especial a Rafa, por enseñarme tanto durante el TFG y a Fernando y Luis por transmitirme su ilusión desde el primer día. Tampoco puedo olvidarme de mis fisicas favoritas, Yohana, Marta, por seguir quedando de año en año y sentir que no ha pasado el tiempo.

A LOGOS, ZientziaAstea, Elhuyar, 11deFebrero.org, y demás asociaciones por ayudarme a descubrir la divulgación y darme la oportunidad de hacer llegar la ciencia a todos y salir un poco del laboratorio y la pantalla.

Y fuera del ámbito científico. A Miguel, Angela e Iratxe, por compartir con vosotros mucho más que un piso, por ser mi familia aquí estos años. Me siento afortunada de haberos tenido como compañeros de vida. A mis amigas, por haber soportado la distancia de los últimos años y por entenderlo. Por los momentos de re-conexión. ¡Vuelvo a casa!

Al paletillo, con quien comparto mi tiempo ahora, aunque no tengamos ni idea que vamos a hacer con 2 tesis menos en nuestras vidas. Si sobrevivir a una tesis es difícil, por conseguir que

hayamos sobrevivido a 2!! Eres quien más ha sufrido la montaña rusa de estos últimos meses y el viaje no hubiese sido lo mismo sin ti. Espero seguir compartiendo muchos más.

A Beltza, Gluten y Ris, por alegrarnos los días de escritura y ayudarnos a desconectar un poco. Y a Iñaki y Maika, por adoptarme y cuidarme tan bien, por ser mi familia aquí en Bilbao. Gracias.

Y lo más importante, a mi familia. Jose, Marco, Mami sois lo mejor de mi vida! Y si estos 3 años tienen un pilar fundamental sois vosotros. Gracias mami por creer siempre en mi y enseñarme que no hay cosas de chicos ni de chicas, que el esfuerzo es necesario y que la toalla no se tira en la meta. Jose, por ser más que un padre y emocionarte con cada paso que doy. Enano, por compartir tu alegría conmigo y por el tiempo que te he robado, estoy deseando devolvértelo. A Papi, por su apoyo. Y a "güela", porque mucho de lo que soy es gracias a ti también, ojalá pudiese compartir este momento contigo. A toda mi familia (sois muchos como para nombraros a todos!), gracias por estar ahí. Os quiero, muchuu!

La verdad, si algo me han traído estos tres años han sido buenos momentos y personas increíbles (además de un título de doctora, claro).

GRACIAS, A TODOS, sois las piezas de este puzzle!

Gracias. Thank you. Eskerrik asko. Obrigado.

CONTENT

3

4

RESUMEN

El mundo se enfrenta a una grave crisis medioambiental marcada, entre otros aspectos, por la elevada contaminación. En particular, el uso de diversos compuestos perjudiciales en áreas como la industria o la minería está cada vez más extendido haciendo que la presencia en nuestro entorno de diversos materiales perjudiciales para la salud sea cada vez mayor. En este contexto, la detección y eliminación de ciertos compuestos tóxicos presentes en el aire o en el agua resultan muy importantes. El problema está en que los métodos tradicionales para detectar estos compuestos son costosos y requieren de tiempos de tratamiento largos lo que hace que resulten poco efectivos para las necesidades actuales. Y es que, actualmente, con las ya conocidas como "ciudades inteligentes", la detección de este tipo de compuestos perjudiciales, de una manera rápida y a distancia, resulta crucial. Por esta razón, la comunidad científica ha centrado su trabajo en el desarrollo de sensores que permitan detectar este tipo de compuestos de una forma rápida y fiable, a un bajo coste. En este contexto, los sensores magnetoelásticos están ganando importancia en el área de detección ya que, además de resultar rápidos y baratos, presentan la capacidad de detectar este tipo de compuestos a distancia, sin necesidad de conexiones, lo que les hace ideales para las necesidades actuales.

El desafío en este tipo de sensores esta en mejorar su rendimiento. En particular, la sensibilidad se ha mejorado, tradicionalmente, mediante la disminución del tamaño de los resonadores para lograr así aumentar la frecuencia de resonancia de los mismos. Sin embargo, al disminuir el tamaño aparecen ciertos problemas como una disminución notable en la señal o dificultad para manejarlos por lo que deben explorarse otras alternativas. Por otro lado, para la mayoría de aplicaciones, estos materiales actúan como transductores de la masa adsorbida en una capa activa, que funciona como adsorbente selectivo. Los materiales utilizados comúnmente como capa activa incluyen polímeros o zeolitas. Sin embargo, la sensibilidad de estos sistemas de detección podría mejorarse utilizando como capas activas otros materiales que permitan una mayor adsorción del compuesto a detectar. En este contexto, los materiales porosos de tipo "Metal Organic

Framework" (MOFs) están ganando mucho interés en el área de la adsorción selectiva debido a sus excelentes propiedades, como sus elevadas áreas superficiales, su alta estabilidad química o la posibilidad de modificar el tamaño de poro y/o agregar grupos funcionales a su estructura. Sorprendentemente, a día de hoy estos materiales no han sido utilizados como capa activa en sensores magnetoelásticos. Es precisamente en este contexto donde surge la presente Tesis, con el fin de mejorar las propiedades de los resonadores magnetoelásticos y de los materiales de tipo MOF y combinarlos para obtener sensores ambientales de alta calidad.

El objetivo principal de esta tesis doctoral es, por tanto, investigar el potencial uso de resonadores magnetoelásticos funcionalizados con materiales de tipo MOF para la detección de contaminantes ambientales. En este contexto, los objetivos de la investigación se centran en: 1) Mejorar la sensibilidad al incremento de masa de los resonadores magnetoelásticos, 2) Investigar y mejorar las propiedades de adsorción de metales pesados (HMs) y/o compuestos orgánicos volátiles (VOCs) en MOFs, 3) Utilizar materiales de tipo MOF como capa activa en resonadores magnetoelásticos y 4) Investigar el uso de los sensores fabricados para la detección, a distancia, de VOCs and HMs. En base a estos objetivos, el trabajo se ha estructurado en 6 capítulos; comenzando por una breve introducción a la problemática actual y a las soluciones propuestas en esta investigación (Capítulo 1).

El segundo de estos capítulos se centra en el análisis de las propiedades de los resonadores magnetoelásticos en función de su geometría y su tamaño. Una exhaustiva caracterización, escasa en la bibliografía hasta la fecha y necesaria para la comprensión y la optimización de los resonadores magnetoelásticos en aplicaciones de detección, se ha llevado a cabo. En particular, se ha comprobado que la geometría del resonador magnetoelástico juega un papel muy importante en sus propiedades magnéticas y magnetoelásticas, teniéndose que cuando se utilizan resonadores con geometrías tales como triángulos o rombos en lugar de los resonadores rectangulares tradicionalmente utilizados, se observa una mejora notable en propiedades tales como la sensibilidad a la masa o el factor de calidad de la resonancia. Por otro lado, se ha analizado el efecto de la geometría en otras propiedades como el factor de la calidad de la resonancia, el efecto delta E o el comportamiento de los micro-dominios magnéticos. Los resultados descritos

en este capítulo resultan de elevado interés para la mejora del rendimiento en este tipo de sensores.

En el capítulo 3 los materiales de tipo MOFs entran en escena. En primer lugar, se investigan diversas metodologías para funcionalizar los resonadores magnetoelásticos con estos MOF, desde técnicas de síntesis directa a métodos de deposición post-síntesis. Los resultados obtenidos muestran que el uso de una técnica u otra depende de las propiedades finales de la capa activa que se desean obtener, así como de las condiciones de síntesis del propio MOF. En particular, un método de crecimiento por síntesis directa resulta adecuado si se quiere obtener una buena adhesión de la capa activa al resonador. Sin embargo, este método resulta lento y además no es valido para la síntesis directa de ciertos MOF que se sintetizan en condiciones agresivas para las cintas. En estos casos, otros métodos de funcionalización deben ser considerados. En particular, la técnica de recubrimiento por spray destaca entre el resto de métodos de deposición post-síntesis investigados ya que permite depositar una capa activa gruesa y homogénea de una manera rápida y sencilla. El mayor inconveniente de esta técnica es que baja adhesión de la capa activa. Por otro lado, en este capítulo se describen la síntesis y caracterización de distintos MOFs de tipo UiO66 con distintos grados de defectos y distintos grupos funcionales. Los dos capítulos siguientes (4 y 5) se centran en la aplicación de estos MOFs y de los sensores funcionalizados con los mismos.

En el capítulo 4, la aplicación de los MOF de tipo UiO66 sintetizados, así como de los sensores fabricados, para la adsorción y detección de HMs se analiza en detalle. En particular, el efecto de la presencia de grupos funcionales y defectos en dichos MOFs en la adsorción y fotoreducción de cromo se ha investigado. Tras el proceso de adsorción, se ha aplicado una metodología novedosa para analizar la especiación del cromo una vez adsorbido en estos materiales mediante la combinación de técnicas de espectroscopía UV-Vis y EPR. Finalmente, se ha analizado la respuesta de los resonadores magnetoelásticos en un medio líquido y se ha investigado la posibilidad de detectar metales pesados in-situ, utilizando los resonadores funcionalizados con MOFs previamente fabricados.

Por otro lado, en el capítulo 5 se analiza la capacidad de detección de VOCs mediante el uso de cintas magnetoelásticas funcionalizadas con MOFs. En particular, los sensores

fabricados se han aplicado para la detección, en tiempo real, de tolueno. El efecto de parámetros tales como la masa de la capa activa en la respuesta del mismo se han analizado en detalle. Los resultados obtenidos muestran la viabilidad de utilizar estos sensores para la detección rápida, precisa y a distancia de VOCs. Por otro lado, el montaje de un sistema para la circulación y detección de VOCs se describe también.

Para finalizar, en el capítulo 6 se recogen las principales conclusiones derivadas de esta investsigación, así como las posibles lineas en las que sería interesante seguir trabajando en el futuro. En general, los resultados recogidos en esta investigación aportan avances en una tecnología de interés para desarrollar la transición hacia sistemas de detección rápidos, precisos y a distancia para las ciudades inteligentes, en línea con los objetivos planteados en el programa de investigación e innovación de la Unión Europea (Horizonte Europa) y en los objetivos de desarrollo sostenible (Agenda 2030).

SUMMARY

The world is facing a global environmental crisis marked, among other things, by the elevated pollution. In particular, the use of different harmful substances in areas such as industry or mining is increasingly widespread, causing the increasing of different harmful materials presence in the environment. In this context, the detection and elimination of certain toxic compounds present in the air or water is highly necessary. The problem is that traditional methods employed to detect these compounds are expensive and time-consuming, which makes them ineffective for current needs. In fact, nowadays, with that already known as "smart cities", the detection of this type of harmful compounds quickly and remotely is essential. For this reason, the scientific community has focused their work on the development of sensors which allow detecting this type of compound in a fast and precise way at a low cost. In this context, magnetoelastic sensors are gaining attention in this area since, in addition to being fast and cheap, they present the ability to detect these types of compounds in a wireless way, which makes them ideal for current needs.

The challenge in this type of sensors is to improve their performance. In particular, sensitivity has been traditionally improved by reducing the resonator size and consequently increase their resonance frequency. However, this reduction on the size results in a notable decrease in the signal or handling issues. Thus, other alternatives should be explored to face these problems. Moreover, for most applications, these materials act as transducers of the adsorbed mass in an active layer that acts as a selective sorbent. Materials traditionally employed as active layers in this type of sensors include polymers or zeolites. However, the sensitivity of these detection systems could be improved using other materials as active layers, which allow for a more significant adsorption of the target compound. In this context, Metal Organic Frameworks (MOFs) porous materials are gaining interest in the area of selective adsorption due to their excellent properties, such as their high surface areas, their high chemical stability or the possibility of tune their pore size and/or add functional groups to their structure. Surprisingly, these materials have not been previously employed as active layers in

magnetoelastic sensors. It is precisely in this context where this thesis arises, with the aim of improving the properties of magnetoelastic resonators and MOF materials itself and combine both to obtain highly sensitive and selective environmental sensors.

The main objective of this thesis is then to explore the potential use of magnetoelastic resonators functionalized with MOFs for the wireless detection of environmental pollutants. In this context, the research objectives are focus on: 1) Improving the mass sensitivity of magnetoelastic resonators, 2) Investigating and improving the adsorption properties of Heavy Metals (HMs) and/or Volatile Organic Compounds (VOCs) in MOFs materials, 3) Functionalizing the magnetoelastic resonators with the MOFs materials using different techniques and 4) Investigating the application of the fabricated sensors for remote detection of HMs and VOCs. Based on these objectives, the work has been structured in six main chapters, starting with a brief introduction to the current problem and the solutions proposed in this research (Chapter 1).

The second of these chapters is focused on the analysis of the properties of magnetoelastic resonators as a function of their geometry and size. An exhaustive characterization, scarce to date and necessary for the understanding and optimization of the magnetoelastic resonators performance has been carried out in this chapter. In particular, it has been found that the geometry of the magnetoelastic resonator plays a very important role in its magnetic and magnetoelastic properties having that when resonators with geometries such as triangles or rhomb are used instead of the traditionally employed rectangular resonators, a notable improvement in the sensors performance is observed. On the other hand, the effect of the geometry on other properties such as the resonance quality factor, the delta E effect or the magnetic micro-domains behaviour has been analysed. The results obtained throughout this chapter result very interesting for improving the performance of this type of sensors.

In Chapter 3 MOFs materials enter in scene. First of all, various methodologies to functionalize magnetoelastic resonators with these materials are investigated, from direct synthesis techniques to post-synthesis deposition methods. Obtained results show that the use of one technique or another depends on the final properties of the active layer to be obtained as well as on the synthesis conditions of the MOF itself. In particular, a direct synthesis growth method is suitable to obtain a good adhesion of the active layer

to the resonator. However, this method is time-consuming and neither valid for the direct synthesis of certain MOFs that are synthesized under harsh conditions for the resonators. In these cases, other functionalization methods should be considered. In particular, the spray coating technique stands out among the rest of the post-synthesis deposition methods considered since it allows to deposit heavy and homogeneous active layers quickly and easily. The major drawback of this technique is the weak adhesion of the active layer. Finally, this chapter describes the synthesis and characterization of different MOFs of the UiO66 type with different degrees of defects and different functional groups. The next two chapters are focus on the application of these MOFs and the sensors functionalized with them.

In Chapter 4, the application of the synthesized UiO66 type MOFs as well as of the fabricated sensors for the adsorption and detection of HMs is analysed in detail. In particular, the effect of the presence of functional groups and defects in said UiO66 based MOFs on the adsorption and photoreduction of chromium has been investigated. After the adsorption process, a novel methodology has been applied to analyse the speciation of chromium once adsorbed on these materials by combining UV-Vis and EPR spectroscopy techniques. Finally, the response of magnetoelastic resonators in liquid media has been analysed and the possibility of sensing heavy metals in-situ using the resonators functionalized with these MOFs has been investigated.

On the other hand, in Chapter 5 the ability of VOCs sensing through the use of magnetoelastic resonators functionalized with MOFs materials has been explored. In particular, the fabricated sensors have been applied for the detection, in real time, of toluene. The effect of parameters such as the active layer mass on the sensor response has been deeply analysed. Obtained results show the feasibility of using these sensors for the rapid, precise and remote detection of VOCs. On the other hand, the assembly of a system for the circulation and detection of VOCs is also described in this chapter.

Finally, in chapter 6 the main conclusions derived from this investigation are collected, as well as the possible lines of investigation in which it would be interesting to continue working in the future. In general, the results collected in this work provide advances in a technology of interest to develop the transition towards rapid, precise and remote detection systems, in line with the objectives set out in the European Union's research

and innovation program (Horizon Europe) and in the sustainable development goals (Agenda 2030).

LABURPENA

Munduak, ingurumen-krisi larrian aurkitzen da. Ainbat arazoen artean, industrian eta meatzaritzan erabilitako konposatu kaltegarriren metaketa gero eta handiagoa da. Honek, airean edo uretan dauden konposatu toxikoak detektatzea eta ezabatzea behartzen du. Zoritxarrez, konposatuak detektatzeko erabiltzen diren metodo tradizionalak, garestiak dira eta lan-denbora luzeak behar dituzte. Beraz, teknika hauek ez dira oso eraginkorrak egungo beharrizanetarako.

Komunitate zientifikoak, sentsoreak garatu ditu arazo honi aurre egiteko. Hauek, konposatu kutsakorrak azkar, modu fidagarrian eta teknika merkeen bidez detektatu ahal baitituzte. Testuinguru horretan, sentsore magnetoelastikoak arreta deitzen dute. Batez ere, azkar neurtzen dutelako eta merkeak direlako. Gainera, urrutiko konposatuak konexiorik gabe detektatzeko gaitasuna dute. Beraz, idealak dira "hiri adimenduetan" erabiltzeko, non haririk gabeko gailuak ezinbestekoak dira.

Gaurko erronka, sentsoreen errendimendua hobetzea da. Horretarako, orain arte erresonadoreen tamaina murriztu egin da, sentsibilitatea handitzeko. Baina, sentsoreen tamaina murriztean, zenbait arazo agertzen dira, hala nola seinalearen murrizketa edo tresneria erabiltzeko zailtasuna. Beraz, beste aukera batzuk aztertu behar dira.

Bestalde, aplikazio gehienetarako, sentsoreak, transduktore gisa jarduten dute, haien gainean jarritako geruza aktibo baten masa aldaketa neurtuz. Normalean polimeroak edo zeolitak geruza aktibo gisa erabiltzen dira. Baina detekzio-sistemen sentikortasuna hobetzeko geruzaren adsortzioa gehiago handitu behar da. Testuinguru horretan, "Metal Organic Framework" (MOFs) motako material-porotsuak interes handia erakarri dute. Batez ere, haien ezaugarri bikainengatik. Adibidez, azaleko eremu handiak dituzte, estabilitate bikaina aurkezten dute, haien barneko poroak kontrolatu ahal dira eta talde funtzional berriak onartzen dituzte. Hori kontuan hartuta, tesi honetan, sentsore magnetoeslatikoak eta MOF materialez egindako gainazal aktiboak konbinatzea proposatzen da. Bi materialen inguruan lan egingo da, haien funtzionamendua hobetzeko eta ingurumen-sentsoreak sortzeko.

Doktoretza tesi honen helburu nagusia, beraz, erresonadore magnetoelatikoak eta MOF konposatuak batzea izango da, ingurumen kutsatzaileak detektatzeko. Testuinguru horretan, ikerketaren helburuak honako hauek dira: 1) erresonadore magnetoelastikoen propietateak hobetzea; 2) metal astunen (HMs) eta/edo konposatu organiko lurrunkorren (VOCs) adsortzio-propietateak ikertzea MOF materialen bidez; 3) MOF motako materialak geruza aktibo gisa erabiltzea erresonadore magnetoelastikoetan, eta 4) fabrikatutako sentsoreak urrutitik VOCs and HMak detektatzeko erabil daitezkeen ikertzea.

Helburu horietan oinarrituta, lana 6 kapituluetan banatu egin da. lehenengo kapituluan, gaur egungo arazoa eta proposatutako irtenbideei buruzko sarrera labur bat egin da. Bigarren kapituluan, erresonadore magnetoelastikoen propietateak aztertu egin dira. Zehazki, geometria eta tamainaren arabera. Honi esker, erresonadore magnetoelastikoen geometriak garrantzi handia duela egiaztatu da. Batez ere haren propietate magnetiko eta magnetoelastikoetan. Hau dela eta, triangeluak edo erronboak bezalako geometriadun erresonadoreak sentsibilitatean hobekuntza nabarmena lortzen dutela ikusi egin da. Gainera, geometriaren eragina beste propietateetan aztertu da, hala nola erresonantziaren kalitatearen faktorea, delta E efektua edo mikro-domeinu magnetikoen portaera. Kapitulu honetan deskribatutako emaitzak ezinbestekoak izan dira sentsoreen errendimendua hobetzeko.

Hirugarren kapituluan, MOF motako materialak aztertu egin dira. Lehenik eta behin, erresonadore magnetoelastikoak MOF horiekin funtzionalizatzeko hainbat metodologia ikertu dira. Lortutako emaitzek, funtzionalizazioaren eragina sentsoreen propietateetan erakutzi dute. Bereziki, sintesi zuzen bidezko hazkunde-metodoen erabilera hondo atxikitako geruza aktiboak sortzeko erabilgarria dela ikusi egin da. Hala ere, metodo hori motela da, eta, gainera, ez da baliagarria zenbait MOF asteko, beharrezko baldintza erasokorrengatik. Kasu horietan, beste funtzionalizazio-metodo batzuk kontuan hartu dira. Bereziki, esprai bidezko estaldura-teknika nabarmentzen da, geruza aktibo lodi eta homogeneoak, azkar eta erraz hazteko gai baita. Teknika horren eragozpenik handiena, geruzaren atxikipena da. Bestalde, kapitulu honek UiO66 motako MOF desberdinen sintesia, akats-maila eta talde funtzional desberdinekin deskribatzen ditu. Hurrengo bi kapituluak MOF horiekin funtzionalizatutako sentsoreen aplikazioak azalduko dira.

Laugarren kapituluan, UiO66 motako MOFen aplikazioa aztertu egin da. Zehazki, metal astunen adsortzio eta detekziorako. Horretarako, MOF talde funtzionalen eta akatsen eragina kromoaren adsortzioan ikertu da. Kromoaren espeziazioa aztertzeko, adsortzio-prozesuaren ondoren, metodologia berri bat aplikatu da, UV-Vis eta EPR espektroskopia-teknikak konbinatuz. Azkenik, erresonadore magnetoelastikoen erantzuna ingurune likidoetan aztertu da. Gainera, metal astunen in-situ detekzioa ikertu da, aldez aurretik fabrikatutako MOFekin funtzionalizatutako erresonadoreak erabiliz.

Bostgarren kapituluan MOFekin funtzionalizatutako zinta magnetoelastikoen gaitasuna VOCak detektatzeko ikertu da. Bereziki, toluenoa detektatzeko. Horretarako, geruza aktiboaren masa eragina aztertu da. Lortutako emaitzek sentsore horiek VOCak azkar, zehatz eta urrutitik detektatzeko gai direla erakusten dute. Bestalde, VOCak zirkulatzeko eta detektatzeko sistema baten muntaia ere deskribatzen da.

Amaitzeko, seigarren kapituluan, ondorio nagusiak jasotzen dira, baita etorkizunerako izan daitekeen ikerketa-ildoak ere. Oro har, ikerketa honetan jasotako emaitzek aurrerapenak ematen dituzte detekzio-sistema azkar, zehatz eta urrunekoetarako trantsizioa garatzeko. Europar Batasuneko ikerketa- eta berrikuntza-programan (Europa Horizontea) eta garapen jasangarriko helburuetan (2030 Agenda) planteatutako helburuekin bat etorriz.

List of Abbreviations and Symbols

AW: Acoustic wave
BET: Brunauer-Emmett-Teller
EPR: Electron paramagnetic resonance
FEM: Finite element analysis
FTIR: Fourier-transform infrared spectroscopy
HMs: Heavy metals
ICP-AES: Inductively coupled plasma atomic emission spectroscopy
LBL: Layer by layer
LMCT: Ligand-to-metal charge transfer
MCL: Microcantilevers
ME: Magnetoelastic
MHS-SPME: Multiple headspace solid-phase microextraction
MOFs: Metal organic frameworks
MOKE Magneto-optic kerr effect
MR: Magnetoelastic resonator
QCM: Quartz crystal microbalance
SBU: Secondary building units
SDGs: Sustainable development goals
SEM: Scanning electron microscope
SURMOFs: Surface-mounted MOFs
TEM: Transmission electron microscope
TGA: Thermogravimetric analysis
VAC: Vapor assisted conversion
VOCs: Volatile organic compounds
VSM: Vibrating-sample magnetometer
XRD: X-ray diffraction
ZIF: Zeolitic imidazolate frameworks

λ: Magnetostriction coefficient
ΔE: Delta E effect
Δf: Frequency shift
Δm: Mass increase
E_{min}: Minimum value of the Young modulus
E_s: Young modulus at the magnetic saturation state
$f_{0\,sim}$: Simulated magnetoelastic resonance frequency
f_0: Magnetoelastic resonance frequency of the bare resonator
f_r: Magnetoelastic resonance frequency
$H_{k\,max}$: Magnetic field at the minimum of the ΔE curve
k: Magnetoelastic coupling coefficient
L: Length of the magnetoelastic ribbons
Q: Resonance quality factor
S: Mass sensitivity

chapter 1

Introduction

Este primer capítulo muestra unas pinceladas de algunos de los problemas ambientales a los que se enfrenta actualmente nuestro planeta, así como la importancia de reducirlos y/o controlarlos, en el marco del cambio hacia una economía más circular y medio-ambientalmente amigable. En este contexto, la adsorción y detección de sustancias nocivas presentes en el agua o en el aire resulta crucial para la prevención medioambiental, pero también en el marco del futuro desarrollo de las ya conocidas como "ciudades inteligentes", donde la monitorización de la calidad del aire y del agua, de forma inalámbrica, es sumamente importante. Por tanto, la importancia de los sensores y, en particular, de los sensores magnetoelásticos en esta digitalización del control medio-ambiental es vital. En particular, en el caso de los sensores magnetoelásticos, la mejora de sus propiedades así como el desarrollo y diseño de capas activas con una elevada capacidad de adsorción es crucial. Es por ello que los materiales porosos de tipo MOF se presentan como una alternativa de interés en este ámbito, ya que podrían dotar al sensor de excelentes propiedades, como su gran área superficial o sus elevadas capacidades de adsorción. Para finalizar se describen los principales objetivos de esta investigación así como la estructura de este trabajo.

Content

1.1. The importance of smart sensors in the transition to a circular economy

September 2020 marked the 5th anniversary of the approval of the 2030 agenda at a time when the world faces a global pandemic which has shown that it is extremely difficult to anticipate the magnitude of the risks that await us. But before the COVID-19 health crisis, the world was already looking for strategic long-term global solutions to reverse the climate change and reduce the environmental stress caused by the anthropogenic activities [1]. Some compare the coronavirus pandemic with that derived from climate change and environmental pollution, but sadly, the first is perceived as closer and more urgent [2,3]. Although it is difficult to transfer this sense of urgency to the fight against the environmental crisis, the population is now realizing about its effects at global ecosystems and economic levels.

Nowadays, both health and environment crisis are the subject of debate in all areas of our society. If there was already a sense of urgency and need for maximum action, now it is imperative to join forces. Fortunately, some of the essential actions that can be taken to address both crises are common. At the society level, the awareness of the population to trigger a change in our behaviour is essential to palliate the impact of these global problems. At research and innovation levels, it is key to reinforce an interdisciplinary, international and coordinated investigation framed within the big "missions" concept, which aims to transform the current linear productive model into a circular environmentally friendly one.

In this context, the objectives of H2020 European research and innovation program were included around a series of strategic sectors to address the main social challenges, promoting at the same time the industrial leadership and reinforcing the excellence science in Europe [4]. Horizon Europe takes the relay of H2020 program setting five strategic mission areas (**Figure 1.1**) that pursue solutions to

Figure 1.1. Five strategic sectors of the research program of the European Union.

some of the greatest challenges that is facing our world [5]: 1) *Adaptation to climate change including societal transformation, 2) Cancer, 3) Climate-neutral and smart cities, 4) Healthy oceans, seas, coastal and inland waters and 5) Soil health and food.* Each of these mission areas collects individual missions which should be solved within a specific timeframe. In parallel, Horizon Europe paves the way to settle an open and quality science towards the development of a sustainable future in relation to the current global challenges.

Figure 1.2. Sustainable Development Goals.

In this line, it is important to mention that about 50% of the projects financed by Horizon 2020 are related to some of the seventeen Sustainable Development Goals (SDGs) [6] of the 2030 Agenda which consist in a plan of action for people, planet and prosperity [7] (**Figure 1.2**).

Thus, the development of quality research should be focus on some of these priority areas of the Horizon Europe and the SD goals. Within this framework, it is clear that sensors would have a key role in the transformation to a circular productive model of the society. The development of smart cities, the continuous monitoring of the aquatic and soil ecosystems health, the detection of diseases at their early stages, and the adaptation of the current productive model to the climate change requires from specifically designed monitoring systems able to follow up and prevent the environmental and health impact of the human activities. As illustrative examples, smart cities need from monitoring systems able to minimize the industrial impact on the environment, securing the water and soil health needs from precise sensing able to quantify that the concentration of environmentally harmful substances are below the legal thresholds, and it is not necessary to mention the importance of monitoring technology to detect pathogens, to prevent diseases at early stages, or to apply mitigation measures in the current COVID-19 pandemic.

In particular, the development of advanced monitoring technologies for the detection of chemical and biological compounds present in the air, food or water is gaining strong attention of the research community and the innovation tissue within Europe. Ensure

that the concentration of high-risk environmental and health substances is below certain legal limits is key to ensure the health of ecosystems as a whole. Nevertheless, given the complexity and varied chemical nature of the pollutants and pathogens that can be found in liquid and air ecosystems, this goal is far to be straightforward. Nowadays, gas chromatography, atomic absorption spectroscopy or inductively coupled plasma-atomic emission spectroscopy are widely applied methods for the detection of harmful compounds. Nevertheless, despite their accuracy, they are complex, expensive and time-consuming techniques which limit their use [8]. Thus, the development of rapid, cheap and accurate techniques for the quick detection of different chemical or biological targeted molecules responsible for different health problems, even when they are present at very low concentrations, has become a worldwide priority.

In recent years, the scientific community has paid special attention to the development of miniaturized and portable sensors, such as Acoustic Wave (AW) [9–11], optical [12,13], electrochemical [14,15] or resistive sensors [16,17] able to provide a fast and precise response upon exposition to different biological or environmental harmful compounds. In particular, AW sensors stand out among other traditional techniques since they are cheap and exhibit a fast response in real-time continuous detection mode. Besides, AW can be endowed of high sensitivity and selectivity upon the proper selection of the active sensing layers [18].

The detection process on these systems is based on the changes of the properties of the acoustic (mechanical) waves travelling through the sensor surface when exposed to different perturbations such as mass loadings or viscosity changes. Besides, for most applications, the sensor surface is functionalized with an active layer able to capture or interact with the target analyte, leading to an enhancement of the mass gain during the pollutant recognition, and hence, a magnified perturbation of the transducer system.

Some of the well-known devices that are based on this operation principle are the quartz crystal microbalance (QCM) or the microcantilevers (MCL). QMC and MCL based sensors have been proved to be highly useful to detect varied chemical and biological parameters both in air and liquid media [19,20]. Nevertheless, despite the high sensitivities and low cost of QMC and MCL, these are non-wireless detection instruments, a characteristic that limits their application in the already known as smart cities [21]. Indeed, fast and wireless environmental, industrial or biological monitoring is highly desirable, if

not crucial, within the digitalization of everything and the Internet of Things (IoT) [22] contexts (**Figure 1.3**).

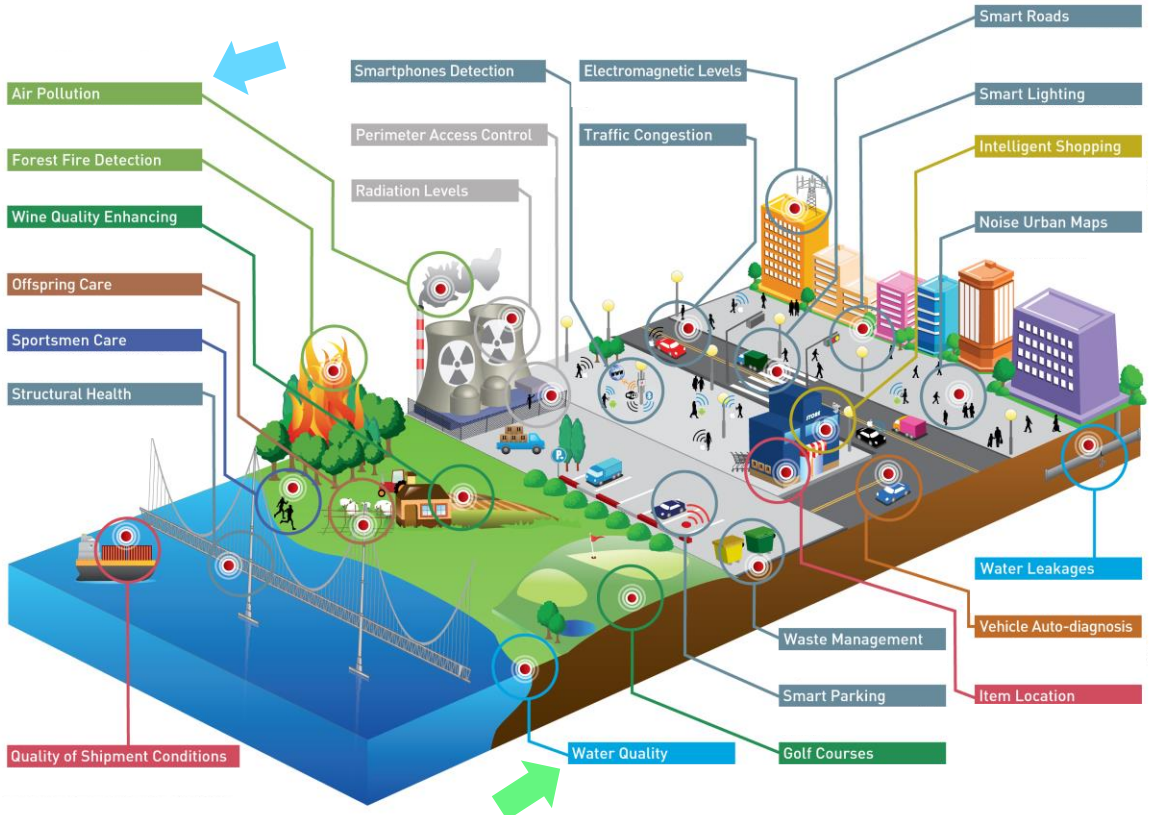

Figure 1.3. Different monitorization systems present in the so-called "smart cities". Reproduced from Libelium [23].

On that context, many researchers are focus on developing not only more sensitive, fast and economically sustainable for large scale applications monitorization techniques, but also capable to operate in a wireless way [24]. In this regard, magnetoelastic (ME) resonance sensors stand out among other AW devices [25]. Their ability to sense in a wireless way makes magnetoelastic sensors so promising for future detection systems compared with other AW based sensors. Nevertheless, their performance remains below expectations, and the improvement of the performance of these devices is crucial. Similarly to other AW systems, magnetoelastic sensors are usually based on two components, the magnetoelastic transducer material and the active layer added to the transducer in order to endow it of the specific capacity to interact with the target compound. Therefore, any improvement of the sensing capacity of magnetoelastic devices pass through:

i) The tuning of the magnetoelastic properties of the transducer.

ii) The improvement of the capacity and selectivity of the active layer to interact with the target chemical.

In the following, the operation principles of magnetoelastic based devices together with the strategies followed by the scientific community to improve their performance will be summarized. Based on this background, the main hypothesis from which this thesis work is structured with the aim of further improving the performance of magnetoelastic systems against the detection of pollutants will be briefly described.

1.2. Magnetoelastic based sensors

1.2.1. Magnetostriction and magnetoelasticity

Magnetoelastic sensors are a class of AW sensors that stand out for offering a quick remote detection of a target by the use of very cheap raw sensing materials. Those materials present a magnetoelastic coupling effect, this is, an effective interchange of energy from magnetic to elastic and vice versa (magnetostriction/magnetoelasticity effects).

The magnetostrictive effect (or Joule effect) consists on the relative deformation suffered by the ferromagnetic material when subjected to an external magnetic field [26]. As a result of the magnetostriction, each magnetic domain is deformed according to its own magnetization. In the absence of the magnetic field, the magnetic domains are oriented towards the direction defined by the magnetic anisotropy with the purpose of minimise its internal energy. On the other hand, under a magnetic field, all the magnetic moments are oriented along its direction, magnetising the magnetic material. The local deformations resulting from the magnetostriction will result into a macroscopic deformation of the material. The magnetoelastic effect (or Villari effect) is the opposite effect, that is, the change in the magnetic state of the material when a mechanical stress is applied to it. Both processes are schematically illustrated in **Figure 1.4**.

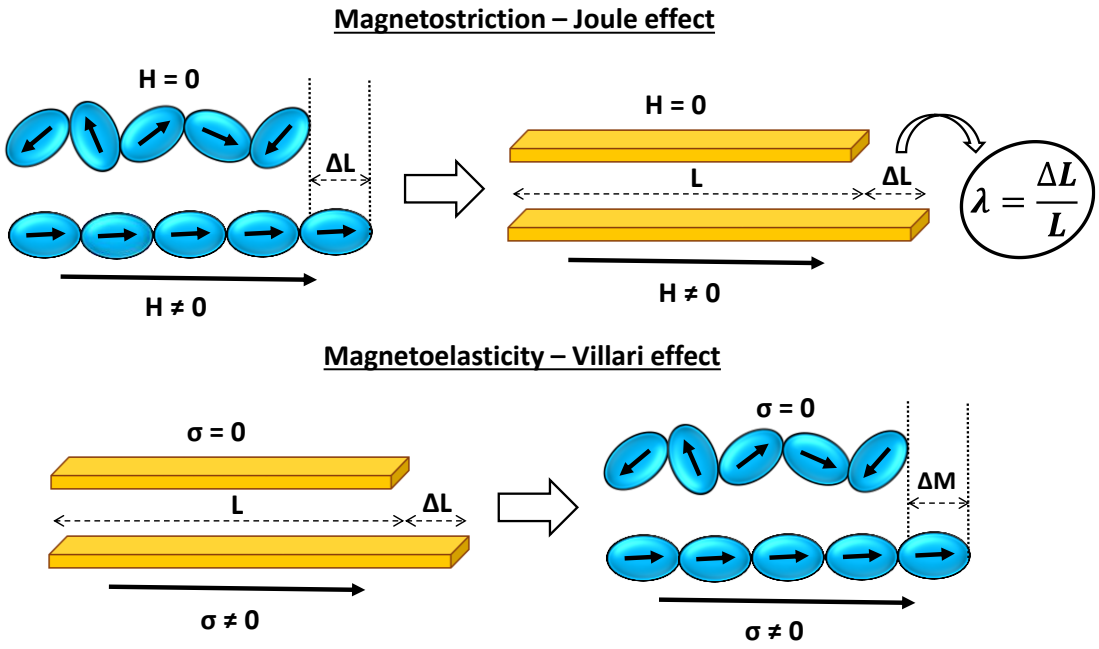

Figure 1.4. Scheme of the magnetostriction and magnetoelasticity effects on a magnetoelastic resonator.

The detection process on magnetoelastic sensors is based on that dependence of their magnetic state under the application of any external force or mechanical load. In particular, when an external alternating excitation magnetic field is applied to a freestanding magnetoelastic ribbon, a standing elastic wave travelling through it is induced. Matching the physical dimensions of the sensing material, the so called magnetoelastic resonance phenomenon appears. This resonance frequency depends on parameters such as the sensor length or composition. In particular, for a rectangular ME resonator of length L, the resonance frequency is given by [27]:

$$f_r = \frac{n}{2L} \cdot \sqrt{\frac{E}{\rho(1-\upsilon)}} \qquad (1.1)$$

where n is the resonance mode and E, ρ and υ are the Young modulus, the density and the Poisson coefficient of the magnetoelastic material, respectively.

Magnetoelastic resonance frequency is inversely proportional to the resonator length *(L)* and directly proportional to the resonance mode *(n)* (**Equation 1.1**). As an illustrative example, resonance curves measured for Metglas 2826MB rectangular resonators of 20, 15 and 10 mm in length are represented in **Figure 1.5a**. The increase on the resonance frequency is accompanied by a reduction in the signal amplitude due to a reduction in the

resonator size (and consequently in the magnetoelastic material mass). Moreover, a common tendency is observed for the first five consecutive resonance modes of a magnetoelastic resonator (**Figure 1.5**b) having that resonance frequencies are higher at higher resonance modes. For that reason, some works select higher resonances modes (n=2, n=3…) to work due to the enhanced shift on the resonance frequency when exposed to a mass load in comparison to the n=1 modes [28,29]. Nevertheless, the signal intensity is strongly reduced at higher resonance modes. For that reason, most of the works on magnetoelastic sensors works in the most intense resonance mode (n=1).

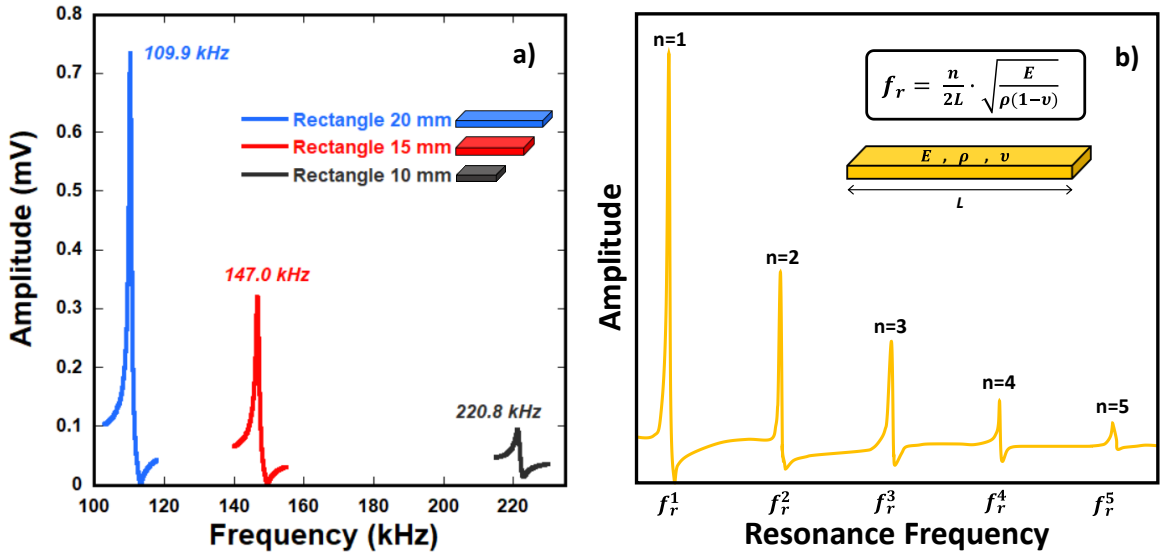

Figure 1.5. (a) Magnetoelastic resonance frequency curves measured for rectangular resonators of different lengths. (b) First five resonance frequencies modes measured for a rectangular magnetoelastic resonator of length L.

1.2.2. Mass sensitivity

In addition to the intrinsic characteristics of the magnetoelastic system, its resonance frequency is affected by different external parameters such as temperature, viscosity or mass loadings. In the particular case of a mass deposition *(Δm)* on the resonator surface, the resonance frequency shifts *(Δf)* to a lower value. This frequency variation *(Δf)* is related with the mass increment *(Δm)* through **equation 1.2** [25]:

$$\frac{\Delta f}{f_0} = -\frac{1}{2} \cdot \frac{\Delta m}{m_0} \qquad (1.2)$$

where f_0 and m_0 are the magnetoelastic resonance frequency and the mass of the bare magnetoelastic resonator, respectively.

The mass increase *(Δm)* on the resonant system when the target compound is adsorbed could be obtained by measuring the resonance frequency shift *(Δf),* being this the base of the sensing process [30]. A scheme of magnetoelastic sensors working principle is represented in **Figure 1.6**.

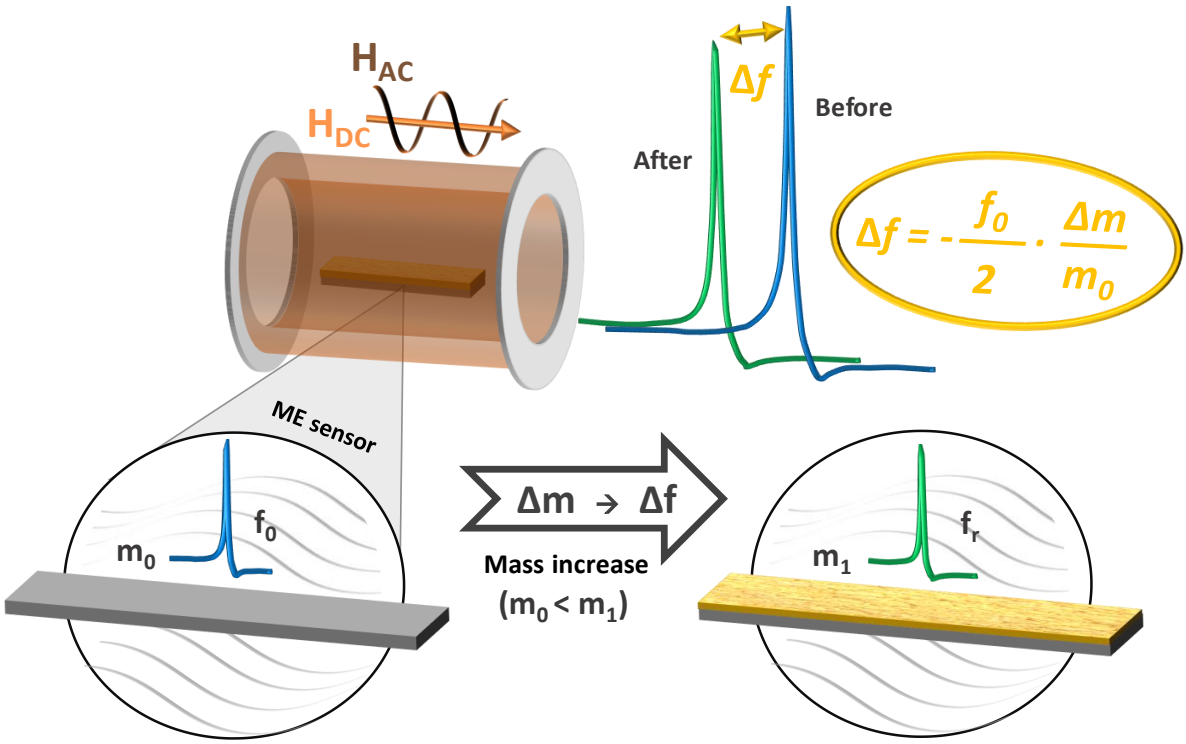

Figure 1.6. Scheme of the resonance frequency change produced in a magnetoelastic resonator due to a mass increase.

The performance of this type of sensors is quantified by its mass sensitivity, which is related to the resonance frequency shift *(Δf)* that the resonant platform undergoes under a mass load *(Δm)*:

$$S = \frac{\Delta f}{\Delta m} \tag{1.3}$$

As sensitivity is critical to quantify the performance of any sensing device, many efforts have been devoted to the improvement of that parameter. In this regard, most of the research in improving the sensitivity rely on the same thing, reduce the size of the

magnetoelastic resonant platform since this lead to an increase on the resonance frequency and hence to an increase on the mass sensitivity [31,32]. Nevertheless, another approaches to increase this parameter should be looking for.

Moreover, as it has been previously mentioned, in most sensing applications, the magnetoelastic resonator acts just as the transducer of the mass adsorbed into its active layer, which is the active part of the device that confers the capacity and selectivity to capture a target compound. Varying the type of the active adsorbent layer *(i.e. polymers, biomolecular-recognition elements, metal-oxides, zeolites or nanoparticles)* many magnetoelastic sensors have been successfully applied to measure different physical and chemical parameters such as pH [33], viscosity [34], humidity [35], microorganisms [36], heavy metals [37], carbon dioxide [38] or VOCs [39].

Some applications reported for magnetoelastic based sensors are summarized in **Table 1.1** together with the magnetoelastic material and the active layer employed in each case. The broad applicability of magnetoelastic sensors demonstrates the versatility of these systems.

Table 1.1. Different chemical, biological and physical parameters detected by using magnetoelastic based sensors functionalized with different active layers.

Analyte	Magnetoelastic material	Active layer	Ref.
	Chemical compounds		
Amonia	Metglas 2826MB	Poly(acrylic acid-co-isooctylacrilate)	40
Ethylene	Metglas 2826MB	Pt-TiO_2 films	41
CO_2	Metglas 2826MB	Zeolite (FAU)	42
VOCs	Metglas 2826MB	Polymer (BAYHYDROL- 110)	39
VOCs	Metglas 2826MB	Zeolites (FAU, LTA and MFI.)	43
Polymer deposition	$Fe_{64}Co_{17}Si_{6.6}B_{12.4}$	-	44
Calcium oxalate and brushite precipitation	Metglas 2826MB	-	45
Fe_3O_4	Metglas 2605S3A ($Fe_{77}Cr_2Si_5B_{16}$)	-	46
Uranium (U)	Metglas 2826MB	Starch gel	47
Mercury (Hg)	Metglas 2826MB	Graphene oxide	48
Pb^{2+}, Cd^{2+} and Cu^{2+}	Metglas 2826MB	Bovine serum albumin (BSA)	37

Analyte	Magnetoelastic material	Active layer	Ref.
	Biological compounds		
Glucose	Metglas 2826MB	pH-sensitive polymer with glucose oxidase	49
Bacillus anthracis spores	Iron–boron alloy	Filamentous landscape phage	50
Bacillus anthracis spores	Metglas 2826MB	Filamentous JRB7 phage	51
Salmonella typhimurium	Metglas 2826MB	Filamentous E2 phage	52
Escherichia coli	Vitrovac 7600 T70 and Metglas 2826MB	Anti-E. coli polyclonal antibodies	53
Swine fever virus	Metglas 2826MB	E2 glycoprotein	54
Hemoglobin oxidation	Metglas 2826MB	ZnO nanoparticles	55
Atrazine	Metglas 2826MB	Atrazine antibody	56
Carcinoembryonic antigen	Metglas 2826MB	CEA antibody,	57
Human serum albumin	Metglas 2826MB	Anti-HSA IgG antibody	58
Mutated DNA	Metglas 2826MB	Thiolated DNA	59
	Other parameters		
Ethanol	$Fe_{83}Ga_{17}$ Wires	-	60
Density and viscosity simultaneously	Metglas 2826MB	TiO_2 layer	61
Oil viscosity	Vitrovac 4040 / 7600	-	34
VOCs and blood viscosity	Metglas 2826MB	-	28
Air, water and acetone viscosity	$Fe_{77.5}Si_{7.5}B_{15}$ Wires	-	62
Humidity	Metglas 2826MB	TiO_2 nanotubes	63
pH	Metglas 2826MB	Poly(acrylic acid-co-isooctyl acrylate)	64

As could be observed, Metglas 2826MB magnetoelastic alloy stands out as the most employed material in the different applications although the research community is also starting to investigate other magnetoelastic materials with different compositions (marked in green in **Table 1.1**). Metglas 2826MB is an iron-rich amorphous ferromagnetic alloy ($Fe_{37}Ni_{42}Mo_4B_{17}$) widely used in magnetoelastic sensing applications due to its good magnetic and magnetoelastic properties, such as high magnetoelastic coupling *(0.98)*, high saturation magnetostriction *(12 ppm)* and high saturation magnetization *(0.88 T)*. In addition, its high corrosion resistance makes it ideal for sensing applications in harsh

environments. All these properties, combined with its low cost, make this alloy perfect to be used for different magnetoelastic sensing applications.

Considering the fundamental principles of magnetoelastic based sensors, the mass gain (Δm) derived from the adsorption capacity and selectivity of the active layer over the target is also a key factor that affects its sensing performance together with the resonator sensitivity. As could be concluded from the state of the art summarized in the **Table 1.1**, very different parameters have been sensed by varying the active layer as well as its physicochemical characteristics. But, it is very important to note that the nature of the active layer and its integration process on the magnetoelastic platform could also have negative effects on the quality and intensity of its magnetoelastic signal [63]. In this regard, it is of paramount importance not only to improve the active layer adsorption capacity and selectivity towards the desired target pollutants but also to maintain the quality and intensity of the magnetoelastic response of the transductor once the active layer is integrated into the sensing device.

On that way, among the broad scope of materials that can be applied as active layers in sensing devices, Metal Organic Frameworks (MOFs) stand up due to their excellent adsorption capacities and outstanding versatility to tune their pore chemistry in order to endow them of high adsorption capacities and selectivities [65]. However, there is no previous research on the use of MOFs materials as the active layer on magnetoelastic sensors, which is a striking fact considering the overall characteristics of these versatile porous organic-inorganic materials to capture many different pollutants.

1.3. Metal Organic Frameworks as potential active layers

Thus, Metal Organic Frameworks represent an outstanding opportunity to further improve the adsorption capacity and selectivity of magnetoelastic based sensors due to their intrinsic characteristics, which will be briefly summarized below.

Proposed in the late 1990s by Omar Yaghi at University of Michigan [66], MOFs have become a rapidly evolving research field. These materials are so promising that in the last twenty years, the number of publications regarding the term “MOFs” has grown exponentially to reach more than 10.000 publications in 2019 (**Figure 1.7**).

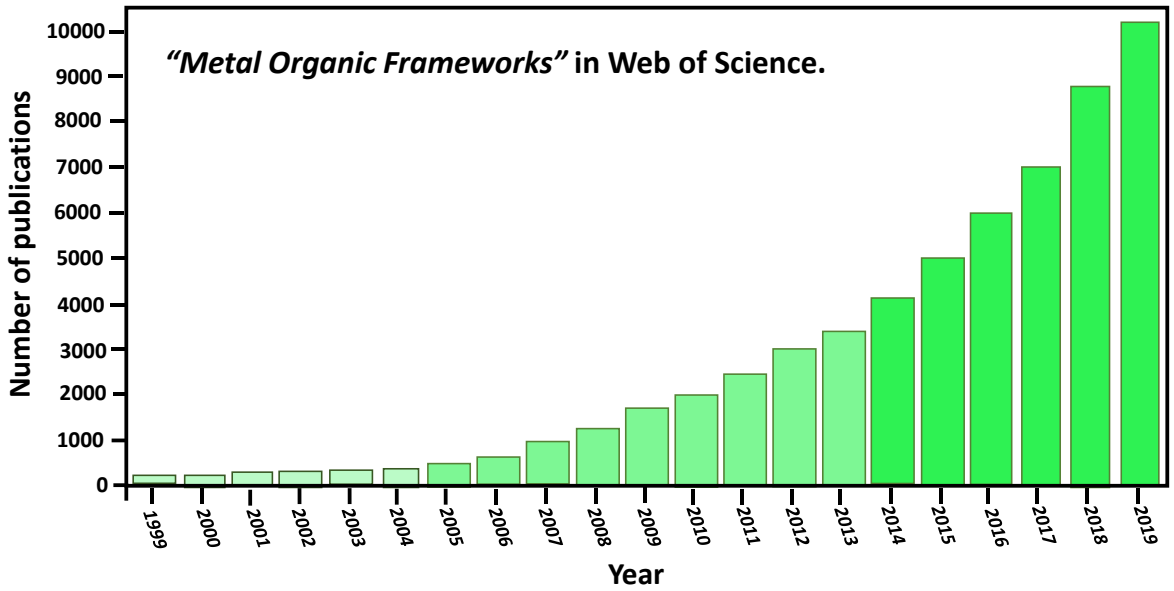

Figure 1.7. Number of publications containing "Metal Organic Frameworks" in their topics. (Source: ISI Web of Science – June, 2020).

MOFs are crystalline porous coordination compounds built out of metal nodes (ions or clusters) connected by organic ligands (linkers) through coordination bonds to give rise to a wide variety of highly porous networks that extend in space. So far, more than 80000 different MOF structures have been reported in the Cambridge Structural Database, and this number grows daily, despite most of them have not been practically applied [67]. This is 330 times the number of reported zeolite structures which account their versatility. In terms of the number of building blocks to assemble MOF materials, 90 different metal nodes with more than 1000 different organic ligands with different geometries and connectivities have been already used to assemble MOF porous materials, without counting MOFs assembled from metal-mixed cluster or multivariate linkers [68,69]. The main properties of these materials, together with the structures of some of the most employed MOFs, are shown in **Figure 1.8**.

MOFs materials stand out since, among other characteristics, they offer the highest surface areas per gram of any known material. These surface areas can range from 1000 up to 10000 m^2/g, thus exceeding significantly that of other porous materials such as zeolites or activated carbons [70]. One of the most interesting characteristics of MOFs regarding their possible use as active layers in magnetoelastic resonators is that their porosity and chemistry can be tuned and directed towards a high capacity and selective recognition of specific adsorbates.

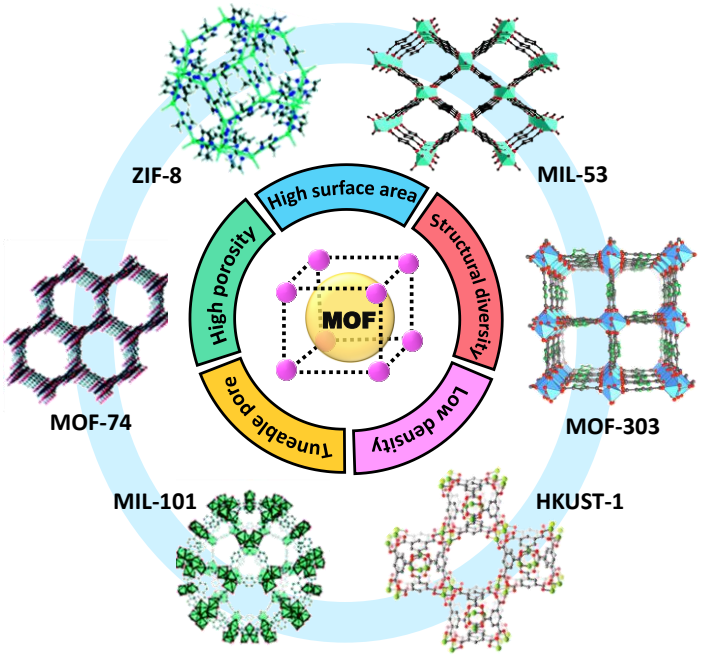

Figure 1.8. Structure of some of the most employed MOFs together with their main properties.

In particular, the pore size in these materials is determined by the characteristics of their basic construction units [71,72] (organic ligands and metal clusters) and how they are assembled in extended frameworks (topology). MOFs´ porosity can be modulated and controlled by extending the net through the incorporation of linkers with different lengths into structures maintaining the same initial connectivity and topology (isoreticular expansion) [73]. Needless to mention the importance of defect chemistry of MOF materials, where vacant sites both at linkers and clusters positions can be partially controlled through the synthesis condition or addition of modulators, having these defective sites a tremendous impact both in the porosity and post-functionalization versatility of MOFs [74]. In retrospective, both, the composition and functions of inorganic and organic building blocks of MOFs can be pre-or post-synthetically tuned until the overall characteristics of the porous materials fits these needed for your application [75].

This tunability at porous, composition and functional levels is the main characteristic that differentiates MOFs from other porous materials such as zeolites or activated carbon, making them the perfect candidates for selective adsorption applications [76,77]. But what makes them fit perfectly when applying as active layers of magnetoelastic systems is that MOF combine these versatilities with very low framework densities, which made that during adsorption their mass increase significantly. And as already pointed, sensitivity of magnetoelastic sensing devices is based fundamentally on mass loading increase during the process.

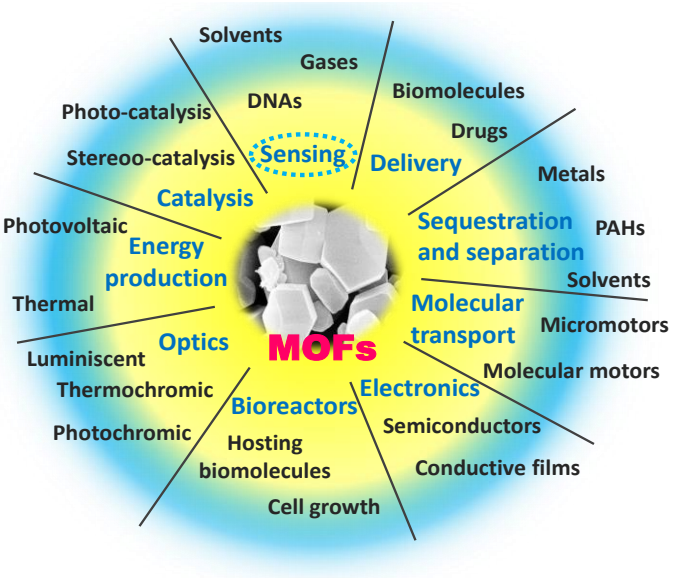

Figure 1.9. Different areas in which MOFs materials have been employed so far.

Due to that excellent properties, applications of MOFs have grown exponentially over the last two decades. Originally applied in areas where specific surface area is critical, such as gas adsorption, gas storage, filtration or catalysis. In recent years it has been shown that these porous materials also present huge potential in other very different areas such optics [78], microelectronics [79], sensing [80], biomedical [81] or energy storage [82] (**Figure 1.9**), since as mentioned before, the physical-chemical properties of the MOFs can be controlled by properly choosing their building blocks and their chemical functionalizations [83].

In the particular area of sensing, MOFs have been already employed for the detection of very different chemical and biological parameters by means of different detection approaches. In principle, any change on the MOF properties under the presence of a target molecule could be used as a sensing response that can be translated into an electrical signal through the proper transduction system. According to the transduction mechanism, sensors based on MOFs have been mostly classified into three main groups [80,84]: Optical, mechanical and electrical sensors (**Figure 1.10**). In the case of optical sensing, the main applied strategy is to endow MOFs of photo-luminescent building blocks, like aromatic or conjugated p moieties in the linkers [85]. When the target compound is adsorbed into the pores of the

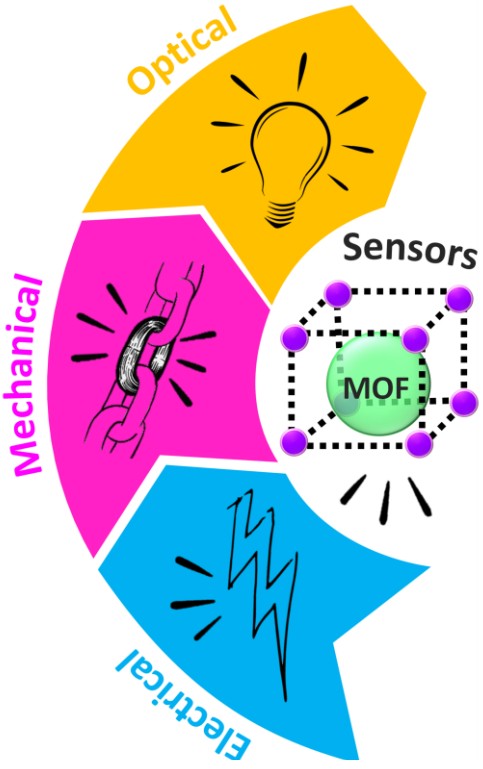

Figure 1.10. Transduction mechanisms on MOF based sensors.

MOF with optical properties, changes on parameters such as the visible colour, luminescence intensity or shifts on the refractive index can be detected, which is the base of the optical sensing process [86]. Secondly, despite the insulating properties of the majority of MOFs, conductive MOFs have been successfully synthesized by using appropriate organic linkers or by doping the MOF with conductive materials such as nanoparticles [87]. This electrical conductive MOFs combine a noticeable variation in the electrical properties (i.e. resistance, capacitance or coupled selective oxidation/reduction process) upon interaction with a target molecule, being that the base of the electrical detection process [88]. Non-conductive MOFs have been also applied in electrical and electrochemical devices by blending or growing the MOF active layer onto conductive substrates.

Finally, MOF mechanical sensors are based on the use of transduction devices to transform the mass gain due to the adsorption of a specific target compound by the MOF structure into a measurable signal (mechanical response). For that purpose, the MOF are deposited as active layers into the transduction device, allowing the adsorption of the analyte into the surface of the mechanical sensor. As mentioned before, this is the sensing mechanism of the AW based sensors. In fact, MOFs have been already successfully employed as the active component in different AW devices, such as MCL [89] or the QCM [90], endowing them of good detection capacities and high sensitivities due to extremely high surface area of the MOF active layers.

Nevertheless, despite the wide variety of applications of MOF materials in the sensing field, and particularly in AW devices, there is no previous research on the use of MOFs as active layers on magnetoelastic resonators, which is a striking fact considering the higher adsorption capacities of these materials in comparison to zeolites, activated carbons or polymeric compounds. For that reason, MOFs as potential active layers in magnetoelastic sensors have been selected in this investigation, exploring their integration into magnetoelastic resonators, and afterwards, their impact on the quality, intensity and wireless sensing capacity of the MOF functionalized magnetoelastic systems in both gaseous and aqueous media.

1.4. Objectives and structure of this thesis

To conclude with this introductory section, the main scientific objectives of this thesis are presented below together with the thesis structure. Taking into account the previously mentioned antecedents and hypothesis, the main objective of this thesis is to assess the feasibility of MOFs based magnetoelastic resonators to detect harmful compounds in air and aqueous media, focusing the analysis in the specific cases of toluene volatile organic compound (VOC) and hexavalent chromium heavy metal (HM).

To this end, highly sensitive magnetoelastic resonators on the one hand, and MOFs with high adsorption capacities for different target VOCs and HMs, on the other, have been developed. Subsequently, the integration of the MOF active layer on the magnetoelastic resonator's surface has been investigated. Finally, the magnetoelastic sensors have been tested for the wireless sensing of the aforementioned target compounds. In this way, a specific system for the detection of VOCs in continuous flux mode has also been assembled to carry out the gas sensing experiments. The main scientific objectives of this work are detailed on the following.

- Scientific objectives

1. To improve the magnetoelastic response of the resonators by modifying its size and geometry.

2. Identify, synthesize and characterize specific MOFs with affinity to sorb HMs and VOCs and compatible with the magnetoelastic resonator system.

3. To integrate at the surface of the magnetoelastic resonators the selected MOFs.

4. Study the HMs sensing capacity of the developed hybrid systems.

5. Develop an experimental set-up capable of controlling the concentration of VOCs to carry out the sensing experiments.

6. Study the VOCs detection capacity of the developed sensors.

Based on these objectives, this work has been structured into several stages that go from the design of the idea to its final application (applied research) passing through the creation of the materials (fundamental research) and their implementation in a single system, in line with the value chain (**Figure 1.11**).

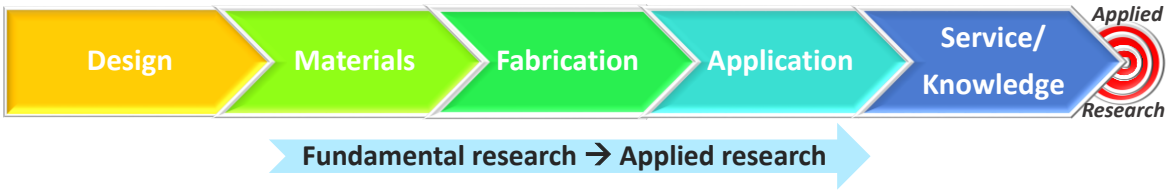

Figure 1.11. Value chain of this investigation (from the fundamental research to the applied research).

Taking into account the previously mentioned objectives, the thesis has been divided into six chapters related to the intermediate milestones to be achieved until the final goal is reached. After the introduction in Chapter 1, the second chapter focuses on the improvement of the mass sensitivity of the magnetoelastic sensors by modifying their geometry. An extensive study of the magnetoelastic properties of resonators with varied geometries, which range from the classically employed rectangular geometry to geometries such as triangles or rhombus, is presented. First, two asymmetric geometries (a triangle and an arched triangle) are introduced and characterized comparing them with the classic rectangle. The effect of the surface coating percentage on these geometries is also deeply analysed. Moreover, a symmetrical geometry, a rhombic one, is later introduced and also compared with the rectangles. The effect of the resonator length on the sensitivity and other magnetoelastic parameters is also deeply analysed. Besides, a multiple sensor design based on the combination of two of these geometries (the rhomb and the rectangle) is proposed and tested. Finally, the magnetic response of magnetoelastic resonators is deeply characterized, and their magnetic microstructure is analysed by Kerr Microscopy.

Afterwards, Chapter 3 is focus on the functionalization of the magnetoelastic resonators with the MOFs materials. This chapter mainly explores the different MOF functionalization processes of the magnetoelastic alloys, as well as their advantages and disadvantages in order to meet the incorporation of the MOF into the resonator and the chemical stability of the magnetoelastic transductor. The functionalization techniques employed have been classified into two main groups: direct synthesis and post-synthesis deposition. The use of one type of functionalization method or another mainly depends on the chemical characteristic of the MOF synthesis media, and specifically of its acidity.

The next two chapters (Chapters 4 and 5) are focus on the characterization and application of the synthesized MOFs and MOF-based resonator systems for the detection of VOCs and HMs. In particular, Chapter 4 is focus on water depollution and monitorization, and most in particular in Heavy Metals (HMs). The work presented in this chapter has been mostly developed at the Advanced Mining Technology Centre (AMTC) and the University of Santiago de Chile (Chile). First, functional groups and linker defect degree of UiO-66-R zirconium terephthalate archetypal MOF have been modified to tune its adsorption and photoreduction capacity over hexavalent chromium. Afterwards, the post-adsorption/photo-reduction MOF samples have been characterized by different techniques in order to investigate the chromium speciation once after the operation process. Finally, the performance of the MOF decorated novel resonators geometries has been tested over the detection of heavy metals in aqueous media.

Secondly, Chapter 5 is focus on air pollution, more in particular in Volatile Organic Compounds (VOCs). In this chapter, the experimental set-up developed for the VOCs sensing experiments is first described in detail. This experimental set-up was developed at BCMaterials thanks to the notions taken from the home-made set-up at the University of Patras (Greece). Secondly, the application of the fabricated sensors with the MOF active layers for the detection of toluene is described. In particular, an exhaustive analysis of the effect of parameters such as the MOF active layer mass or selectivity on the sensing process has been performed herein.

Finally, in Chapter 6, the main conclusions derived from the whole thesis are presented together with the open perspectives. The general objectives and the thesis structure are outlined in **Figure 1.12**.

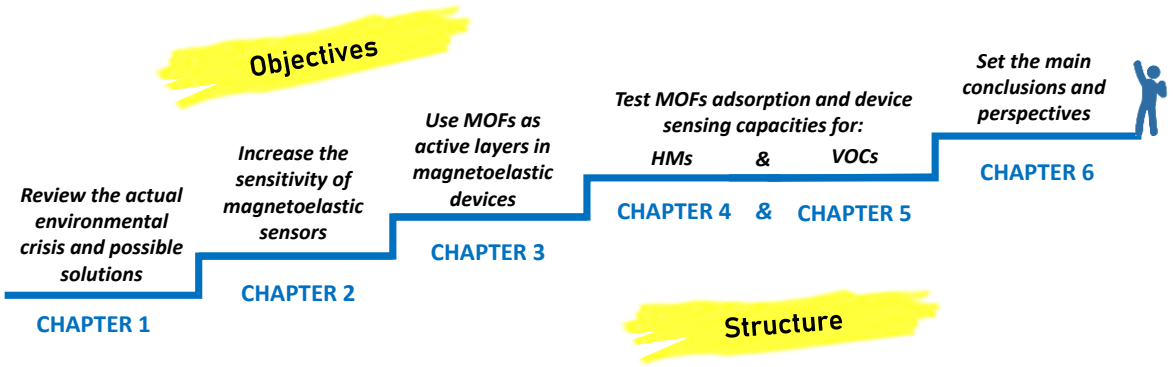

Figure 1.12. Scheme of the main objectives of this thesis together with the structure of the same.

Moreover, Annex A collect the detailed experimental part of the whole thesis, from the magnetoelastic resonators fabrication to the characterization techniques employed for the characterization of the MOFs and the active layers deposited onto the magnetoelastic resonators. All the analytical calculations performed are detailed in Annex B, and all the works arising from this thesis and from other collaborations are collected on Annex C.

1.5. References

1. Pink, R. M. *The climate change crisis: Solutions and adaption for a planet in peril*. (Springer US, 2018).

2. Manzanedo, R. D., & Manning, P. COVID-19: Lessons for the climate change emergency. *Sci. Total Environ.* **742**, 140563 (2020).

3. Ruiu, M. L., Ragnedda, M., & Ruiu, G. Similarities and differences in managing the Covid-19 crisis and climate change risk. *J. Knowl. Manag.* (2020). doi:10.1108/JKM-06-2020-0492

4. Horizon 2020. *European comission* 09/2020 Available at: https://eshorizonte2020.es/. (Accessed: 18th September 2020)

5. Horizon Europe. *European comission* 09/2020 Available at: https://ec.europa.eu/info/horizon-europe-next-research-and-innovation-framework-programme_en. (Accessed: 18th September 2020)

6. Sustainable development goals (2030 agenda). Available at: https://www.un.org/sustainabledevelopment/sustainable-development-goals/.

(Accessed: 18th September 2020)

7. 2030 Agenda. Available at: https://www.agenda2030.gob.es/objetivos/home.htm. (Accessed: 20th September 2020)

8. Spinelle, L., Gerboles, M., Kok, G., Persijn, S. & Sauerwald, T. Review of portable and low-cost sensors for the ambient air monitoring of benzene and other volatile organic compounds. *Sensors* **17**, 1–30 (2017).

9. Viespe C., & Miu, D. Characteristics of surface acoustic wave sensors with nanoparticles embedded in polymer sensitive layers for VOC detection. *Sensors* **18**, 1–9 (2018).

10. Sartore, L., Barbaglio, M., Borgese, L., & Bontempi, E. Chemical polymer-grafted QCM chemical sensor and application to heavy metal ions real time detection. *Sensors Actuators B. Chem.* **155**, 538–544 (2011).

11. Zhao, R. & Sun, Y. Polymeric flexible immunosensor based on piezoresistive micro-cantilever with PEDOT/PSS conductive layer. *Sensors (Switzerland)* **18**, (2018).

12. Yan, X., Li, H. & Su, X. Review of optical sensors for pesticides. *TrAC - Trends Anal. Chem.* **103**, 1–20 (2018).

13. Correa-Mena, A. G., Gonzalez, L. A., Quintero-Rodriguez, L. J. & Zaldivar-Huerta, I. E. Review on integrated optical sensors and its applications. *IEEE Mex. Humanit. Technol. Conf.* 170–173 (2017). doi:10.1109/MHTC.2017.7926204

14. Cardoso, R. M., Kalinke, C., Rocha, R. G., dos Santos, P. L., Rocha, D. P., Oliveira, P. R.., Janegitz, B. C., Bonacin, J. A., Richter, E. M., & Munoz, R. A. A. Additive-manufactured (3D-printed) electrochemical sensors: A critical review. *Anal. Chim. Acta* **1118**, 73–91 (2020).

15. Kempahanumakkagari, S., Deep, A. Kim, K. H., Kumar Kailasa, S., & Yoon, H. O. Nanomaterial-based electrochemical sensors for arsenic - A review. *Biosens. Bioelectron.* **95**, 106–116 (2017).

16. Mirzaei, A., Kim, J. H., Kim, H. W. & Kim, S. S. Resistive-based gas sensors for detection of benzene, toluene and xylene (BTX) gases: A review. *J. Mater. Chem. C* **6**, 4342–4370 (2018).

17. Wong, Y. C., Ang, B. C., Haseeb, A. S. M. A., Baharuddin, A. A., & Wong, Y. H. Conducting polymers as chemiresistive gas sensing materials: A review. *J. Electrochem. Soc.* **167**,

037503 (2020).

18. Devkota, J., Ohodnicki, P. R. & Greve, D. W. SAW sensors for chemical vapors and gases. *Sensors* **17**, 13–15 (2017).

19. Bao, Y., Xu, P., Cai, S., Yu, H., & Li, X. Detection of volatile-organic-compounds (VOCs) in solution using cantilever-based gas sensors. *Talanta* **182**, 148–155 (2018).

20. Noi, K., Iwata, A., Kato, F., & Ogi, H. Ultrahigh-frequency, wireless MEMS QCM biosensor for direct, label-free detection of biomarkers in a large amount of contaminants. *Anal. Chem.* **91**, 9398–9402 (2019).

21. García, L., Jiménez, J. M., Taha, M. & Lloret, J. Wireless technologies for IoT in smart cities. *Netw. Protoc. Algorithms* **10**, 23–64 (2018).

22. Alaba, F. A., Othman, M., Abaker, I., Hashem, T., & Alotaibi, F. Internet of Things security : A survey. **88**, 10–28 (2017).

23. Libelium. IoT applications to reduce management costs. Available at: https://www.libelium.com/. (Accessed: 15th July 2020)

24. Kassal, P., Steinberg, M. D. & Steinberg, I. M. Wireless chemical sensors and biosensors: A review. *Sensors Actuators, B Chem.* **266**, 228–245 (2018).

25. Grimes, C. A., Mungle, C. S., Zeng, K., Jain, M. K., Dreschel, W. R. Paulose, M., & Ong, K. G. Wireless magnetoelastic resonance sensors : A critical review. *Sensors* **2**, 294–313 (2002).

26. Le Bras, Y., & Greneche, J. M. Magnetoelastic resonance: Principles, modeling and applications. *Resonance* **2**, 13–34 (2017).

27. Liang, C., Morshed, S., & Prorok, B. C. Correction for longitudinal mode vibration in thin slender beams. *Appl. Phys. Lett.* **90**, 221912 (2007).

28. Cheng, P., Gao, S. & Zhang, W., Wang, T., Jian, A., & Sang, S. Resonance modes of freestanding magnetoelastic resonator and the application in viscosity measurement. *Smart Mater. Struct.* **24**, (2015).

29. Zhang, K., Zhang, L. & Chai, Y. Mass load distribution dependence of mass sensitivity of magnetoelastic sensors under different resonance modes. *Sensors* **15**, 20267–20278 (2015).

30. Grimes, C. A., Roy, S. C., Rani, S. & Cai, Q. Theory, instrumentation and applications of magnetoelastic resonance sensors: A review. *Sensors* **11**, 2809–2844 (2011).

31. Sagasti, A., Gutiérrez, J., Sebastián, M. S. & Barandiarán, J. M. Magnetoelastic resonators for highly specific chemical and biological detection : A critical study. *IEEE Trans. Magn.* **53**, 10–13 (2017).

32. Cheng, Z. Y., Li, S. Q., Zhang, K. W., Fu, L. L. & Chin, B. A. Novel magnetostrictive microcantilever and magnetostrictive nanobars for high performance biological detection. *Adv. Sci. Technol.* **54**, 19–28 (2008).

33. Cai, Q. Y. & Grimes, C. A. A remote query magnetoelastic pH sensor. *Sensors Actuators, B Chem.* **71**, 112–117 (2000).

34. Bravo, I., Arnaiz, A. & Garcia-Arribas, A. Damping of magnetoelastic resonance for oil viscosity sensing. *IEEE Trans. Magn.* **55**, (2019).

35. Jain, M. K., Schmidt, S., Ong, K. G., Mungle, C. & Grimes, C. A. Magnetoacoustic remote query temperature and humidity sensors. *Smart Mater. Struct.* **9**, 502–510 (2000).

36. Huang, S., Yang, H., Lakshmanan, R. S. Johnson, M. L., Wan, J., Chen, I., Wikle III, H. C., Petrenko, V. A., Barbaree, J. M., & Chin, B. A. Sequential detection of Salmonella typhimurium and Bacillus anthracis spores using magnetoelastic biosensors. *Biosens. Bioelectron.* **24**, 1730–1736 (2009).

37. Guo, X., Sang, S., Jian, A., Gao, S., Duan, Q., Ji, J., Zhang, Q., & Zhang, W. A bovine serum albumin-coated magnetoelastic biosensor for the wireless detection of heavy metal ions. *Sensors Actuators, B Chem.* **256**, 318–324 (2018).

38. Cai, Q. Y., Cammers-Goodwin, A. & Grimes, C. A. A wireless, remote query magnetoelastic CO_2 sensor. *J. Environ. Monit.* **2**, 556–560 (2000).

39. Baimpos, T., Boutikos, P., Nikolakis, V. & Kouzoudis, D. A polymer-Metglas sensor used to detect volatile organic compounds. *Sensors Actuators, A Phys.* **158**, 249–253 (2010).

40. Cai, Q. Y., Jain, M. K. & Grimes, C. A. A wireless, remote query ammonia sensor. *Sensors Actuators, B Chem.* **77**, 614–619 (2001).

41. Zhang, R., Tejedor, M. I., Anderson, M. A., Paulose, M. & Grimes, C. A. Ethylene detection using nanoporous PtTiO2 coatings applied to magnetoelastic thick films. *Sensors* **2**, 331–338 (2002).

42. Giannakopoulos, I. G., Kouzoudis, D., Grimes, C. A. & Nikolakis, V. Synthesis and characterization of a composite zeolite-metglas carbon dioxide sensor. *Adv. Funct. Mater.* **15**, 1165–1170 (2005).

43. Baimpos, T., Gora, L., Nikolakis, V. & Kouzoudis, D. Selective detection of hazardous VOCs using zeolite/Metglas composite sensors. *Sensors Actuators, A Phys.* **186**, 21–31 (2012).

44. Sagasti, A., Gutierrez, J., San Sebastian, M. & Barandiaran, J. M. Magnetoelastic resonators for highly specific chemical and biological detection: A critical study. *IEEE Trans. Magn.* **53**, (2017).

45. Bouropoulos, N., Kouzoudis, D. & Grimes, C. The real-time, in situ monitoring of calcium oxalate and brushite precipitation using magnetoelastic sensors. *Sensors Actuators, B Chem.* **109**, 227–232 (2005).

46. Atalay, S., Kolat, V. S., Atalay, F. E., Bayri, N., Kaya, H., & Izgi, T. Magnetoelastic sensor for magnetic nanoparticle detection. *J. Magn. Magn. Mater.* **465**, 151–155 (2018).

47. Zhao, Z., Liao, L., Xiao, X., Du, N. & Lin, Y. Determination of uranium in water based on enzyme inhibition using a wireless magnetoelastic sensor. *Int. J. Environ. Anal. Chem.* **93**, 613–622 (2013).

48. Huang, Y.Q., Yin, J.C., Wang, Y. S., Xiao, X. L., Zhou, B., Xue, J. H., Tang, X., Wang, X. F., Zhu, Y. F., & Chen, S. H. Streptavidin and gold nanoparticles-based dual signal amplification for sensitive magnetoelastic sensing of mercury using a specific aptamer probe. *Sensors Actuators, B Chem.* **235**, 507–514 (2016).

49. Gao, X., Yang, W., Pang, P., Liao, S., Cai, Q., Zeng, K., & Grimes, C. A. A wireless magnetoelastic biosensor for rapid detection of glucose concentrations in urine samples. *Sensors Actuators, B Chem.* **128**, 161–167 (2007).

50. Johnson, M. L., Wan, J., Huang, S., Cheng, Z., Petrenko, V. A., Kim, D. J., Barbaree, J.M., Hong J. W., & Chin, B. A. A wireless biosensor using microfabricated phage-interfaced magnetoelastic particles. *Sensors Actuators, A Phys.* **144**, 38–47 (2008).

51. Shen, W., Lakshmanan, R. S., Mathison, L. C., Petrenko, V. A. & Chin, B. A. Phage coated magnetoelastic micro-biosensors for real-time detection of Bacillus anthracis spores. *Sensors Actuators, B Chem.* **137**, 501–506 (2009).

52. Li, S., Li, Y., Chen, H., Horikawa, S., Shen, W., Simonian, A., & Chin, B. A. Direct detection of Salmonella typhimurium on fresh produce using phage-based magnetoelastic biosensors. *Biosens. Bioelectron.* **26**, 1313–1319 (2010).

53. Xue, C., Yang, C., Xu, T., Zhan, J. & Li, X. A wireless bio-sensing microfluidic chip based on resonating 'μ-divers'. *Lab Chip* **15**, 2318–2326 (2015).

54. Guo, X., Sang, S., Guo, J., Jian, A., Duan, Q., Ji, J., Zhang, Q., & Zhang, W. A magnetoelastic biosensor based on E2 glycoprotein for wireless detection of classical swine fever virus E2 antibody. *Sci. Rep.* **7**, 1–8 (2017).

55. Sagasti, A., Bouropoulos, N., Kouzoudis, D. Panagiotopoulos, A., Topoglidis, E., & Gutiérrez, J. Nanostructured ZnO in a Metglas/ZnO/hemoglobin modified electrode to detect the oxidation of the hemoglobin simultaneously by cyclic voltammetry and magnetoelastic resonance. *Materials (Basel).* **10**, 1–17 (2017).

56. Sang, S., Guo, X. Liu, R., Wang, J., Guo, J., Zhang, Y., Yuan, Z., & Zhang, W. A novel magnetoelastic nanobiosensor for highly sensitive detection of atrazine. *Nanoscale Res. Lett.* **13**, (2018).

57. Wang, Ji. Guo, X. Liu, R. Guo, J. Zhang, Y. Zhang, W. & Sang, S. Detection of carcinoembryonic antigen using a magnetoelastic nano-biosensor amplified with DNA-templated silver nanoclusters. *Nanotechnology* **31**, (2020).

58. Liu, R. Guo, X. Wang, J. Guo, J. Zhang, Y. Zhang, W. & Sang, S. High sensitivity detection of human serum albumin using a novel magnetoelastic immunosensor. *J. Mater. Sci.* **54**, 9679–9688 (2019).

59. Guo, X. Wang, J. Zhao, Y. Liu, R. Zhang, Q. Yuan, Z. & Sang, S. A wireless magnetoelastic DNA-biosensor amplified by AuNPs for the detection of a common mutated DNA causing β-thalassaemia. *Biochem. Eng. J.* **156**, (2020).

60. Sang, S., Cheng, P. Zhang, W. Li, P. Hu, J. Li, G., & Jian, A. Investigation on a new $Fe_{83}Ga_{17}$ wire-based magnetoelastic resonance biosensor. *J. Intell. Mater. Syst. Struct.* **26**, 980–987 (2015).

61. Grimes, C. A., Kouzoudis, D., Mungle, C. & Grimes, C. A. Simultaneous measurement of liquid density and viscosity using remote query magnetoelastic sensors. **3822**, 15–18 (2012).

62. Atalay, S., Kolat, V. S., Bayri, N. & Izgi, T. Magnetoelastic sensor studies on amorphous magnetic FeSiB wire and the application in viscosity measurement. *J. Supercond. Nov. Magn.* **29**, (2016).

63. Atalay, S., Izgi, T., Kolat, V. S., Erdemoglu, S. & Inan, O. O. Magnetoelastic humidity sensors with TiO_2 nanotube sensing layers. *Sensors* **20**, 1–12 (2020).

64. Ruan, C., Zeng, K. & Grimes, C. A. A mass-sensitive pH sensor based on a stimuli-responsive polymer. *Anal. Chim. Acta* **497**, 123–131 (2003).

65. Maurin, G., Serre, C., Cooper, A., & Férey, G. The new age of MOFs and of their porous-related solids. *Chem. Soc. Rev.* **46**, 3104–3107 (2017).

66. Li, H., Eddaoudi, M., O'Keeffe, M., & Yaghi, O. M. Design and synthesis of an exceptionally stable and highly. *Nature* **402**, 276–279 (1999).

67. NovoMOF. Putting MOFs in Numbers – an Infografic. (2016). Available at: https://novomof.com/blog/putting-mofs-in-numbers-an-infografic/. (Accessed: 8th September 2020)

68. Lu, W., Wei, Z., Gu, Z. Y., Liu, T. F. Park, J., Park, J., Tian, J., Zhang, M., Zhang, Q., Gentle, T., Bosch, M., & Zhou, H. C. Tuning the structure and function of metal-organic frameworks via linker design. *Chem. Soc. Rev.* **43**, 5561–5593 (2014).

69. Liu, J. & Christof, W. Surface-supported metal organic framework thin films: fabrication methods, applications, and challenges. *Chem. Soc. Rev.* **46**, 5730–5770 (2017).

70. Falcaro, P., Ricco, R., Doherty, C. M., Liang, K., Hill, A. J., & Styles, M. J. MOF positioning technology and device fabrication. *Chem. Soc. Rev.* **43**, 5513–5560 (2014).

71. Vellingiri, K., Szulejko, J. E., Kumar, P., Kwon, E. E., Kim, K-H, Deep, A., Boukhvalov, D. W., & Brown, R. J. C. Metal organic frameworks as sorption media for volatile and semi-volatile organic compounds at ambient conditions. *Sci. Rep.* **6**, 1–11 (2016).

72. Wen, J., Fang, Y. & Zeng, G. Progress and prospect of adsorptive removal of heavy metal ions from aqueous solution using metal–organic frameworks: A review of studies from the last decade. *Chemosphere* **201**, 627–643 (2018).

73. Zhao, D. A. N., Timmons, D. J. & Yuan, D. Tuning the topology and functionality of metal-organic frameworks by ligand design. *Acc. Chem. Res.* **44**, 123–133 (2011).

74. Johnstone, D. N., Firth, F. C. N. & Grey, C.P., Midgley, P. A., Cliffe, M. J., & Collins, S. M.

Direct imaging of correlated defect nanodomains in a metal-organic framework. *JACS* **142**, 13081–13089 (2020).

75. Ji, Z., Wang, H. Canossa, S., Wuttke, S., & Yaghi, O. M. Pore Chemistry of Metal – Organic Frameworks. *Adv. Funct. Mater.* **2000238**, 1–24 (2020).

76. Bahri, M., Haghighat, F., Kazemian, H. & Rohani, S. A comparative study on metal organic frameworks for indoor environment application: Adsorption evaluation. *Chem. Eng. J.* **313**, 711–723 (2017).

77. Vellingiri, K., Kumar, P. & Kim, K. Coordination polymers : Challenges and future scenarios for capture and degradation of volatile organic compounds. *Nano Res.* **9**, 3181–3208 (2016).

78. Nguyen, T. N., Ebrahim, F. M., & Stylianou, K. C. Photoluminescent , upconversion luminescent and nonlinear optical metal-organic frameworks: From fundamental photophysics to potential applications. *Coord. Chem. Rev.* **377**, 259–306 (2018).

79. Mendiratta, S., Usman, M., & Lu, K. Expanding the dimensions of metal – organic framework research towards dielectrics. *Coord. Chem. Rev.* **360**, 77–91 (2018).

80. Lei, J., Qian, R., Ling, P. & Cui, L., & Ju, H. Design and sensing applications of metal-organic framework composites. *TrAC - Trends Anal. Chem.* **58**, 71–78 (2014).

81. Yang, J., & Yang, Y. Metal – organic frameworks for biomedical applications. *Small* **1906846**, 1–24 (2020).

82. Wang, H., Zhu, Q., Zou, R., & Xu, Q. Metal-organic frameworks for energy applications. *Chem* **2**, 52–80 (2017).

83. Safaei, M., Mehdi, M., & Ebrahimpoor, N. A review on metal-organic frameworks : Synthesis and applications. *Trends Anal. Chem.* **118**, 401–425 (2019).

84. Li, Y., Xiao, A., Zou, B., Zhang, H., Yan, K., & Lin, Y. Advances of metal – organic frameworks for gas sensing. *Polyhedron* **154**, 83–97 (2018).

85. Hu, Z., Deibert, B. J., & Li, J. Luminescent metal–organic frameworks for chemical sensing and explosive detection. *Chem. Soc. Rev.* **43**, 5815–5840 (2014).

86. He, J., Xu, J., Yin, J., Li, N., & Bu, X. H. Recent advances in luminescent metal-organic frameworks for chemical sensors. *Sci. China Mater.* **62**, 1655–1678 (2019).

87. Anik, U., Timur, S., & Dursun, Z. Metal organic frameworks in electrochemical and optical sensing platforms : a review. *Microchim. Acta* **186**, 18–24 (2019).

88. Liu, C. S., Li, J., & Pang, H. Metal-organic framework-based materials as an emerging platform for advanced electrochemical sensing. *Coord. Chem. Rev.* **410**, 213222 (2020).

89. Cai, S., Li, W., Xu, P., Xia, X., Yu, H., Zhang, S., & Li, X. In situ construction of metal–organic framework (MOF) UiO-66 film on Parylene-patterned resonant microcantilever for trace organophosphorus molecules detection. *Analyst* **144**, 3729–3735 (2019).

90. Haghighi, E., & Zeinali, S. Nanoporous MIL-101 (Cr) as a sensing layer coated on a quartz crystal microbalance (QCM) nanosensor to detect volatile organic compounds (VOCs). *RSC Adv.* **9**, 24460–24470 (2019).

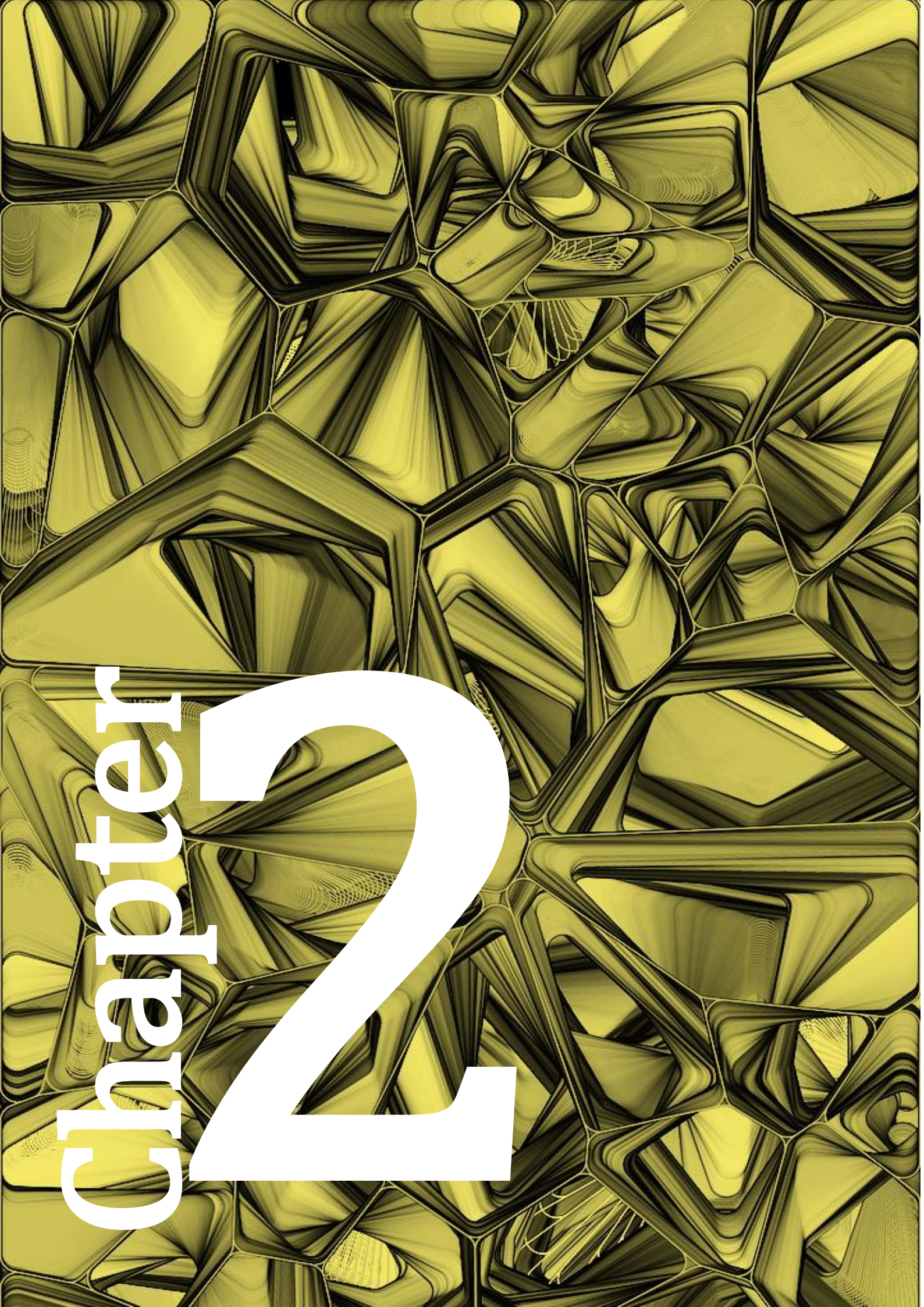
Chapter 2

Sensitivity improvement on magnetoelastic resonators

Este segundo capítulo presenta un análisis detallado de las propiedades magnetoelásticas de resonadores de Metglas 2826MB con distintas geometrías (desde la geometría rectangular empleada clásicamente a otras novedosas como triángulos o rombos). Los resultados obtenidos revelan la importancia de la geometría del resonador en parámetros tales como el efecto ΔE, el factor de calidad de la resonancia *(Q)* o la sensibilidad. Además, el efecto de parámetros tales como el porcentaje de recubrimiento o la longitud del resonador se analizan también en profundidad en este capítulo. Por otro lado, un diseño de sensor múltiple basado en la combinación de dos de estas nuevas geometrías se propone y analiza. Finalmente, los diferentes resonadores propuestos se han caracterizado por microscopía Kerr y magnetometría VSM buscando una correlación entre el micromagnetismo de los resonadores y sus propiedades magnéticas y magnetoelásticas. Los resultados descritos en este capítulo muestran el papel clave de la geometría del resonador en sus propiedades magnéticas y magnetoelásticas.

Content

*Publications in which this chapter is based.

Some of the results shown in this chapter have been exposed in different indexed scientific publications: 1) "**Enhanced mass sensitivity in novel magnetoelastic resonators geometries for advanced detection systems**", *Sensors and Actuators B: Chemical (D1), 296, 2019, DOI:* doi.org/10.1016/j.snb.2019.05.089 ; 2) **"Theoretical and Experimental analysis of novel rhombus shaped magnetoelastic sensors with enhanced mass sensitivity"**, *IEEE Sensors (Q1)*, 2020, *DOI:* doir.org/10.1109/JSEN.2020.3006379 ; and 3) **"Influence of the magnetic domain structure in the mass sensitivity of magnetoelastic sensors with different geometries"**, Journal of alloys and compounds (Q1), 2020, *(under review);* as well as in some of the conferences presented in Annex C (Results dissemination).

2.1. Introduction

As stated in the first chapter, the overall performance of magnetoelastic based sensors depends on the combined properties of the magnetoelastic resonator platform, together with the adsorptive properties of the active layer integrated into the system. In this context, improve the mass sensitivity of magnetoelastic resonators is highly necessary to improve their performance. For that reason, many research efforts have been focus on the improvement of this parameter. However, most of them rely on the reduction of the size of the magnetoelastic resonant platform keeping the classical rectangular geometry [1,2]. Rectangular millimetric resonators with high sensitivities have been traditionally fabricated by mechanical polishing and dicing of commercial magnetoelastic alloys [3,4]. Aiming to further increase the sensitivity, magnetoelastic "microparticles" have been also fabricated using microelectronic shaping techniques (**Figure 2.1**) such photolithography and sputtering [5,6]. The miniaturization of magnetoelastic sensors leads to a huge increase on the resonance frequency (to MHz), and consequently, to an appreciable improvement on the mass sensitivity (Hz/pg). These findings are easily explained considering the **equation 2.1,** that is, the lower the resonator size/mass, the higher the sensitivity of the system.

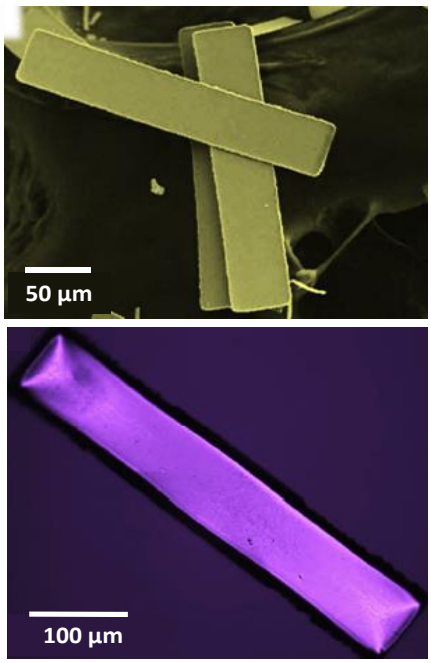

Figure 2.1. Magnetoelastic particles of $Fe_{79}B_{21}$ fabricated by microelectronic techniques [5].

Table 2.1 summarized the frequency and mass sensitivity dependence on the size and composition of the magnetoelastic resonator. As could be observed from the data summarised in the **Table 2.1**, the reduction on the resonator size is a key factor to increase the mass sensitivity of magnetoelastic based sensors. However, size reduction also results on counterpart drawbacks such a reduction on the quality factor and intensity of the measured resonance curve. In addition to this, the downsizing of magnetoelastic platforms also gives rise to a reduction of the total surface where later on the active layer is incorporated. Moreover, other drawbacks such as edge defects, lack of dimensional repeatability or handling issues also appear when working at the microscale [5].

Table 2.1. Dependence of the mass sensitivities of different magnetoelastic sensors with the resonator size. Showed results are for different analytes. * indicate the values measured in this chapter.

Magnetoelastic material	Size	f_r	Analyte	S	Ref
Metglas 2826MB	25 mm x 5 mm	87725 kHz	Gold	1.22 Hz/μg	*
	25 mm x 2.5 mm	88175 kHz		2.22 Hz/μg	
	15 mm x 1.5 mm	147.0 kHz		12.6 Hz/μg	
	10 mm x 1 mm	220.8 kHz		47.2 Hz/μg	
$Fe_{64}Co_{17}Si_{6.6}B_{12.4}$	30 mm x 2 mm	67 kHz	Polysty-rene	7.5 Hz/μg	1
	20 mm x 2 mm	102 kHz		18.1 Hz/μg	
	10 mm x 2 mm	206 kHz		52.4 Hz/μg	
$Fe_{79}B_{21}$	1000 μm x 200 μm	2000 MHz	Bacillus anthracis spores	0.042 Hz/pg	5
	500 μm x 100 μm	4000 MHz		0.338 Hz/pg	
	250 μm x 50 μm	8000 MHz		13.5 Hz/pg	
	100 μm x 20 μm	20000 MHz		333.3 Hz/pg	

Thus, alternatives to the magnetoelastic platform size reduction should also be considered in the search for greater sensitivity. With this purpose, an in-depth analysis of the influence of Metglas 2826MB resonators with different geometries, alternative to the traditional rectangular ones, in their mass sensitivity and in their magnetic and magnetoelastic properties has been done in this chapter. A total of four geometrical configurations have been investigated: rectangle, triangle, arched triangle and rhomb. Moreover, the effect of partial mass coatings has also been deeply analysed in order to quantify the mass sensitivity dependence on the resonator shape. Obtained results point that there is a huge dependence of the magnetic and magnetoelastic properties of the resonator and its geometry, confirming that resonators shaping is an innovative and effective alternative to size reduction in order to achieve high sensitive magnetoelastic platforms. Besides, results have confirmed that it is possible to fabricated multi-resonators with different geometries, and hence different resonant frequencies and mass sensitivities, in the same sensor. This approach paves the way to the design of multi-sensors based on the combination of different geometries, and consequently, different magnetoelastic responses when exposed to the target analyte.

2.2. Magnetoelastic parameters affected by the resonator shape

There are three critical parameters that define the performance of sensors based on magnetoelastic resonators: the mass sensitivity *(S),* the resonance quality factor *(Q)* and the magnetoelastic coupling *(k).* A more detailed description of some of these parameters could be found in **Annex A**.

Mass sensitivity *(S)* relates the resonance frequency shift *(Δf)* that the resonant platform undergoes under a mass load *(Δm).* Mass sensitivity is commonly given by [7]:

$$S = -\frac{\Delta f}{\Delta m} = \frac{f_r}{2m_0} \tag{2.1}$$

where m_0 is the initial mass of the non-loaded magnetoelastic platform, and f_r is its corresponding resonance frequency. Thus, a higher resonance frequency or a lower resonator mass is translated into an overall higher sensitivity value. It should be noted that this relationship is just an approximation of a more general expression and that it is not always valid to explain the frequency shift of the system. For this reason, the obtained results are sometimes adjusted to expanded equations that take into account other parameters [8].

Moreover, the quality factor *(Q)* is a parameter that quantifies the energy losses of the resonator, associated with damping effects, and it is related to the sharpness of the measured resonance curve. Quality factor is usually calculated from the following equation [9]:

$$Q = \frac{f_r}{\Delta f} \tag{2.2}$$

where f_r is the resonance frequency and Δf the full width at half maximum intensity. A high Q value indicated low energy losses and is associated with narrower and sharper resonance curves. Opposite, a small Q value is related to a higher rate of energy losses and wider resonance curves.

Another important magnetoelastic parameter to describe the performance of the sensor is the magnetoelastic coupling coefficient *(k)*. This is related to the coupling between the magnetic and elastic energies. This parameter is calculated by using the following equation [10]:

$$k^2 = \frac{\pi^2}{8}\left[1 - \left(\frac{f_r}{f_a}\right)^2\right] \quad (2.3)$$

where f_r is the resonance frequency and f_a the antiresonance frequency. The magnetoelastic coupling coefficient is dependent on the applied magnetic field (**Figure A.5b**) as so the magnetoelastic resonance frequency. The dependence of the resonance frequency and the magnetoelastic coupling with the applied magnetic field is related to the so-called *ΔE* effect (**Figure A.5**). Magnetoelastic measurements are usually performed at the magnetic field at which the ΔE effect turns out to be maximum since magnetoelastic coupling (k) and signal amplitude are maximum at this field ($H_{k\ max}$). The ΔE effect is calculated by [11]:

$$\Delta E = \frac{E_s - E_{min}}{E_s} \times 100 \quad (2.4)$$

where E_s is the Young modulus at the magnetic saturation state, and E_{min} is the minimum value of the Young modulus. E_s and E_{min} values are directly related with the resonance frequency (f_r) at that points and can be calculated, for a rectangular shaped resonator, through **equation 2.5**:

$$E(H) = \rho(1 - \upsilon)(n2Lf_r)^2 \quad (2.5)$$

where ρ, υ and L are the density, the Poisson coefficient and the length of the magnetoelastic resonator and n is the resonance mode.

Thus, the overall response of magnetoelastic based sensors depends on all these parameters, being key to improve and balance them to obtain the higher intensity, signal quality and mass sensitivity as possible.

For that reason, the dependence of all these parameters with the sensor geometry has been deeply analysed along this chapter looking for higher resonance frequencies and mass sensitivities while avoiding the reduction of the resonator's active surface and resonance signal quality.

2.3. New resonator geometries for improved mass sensitivities

In the following, a comprehensive and systematic study of the influence of different resonators geometries in the mass sensitivity and in the previously introduced magnetoelastic parameters is reported. As said before, a total of four different geometrical configurations have been investigated: the classically used rectangular one, a triangular, an arched triangular and a rhombic shaped one. Both magnetoelastic resonance frequency and mass sensitivity measurements have been investigated through real experiments and computer simulations. Besides, the effect of the sensor length and/or partial mass coatings have also been studied. Finally, a multiple sensor based on the combination of two of these geometries has been proposed and tested. All the measurements have been carried out at the first resonance mode. Metglas 2826MB alloy has been used for all the experiments. Metglas 2826MB has been widely employed for magnetoelastic sensors applications, which allows comparing the performance of our systems with the previously reported ones in the literature. A detailed description of the composition and magnetic and magnetoelastic properties of this alloy could be found in **Annex A**.

2.3.1. Triangular and arched triangular asymmetric geometries

First, triangular and arched triangular shaped resonators have been deeply analysed and compared with classic rectangular resonators of the same length. Starting from a long ribbon of Metglas® 2826MB, free-standing resonators of 25 mm in length were cut in rectangles, triangles and arched triangles shapes, using picosecond pulsed laser ablation. A detailed description of this technique could be found in **Annex A** (Section A.1.2). It should be noted that a fix resonators length was selected to compare the sensitivity of the different geometries, despite if smaller lengths were used this parameter would be improved for all the studied geometries. In addition, a second rectangular geometry with a smaller width and equal surface area of the triangular resonator was also studied in order to obtain a meaningful comparison of the performance of resonators with different geometries and equal surface areas. Schemes of the different samples analysed and their given names are shown in **Figure 2.2**.

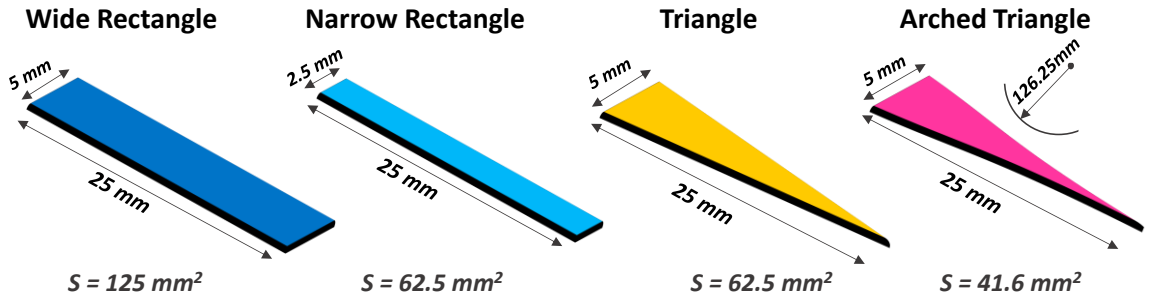

Figure 2.2. Scheme of the different resonators geometries analysed in this part.

- *Magnetoelastic parameters dependence with the geometry*

Once fabricated, the characterization of the magnetoelastic properties of all the samples was performed in order to analyse the influence of that novel shapes in those properties. First of all, the normalized variation of the resonance frequency as a function of the applied DC magnetic field (ΔE effect) was measured. Results are presented in **Figure 2.3**.

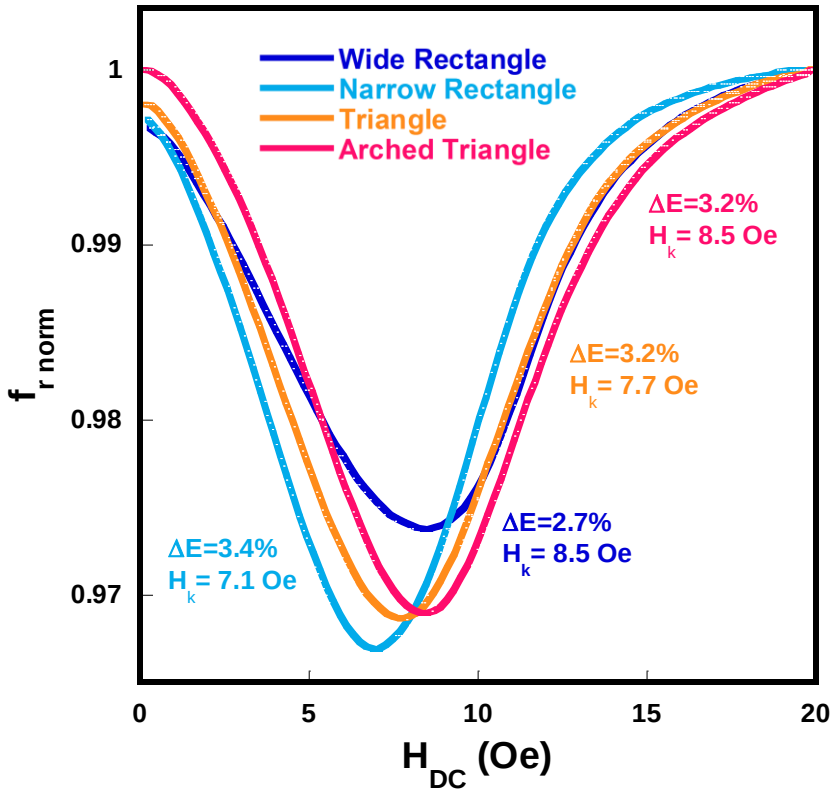

Figure 2.3. Variation of the magnetoelastic resonance frequencies as a function of applied magnetic bias field for the different sensor platforms.

The values of the ΔE effect were calculated from the plots shown in the **Figure 2.3** by using the **equation 2.4**. Obtained results are collected in **Table 2.2**. Despite not very significant, some differences can be appreciated in the ΔE effect values as well as on the bias field required to maximize it ($H_{k\,max}$). The wider rectangular ribbon presents the lower value of ΔE (2.7 %), followed by the triangular and arched triangular shaped samples (3.2 %), and finally, by the narrow rectangle (3.4 %). Moreover, the magnetic field at which the ΔE is maximum ($H_{k\,max}$) was also quantified. The lower value of $H_{k\,max}$ is measured for the narrow rectangle (7.1 Oe), followed by the triangular shaped sample (7.8 Oe). Finally, both the wide rectangle and arched triangle samples present the highest $H_{k\,max}$ (8.5 Oe). These differences on the $H_{k\,max}$ are probably related to the demagnetizing field on the samples. In the case of rectangular shaped resonators, this is homogeneous along the platform and is higher for lower length to width ratio [11,12]. Thus, the increase of ΔE effect, as well as the reduction of $H_{k\,max}$, from the wide to the narrow rectangle could be expected. Moreover, in the case of the non-rectangular shaped resonators, the demagnetization field is probably not uniform all over the platform, which results in a non-uniform effective magnetic field in these platforms. This fact can also explain the origin of the different magnetic fields needed to maximize the ΔE effect of these samples.

Table 2.2. Resonance frequency (f_0), ΔE effect (ΔE), quality factor (Q), magnetoelastic coupling coefficient (k) and applied bias field ($H_{k\,max}$) of the bare resonant platforms.

Sample	f_0 (Hz)	ΔE (%)	Q	k	$H_{k\,max}$ (Oe)
Wide Rectangle	87725	2.7	158.1	0.225	8.5
Narrow Rectangle	88175	3.4	141.1	0.225	7.1
Triangle	106660	3.2	139.2	0.224	7.7
Arched Triangle	118062	3.2	149.6	0.207	8.5

The resonance curves measured for each sample at their corresponding $H_{k\,max}$ fields are shown in **Figure 2.4**. From those curves, the initial resonance frequency (f_0), the quality factor *(Q),* and the magnetoelastic coupling coefficient *(k)* of the resonance could be estimated. All the obtained parameters are summarized in **Table 2.2**.

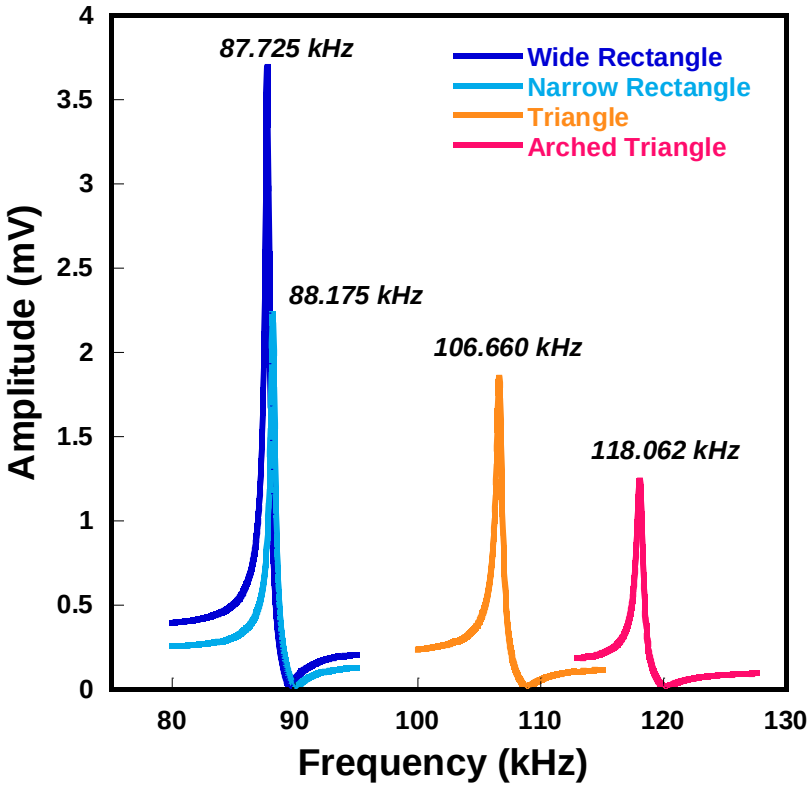

Figure 2.4. Magnetoelastic resonance curves of all the samples, measured at their corresponding H_k field.

As expected, the resonance frequency of the wide and narrow rectangles are very similar (87725 and 88175 Hz, respectively), despite the lower mass of the narrow rectangle reduces its resonance amplitude. In the case of the triangle and arched triangle geometries, a significant increase in their resonance frequency (f_0) is observed if compared with the rectangular shapes. As in the case of the narrow rectangle, there is a decrease in the signal of the resonance amplitude, which is again attributed to the lower mass of magnetoelastic material in these shapes. However, the sharpness of the peak is not significantly affected, as it can be confirmed by the similar or even improved values of the quality factors *(Q)*. Regarding the magnetoelastic coupling coefficient, no significant changes are observed among the different samples. Thus, considering the results as a whole, it can be concluded that the main magnetoelastic parameters of the magnetoelastic ribbons are not affected by the geometry of the resonator while an increase of the resonance frequency for specific shapes is observed. These experimental findings are so promising, since having in mind the **equation 2.1**, the higher the resonance

frequency, the better the mass sensitivity of the resonators. Therefore, in the next step, the effect of the resonator geometry on the mass sensitivity is deeply analysed.

- *Mass sensitivity dependence with the geometry*

After that initial magnetoelastic characterization, the influence of the different geometries on their mass deposition sensitivity was studied. For that purpose, five successive homogeneous gold layers with controlled masses were deposited on the sensor surface of the magnetoelastic resonator (MR) using sputtering techniques. The experimental procedure is fully described in **Annex A** (Section A.1.6). Gold was used as a model to control the weight and position of the mass load at the resonators in order to quantify its magnetoelastic response in simulated sensing conditions, that is, the gold here simulates the mass loading due to the target analyte adsorption in the MR. After each deposition, the magnetoelastic resonance frequency value was measured. The variation of the magnetoelastic resonance frequency as a function of the successive mass loadings for each sample is shown in **Figure 2.5**.

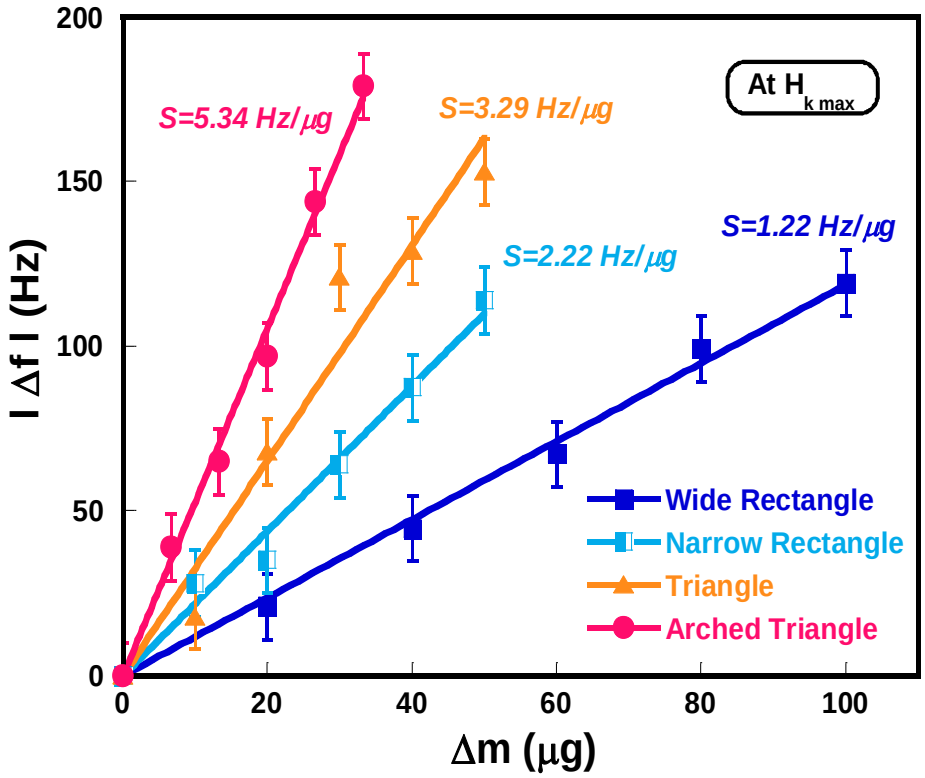

Figure 2.5. Shift on the resonance frequency under a specific change in mass for the different sensor platforms geometries completely coated.

A marked difference between the magnetoelastic responses of the different samples could be observed. The fitting of the experimental results shown in the Figure 2.6 allows quantifying the experimental mass sensitivity (S = slope of the Δf/Δm plot). Results are summarized in **Table 2.3**, together with the initial frequencies and masses of all the MR, as well as with the gold mass loaded in each deposition.

Table 2.3. Initial mass (m_0), experimental resonance frequency (f_0), simulated resonance frequency (f_0 sim), mass loaded on each deposition (Δm) and mass sensitivity (S) for the different resonant platforms.

Sample	m_0 (mg)	f_0 (Hz)	$f_{0\,sim}$ (Hz)	Δm (μg)	S (Hz/μg)
Wide Rectangle	31.6468	87725	87565	20.000	1.22
Narrow Rectangle	15.5261	88175	87688	10.000	2.22
Triangle	15.9108	106660	106540	10.000	3.29
Arched Triangle	11.3751	118062	124850	6.645	5.34

The wide rectangular MR presents a sensitivity of *1.22 Hz/μg*. This value is almost doubled in the case of the narrow rectangular strip *(2.22 Hz/μg)* and further increases a 148 and 240 % when using the triangular *(3.29 Hz/μg)* and arched triangular *(5.34 Hz/μg)* shaped strips, respectively. Considering **equation 2.1**, the improvement of the mass sensitivity from the wide to the narrow rectangular resonant platform could be expected due to the reduction of its mass. However, for MR with equal mass but different geometries (i.e. the narrow rectangle and the triangle), the triangular shaped MR improves the sensitivity values of the rectangular MR due to its higher resonance frequency. Moreover, the lower mass of the arched triangle shaped MR together with its higher resonance frequency value results in the highest measured sensitivity (S). Arched triangle shaped MR shows the highest sensitivity S coming from its higher resonance frequency value, which in turn is related to the lower mass of the platform. This clearly demonstrates that the sensitivity can also be tailored by engineering the MR geometry in order to shift the magnetoelastic resonance frequency to higher values.

- *Simulations of the resonance behaviour for the different geometries*

In order to extend the knowledge about these samples and look for possible ways to improve even more the sensitivity, computer simulations were performed using the commercially available COMSOL Multiphysics® software program. The first resonance frequency mode and the shift on the frequency under a given mass load were simulated for all the samples. A detailed description of the simulations could be found in **Annex A** (Section A.1.5).

The simulated vibrations and the obtained frequencies for the different shaped MR are shown in **Figure 2.6**. In this figure, the displacement that the magnetoelastic resonators undergo at the obtained resonance frequency has been illustrated through a scale of colours from blue (null displacement) to red (maximum displacement). Results for the resonance frequencies simulated together with the experimental results are shown in **Table 2.3**

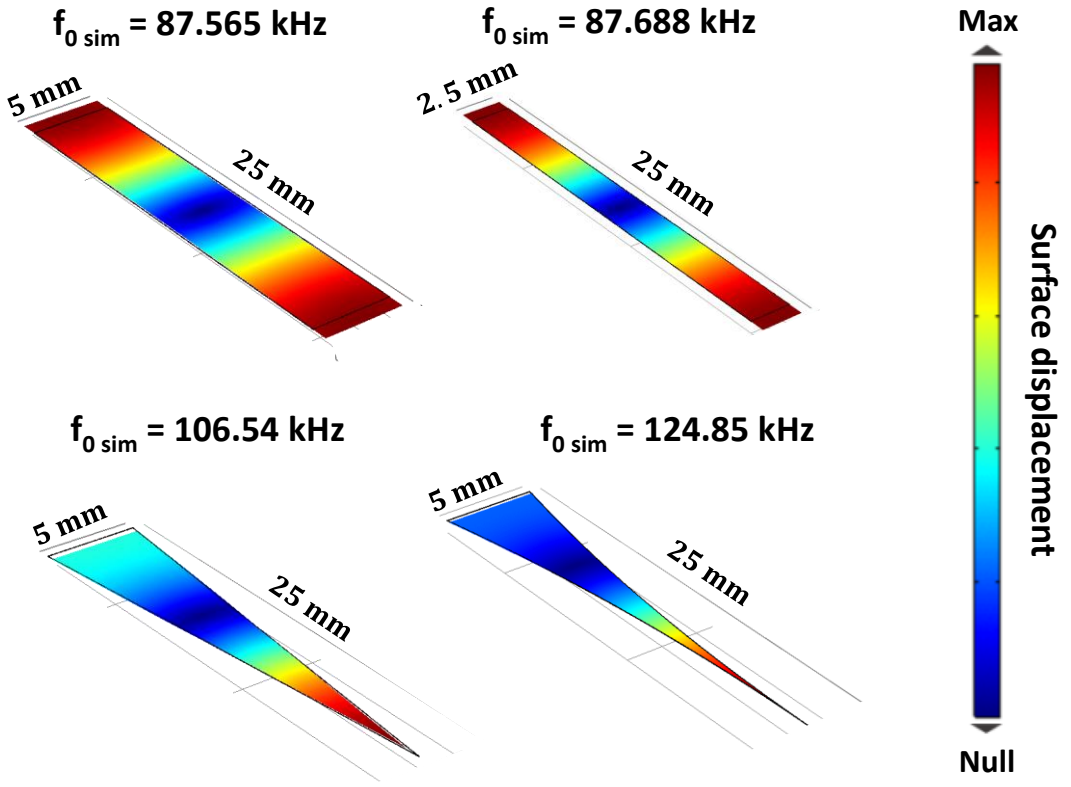

Figure 2.6. Images of the resonance frequency simulations performed for the different samples.

Experimental (f_0) and simulated values ($f_{0\,sim}$) of the resonance frequency are in very close agreement. The slight differences observed can be attributed to some deviations between the pure elastic wave, considered in the simulation, and the experimentally measured magnetoelastic wave. This magnetoelastic wave is a direct consequence of the magnetoelastic coupling, which plays a key role in this aspect [13]. Moreover, the experimental Young's Modulus value of the rectangular MR was used in the simulation experiments for all the studied geometries, an approach that could result in some degree of mismatch between the experimental and simulated data. This fact can be in the origin of the higher (although small) variations observed between the experimental and simulated frequency values of the triangular and arched triangular shaped MRs.

Looking at the results, additional information stands out. Despite most of the studies distribute the mass load uniformly all over the MR surface, according to the results showed in **Figure 2.6**, the deformation is not uniform. Actually, the rectangular sample vibrates around a nodal point placed in the centre of the strip. At this nodal point (in dark blue), the displacement is null, and on the contrary, it is maximum at the edges of the ribbons (in red). In the case of triangular and arched triangular shaped MR, an asymmetric distribution of the deformation is observed as a direct consequence of their asymmetric shape. In this case, the node position is displaced further away from the tip, where the highest deformation is located. The normalized total displacement as a function of the distance from the edge/tip of the studied MR is represented in **Figure 2.7**.

As it can be observed, the position of the nodal point depends on the sample geometry. For both rectangles, the node is located at the centre (at 12.5 mm from the edges of the rectangle), while for the triangular and arched triangular shaped resonators this position moves away from the centre of the resonator to approximately 16 mm and 17.5 mm measured from the tip, respectively. Considering these results and some previous studies [14,7], it can be predicted that the different zones of the sensor surface will not be equally sensitive. Moreover, if the nodal point is farther from the tip in the triangle and arched triangle shaped resonators, the tip of these sensors should be much more sensitive than the edges of the rectangular ones, because they will undergo a higher degree of deformation that the edge zones of the rectangular resonators.

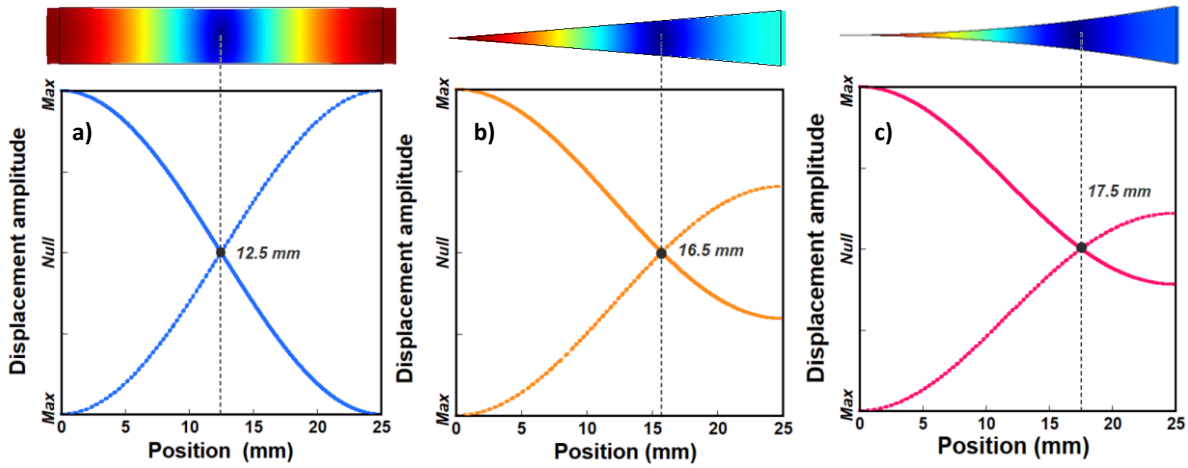

Figure 2.7. Normalized displacement at the different zones of the sensor platform for: (a) Both rectangular shape, (b) triangular shape and (c) arched triangular shape MRs.

In order to prove this hypothesis, five successive gold mass depositions were performed covering partially the surface of the MRs. The experimental and theoretical simulated frequency shifts (Hz) for each case study are presented in the following.

- *Sensitivity dependence with the coated surface*

An exhaustive experimental study of the dependence of mass sensitivity with the coated area was carried out following the previously described coating procedure. The depositions were performed from the tip of the resonators to 4 mm, 8 mm, the node position and a point beyond the node (to 17 mm for both rectangles and to 22 mm for the triangular and arched triangular shape samples) of the different resonant platform (see insets in **Figure 2.8**). All the results were compared with that of the completely coated sensor. The experimentally measured variation of the resonance frequency value for each coated distance as a function of the mass change is shown in **Figure 2.8**.

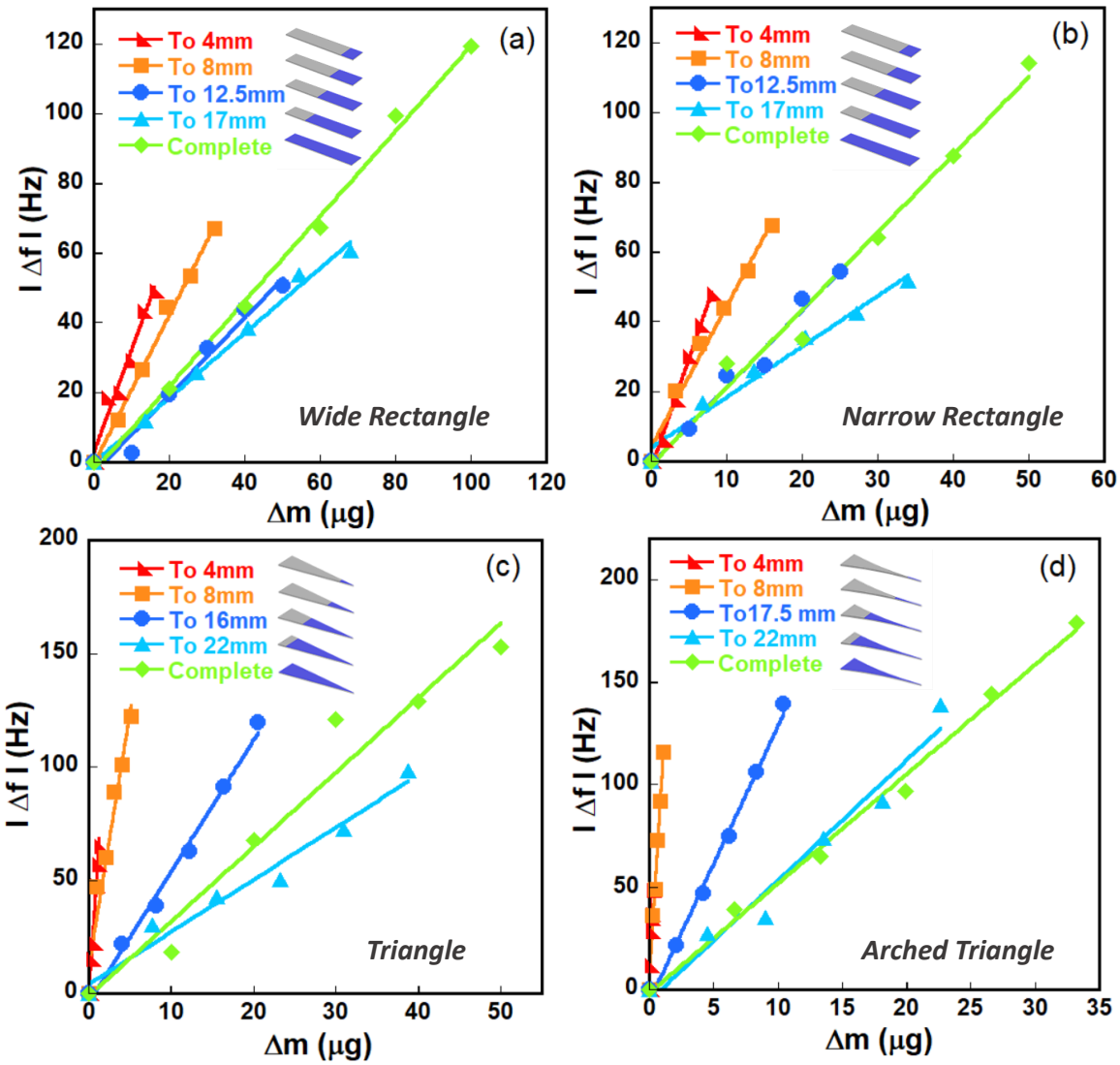

Figure 2.8. Frequency shift at different distances from the edge/tip as a function of the mass load deposition obtained experimentally for the: (a) Wide rectangle, (b) narrow rectangle, (c) triangle, and (d) arched triangle.

Additionally, partial depositions of 90 nm gold layers on the surface of the MRs were also simulated, for comparison. Considering the difference between the experimental and simulated thickness of the gold deposited layer (5×15 nm and 90 nm, respectively), the variation of resonance frequency values were normalized by dividing the value of a resonance frequency at a specific coat distance of MR (Δf) by the value of the frequency shift under the complete coating (Δf_{max}). This normalized variation is represented as a function of the coated distance (measured from the edge) in **Figure 2.9**. The black points and line correspond to simulated results whilst the colour points correspond to the normalized frequency shift obtained experimentally from **Figure 2.8**.

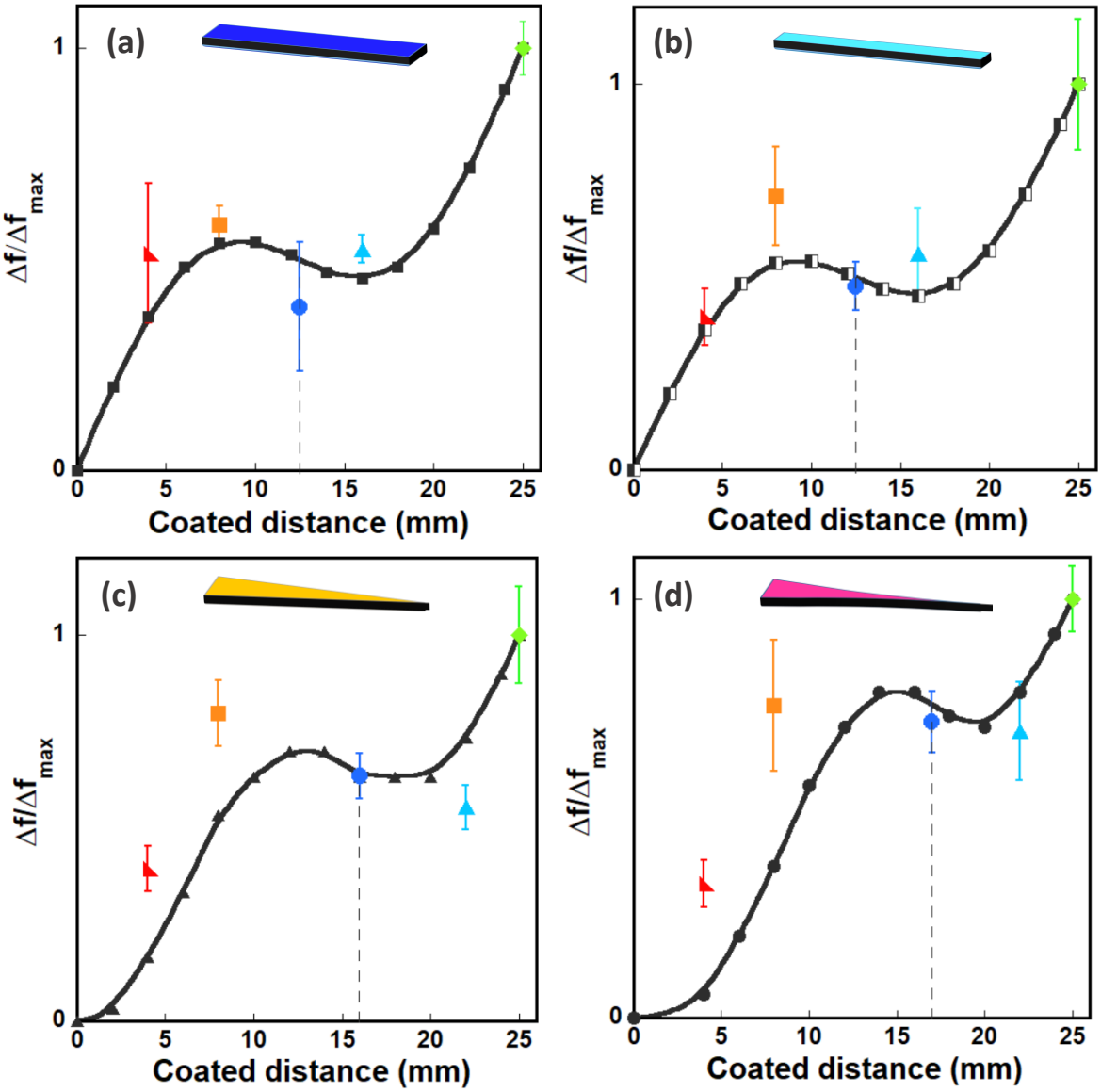

Figure 2.9. Normalized frequency shift as a function of the different distances obtained by computer simulations (black line) and normalized experimental results of the average frequency shift obtained for the different depositions (colour points) for the: (a) Wide rectangle, (b) Narrow rectangle, (c) Triangle, and (d) Arched triangle.

The simulations show that until a specific value of the coated distance, the resonance frequency shift increases as the coated distance does. Considering **equation 2.1**, and taking into account that we are increasing the loaded mass, these results were expected. Nevertheless, when the mass deposition distance is reaching the position of the vibration node of the sample, the frequency shift stabilizes. Moreover, the frequency shift even decreases at a point below the nodal point of each sensor (9.3, 13.2 and 15.5 mm for the

rectangular, triangular and arched triangular shape samples, respectively). Finally, for a subsequent increase of the coated distance, the variation of the frequency value increases again, reaching its maximum when the totality of the MR is coated. This behaviour clearly manifests that the mass sensitivity depends on the coated area of the sensor. In the same way, the obtained results show that a higher amount of mass loaded not always results in a higher variation of the resonance frequency. The equivalent experimental measurements performed, show a similar trend to that of the simulated results, (**Figure 2.9**).

Furthermore, from the different slopes of the results in **Figure 2.8**, it could be observed that the sensitivity, $S=\Delta f/\Delta m$, is dependent on the coated surface of the sample. The experimental results of sensitivity as a function of the amount of coated surface are represented in **Figure 2.10**a. In addition, COMSOL simulations were also performed in order to simulate the partial gold depositions at a larger number of different coated distances. These results are presented in **Figure 2.10**b. It is observed that the sensitivity decreases as the amount of coated surface increases. Moreover, in the case of rectangular and triangular shaped samples, it can be appreciated a minimum in the sensitivity when the deposition transcends the distance of the nodal point (inset **Figure 2.10**) which increases again when the entire surface of the strip is covered. This behaviour has already been observed for the well-studied rectangular geometry [15]. Nonetheless, the decrease on the minimum mass quantity that the MR can detect (mass sensory threshold) close to the tip becomes much more remarkable in the novel geometries presented here (triangular and arched triangular shaped).

The sensitivity of the MR when 4 mm of edge/tip are coated is increased by about 250, 1620 and 6400% for the rectangular, triangular and arched triangular shaped samples, respectively, if compared with the completely covered MR. Again, the trend of the mass sensitivity values is quite similar for both theoretical and experimental results at large coated distances. Nonetheless, some significant discrepancies in the absolute values are observed at small coated distances. In this case, the experimental sensitivities are higher than the ones obtained by simulations. These differences can be attributed to the higher experimental measurement error for small coated distances when compared with the complete coated samples. Additionally, previous studies show the dependence of mass sensitivity with the properties of the material that is used in the coating process,

particularly the dependence on their elastic properties [16]. Thus, the differences of the elastic properties between the sputtered gold layer used in the experimental measurements and the perfectly uniform and compact gold sheet simulated are also on the basis of this discrepancies [13].

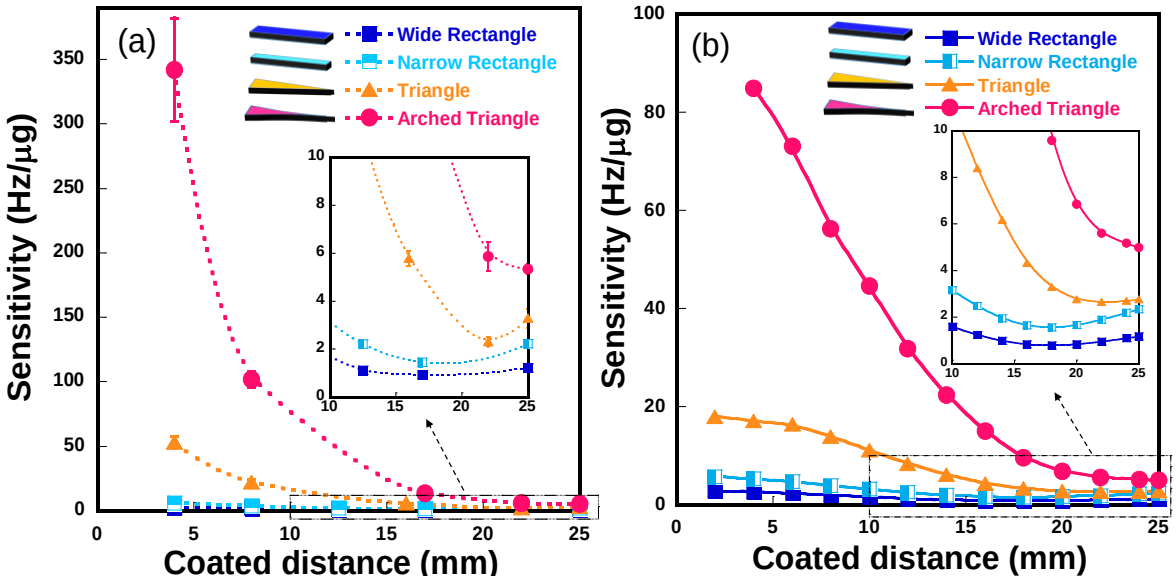

Figure 2.10. Sensitivity as a function of the coated distance for the different samples obtained: (a) experimentally and (b) by computer simulations. Inset: Detail of the lowest mass sensitivity response indicated by the rectangular box.

Considering the results presented in this work, it is clear the key role that the shape of the MR plays in the increase of mass load sensitivity. Furthermore, this work is fundamental to understand that the total coverage of the platform is the optimal way to obtain a higher variation in the frequency shift, while a tip located load mass represents a huge reduction of the mass sensory threshold. Thus, a deeper analysis of these novel geometries combined with the search for new ones is highly necessary.

2.3.2. New symmetric geometries - Rhombic resonators

The earlier achieved knowledge makes clear that tips are the most sensitive area of the triangular and arched triangular sensors. To find geometries that could maximize this effect is critical. For that reason, a novel sensor design based on a rhombic resonator was proposed, and its performance was deeply analysed in this section. This sensor geometry contains two tips, keeping the same active surface as the rectangle and the triangle and also maintaining the symmetrical displacement character of the classic rectangle.

Before the experimental measurements, a theoretical analysis was done to obtain a mathematical expression for the resonance frequency in rhombus shaped resonators. Finally, rectangular and rhombic resonator with the same active surface where compared in order to validate the theoretical model and to compare their magnetoelastic performance, including a complete analysis of its mass sensitivity. Different sensors lengths were compared in order to further validate the theoretical equation for different sensor lengths and to investigate the effect of the length on the mass sensitivity.

- *Theoretical resonance frequency for the rhombic geometry*

The classically used rectangular shaped magnetoelastic resonator is a widely explored and applied system [17]. Several studies describe its resonance frequency corresponding equations or its mass sensitivity behaviour [8]. Instead, everything remains to be studied for non-rectangular ME resonators. For that reason, it is necessary to develop new mathematical equations representative of the resonance frequency of those geometries, which is one of the main parameters defining their mass sensitivity (see **equation 2.1**). It is well known that the displacement function ($u(x,t)$) of a longitudinal elastic wave propagating along the length direction (in the following, supposed to be the x axis) of a ME resonator of length L is given by [18]:

$$u(x,t) = u_o \cos\left(\frac{n\pi}{L}x\right) e^{i2\pi f_n t} = u(x)e^{i2\pi f_n t} \qquad (2.6)$$

where u_0 is a constant and f_n is the resonance frequency of the n-th harmonic mode. So, all points in the sensor material oscillate at the same frequency but with different amplitudes, since these depend on the distance from the ends.

In addition, the kinetic energy *(T)* and the potential energy *(V)* of a free-standing ME resonator vibrating along the x-axis are given by [15]:

$$T = \frac{1}{2}\int_0^L \rho \cdot A_s \cdot \left(\frac{\partial u(x,t)}{\partial t}\right)^2 dx \qquad (2.7)$$

$$V = \frac{1}{2}\int_0^L \frac{E}{1-\upsilon} \cdot A_s \cdot \left(\frac{\partial u(x,t)}{\partial x}\right)^2 dx \qquad (2.8)$$

where ρ, E and ν are the density, the Young's modulus and the Poisson's ratio of the bare ME resonator and A_s its cross-sectional area. This cross-section is constant for

rectangular shaped materials, but in the case of rhombus shaped sensor, its width is variable *(W(x)),* and so its cross-section is also variable *($A_s = A(x) = W(x) \cdot h$),* where h is the sensor thickness. This variable cross-section *(A(x))* can be analytically expressed as:

$$A(x) = \begin{cases} \frac{xhw_m}{L/2} & (0 \le x \le L/2) \\ (L-x) \cdot \frac{2hw_m}{L} & (L/2 \le x \le L) \end{cases} \quad (2.9)$$

where w_m is the maximum width of the rhombus (width at its longitudinal centre) and L is the length of the ribbon. Solving the above equations and equalling the maximum kinetic and potential energies [19], the theoretical equation for the resonance frequency of a free-standing rhombus shaped magnetoelastic resonator of length L can be obtained. In the case of the first resonance mode (n=1), the frequency is given by:

$$f_r^{rh} = \sqrt{\frac{\pi^2+4}{\pi^2-4}} \cdot \left(\frac{1}{2L} \cdot \sqrt{\frac{E}{\rho(1-\upsilon)}} \right) \quad (2.10)$$

where again E is the Young modulus, ρ is the density and ν is the Poisson coefficient of the sensing material. By direct comparison of the equation for the resonance frequency of a rectangular resonator (**equation 1.1**) with this last one, when Young's modulus of both samples is the same, the relationship between the resonance frequency of the rhombus and the rectangular shaped resonators is given by:

$$f_r^{rh} = \sqrt{\frac{\pi^2+4}{\pi^2-4}} \cdot f_r^{rec} \approx 1.53 \cdot f_r^{rec} \quad (2.11)$$

Equation 2.11 shows that, for the same length L of the resonant platform, the resonance frequency of the rhombus shaped ribbon is higher than the resonance frequency of the rectangle shape one, what results by following **equation 2.1** in a higher mass sensitivity. A detailed description of these calculations could be found in **Annex B.**

- ***Magnetoelastic characterization and resonance frequency simulations***

Looking at the proposed mathematical equation for the rhombus shaped ribbon, an improved performance of the rhombic resonator compared with the rectangular and the triangular ones could be expected. For that, an extensive and comprehensive analysis of

the differences among rectangular and rhombic shape resonators of different lengths has been developed and different experimental measurements have been carried out for the equation validation and to compare their magnetoelastic properties. Thus, Metglas 2826MB rectangular and rhombic resonators of different lengths were cut by picosecond pulse laser. A scheme of the analysed samples together with their given names is represented in **Figure 2.11**.

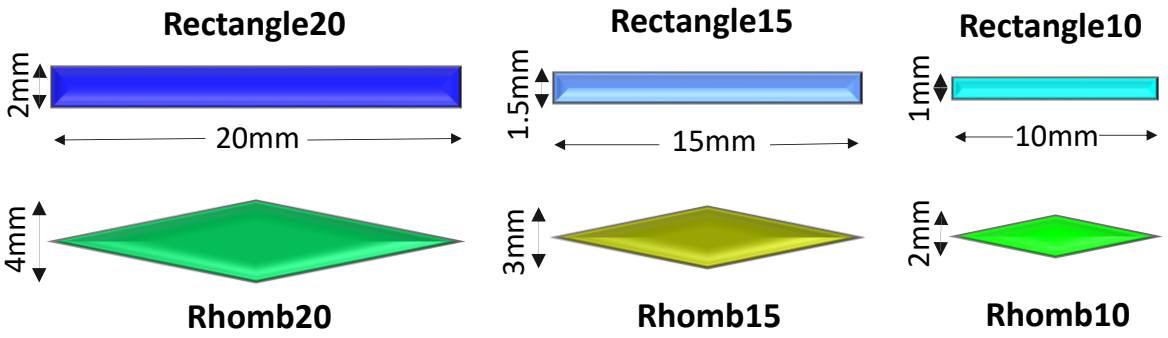

Figure 2.11. Scheme of the Metglas resonators analysed in this part.

First of all, the variation of the resonance frequency with the applied DC magnetic field, normalized by the resonance frequency at the magnetic saturation was measured for all the samples. Results are represented in **Figure 2.12**. As previously stated, this variation of the resonance frequency with the applied magnetic field is related to the Young's modulus (ΔE effect) through **equations 1.1** and **2.10** for the rectangular and rhombic geometries, respectively, and considering the **equation 2.4** previously introduced.

All the parameters obtained from **Figure 2.12** are summarized in **Table 2.4.** Some differences in the ΔE effect value can be observed. While the rectangles have hardly any difference in the value of the ΔE effect (3.4 % for the samples of 20 mm and 15 mm and 3.1 % for the sample of 10 mm), the rhombic samples present slightly larger differences (3.3 %, 3.1% and 2.5% for the 20, 15 and 10 mm in length respectively), always showing a drop when decreasing the size of the sample. Moreover, when comparing rhombic and rectangular resonators with the same length, it can be observed that the ΔE effect value is always smaller in the rhombic sample. The Young modulus value of the different samples at the minimum point of the curve (E_{min}) was estimated by using **equations 1.1** and **2.10**. Results are also shown in **Table 2.4**.

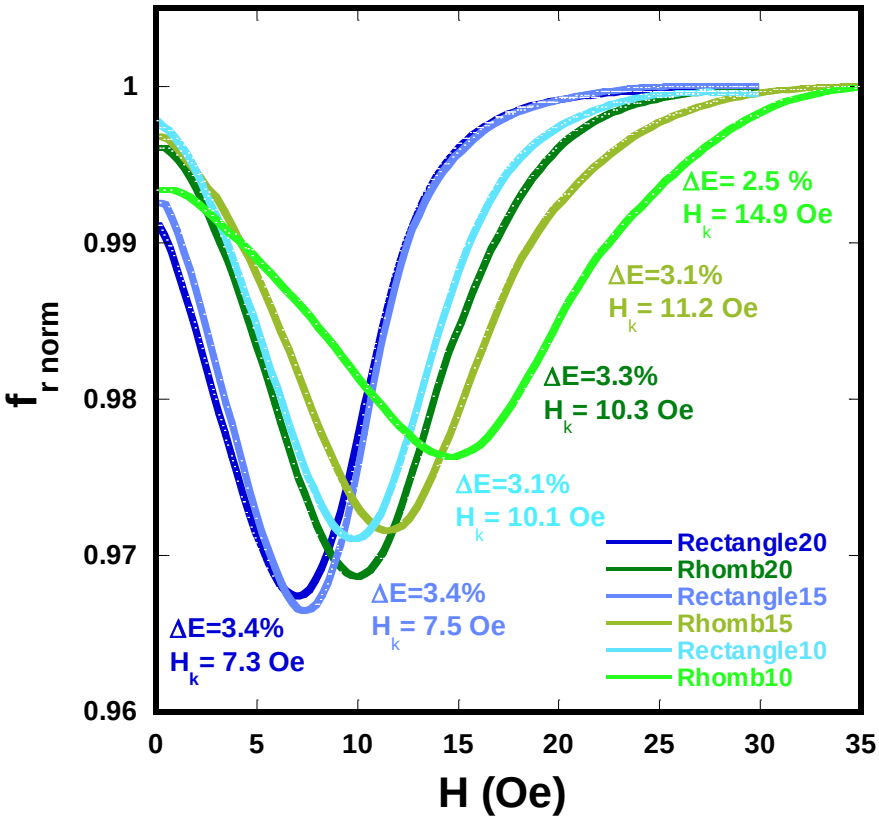

Figure 2.12. Variation of the magnetoelastic resonance frequency as a function of the applied magnetic field for the different samples. Resonance frequency values appear normalized by dividing by the resonance frequency of the sample at the magnetic saturation.

Table 2.4. ΔE effect (ΔE), minimum Young modulus value (E_{min}) and applied bias field at the minimum ($H_{k\,max}$) obtained from **Figure 2.12** for the different samples studied in this work.

Sample	ΔE (%)	$H_{k\,max}$ (Oe)	E_{min} (Gpa)
Rectangle20	3.4	7.3	152
Rhomb20	3.3	10.3	151
Rectangle15	3.4	7.5	153
Rhomb15	3.1	11.2	151
Rectangle10	3.1	10.1	154
Rhomb10	2.5	14.9	152

In addition, when analysing the DC magnetic field at which the minimum of the E(*H*) curve occurs ($H_{k\,max}$), interesting differences are also found. The lowest value of this field (7.3 Oe) is observed for the longest rectangle, while the maximum value (14.9 Oe) is measured for the shortest rhombic resonator. This trend is observed to happen both with size and shape of the magnetoelastic ribbons: it always increases when reducing the size, and it is always smaller for the rectangle than for the rhombus shape when sensors of the same size are compared. Furthermore, the $H_{k\,max}$ of the rhomb is always amplified by a factor of nearly 1.4 with respect to the $H_{k\,max}$ of the rectangle (see **Table 2.4**). This increase in the $H_{k\,max}$ value in geometries different from the classical rectangle is similar to that observed previously for the triangular and arched triangular geometries. These differences have been attributed to the demagnetizing field which is homogeneous along the rectangular shaped sensor but not in the case of the non-rectangular ones, leading to a non-uniform effective magnetic field inside the rhombic resonators [12].

Considering that the $H_{k\,max}$ value matches with the magnetic field at which the amplitude of the resonance is maximum, all the measurements were performed under this characteristic magnetic field. Resonance frequency curves measured at the corresponding $H_{k\,max}$ for each studied sample are shown in **Figure 2.13**, together with the calculated multiplicative factor between the resonance frequencies of the rectangular and rhombic geometries with the same length.

As expected from **equation 2.11**, the resonance frequency value for the rhombic samples is always higher than for the same length rectangular ones. In fact, an experimental relationship factor of around $f_r^{rh}/f_r^{rec} \sim 1.52$ has been obtained between the resonance frequencies of the rhombic and the rectangular shaped resonators, a factor which is very similar to the one calculated theoretically (1.53) through the **equation 2.11.** Moreover, a decrease on the resonance amplitude as well as an increase on the resonance frequency value is always observed in samples with the same shape when the size of the sensor is reduced, which is related with the less amount of magnetoelastic material.

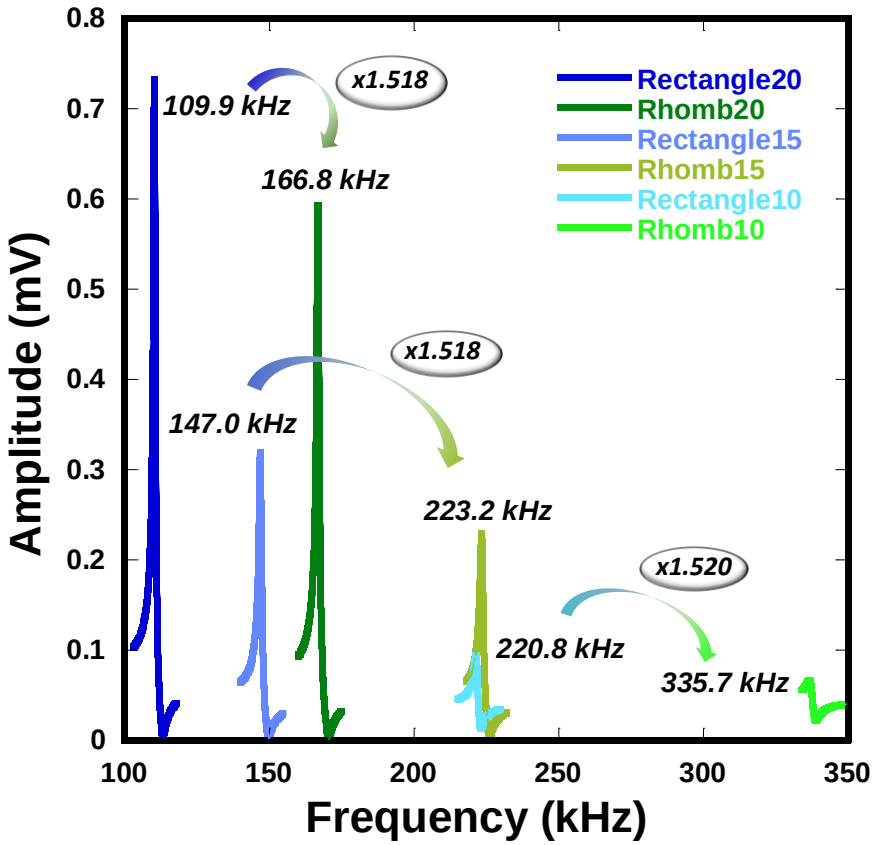

Figure 2.13. Magnetoelastic resonance curves of all the samples, measured at the magnetic field at with the ΔE effect is maximum ($H_{k\,max}$).

The quality factor *(Q)* and the magnetoelastic coupling coefficient *(k)* of the measured resonance curves represented in **Figure 2.13** were calculated considering the **equations 2.2** and **2.3**, respectively. **Table 2.5** summarizes all these obtained values. It can be observed that the quality factor *(Q)* decreases as the length of the ribbon decreases. Nevertheless, when comparing rectangular and rhombic resonators of the same length, the quality factor is very similar for both samples. This fact indicates that the sharpness of the resonance peak, that is representative of the frequency values resolution, is maintained for the new geometries.

Concerning the magnetoelastic coupling coefficient *(k),* a reduction of this parameter is observed when the length of the resonator is reduced, being always slightly lower for the rhombic shaped resonator.

Table 2.5. Quality factor (Q), magnetoelastic coupling coefficient (k), measured resonance frequency (f_0) at H_k, multiplicative factor between the resonance frequency of both geometries (f_r^{rh}/f_r^{rec}) and simulated resonance frequencies ($f_{0\,sim}$).

Sample	Q	k	f_0 (kHz)	f_r^{rh}/f_r^{rec}	$f_{0\,sim}$ (kHz)
Rectangle20	190.3	0.25	109.9 ± 0.3	1.518	109.66
Rhomb20	205.9	0.23	166.8 ± 0.2		165.24
Rectangle15	172.7	0.22	147.0 ± 0.2	1.518	146.69
Rhomb15	194.2	0.17	223.2 ± 0.1		220.31
Rectangle10	106.3	0.14	220.8 ± 0.4	1.520	220.76
Rhomb10	97.9	0.13	335.7 ± 0.7		331.56

In order to validate the experimental results, simulations of the resonance frequencies were performed again using COMSOL Multiphysics. Pictures of the simulations for the rectangular and rhombic samples of 10 mm in length are shown in **Figure 2.14** together with the simulated frequencies. It can be observed that unlike the triangle and the arched triangle, the rhomb present a symmetrical displacement like that of the rectangle, which was expected. Moreover, at resonance condition, the amplitude of the displacement in both geometries is null at the centre of the resonator (red colour) and maximum at both ends (blue colour). These behaviour has been already observed for the samples presented previously and has been translated into different mass sensitivities on the different zones of the sensor [7].

The simulated resonance frequencies of all the samples were obtained using the previously determined Young's modulus (**Table 2.4**). Looking at the results presented in **Table 2.5**, it can be appreciated that similar results are obtained both for the experimental and the simulated resonance frequencies. Small differences between both values could be attributed to slight deviations between the magnetoelastic wave (consequence of the magnetoelastic coupling) measured experimentally and the pure elastic wave considered in the simulations [13].

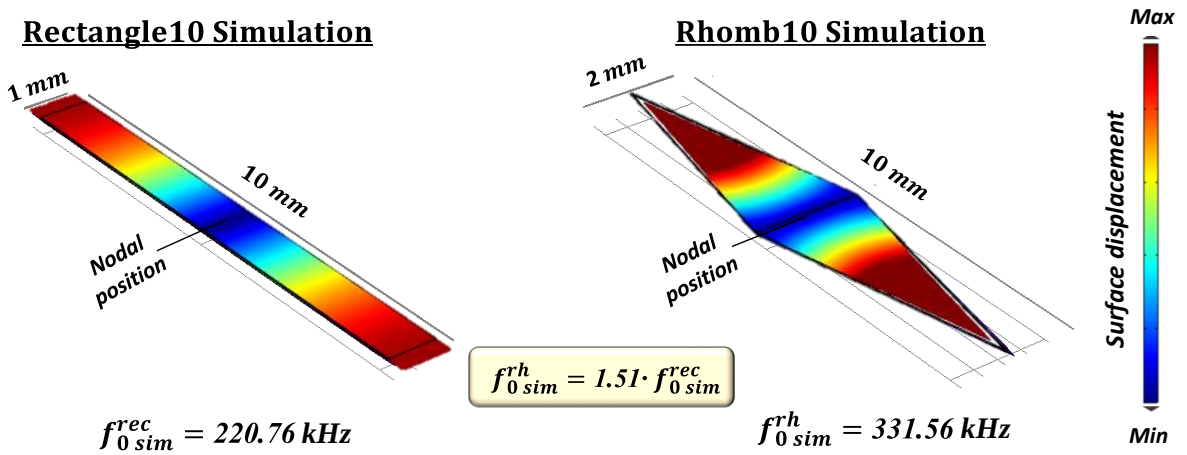

Figure 2.14. Images of the resonance frequency simulations performed in the rectangular and rhombic samples of 10 mm in length. Colours in the draws indicate the displacement that each part of the sensor suffers in the resonance (Being purple the maximum displacement and red a null displacement).

- *Dependence of the mass sensitivity with the resonator geometry and size*

Taking into account that rhombus-shape ribbon presents a higher resonance frequency than the classical rectangle shaped ribbon, a considerable improvement in the sensitivity is expected according to **equation 2.1**. In this way, the effect of the sensor geometry and size on the mass sensitivity was carefully analysed by again depositing five successive gold layers on the sensor platform surface and measuring the resonance frequency value after each deposition. The resonance frequency variation as a function of the mass load is represented in **Figure 2.15**.

Experimental mass sensitivities *(S)* obtained from **Figure 2.15**a are collected in **Figure 2.15**b. From these figures, the higher sensitivities of the rhombic shaped sensors when using devices of the same length are evident. Furthermore, as it could be expected, the lower the size of the sensor, the higher is its sensitivity [20]. In particular, the longest rectangular sensor (20 mm length) presents the lowest sensitivity of 4.4 Hz/μg, while the shortest rhombic sensor (10 mm length) presents the highest measured sensitivity of 68.7 Hz/μg, 15 times higher.

Therefore, although the mass deposited on both sensors of the same length is the same (due to the equal active surface), the rhombic sensor will be always more sensitive to a given mass deposition than the rectangular one. All these results make clear again the advantages of using these new sensor geometries instead of the common rectangular devices, and the necessity to still exploring this new line of research.

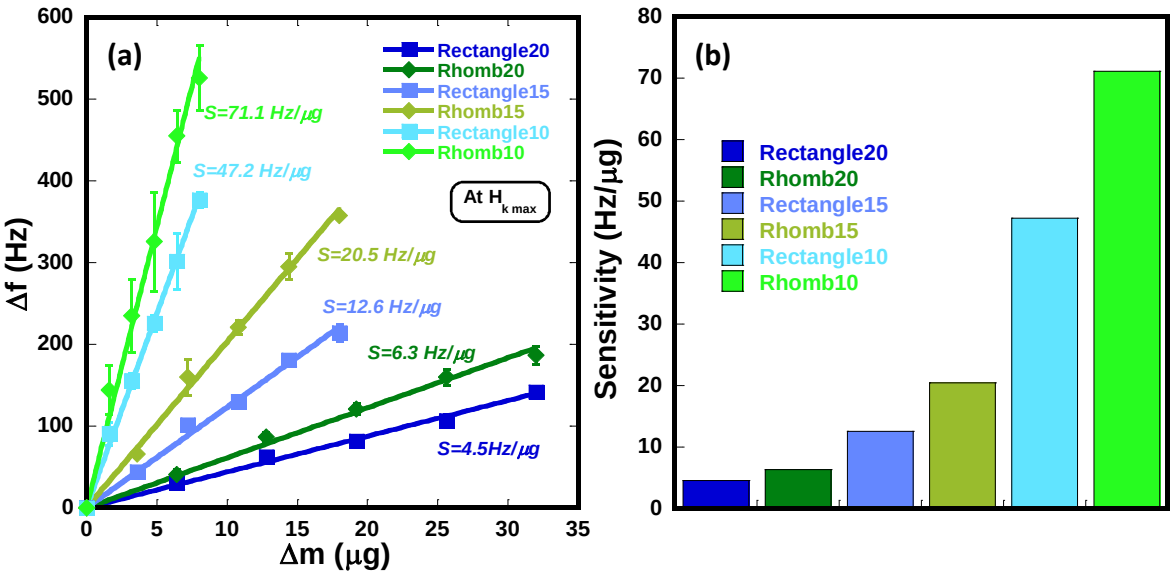

Figure 2.15. (a) Shift on the resonance frequency as function of the deposited mass on the different samples. The five experimental points represent each gold deposition on the sensor surface. (b) Histogram with sensitivity values obtained from **Figure 2.15**a.

- ***Multiple sensor design and characterization***

Finally, aiming to address the lack of sensors able to detect simultaneously multiple and different targets, a novel multiple sensor design based on the combination of both of the previously studied geometries is proposed. This multiple sensor consists on a combination of one rectangular plus one rhombic magnetoelastic platforms in a single sensor. This novel sensing device design allows developing a multiple and simultaneous detection system based on the multiple resonance frequency peaks obtained from the MR with different geometries incorporated in the same device.

For the fabrication of this multiple sensor, the rectangle and the rhomb of 10 mm in length were chosen. It should be noted that both resonant platforms are connected by the nodal position of the geometries, which is not deformed under resonance conditions, in order to avoid the corresponding damping. An optical microscope image of the multiple

fabricated sensor, covered with a gold layer, is shown in **Figure 2.16**.

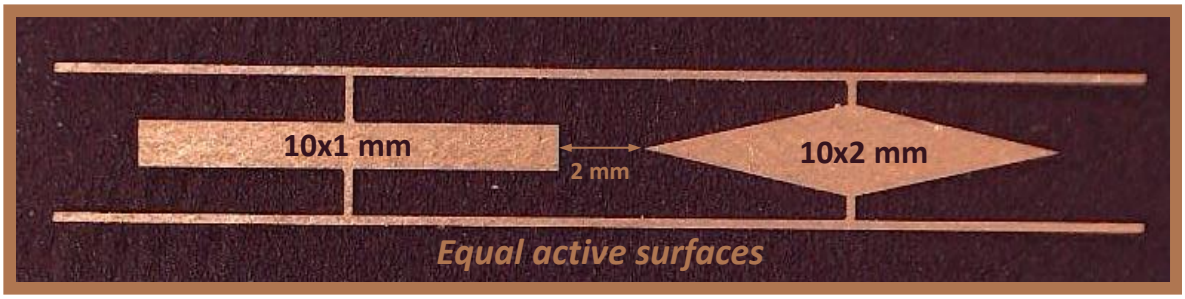

Figure 2.16. Microscope image of the multiple sensor design covered by a gold layer.

Once after the multiple sensor fabrication, both ΔE effect and magnetoelastic resonance frequencies of the connected magnetoelastic platforms were characterized and compared with the free-standing ones. Results are shown in **Figure 2.17**.

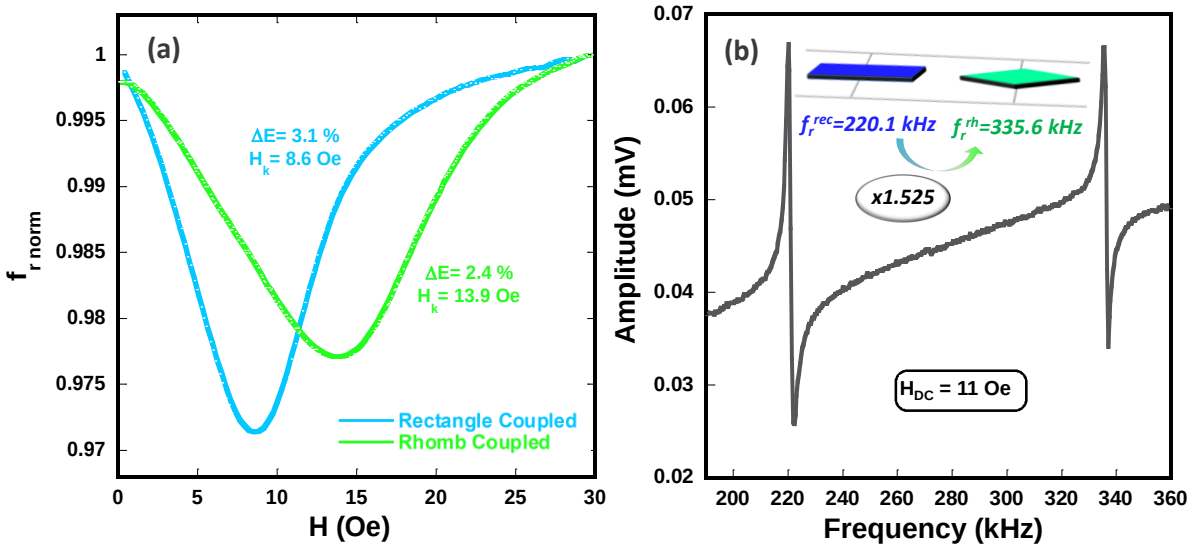

Figure 2.17. (a) Variation of the normalized magnetoelastic resonance frequency as a function of the applied magnetic field for the rectangle-rhomb multiple sensor, (b) Magnetoelastic resonance curves for both geometries, measured at 11 Oe (chosen as H_{opt}, midfield between the two corresponding H_k values and optimal to have similar amplitudes for both resonances).

The different parameters obtained from **Figure 2.17** are summarized in **Table 2.6**. Looking at the results and comparing them with the previously obtained ones for the corresponding free-standing geometries, it can be observed that the ΔE value remain almost constant after coupling both geometries in a single sensor. However, the

measured H_k values decrease about 1 Oe for the coupled ribbons with respect to the free-standing ones. In this multiple sensor, and considering the impossibility to apply the corresponding H_k magnetic field for each different geometry in just a single measurement, an average of both H_k values was used (11 Oe). Measured magnetoelastic resonance curve of the multiple sensor ($f_{0\,MS}$), obtained under this applied external field, is represented in **Figure 2.17**b.

Table 2.6. ΔE effect (ΔE), bias field at the minimum (H_k), resonance frequency measured at H = 11 Oe ($f_{0\,MS}$), multiplicative factor (f_{Re}/f_{Rh}) and sensitivities (S) obtained for the two geometries that conform the multiple sensor.

Sample	ΔE (%)	H_k(Oe)	$f_{0\,MS}$ (kHz)	f_r^{rh}/f_r^{rec}	S (Hz/μg)
Rectangle10 Coupled	3.1	8.6	220.1	1.525	45.0 ± 1.8
Rhomb10 Coupled	2.4	13.9	335.6		69.3 ± 1.4

After this initial characterization of the multiple sensor, its mass sensitivity was also determined using the previously reported method. **Figure 2.18** shows the shift on the resonance frequency *(Δf)* as a function of the deposited gold mass *(Δm)* measured simultaneously for the rectangular and the rhombic geometries in the multiple sensor configuration.

As it can be observed, the obtained mass sensitivity values are very similar to the ones previously obtained for the free-standing sensors. Therefore, in view of all the obtained results, it could be affirmed that the integration of both geometries in a unique sensor does not affect the main magnetoelastic parameters obtained for the free-standing resonant platforms.

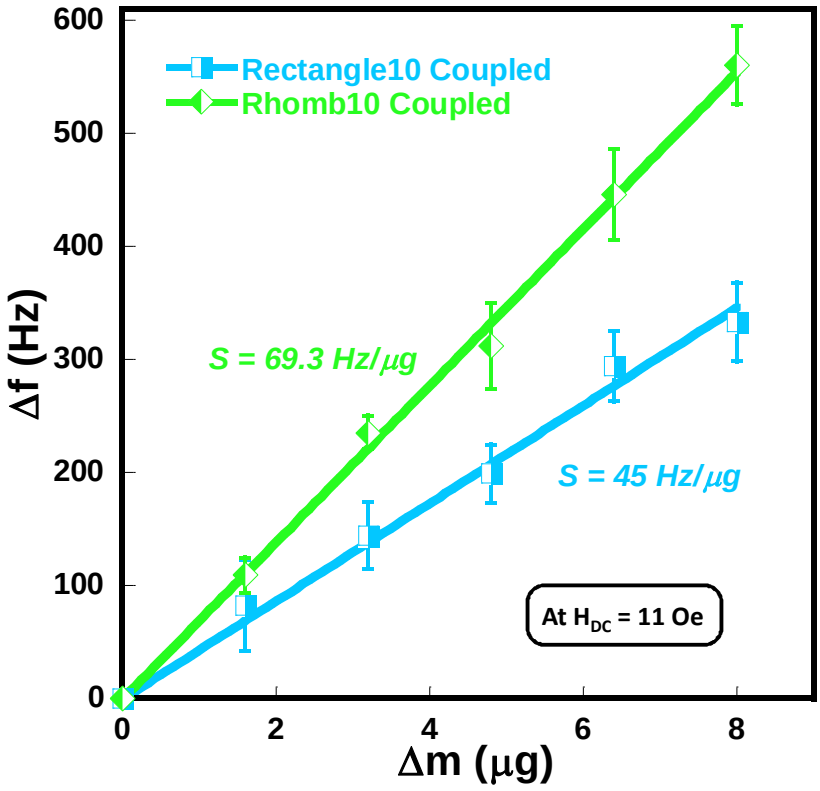

Figure 2.18. Shift on the resonance frequency under successive mass depositions measured at H_{opt} for both coupled geometries.

Finally, the double sensor configuration applicability was tested by using it as a double balance detection system. For this purpose, a gold layer of an aleatory mass was deposited in each resonator geometry of the multiple sensor. This aleatory mass added was afterwards determined from the magnetoelastic resonance frequency variation (**Figure 2.19**) by using the sensitivity values previously determined and by using a microbalance. The mass values obtained by using both procedures were compared and are collected in **Table 2.7**.

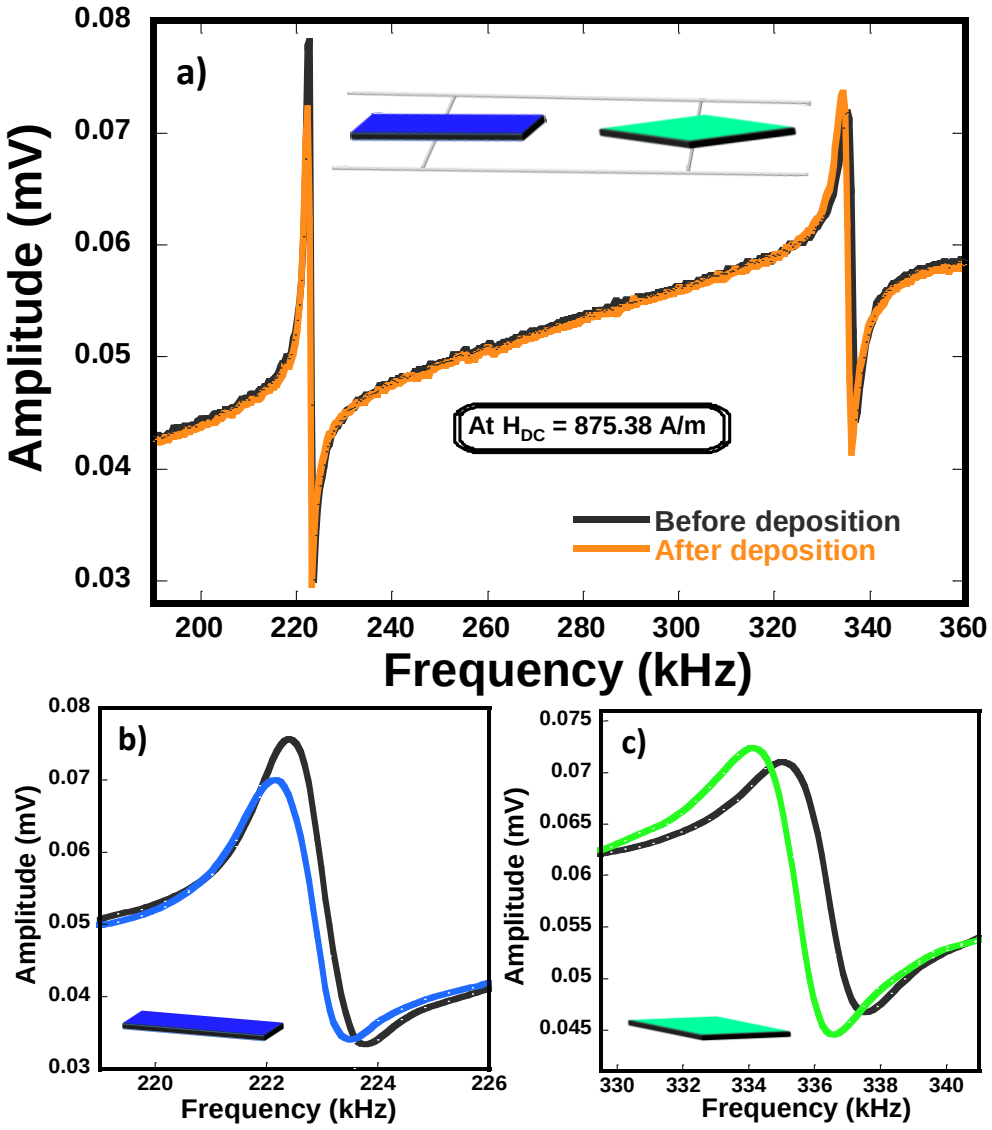

Figure 2.19. Results obtained for the test of the multiple sensor application. Whole resonance curve measured (a) and detail of the measured curves of the rectangle (b) and the rhomb (c).

Table 2.7. Resonance frequency shift measured (Δf), mass increase estimated from the magnetoelastic multiple sensor (Δm_{MS}) and mass weighted with the microbalance ($\Delta m_{balance}$).

Sample	Δf (Hz)	Δm_{MS} (μg)	$\Delta m_{balance}$ (μg)
Rectangle10 Coupled	313	7.0±0.6	7.1±0.1
Rhomb10 Coupled	1000	14.4±0.5	13.8±0.1

As it can be appreciated, the values obtained from the magnetoelastic multiple sensor are in agreement with the ones obtained by using the microbalance. Experimental errors are on the basis of the small differences between the two obtained values. Thus, the obtained results demonstrate that our magnetoelastic multiple sensor works and opens up new perspectives in the field of simultaneous and multiple target detection systems. So far, there is just a couple of works describing multiple magnetoelastic sensor [21,22]. However, that designs are focused on the effect of the size of each strip in a multiple rectangular resonators sensor, which also leads to different resonance frequencies but using resonators with different detection active surfaces. The advantage of our proposed design is that it combines sensors of equal active surfaces but with different geometries, leading to different detection peaks at different resonance frequencies. The proposed approach could be extended to the other geometries in order to detect more than two compounds at the same time.

In conclusion, mass sensitivity, as well as other properties of magnetoelastic sensors, could be improved by changing the resonator geometry from the classical rectangular one to other geometries such a rhomb or a triangle. Nevertheless, the use of ME resonators with geometries different from the commonly used rectangular one is just in its infancy and a deeper knowledge of their magnetic and magnetoelastic properties dependence with the geometry is highly necessary. Thus, the magnetic properties of the samples have been analysed to better understand the behaviour of that new magnetoelastic resonators geometries.

2.4. Influence of the geometry in the magnetic domain structure of the resonators (MOKE effect)

As previously stated, there is a considerable effect of the magnetoelastic resonator geometry on its mass sensitivity. Nevertheless, the use of the ME resonators with non-rectangular geometries is just in its infancy and a deeper knowledge of their magnetic and magnetoelastic properties, their interplay, and their influence in the detection capabilities is highly necessary. In the attempt to better understand the performance of these new ME platforms, an analysis of the relation between their macroscopic magnetic behaviour and their magnetic microstructure has been performed in this section. Three different geometries have been selected for this analysis: the classic rectangle, a triangle

and a rhomb, all of them with a length of 12 mm and equal surface area. A scheme of the analysed resonators is shown in **Figure 2.20**.

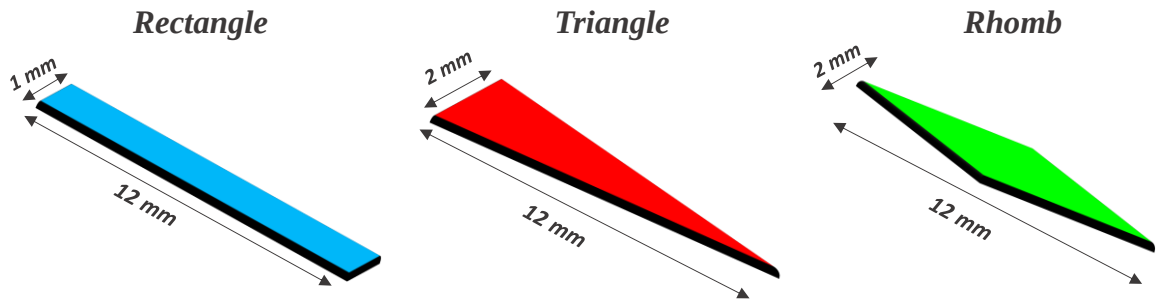

Figure 2.20. Scheme of the magnetoelastic resonators of 12 mm in length analysed in this part.

First of all, the macroscopic hysteresis loops of these samples have been measured using standard measurement methods by vibrating sample magnetometry (VSM). Results are shown in **Figure 2.21**.

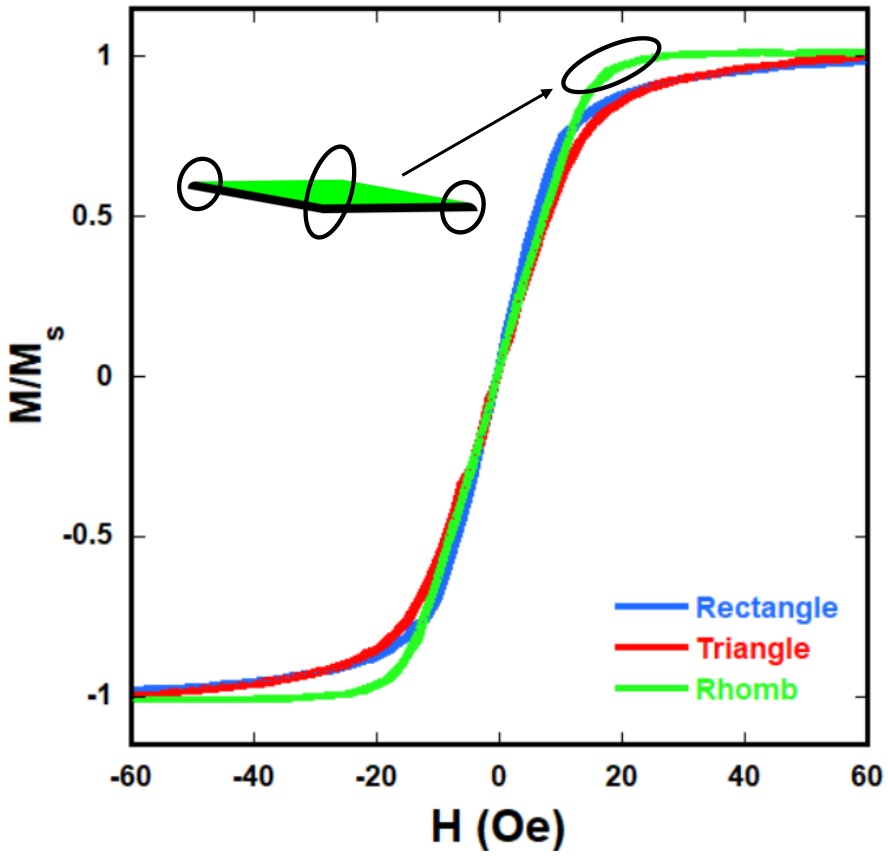

Figure 2.21. Macroscopic hysteresis loops measured for the different samples.

Looking at the results, it can be observed that, while the coercivity of the three resonators remains similar and close to zero, the different geometries show different behaviour towards saturation. More concretely, it is clear that, while the rhomb reaches saturation at around 20 Oe, both the rectangle and the triangle need higher fields to saturate. The different macroscopic magnetic behaviours can be attributed to the different sizes and distributions of the micromagnetic domains along the different geometries, as will be discussed hereafter. Actually, the anisotropy field of each sensor (and therefore the magnetization saturation) is highly dependent on the domain distribution which, in turn, depends, among others, on the different competing anisotropy terms [23], being in this particular case magnetocrystalline anisotropy (which is composition dependent and, therefore, similar in all the resonators) and shape anisotropy. As a consequence, the strength of the magnetic fields needed to orientated the micro-magnetic domains present in each resonator towards saturation differ substantially. A direct inspection of the local magnetic microstructure of the resonators will help to correlate that different macroscopic magnetic behaviours observed with the magnetic microstructure in each sample [24].

Thus, in order to better understand the dependence of the magnetic properties with the resonator geometry, an analysis of the local magnetic microstructure of the samples by means of magneto-optic Kerr effect (MOKE) microscopy imaging [25] is proposed. Local hysteresis loops, together with their corresponding real-time images of the magnetic domains present in the region inspected, have been measured with the field applied along the long axes of the samples. Three critical zones of each resonator have been particularly investigated: one edge, the centre of the resonator, and the other edge. The critical zones have been determined due to their different magnetic behaviour and underlying magnetic domain structures. The recorded local hysteresis loops in these critical zones, which are similar in each of the different geometries within the same zone, are presented in **Figure 2.22a** together with a scheme of the resonators with the different analysed zones marked in different colours. The magnetic domain images recorded at remanence in these zones, which are similar in the three samples and whose representative images are shown in **Figure 2.22**b, have been labelled as type 1 (orange), type 2 (blue) and type 3 (pink). The domain structures and sizes are clearly distinguishable within the images measured at remanence in each of these zones.

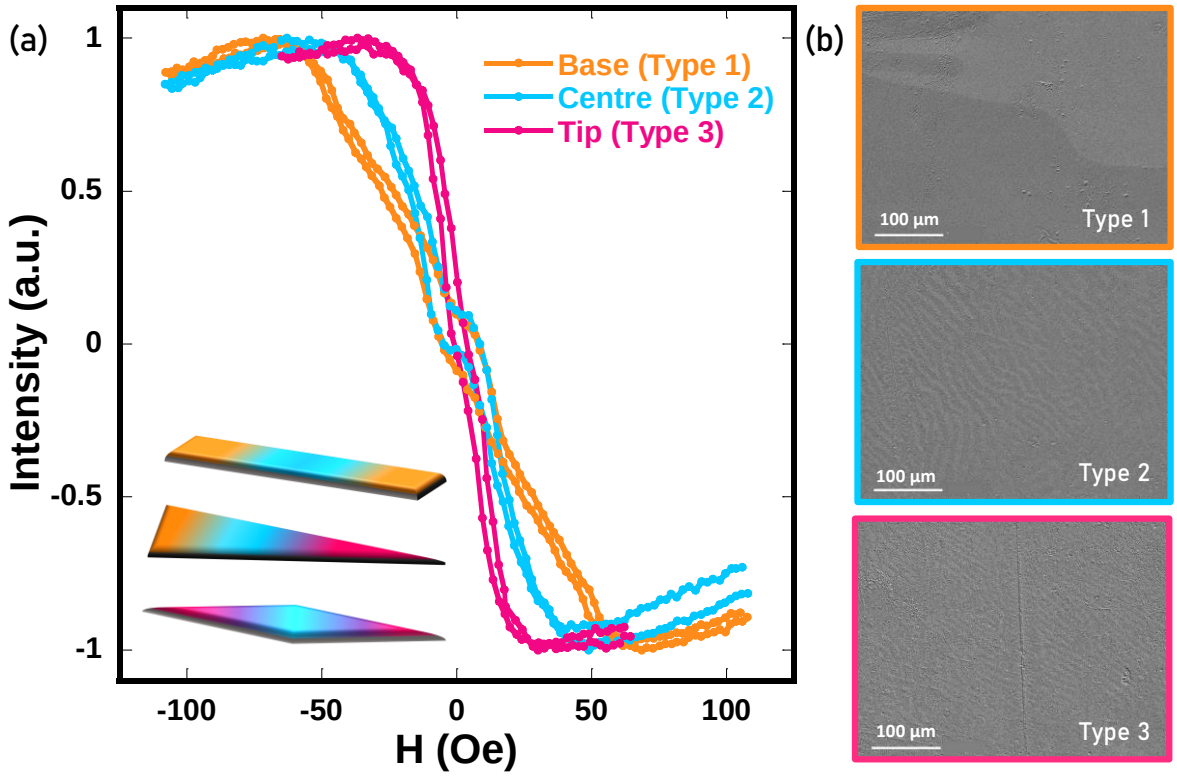

Figure 2.22. (a) Microscopic hysteresis loop measured at different characteristic zones of the analysed geometries (inset) (b) Representative magnetic domains images measured at the remanence on the different zones of the resonators analysed: the base (orange), the centre (blue) and the tip of the samples (pink).

Analysing the results, a common trend in the magnetic domain sizes is observed in all the samples: the type 1 domains are the largest one and are always found at the wider ends (orange), whereas closer to the tip (pink) smaller domains are found (type 3). In the centre of the samples intermediate size domains are found (type 2). This means that the smallest domains (type 2) are found at the centre (blue) in the case of the rectangle, while for the rhomb and the triangle they are found at the tips (type 3, pink). The appearance of smaller domains close to the narrow edges of the two samples with tip-ends (triangle and rhomb) is attributed to two effects: (i) the magnetostatic energy in this region is lower due to the presence of a sharp edge, where stray fields would otherwise be created, therefore resulting into the formation of small domains that minimize the combination of the magnetic exchange and magnetostatic energy; and (ii) the presence of numerous pinning points which favours the nucleation of magnetic domains due to the presence of more shape irregularities in the sample [26].

As a consequence, the magnetization reversal process of the samples starts at these sharp edges (when present), where the smallest domains are nucleated at a certain (small) applied field. When the applied field is increased towards saturation, the small domains not pointing at the applied field direction begin to rotate towards it. This process leads to the formation of bigger domains that propagate towards the broad end of the sample, resulting into the observation of intermediate-size magnetic domains in the central part of the sample (type 2) and bigger domain sizes in the broad part of the sample (type 1). This reversal mechanism explains (i) the trend in the coercive fields (H_c) deducted from the local hysteresis loops depicted in **Figure 2.22**a, being a direct correlation between the domain size and H_C; and (ii) the trend in the fields at which saturation is reached in each local measurement, being these also directly correlated with the domain size.

The reversal mechanism is different in the sample without a narrow tip edge (rectangle), where the closure domains at the broad edges are much larger than these found in the sharp edges of the other two samples. The presence of pinning points and shape irregularities in the edges of the rectangular resonator is not enough to cause the magnetostatic energy to overcome the exchange energy avoiding, in this way, the formation of smaller closure domains similar to these found in the sharp edges of triangular and rhombic shaped platforms. Indeed, for the rectangular resonator, the magnetization reversal mechanism begins far from the edges (in the centre of the sample) and propagates towards the broad edges when increasing applied field.

In contrast, the lack of those bigger domains in the rhomb sample, which do not need to be reversed to saturate the magnetization, is responsible for the lower value of M_S, observed in this sample, with respect to the ones presenting broad edges, as can be seen in the macroscopic hysteresis loops presented in **Figure 2.21**.

In view of the results, it could be concluded that the mass sensitivity is directly related to the magnetic microstructure present in the magnetoelastic resonators, with the smallest average domain size of the resonators resulting into the most sensitive geometry (the rhomb). Both triangular and rhombus magnetoelastic platforms present larger areas where big and small magnetic domains coexist and where the magnetic instability is maximized. This is particularly evident in the case of the rhomb, where the bigger domains are not present. These samples with a larger area of unstable magnetic domains

are also the ones that present higher mass sensitivity indicating that apparently, there is a close relation between these two factors.

2.5. Summary and conclusions

In this chapter, the role of the geometry of magnetoelastic resonant platforms on its load mass sensitivity, quality factor and magnetoelastic coupling has been deeply analysed. Theoretical and experimental measurements have been carried out in order to compare the performance of magnetic resonators with novel geometries (triangular, arched triangular and rhombic) with respect to the classical rectangular one. Results show a huge increase of the sensitivity from the classic rectangular to the triangular, the arched triangular and the rhombic magnetoelastic resonators.

In particular, the use of triangular and arched triangular shaped MR results in an increase of more than 148 % and 240 % in the mass load sensitivity in comparison with traditional rectangular systems. Moreover, it was also noticed that the sensitivity can be further improved by the partial coating of the edge/tip of the magnetoelastic resonant platform when compared to the completely covered surface. Again, this sensitivity enhancement is higher on the novel triangular and arched triangular sensors. Indeed, by the selective tip/edge coating of MR until a distance of 4 mm an increase of about 250, 1620 and 6400 % of the sensitivity can be achieved for the rectangular, triangular and arched triangular shaped sensors, respectively.

Moreover, a novel rhombic symmetric geometry (with double number of tips) has also been investigated. In particular, the magnetoelastic properties and mass sensitivity of rhombic shaped resonators outperform by much the ones of rectangular systems with the same length and surface areas. This conclusion was further supported and validated through theoretical simulations and experimental measurements that were performed after the deduction of the mathematical equation for the magnetoelastic resonance frequency of rhombic geometries. In both cases, a ratio of $f_r^{rh}/f_r^{rec} \sim 1.53$ between the resonance frequencies of the rhombus and rectangular shaped resonators of the same length has been obtained.

In addition, it has been firmly demonstrated that it is possible to combine MR with different geometries (rhombic geometry and the classically used rectangular one) in a multiple and simultaneous mass detection system. Indeed, the integration of both

geometries in a unique multiple sensor does not affect to the main magnetoelastic parameters of the free-standing resonant platforms.

Finally, the macroscopic and microscopic magnetic structure and properties of the resonators with different shapes have been investigated by VSM and KERR microscopy techniques. The results drawn by VSM and KERR combined characterizations show that the magnetic closing domains are mostly neglected at the tips while are very big at the wider edges, and henceforth, that the geometry of the MR affects its magnetic microstructure, and consequently its magnetoelastic properties.

As general, the size, geometry, selective coating and magnetic microstructure of MR affect their magnetoelastic response and have been identified as key parameters to improve the performance of future mass detection wireless sensors based on magnetoelastic platforms. In particular, there is still a room of improvement in term of sensitivity gain by further tuning the geometry and partial coating of MRs, especially if these modifications are combined with the reduction on the resonator size to the microscale. There are plenty of opportunities to engineer higher sensitive sensors based on the conclusions drawn by our results, a potential that can further extend the range of applications of MR platforms.

2.6. References

1. Sagasti, A., Gutierrez, J., San Sebastian, M. & Barandiaran, J. M. Magnetoelastic resonators for highly specific chemical and biological detection: A critical study. *IEEE Trans. Magn.* **53**, (2017).

2. Shen, W., Mathison, L. C., Petrenko, V. A. & Chin, B. A. Design and characterization of a magnetoelastic sensor for the detection of biological agents. *J. Phys. D. Appl. Phys.* **43**, (2010).

3. Lakshmanan, R. S., Guntupalli, R., Hu, J., Petrenko, V. A. Barbaree, J. M., & Chin, B. A. Detection of Salmonella typhimurium in fat free milk using a phage immobilized magnetoelastic sensor. *Sensors Actuators, B Chem.* **126**, 544–550 (2007).

4. Zhang, K., Fu, L., Zhang, L., Cheng, Z. & Huang, T. Magnetostrictive particle based biosensors for in situ and real-time detection of pathogens in water. *Biotechnol. Bioeng.* **111**, 2229–2238 (2014).

5. Johnson, M. L., Wan, J., Huang, S., Cheng, Z., Petrenko, V. A., Kim, D. J., Barbaree, J.M., Hong J. W., & Chin, B. A. A wireless biosensor using microfabricated phage-interfaced magnetoelastic particles. *Sensors Actuators, A Phys.* **144**, 38–47 (2008).

6. Johnson, M. L., LeVar, O., Yoon, S. H., Park, J. H., Huang, S., Kim, D. J., Cheng, Z., & Chin, B. A. Dual-cathode method for sputtering magnetoelastic iron-boron films. *Vacuum* **83**, 958–964 (2009).

7. Zhang, K., Zhang, L. & Chai, Y. Mass load distribution dependence of mass sensitivity of magnetoelastic sensors under different resonance modes. *Sensors* **15**, 20267–20278 (2015).

8. Zhang, K., Zhang, L., Fu, L., Li, S., Chen, H., & Cheng, Z. Y. Magnetostrictive resonators as sensors and actuators. *Sensors Actuators, A Phys.* **200**, 2–10 (2013).

9. Lopes, A. C., Sagasti, A., Lasheras, A., Muto, V., Gutierrez, J., Kouzoudis, D., & Barandiaran, J. M. Accurate determination of the Q quality factor in magnetoelastic resonant platforms for advanced biological detection. *Sensors* **18**, 1–12 (2018).

10. Marín, P., Marcos, M. & Hernando, A. High magnetomechanical coupling on magnetic microwire for sensors with biological applications. *Appl. Phys. Lett.* **96**, 1–4 (2010).

11. Sagasti, A., Gutiérrez, J., Lasheras, A., & Barandiarán, J. & .M. Size dependence of the magnetoelastic properties of metallic glasses for actuation applications. *Sensors* **19**, 1–10 (2019).

12. Grimes, C. A., Mungle, C. S., Zeng, K., Jain, M. K., Dreschel, W. R. Paulose, M., & Ong, K. G. Wireless magnetoelastic resonance sensors : A critical review. *Sensors* **2**, 294–313 (2002).

13. Schmidt, S. & Grimes, C. A. Characterization of nano-dimensional thin-film elastic moduli using magnetoelastic sensors. *Sensors Actuators A Phys.* **94**, 189–196 (2001).

14. Li, S. & Cheng, Z. Nonuniform mass detection using magnetostrictive biosensors operating under multiple harmonic resonance modes. *J. Appl. Phys.* **107**, (2010).

15. Zhang, K., Zhang, K. & Chai, Y. Study of 'blind point' and mass sensitivity of a magnetostrictive biosensor with asymmetric mass loading. *AIP Adv.* **4**, (2014).

16. Zhang, R., Tejedor-tejedor, M. I., Grimes, C. A. & Anderson, M. A. Measuring the mass of thin films and adsorbates using magnetoelastic techniques. *Anal. Chem.* **79**, 7078–7086

(2007).

17. Grimes, C. A., Roy, S. C., Rani, S. & Cai, Q. Theory, instrumentation and applications of magnetoelastic resonance sensors: A review. *Sensors* **11**, 2809–2844 (2011).

18. Li, S. & Cheng, Z. Y. Nonuniform mass detection using magnetostrictive biosensors operating under multiple harmonic resonance modes. *J. Appl. Phys.* **107**, (2010).

19. Hosseini, R. & Hamedi, M. An investigation into resonant frequency of triangular V-shaped cantilever piezoelectric vibration energy harvester. *J. Solid Mech.* **8**, 560–567 (2016).

20. Johnson, M. L., Wan, J., Huang, S., Cheng, Z., Petrenko, V. A., Kim, D. J., Barbaree, J.M., Hong J. W., & Chin, B. A. A wireless biosensor using microfabricated phage-interfaced magnetoelastic particles. *Sensors Actuators, A Phys.* **144**, 38–47 (2008).

21. Mungle, C., Grimes, C. A. & Dreschel, W. R. Magnetic field tuning of the frequency-temperature response of a magnetoelastic sensor. *Sensors Actuators, A Phys.* **101**, 143–149 (2002).

22. Huang, S., Yang, H., Lakshmanan, R. S. Johnson, M. L., Wan, J., Chen, I., Wikle III, H. C., Petrenko, V. A., Barbaree, J. M., & Chin, B. A. Sequential detection of Salmonella typhimurium and Bacillus anthracis spores using magnetoelastic biosensors. *Biosens. Bioelectron.* **24**, 1730–1736 (2009).

23. Welp, U., Vlasko-Vlasov, V. K., Crabtree, G. W., Thompson, C., Metlushko, V., & Ilic, B. Magnetic domain formation in perforated permalloy films. *Appl. Phys. Lett* **79**, 1315 (2001).

24. Bertotti, G. Ã. Connection between microstructure and magnetic properties of soft magnetic materials. *J. Magn. Magn. Mater.* **320**, 2436–2442 (2008).

25. Qiu, Z. Q. & Bader, S. D. Surface magneto-optic Kerr effect. *Review of Scientific Instruments* **71**, 1243–1255 (2000).

26. Zhao, Y. P., Gamache, R. M., Wang, G. C., Lu, T. M., Palasantzas, G., & De Hosson, J. T. M. Effect of surface roughness on magnetic domain wall thickness, domain size, and coercivity. *J. Appl. Phys.* **89**, 1325 (2001).


Chapter
ب

MOFs as active layers in magnetoelastic resonators

En este tercer capítulo se introducen los diferentes métodos de funcionalización empleados en esta investigación para integrar los MOF como capas activas en los resonadores magnetoelásticos. En un primer paso se ha investigado la respuesta de los resonadores bajo las condiciones de síntesis de diferentes MOF para, posteriormente, diseñar una vía de integración que asegure tanto la estabilidad de la cinta magnetoelástica, como la capacidad de adsorción de la capa activa del MOF. En base a los resultados obtenidos, estos métodos se han clasificado en: 1) crecimiento directo del MOF sobre el resonador y 2) deposición controlada del MOF una vez sintetizado mediante spin coating o impresión por spray. Las principales ventajas y desventajas así como las propiedades de las capas depositadas mediante estos métodos se discuten en detalle. Para finalizar, se han sintetizado diversos MOF de la familia del UiO-66, los cuales se han modificado con diferentes grupos funcionales y grados de defectos en sus estructuras, con el fin de amoldar sus propiedades y sus capacidades de adsorción, y estudiar, a posteriori, su comportamiento una vez integrados en los resonadores magnetoelásticos (capítulos 4 y 5).

Content

*** Publications in which this chapter is based.**

Some of the results shown in this chapter have been exposed in different indexed scientific publications: 1) **"Rhombic-magnetoelastic/metal-organic framework functionalized resonators for high sensitive toluene detection"**, *Journal of Materials Chemistry C (Q1), 2020, DOI:* doi.org/10.1039/D0TC02612C; and 2) **"Chromium speciation in Zr-based Metal-Organic Frameworks for environmental remediation"**, *Chemistry - A European Journal (Q1), 2020, DOI:* doi.org/10.1002/chem.202001435*;* as well as in some of the conferences presented in Annex C (Results dissemination).

3.1. Introduction

The improvement of the magnetoelastic sensors not only depends on the resonator properties, as explained in the previous chapter but also on the intrinsic properties of the active layer and its integration in the resonator platform. Therefore, as sensing process with magnetoelastic resonators depends on the mass gain when the system is in contact with the target analyte, increasing the adsorption capacity of the active layer is critical. In this regard, the use of highly porous materials such as MOFs could be a smart approach to increase the overall sensing response of magnetoelastic based sensors.

In this regard, the integration of the MOF active layer on the magnetoelastic resonator surface is also crucial, since its properties (*such as mass, homogeneity, arrangement of the MOF particles or mechanical stability*) will contribute to shaping the adsorption capacity and kinetics of the MOF based resonators, and hence, will modulate the magnetoelastic sensing response of the system.

The assembly of MOF as thin films has become a rapidly evolving field in the last years due to the need of many applications to shape MOFs as continuous layers deposited or growth on different substrates, instead of applying the MOF in its powder form [1]. For that reason, many works have reviewed the techniques and strategies employed for the integration of MOFs thin layers in different devices so far [2–4]. These approaches could be divided into two main groups: those involving a direct growth of the MOF into the substrate or those involving a post-synthesis deposition of the powder material.

Many techniques have been employed for the direct growth of MOF layers into different substrates, but the most commonly applied ones are the layer by layer (LBL) approach [5] and the MOF layer crystallization through the direct immersion of the substrate in the synthesis media [6]. The sequential incorporation of the MOF building blocks (metal nodes and linkers) by the LBL method lead to the already known as surface-mounted MOFs (SURMOFs). This term was firstly introduced by Fischer and co-workers in 2007 [7,8]. SURMOFs lead to continuous films with an extended ordered arrangement without cracks. Besides, the layer thickness and the MOF crystals orientation could be controlled by the number of immersion cycles as well as by the functionalization of the substrate, respectively [9,10]. The main drawback of the LBL technique is that in addition to being time-consuming, the overall amount of MOF contained in the SURMOF layer is low

even after several LBL cycles. It is worthy to mention that the quality of the MOF layers obtained by LBL is very suitable for gas separation applications, just to cite one of the most explored fields in this sense. Nevertheless, in the specific case of magnetoelastic sensors, the larger the mass of MOF material integrated into the active layer, the higher the amount of target analyte adsorbed, and the higher the magnetoelastic frequency shift.

An alternative to LBL is the direct growth of the MOF layer by the immersion of the substrate in the synthesis media. This approach leads to a direct crystallization of the MOF into the substrate from the mother solution, and results in a well-attached layer in a shorter period of time, but with a disordered arrangement of the MOF crystals that usually leads to crack or pinholes within the MOF membrane. Other works report the use of chemical vapour deposition (CVD) [11] or vapour-assisted conversion (VAC) [12] in which the contact of the substrate with the synthesis media is substantially reduced.

The direct growth of high-quality MOF layers at a resonator substrate avoiding its corrosion or oxidation is still challenging since the synthesis of many MOFs are usually performed on aggressive solvents, varied acidic media (depending on the metal), and in some cases, under harsh temperature and pressure conditions. Indeed, this is the case of UiO-66 functionalization of magnetoelastic resonators based on Fe-B ferromagnetic alloys explored in this chapter.

On that context, the exploration of alternative approaches to achieve the MOF post-synthesis integration into the metallic resonators becomes necessary. In particular, most common post-synthesis deposition techniques include dip coating [13], spin coating [14] or spray coating [15], which allow integrating homogeneously higher amount of mass in the active MOF layer in comparison to LBL or direct growth approaches. In addition, these techniques are faster, are currently implemented at industrial scales, and prevent the substrate from corrosion since they allow selecting a wide variety of solvents and soft deposition conditions, overriding the contact of the substrate with the MOF synthesis medium. However, the use of these post-synthesis techniques with powder type materials presents also some disadvantages, being especially critical the weak adhesion of the MOF layer to the substrate. A way to improve the adhesion as well as the mechanical properties of the MOF layer could be the use of a polymer acting as a binder, but always taking into account that the higher the ratio of the polymer incorporated with the MOF, the lower the adsorption capacity of the finally integrated layer.

Thus, taking all the above explained considerations, the most appropriate integration path will also depend on the specific requirements of the final applications, as well as on its compatibility with the properties of the substrate.

By using the previously described techniques, MOF materials have been successfully integrated into substrates such as gold [16], silicon [17], nanoparticles (such Fe_3O_4 [18] or ZnO [19]) or polymers (such polyacrylamide [20] or polystyrene [21]), among many others. Nevertheless, there are no previous works reporting the deposition of MOFs layers in magnetoelastic resonators, and most in particular, in Metglas 2826MB substrates.

The analysis of the corrosion properties of the Metglas alloy (magnetoelastic ribbon used as platform in our sensors) has been the subject of many studies, showing its good corrosion resistant properties under exposure to different environments [22]. Until date, different materials such as zeolites, polymers or nanoparticles have been successfully integrated as active layers on magnetoelastic resonators (**Table 1.1**). In particular, many responsive polymers have been deposited in Metglas resonators by dip coating [23] or spin coating [24] techniques. Moreover, metal oxide nanoparticles have also been deposited on Metglas ribbons by direct casting the particles onto the resonator surface [22,25] and by dip coating methods [26]. Other materials such zeolites have been effectively grown by direct synthesis methods [27,28] showing a good response of the Metglas resonators to the synthesis conditions. Nevertheless, it is worthy to note that there are some applications (especially in biosensing) for which the working conditions results too aggressive for Metglas supports leading to its corrosion or degradation [29]. In these cases, gold or polymers layers are frequently employed to protect the magnetoelastic resonators from the corrosive media and so to prevent their degradation [29–31].

Nevertheless, although the good corrosion resistant properties reported for Metglas 2826MB under different conditions, there is a lack of knowledge regarding the stability of this system when exposed to the conditions and chemicals used in the MOF synthesis. MOF materials reported until now have been synthesized by different techniques (Solvothermal, microwave, sonochemical or electrochemical) and in very different solvents depending on the acidity of the metal ions and the solubility of the organic linkers (water, methanol or DMF, among others). Thus, the selection of the adequate MOF, as well as its synthesis conditions, will be a key factor to achieve the direct growth of MOF materials into the magnetoelastic resonators, post-synthesis techniques should

be considered when this is not possible. In particular, two case studies for direct growth have been explored in this chapter: 1) the direct growth of divalent zeolitic imidazole framework (ZIF) and 2) the direct growth of zirconium based metal organic frameworks (concretely the widely studied UiO-66 materials). These two cases can be understood as the extreme points in terms of the synthesis conditions softness (ZIF) or harshness (UiO-66) of MOF materials. It is worthy to mention that some aluminium and chromium MOF materials exceed by much the temperatures and acidities applied for the synthesis of UiO-66 material. Nevertheless, the explored case studies lies within the synthesis conditions applied to obtain a large number of MOFs reported so far. It is also important to note that both ZIF and UiO-66 families have been widely used in different applications due to their excellent adsorption properties.

In particular, ZIFs present structural arrangement similar to that of zeolites, in which there are metal ions with tetrahedral coordination (Zn or Co, among others) linked by 2-metylimidazole ligands [32]. This connectivity gives rise to a sodalite (SOD) type structure, with a pore diameter close to 11.6 Å, but accessible through small pore windows of around 3.4 Å [33]. In particular, ZIF-7 stands out for its exceptional chemical and thermal stability combined with a high hydrophobic pore surface. Moreover, some ZIFs are usually synthesized at very soft conditions, this is, at room temperature and in non-aggressive solvents (such as water [34] or methanol [33]). The structure of ZIF-8 and ZIF-67, together with their main synthesis conditions, are shown in **Figure 3.1**

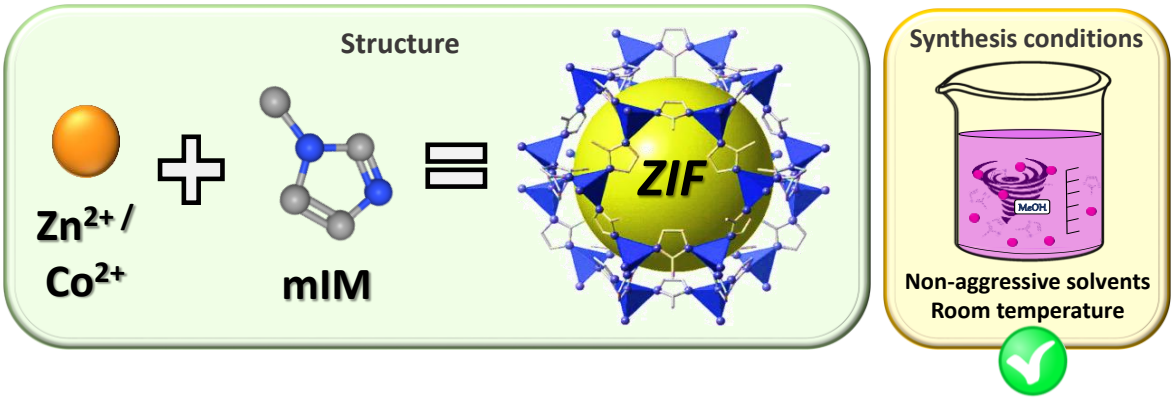

Figure 3.1. Basic units of construction and crystal structure of the ZIF-8 and ZIF-67 together with their synthesis conditions.

On the other side, UiO-66 is a (UiO=University of Oslo) zirconium based terephthalate MOF that consist on cubic structures built up from $Zr_6O_4(OH)_4(\text{-}COOH)_{12}$ hexanuclear

clusters connected through twelve terephthalate type organic linkers, as shown in **Figure *3.2***. The "fcu" cubic structure of UiO-66 contains two types of pores with different geometries, an octahedral cage formed by six zirconium hexanuclear units connected through organic terephthalate linkers, and tetrahedral cages with smaller pore volume assembled from four zirconium hexanuclear units [35]. Zr-based MOFs, and in particular the UiO-66 family stands out especially because both their inorganic and organic structural units are easily tuneable. Indeed, many chemical motifs bringing varied functionalities have been included within the UiO-66 framework in order to improve its adsorptive properties or endow the materials with light harvesting, catalytic or photo-catalytic properties. Moreover, UiO-66 exhibits a quite interesting defect chemistry, in such a way that different degrees of organic linker or even cluster defects can be randomly introduced within its crystal structure depending on the synthesis conditions. Indeed, it is possible to reduce the clusters connectivity from twelve up to eight linkers [36–39] ("*defect engineering*"), a characteristic that affects the pore distribution and adsorption capacity of the material significantly. UiO-66 is commonly prepared by solvothermal methods and in harsh conditions, marked in part by the acidity of the initial reagents usually employed to synthesize the material (Zirconium chloride and dicarboxylic acid).

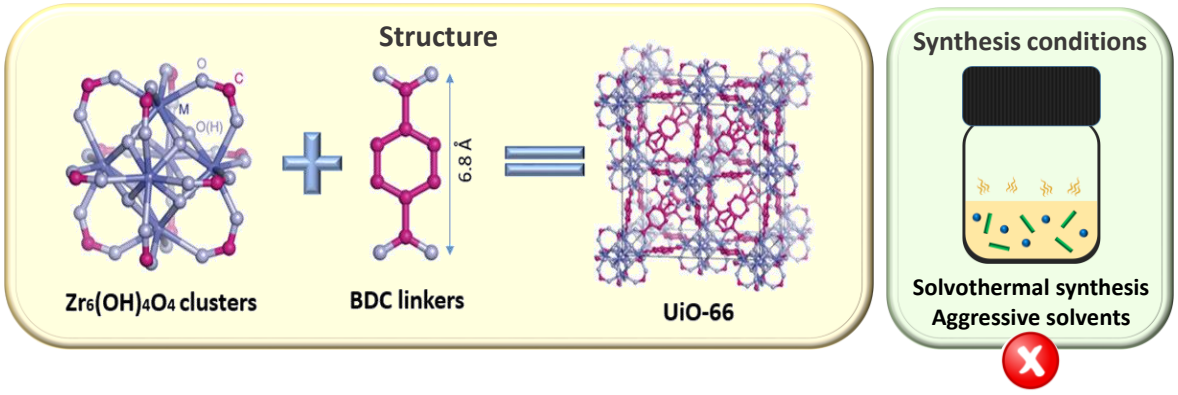

Figure 3.2. Basic units of construction and crystal structure of the UiO-66 type MOFs together with their synthesis conditions.

Moreover, a scan of the stability of Metglas resonators under different metal salts, organic ligands and solvents has been carried out also in order to understand what type of MOFs could be grown in the magnetoelastic resonators by means of the direct synthesis method.

Bearing all these previous considerations in mind, the purpose of this chapter is to find out a straightforward methodology to integrate MOF active layers onto magnetoelastic resonators. Thus first, the stability of the Metglas resonator platform has been studied under the synthesis conditions usually employed to obtain these MOF materials. Once identified the stability windows of Metglas alloys, the advantages and disadvantages of different MOF integration techniques will be deeply described and analysed. Finally, for the specific case of UiO-66 material, the strategy to modulate its adsorptive, chemical reductive and photo-catalytic properties by means of linker defect generation and functional groups encoded within its structure is described, not only to improve the performance of the bulk material but also of the active layer after its integration on the resonator transductor platform.

3.2. Magnetoelastic resonators functionalization methods

The methodologies considered for the MOF integration at the resonator platforms have been classified as *direct growth*, if the deposition have been carried out directly during the synthesis of the MOF, or as *post-synthesis deposition*, in case the deposition have been performed after synthesizing the MOF. It should be noted that prior to the coating process, the magnetoelastic resonators have been always washed with acetone for 15 minutes in the ultrasonic bath in order to clean the resonator's surface. A scheme with the main techniques considered along this thesis is presented in **Figure 3.3**. Obtained results, organized according to the method employed to integrate the MOF layer in the magnetoelastic resonator, are shown on the following.

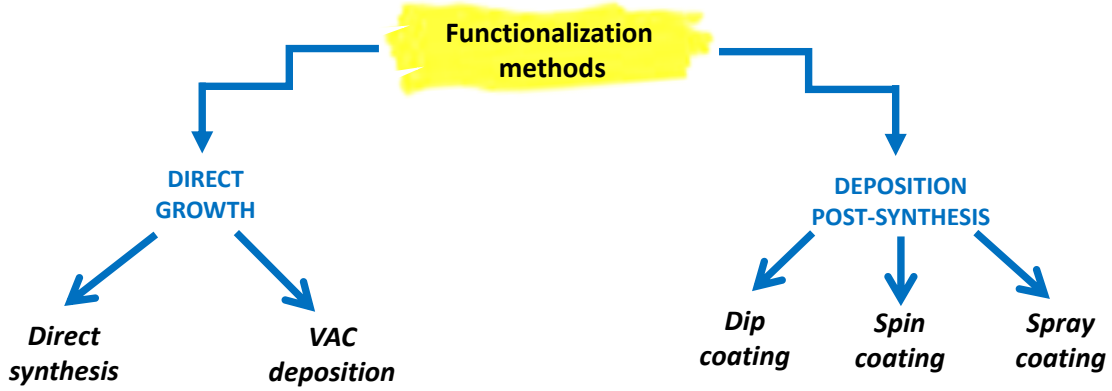

Figure 3.3. Scheme of the different functionalization processes tested along this thesis.

3.1.1. Direct growth methods

A direct growth in the magnetoelastic resonator's surface during the MOFs synthesis is preferable to obtain a good attachment of the MOF to the sensor surface. Nevertheless, as previously stated, the direct growth of MOF layers into the Metglas resonators is challenging since they need to meet the chemical stability window of the resonator with the temperature, pressure, acidity, reagents and solvents used for the MOF synthesis. In the present work, the MOF crystallization on the resonator platform has been tried out by immersing the Metglas ferromagnetic alloy directly on the synthesis media as well as by vapour assisted crystallization (VAC) process in order to minimise the exposure time of the magnetoelastic ribbons to the reagents and media applied to growth the MOF. In particular, the analysis has been focused in the concrete cases of ZIF-8, ZIF-67 and UiO-66 metal organic frameworks for their integration on Metglas 2826MB resonators by these methods. First, the chemical stability of the Metglas resonators in the synthesis media of the abovementioned MOFs has been analysed; to later on study the MOF integration by post-synthesis deposition of these MOFs which synthesis conditions alter somehow the Metglas ferromagnetic alloys. Moreover, the stability of the Metglas resonators under different metallic salts, organic linkers and solvents have been investigated as a screening of the tolerable conditions for the resonators. Both methods, as well as the corrosion evaluation, are described on the following.

- *Direct synthesis*

The direct growth of the MOF active layer on the resonator surface has been tested for the ZIF-8, ZIF-67 and UiO-66 materials. A scheme of this functionalization method is represented in **Figure 3.4**. As could be observed, the method consists on the magnetoelastic resonator immersion in the synthesis media were the MOF building blocks (metal nodes and linkers) are dissolved, and afterwards, trigger the MOF crystallization by applying temperature and/or pressure if necessary. It is well known that the energy barrier of the nucleation process is lowered when the crystals growth in contact with rugose surfaces, since the crystallization benefits from the imperfections found on the resonator surface using them as low preferential nucleation positions (small fails, pinholes…). Therefore, any rugosity at the surface of the Metglas alloy is foreseen to favour the MOF crystallization, being the chemistry of the surface itself also an important parameter that can favour or slows down the process.

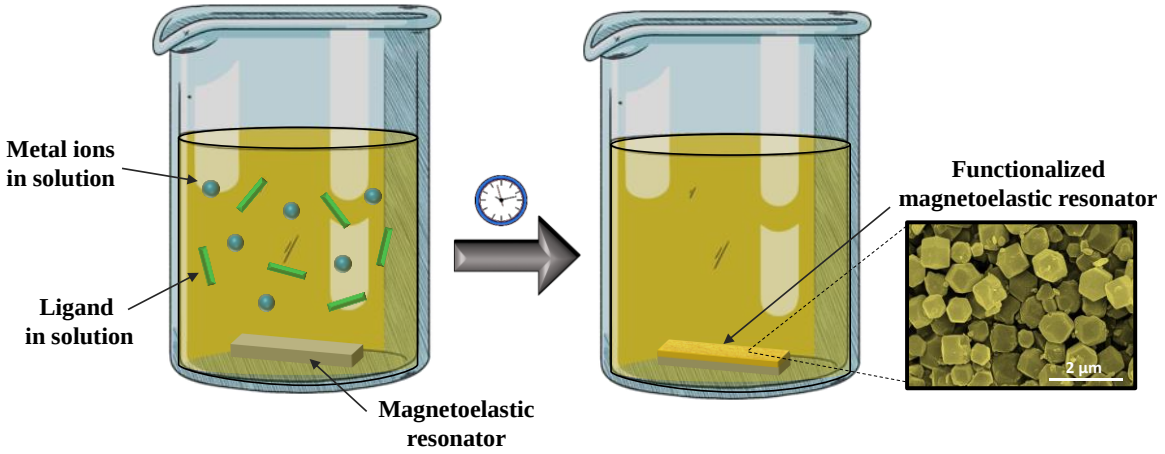

Figure 3.4. Scheme of the direct growth in the magnetoelastic resonator surface during the MOF synthesis process.

Direct growth functionalization method was initially tested for the ZIF-67 (cobalt) and the ZIF-8 (zinc) MOFs due to their softer synthesis conditions compared with that of the UiO-66 MOFs. Before to the ZIF-8 and ZIF-67 synthesis on the resonators, a piece of the Metglas alloy was immersed separately in methanol, cobalt nitrate, zinc nitrate and imidazole solutions in methanol. A visual inspection of the alloy under a binocular microscope after one day of exposition does not reveal any alteration of the resonator. Afterwards, the functionalization process of the Metglas resonators was performed immersing them in the ZIFs crystallization media under the same synthesis conditions reported in **Annex A** but lowering the reactive amounts. Thus, all the ZIF reagents were mixed in a glass vial and subsequently the magnetoelastic resonator was added to the reaction media and the mixture was lead under slow mechanical stirring promoting the growth of the ZIF particles in the resonator surface. After the process, the Metglas ribbon was extracted from the synthesis media and washed by immersing it in methanol three times during one hour. The visual inspection of the Metglas@ZIF resonator reveals the presence of a translucent white (ZIF-8) or purple (ZIF-67) layer in both faces of the Metglas ribbons. It is worthy of highlighting the simplicity of the process. Nevertheless, even when the MOF adhesion is quite good, the metglas@ZIF resonator needs to be handled carefully, since the ZIF layer is easily damaged when contacted with metallic tools, such as tweezers or spatulas.

Thanks to the magnetoelastic resonators wireless response, the ZIF-8 and ZIF-67 growth of the magnetoelastic resonators could be followed in real time by measuring the magnetoelastic resonance frequency shift as a function of the time (Inset **Figure 3.5**b). Results for the ZIF-67 growth in a 20x2 mm rhombic Metglas resonator are shown in **Figure 3.5**. As revealed by the kinetic profile of **Figure 3.5**a, the ZIF-67 growth occurs mainly during the first four hours, but it is extended above the 14h with slower rates.

This ability of magnetoelastic resonators to follow the crystallization and deposition of MOFs is extremely interesting and could give some insights on the crystallization kinetics of many MOFs (e.g. SURMOFS) that are obtained close to room temperature.

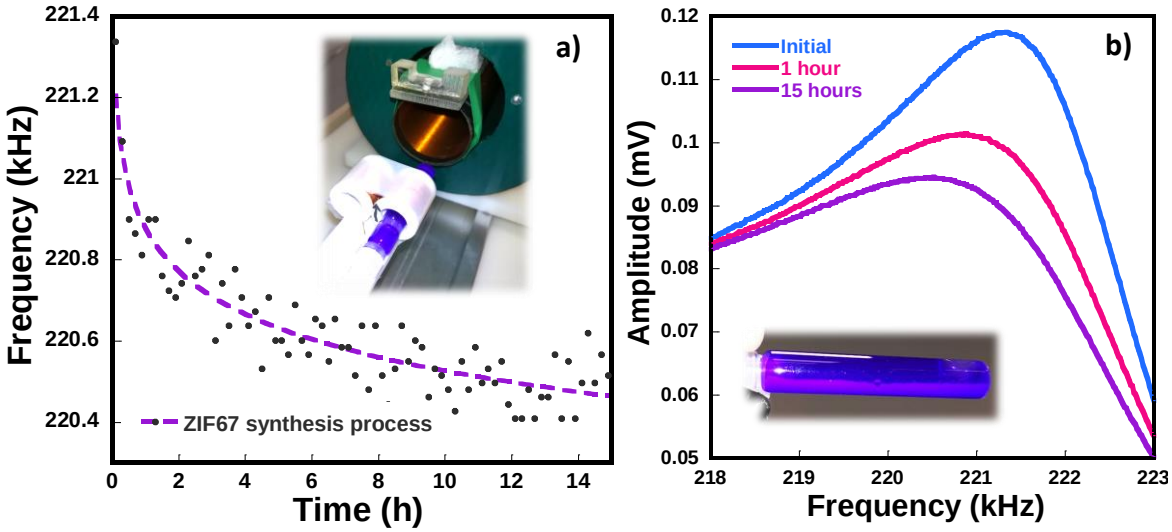

Figure 3.5. (a) Magnetoelastic resonance frequency as function of the time during the ZIF 67 synthesis (Inset: Glass vial placed in the magnetoelastic system during the synthesis). (b) Magnetoelastic resonance frequency curves measured at different times (Inset: Glass vial after the MOF synthesis process).

In fact, the resonance frequency decreases significantly, near 1 kHz, indicating a high mass deposition on the magnetoelastic sensor. This resonance frequency shift is related to the sum of the ZIF-67 particles crystallized and deposited on the resonator surface. It should be noted that due to the selected synthesis conditions, a significant amount of MOF precipitate in the vial and a great part is deposited on the resonator (Inset **Figure 3.5**b), but not all these particles are directly attached to the surface, although them contributes to the frequency shift. In fact, the resonance frequency shift measured after cleaning the Metglas resonator is quite low (below 200 Hz), which indicates that the ZIF-67 directly

growth on the resonator represents a small portion in comparison to the fraction precipitated in the vial. A strength of the MOF direct growth approach is that the resonator is not damaged under the functionalization process, which indicates that the soft synthesis conditions of some ZIFs are compatible with the Metglas composition.

The functionalized resonators were further characterized by X-ray diffraction and microscopy (optical and SEM) in order to further analyse the deposited active layers. Results are shown in **Figure 3.6**.

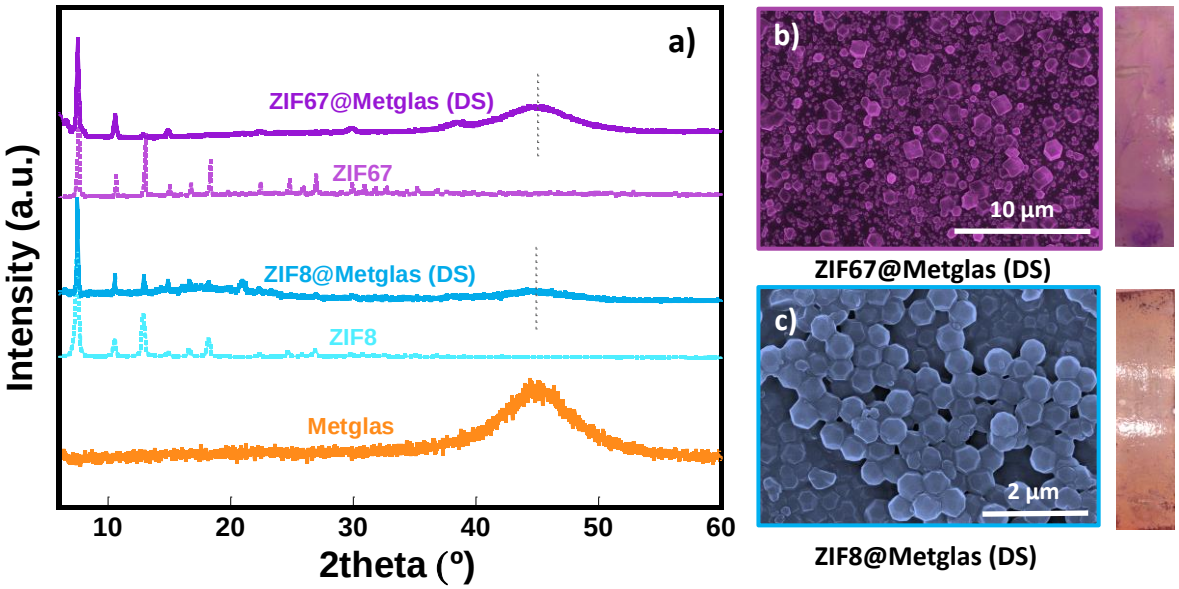

Figure 3.6. (a) X-ray diffractograms of the bare Metglas resonator, the ZIF8 and ZIF67 MOFs and the Metglas ribbons after the immersion in the ZIF8 and the ZIF67 water reaction media for 24 hours. SEM and optical microscope images of the magnetoelastic ribbons surface after the: (b) ZIF67 deposition and (c) ZIF8 deposition.

Both XRD and SEM results demonstrate the growth of the ZIF active layer on the Metglas surface. The X-ray diffraction maxima ascribed to the ZIFs materials could be observed in the functionalized resonators (**Figure 3.6**a). Besides, these diffraction patterns show an additional broad diffraction peak around 44.5 °, which is related to the (110) reflections of the α-Fe(Co) in the Metglas alloy structure [40].

The deposited layer seems very homogeneous at first sight under the binocular microscope, although the SEM images show that the particles grow as separate crystals over the entire surface (**Figure 3.6**b-c). The ZIF-8 and ZIF-67 particles present the typical

dodecahedral crystal morphology characteristic of that MOFs [41], with a medium particle size of around 0.8 μm for the ZIF8 particles and of around 1.6 μm for the ZIF67 particles. The mass of ZIF integrated within the resonator has been estimated based on the experimental frequency shift and normalized by surface unit (μg/mm^2) in order to compare the results with alternative deposition methods as well as bibliographic results. The total normalized mass achieved in each deposition cycle was calculated to be of around 0.8 μg/mm^2.

Summarizing, MOFs synthesized at soft conditions can growth by direct MOF synthesis at the resonator surface, but the overall amount of MOF layer is still small if we take into account that the detection process is driven by the mass gain of the MOF active layer during the target analyte adsorption. It will be highly desirable to obtain a thicker and heavier active layer to improve the detection process.

The reiteration for several cycles of the functionalization process by MOF direct growth approach could be a solution in order to get a thicker and heavier MOF active layer, but this approach will result time and resource consuming making difficult to be implemented at larger industrial scales.

Once proved that the integration of divalent metals based MOFs on the Metglas resonators is possible, the next milestone of this thesis was to transfer this approach to MOF materials synthesized on more aggressive conditions. This is the case of the archetypal UiO-66-NH_2 zirconium amino-terephthalate. With this aim, the direct growth of UiO-66-NH_2 in a Metglas ribbon was tested. Again, the functionalization process was performed under the same UiO-66-NH_2 synthesis conditions collected in **Annex A** but lowering the reactive amounts. All the reagents were mixed in a glass vial and the Metglas resonator was added. Then, the vial was sealed and introduced in the oven at 80 °C during 24 hours. Afterwards, the Metglas ribbons were inspected visually and under a binocular microscope (**Figure 3.7**a). The degree of corrosion/oxidation of the Metglas magnetoelastic resonators after their exposure to the synthesis media is quite evident. Metglas ribbons get damage also when exposed to separate zirconium chloride or terephthalic acid DMF solutions at 80ºC during 24h (**Figure 3.7**b). More probably, the acidity of the media generated when dissolving $ZrCl_4$ and amino-BDC components is the driven factor that induces the Metglas ribbons corrosion and oxidation.

Figure 3.7. (a)Image of the direct synthesis process of the UiO-66-NH_2 MOF in a Metglas resonator inside and after (inset) remove it from the reaction media, (b) test of the Metglas response after the different reagents exposure (BDC and $ZrCl_4$) and (c) image of different magnetoelastic resonators compositions after exposure to the UiO-66-NH_2 synthesis media.

Thus, the good corrosion resistant properties reported for the Metglas 2826MB alloy under different conditions are not enough to resist the integration of UiO-66-NH_2 by its direct synthesis. In order to protect the resonator from corrosion, it was covered with a gold protective layer [29]. Besides, the chemical stability of other home-made magnetoelastic alloys doped with chromium for higher corrosion resistance was also investigated [42,43]. Moreover, a commercial Vitrovac alloy [44] was also tested in addition to the gold-covered and chromium doped resonators. Unfortunately, all the studied platforms get appreciable damaged (oxidized/corroded) under that hard UiO-66-NH_2 synthesis conditions, independently on the protective additional gold layers or their improved composition.

An image of some of the magnetoelastic alloys tested after being exposed to the UiO-66-NH_2 synthesis is shown in **Figure 3.7**. Two are the key factors that can explain the resonators degradation. First, the higher the charge density of the metal ions used to synthesized the MOF, the lower the pH value that is generated on the synthesis media. Second, the Metglas alloys are based on metallic zero valent elements prompt to be dissolved or oxidized when contact acid solutions with high ionic strength. Thus, alternatives to diminish as much as possible the exposure of magnetoelastic resonators to the synthesis media of UiO-66 based MOFs need to be explored.

- ***Vapour assisted conversion***

A recently published work reported by Virmani et al. [12] described a vapour assisted conversion (VAC) growth to functionalize different substrates with UiO-66 based MOFs. Inspired by the VAC techniques applied in zeolites, the authors demonstrated that it is possible to control the thickness and characteristics of the UiO-66 film growth on the substrate just by modifying some experimental parameters. In addition, VAC diminishes appreciably the contact and MOF synthesis time, which could prevent the resonator degradation.

The VAC experimental protocol is summarized in **Figure 3.8**. First of all the precursor solution was prepared by dissolving all the reagents needed for the UiO-66-NH_2 synthesis (60 mg of $ZrOCl_2$, 36 mg of BDC-NH_2 and 133µL of acetic acid as modulator) in 10 mL of DMF. Then, DMF and acetic acid (16.8 mL and 3.2 mL, respectively) were mixed in a Pyrex glass bottle as the vapour source. After that, a glass platform was introduced inside the bottle and the magnetoelastic resonator was located above it. Then a couple of drops (100 µL) of the precursor solution were deposited on the resonator surface in order to promote the active layer growth. After that, the bottle was sealed and placed in the oven preheated at 100 °C for 3 hours. Finally, the glass bottle was removed from the oven. The advantage of this technique is that the contact time of the ribbon with the $ZrCl_4$ and DMF is limited since it is not immersed in the DMF solution, it is just in contact with the DMF atmosphere, a condition that could prevent the magnetoelastic ribbon from corrosion.

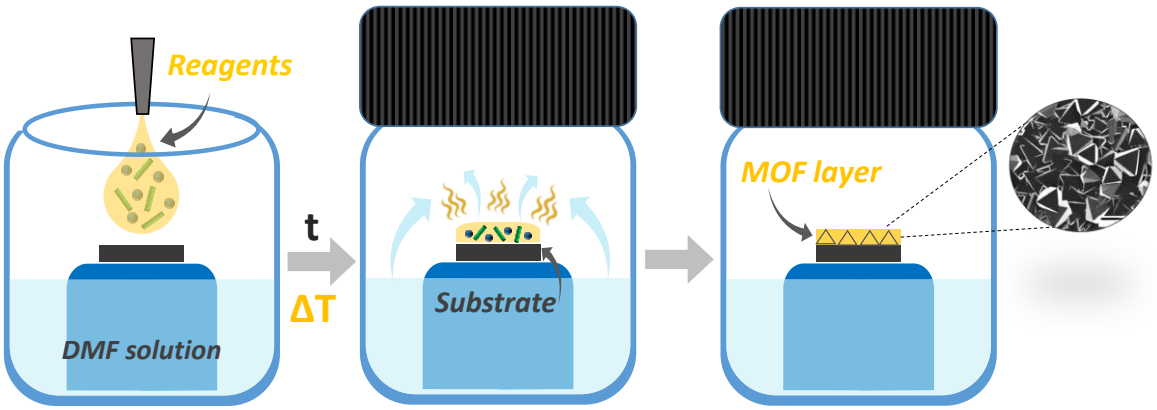

Figure 3.8. Scheme of the VAC functionalization method tested for the UiO-66-NH_2 MOF growth on the magnetoelastic resonators surface.

An image of the glass bottle with the magnetoelastic resonators at this point is shown in **Figure 3.9** together with SEM and optical microscope images of the ribbon surface at this point (**Figure 3.9**c) and the diffraction pattern measured for that sample (**Figure 3.9**b). It should be noted that again two Metglas resonators were tested (with and without a protective gold layer), but sadly, even limiting their exposure to the MOF synthesis media, the same corrosion degree was observed at the Metglas and gold-sputtered Metglas ribbons.

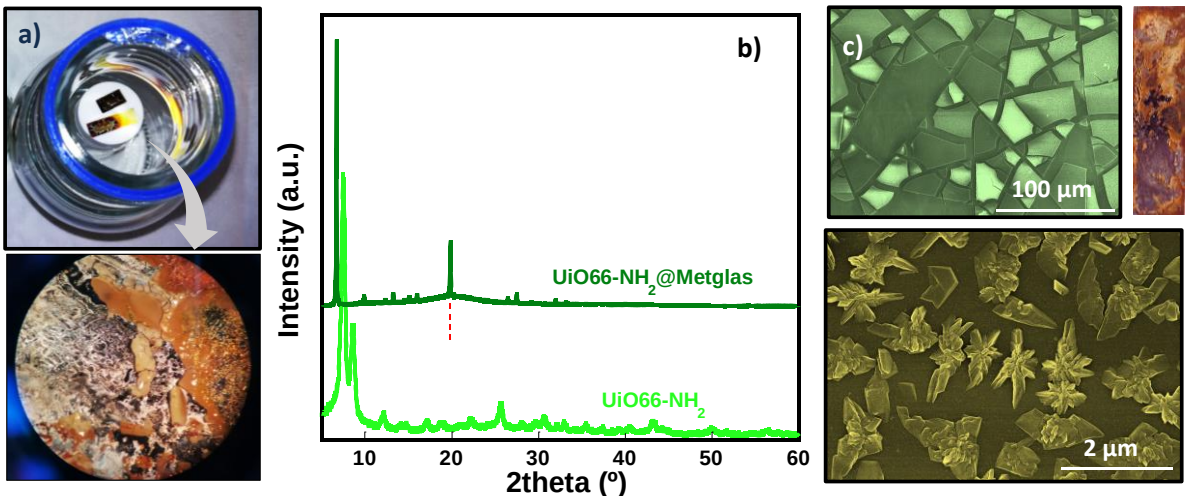

Figure 3.9. (a) Image of the magnetoelastic resonator just after remove the glass bottle from the oven. (b) X-ray diffraction patterns of the UiO-66-NH_2 MOFs and the Metglas ribbons after the direct UiO-66-NH_2 growth by VAC. (c) SEM and optical microscope images of the magnetoelastic ribbon surface after the MOF deposition.

It is particularly remarkable the X-ray diffraction pattern measured for the Metglas ribbons after VAC process, which shows diffraction peaks not related with the UiO-66-NH_2 structure, neither to the Metglas resonator. The new diffraction maxima have also been compared to the calculated patterns of different iron-based amino-terephthalate MOFs (e.g. MIL-88B-NH_2, MIL-101-NH_2 and MIL-53B), but it was difficult to certainly assure that the observed peaks belong to one these phases because of the high preferential orientational growth of the compound crystallized at the surface of the resonator. SEM images shown that this phase growth as mountain/stair like crystals of around 1 μm.

- ***Evaluation of the magnetoelastic resonators response under different metallic salts and organic linkers***

Metglas magnetoelastic resonators behave in a very different way depending on the synthesis conditions which is probably related with the acidity of the reaction media which is mainly affected by the solvent as well as by the metal and linkers reagents. There are many different MOFs and synthesis conditions so investigate which conditions affect the Metglas resonators and which not results difficult due to the high number of possibilities. But, to make a general screening could be possible by taking into consideration the main reagents and solvents employed to synthesized MOFs. As previously stated, MOFs are formed by metal centres linked by organic ligands. Among the many metal centres usually employed they could be classified according to its valence as: divalent, trivalent and tetravalent. Moreover, common organic linkers employed for MOF synthesis are based on dicarboxylic acids, imidazolates or pyridines. Finally, water, methanol and DMF are the most commonly employed solvents.

Taking this into account, the main purpose of this part is to analyze the stability of Metglas resonators in different possible reaction conditions in order to have an idea of what MOF families could be integrated into Metglas resonators by direct growths methods. As a first step, a sweep of various metals of different groups with different reduction potentials and valences was carried out. The different metallic salts employed have been: Zinc, cobalt, iron, copper, yttrium, chromium and zirconium. The different metallic salts were dissolved in two different solvents (water and DMF) and pieces of Metglas were added to the solutions and lead undisturbed during 24hours at room temperature or 80 °C in order to investigate their corrosion resistant. Some of the

solutions before and after the experiments are collected in **Figure 3.10** together with the Metglas resonators and zoom images of the most corrode samples.

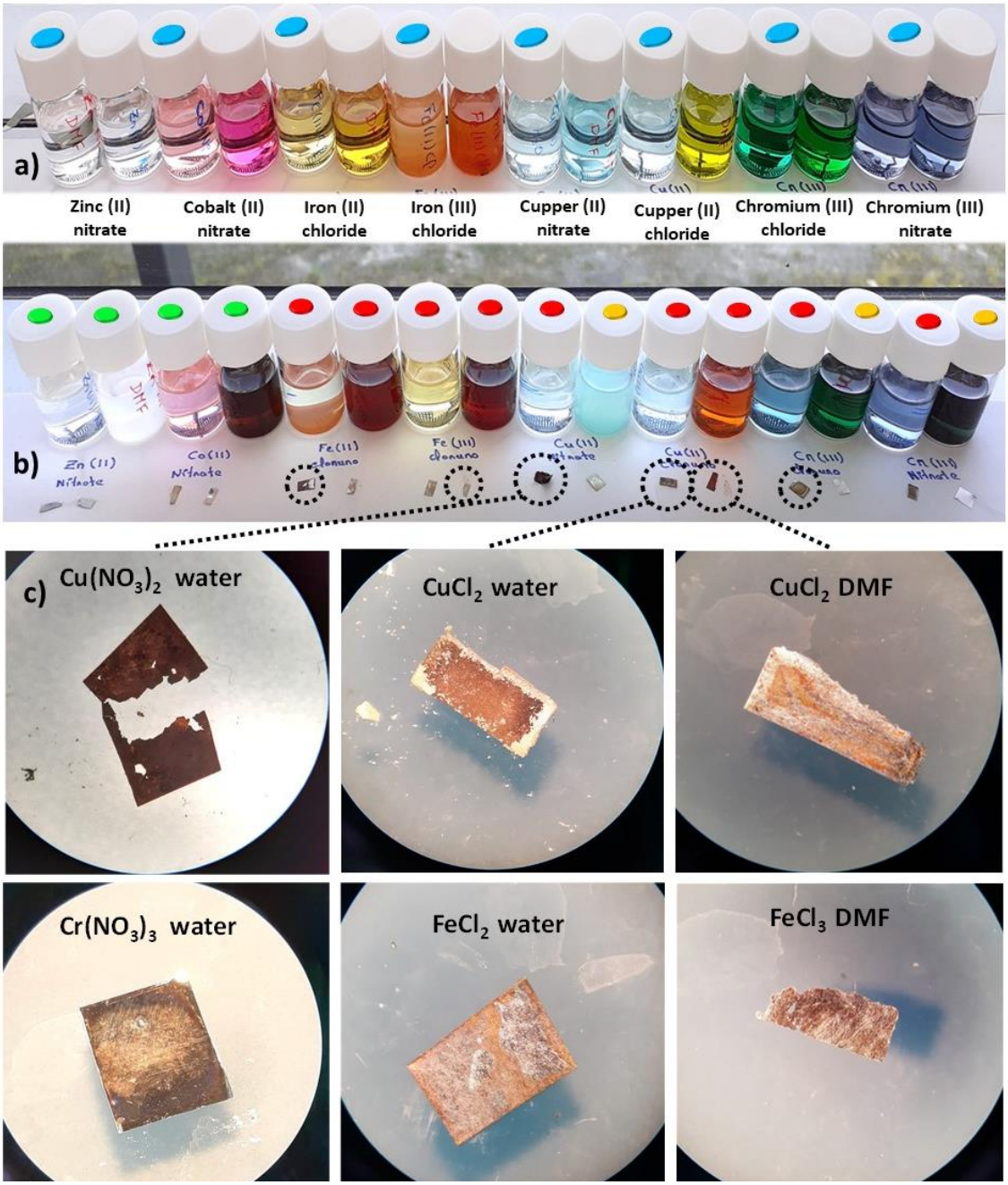

Figure 3.10. Evaluation of Metglas resonators performance under different metal salts: (a) Before* and (b) After** exposure to the media during 24 hours. *Blue circles indicate the solutions in water, no circles indicate solution in DMF. ** Coloured circles indicate the response of the Metglas resonators: Green: Very good, nothing is observed, Orange: Some oxidation is observed but very slight, Red: High corrosion of the resonators. (c) Images of some of the samples after exposure to different media.

After 24 hours, Metglas samples were removed from the solutions and inspected by microscopy. Very different behaviours were observed. Their response has been classified as: No-damage (green), slight corrosion (orange) or high corrosion and even breakdown (red). First of all, it was noticed that Metglas resonators behave differently in water and DMF, having that, for the same metal salt, samples always present lower tendency to corrosion in DMF. This is particularly remarkable for the cupper and chromium specific cases where samples in water present a very bad aspect ad even a fracture (in the case of the copper nitrate - **Figure 3.10**c) while in DMF they present a much better aspect. No remarkable differences were observed between the samples heated at 80 °C and the samples left at room temperature.

Moreover, a very different behaviour between the different metal salts could be observed. In particular, it was noticed that zinc and cobalt salts do not affect to the magnetoelastic resonators (neither in water nor DMF). This is probably related with the low acidity of this divalent metallic salts. Observed behaviour could be expected to be extended to other similar metals (i.e. cadmium, nickel, manganese…).

Nevertheless, other divalent metals such as copper present a worst behaviour, which is probably related to the higher oxidation potential of this species. In fact, samples present one of the worst response to copper salts, as could be observed in **Figure 3.10**c.

When increasing the metal acidity and goes through trivalent metals (i.e. iron or chromium), an increase on the resonators corrosion is observed, although again it is less remarkable in DMF than in water. In a similar way, tetravalent metals (i.e. zirconium) lead to a corrosion of the Metglas. Ytrium was also investigated as representative of the lanthanids showing that this metallic salt promotes the corrosion of the magnetoelastic resonators just in water but not in DMF.

The derived conclusions of which metals could be integrated into the magnetoelastic resonators by direct synthesis (green), which not (red) and which depends on the solvents and so must be taken with care (red/orange) are summarized in **Figure 3.11**.

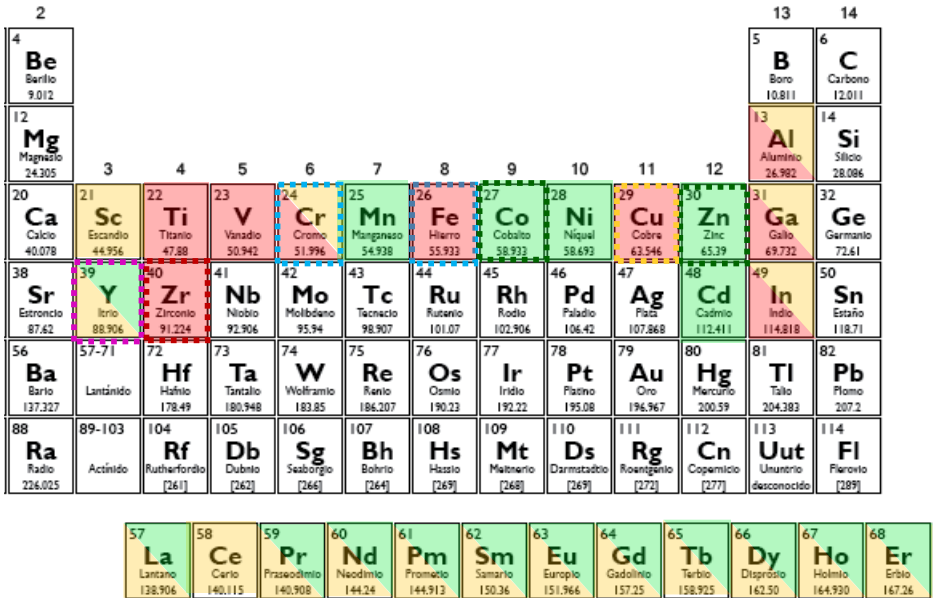

Figure 3.11. Periodic table scheme with the estimation of the metals salts which could be used for direct synthesis MOF growth. *Red: Corrosion both in water and DMF, Orange/red: Synthesis in DMF may be possible but not in water, Green: Resonators behave well under these metals.

Thus, the range of metals that can be used for the direct growth of MOFs is not very wide. Regarding solvents, it has been observed that DMF protects tapes more from corrosion than water. The last part of this study concerns the investigation of the possible organic ligands that could be employed for direct MOF growth. Most common employed linkers for MOFs synthesis include: Carboxylates, imidazoliums and pyridines. In this context, BDC, BDC-NH_2, BDC-$(OH)_2$, fumaric acid, aspartic acid, tartaric acid, 2-methylimidazole and 4-4'-bipyridine has been employed for this analysis. The solvent employed has been DMF due to its better performance. Samples have been lead unaltered during 24 h at 80 °C. Images of the samples before and after this time together with a microscope image of the two most damaged samples is shown in **Figure 3.12**.

It could be observed that magnetoelastic resonators present a very good response (no corrosion) under most of the organic ligands tested. Corrosion of the Metglas resonators is found when using BDC-NH_2, BDC-$(OH)_2$ and tartaric acid which indicate that the presence of reactive functional groups at the organic linkers promote the corrosion of the resonators.

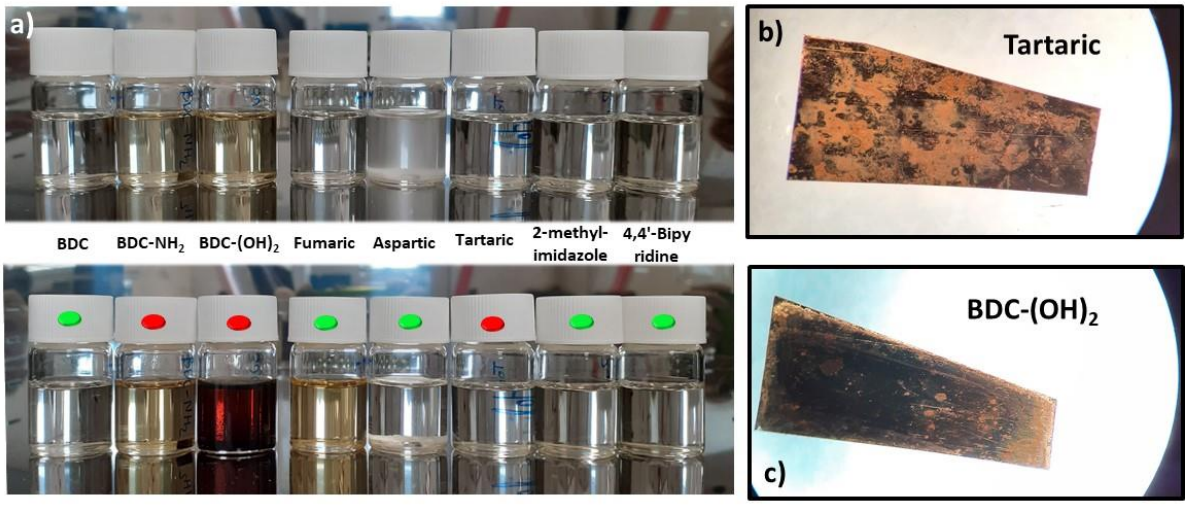

Figure 3.12. (a) Evaluation of Metglas resonators performance under different organic ligands in DMF*. (b-c) Images of the Metglas resonators after exposure to (b) tartaric and (c) BDC-$(OH)_2$ ligands in DMF. * Coloured marks indicate the response of the Metglas resonators: Green: Very good, nothing is observed, red: Corrosion of the resonators.

Thus, direct synthesis methodologies are feasible for integrate MOF active layers onto magnetoelastic resonators but is limited by the stability of the sensor in the reaction media (i.e. metal acidity, functional groups, solvents, acids…). Only that MOFs which are synthesized at "soft conditions" could be integrated by this technique since under more aggressive conditions, such as these of UiO-66, even though the exposition of the tape is limited when VAC is applied, the resonators get corroded.

Moreover, although the direct growth of the MOF at the resonator can result on an optimum attachment of the active layer to the substrate, the overall thickness and mass of the MOF active layer are still quite low if only one synthesis cycle is applied. The resonator functionalization process should be repeated for many cycles to achieve a proper characteristic of the MOF active layer, resulting in a less efficient processing methodology in terms of time and reagents cost.

Therefore, alternative integration methods of MOF materials need to be tested in order to avoid the exposure of the resonators to the MOF synthesis media and deposit heavier active layers. Among the multiple alternatives, the deposition of the MOF after its synthesis stands out giving that soft solvents can be selected what will prevent the

resonator corrosion. The main post-synthesis deposition methods considered along this thesis are described on the following.

3.1.2. Post-synthesis deposition

Post-synthesis MOF deposition methods involve first synthesizing the MOF and later on depositing it on the resonator surface. On that context, different post-synthesis deposition methods have been explored along this thesis: dip coating, spin coating and spray coating.

In particular, dip coating was the first tested method because it is a very common technique, easy and fast to implement, which does not require from any specific equipment. Dip coating has been successfully employed to deposit materials such as polymers at resonator platforms [45]. Nevertheless, as a result of the several tests that we performed, a negligible amount of non-homogeneously dispersed MOF was deposited on the resonator by using this technique. These results led to conclude that dip coating is not a suitable method to deposit MOF layers on magnetoelastic resonators and so was discarded as an option in the process of magnetoelastic sensors functionalization.

In a second attempt, spin and spray coating techniques were applied to properly shape the MOF active layer on the resonator surface. The deposition of MOF layers by these techniques, together with the advantages and disadvantages observed for each one, are described on the following.

- *Spin coating*

  The spin coating technique is a simple and fast method employed to deposit uniform thin films onto different substrates. This method consists on the deposition of a small amount of coating materials dispersed in a volatile solvent (i.e. MOF dispersion) on the centre of the substrate and then rotated it at high revolutions in order to spread the coating solution by centrifugal force. During the process, while the MOF dispersion covers all the substrate, the solvent evaporates leading to high uniform layers. The properties of the deposited layer depend on factor such as the viscosity and concentration of the dispersion, volatility and viscosity of the solvent, as well as on the time and revolutions of the spinning process. A scheme of the spin coating method employed to functionalize the magnetoelastic resonators is shown in **Figure 3.13**.

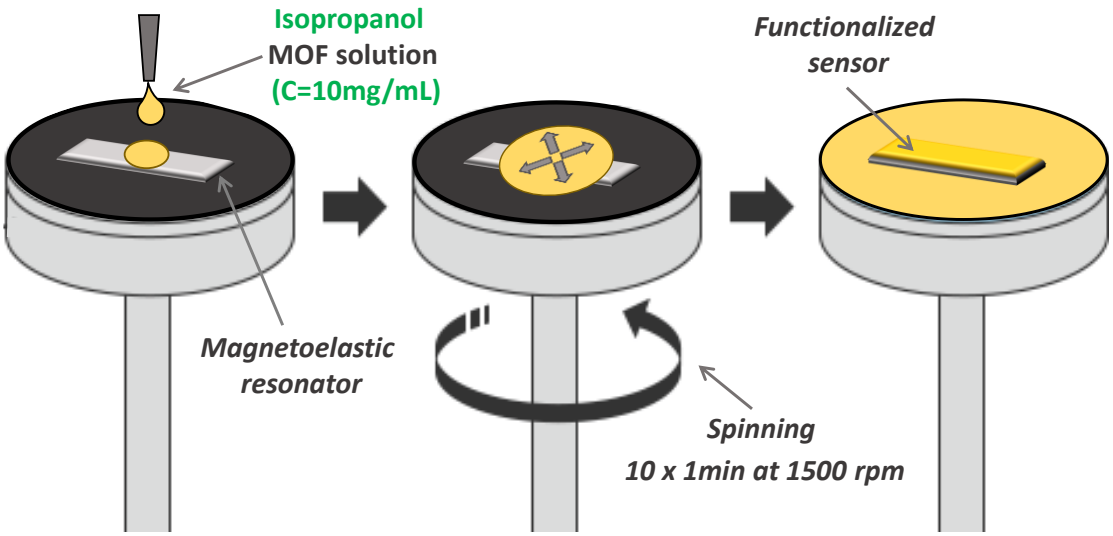

Figure 3.13. Scheme of the MOF integration process on the magnetoelastic resonators by the spin coating technique.

This functionalization process was tested for the UiO-66-NH_2. For that, the MOF was dispersed in isopropanol by ultrasonication with a 10mg/mL concentration, and then deposited and spin coated on the magnetoelastic resonator surface using a Laurell WS-650-23 B spin coater. Afterwards, the MOF functionalized resonators were characterized by X-ray diffraction and optical and scanning electron microscopies. Results are shown in **Figure 3.14**.

At first glance, spin coating promotes the deposition of the MOF active layer into the resonator surface, maintaining the stability of the resonator alloy. The characteristic X-ray diffraction maxima ascribed to the UiO-66 material as well as the broad diffraction peak around 44.5° related to the amorphous Metglas alloy structure are observed in the diffraction pattern of the functionalized resonator, confirming the presence and chemical stability of the UiO-66-NH_2 after its deposition on the Metglas resonator (**Figure 3.14**a). Moreover, SEM images confirmed also the MOF deposition at the resonator. The macro-mesoporous structure of the MOF layer is the consequence of the disordered arrangement of the MOF particles during the spin-coating process. The morphology and size of the UiO-66-NH_2 particles in the active layer are similar to that observed for the UiO-66-NH_2 material before its deposition (**Figure 3.14**b). Nevertheless, the optical microscope image of the UiO-66-NH_2@Metglas resonator reveals the inhomogeneity of the MOF layer deposited by this method (**Figure 3.14**c).

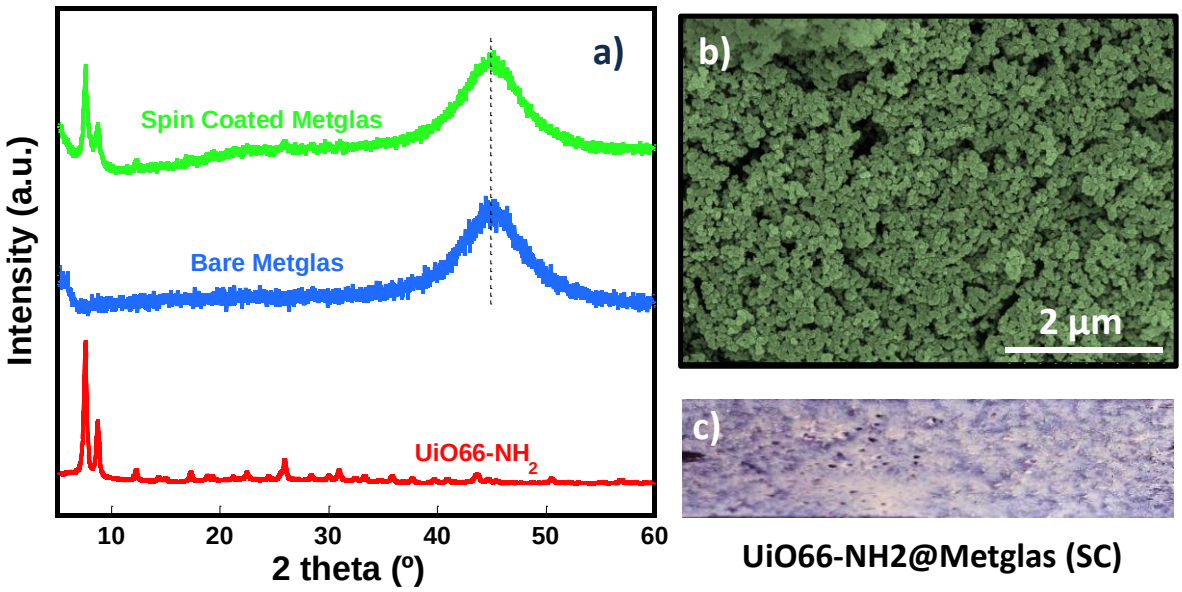

Figure 3.14. (a) X-ray diffractograms of the UiO-66-NH_2 MOF, the bare Metglas resonator and the Metglas resonators after the functionalization by direct coating with the UiO-66-NH_2 MOF. (b) SEM and (c) optical microscope images of the magnetoelastic ribbon surface after the deposition process.

- *Spray coating*

Spray coating method was also tested looking for a faster, easier and more homogeneous integration of the MOF layer on the resonator surface. Spray coating consists on spraying the MOF dispersion on the surface of the resonator using an airbrush. There are several parameters that affect the properties of the spray printed MOF layer such as: the vapour pressure of the solvent, its evaporation rate when contacting the substrate heated at a given temperature, the concentration and the overall volume of the MOF dispersion, the spraying angle and distance with respect to the substrate or the airbrush air pressure. A scheme of this deposition technique is shown in **Figure 3.15**.

Spray coating functionalization process was again tested for the UiO-66-NH_2 material. Similarly to spin coating, the MOF was dispersed in isopropanol by ultrasonication and later on sprayed with an Iwata eclipse HP-SBS model spray airbrush. At first sight, it was observed that the UiO-66-NH_2 powder was deposited in the resonator surface, leading to a homogeneous layer. Just like for spin coating technique, the MOF layer is detached easily from the surface, so the MOF based resonators need to be handled carefully. In

comparison with the spin coating technique, spray coating allows obtaining a higher amount of MOF deposited per mm^2 of the resonator surface, and a lower volume of MOF dispersion lost during the process.

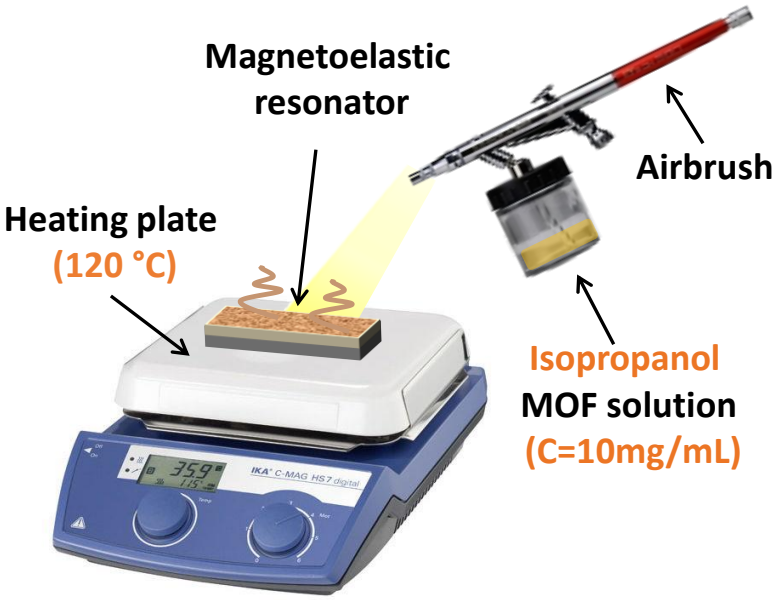

Figure 3.15. Scheme of the spray coating technique carried out in this thesis (words in orange indicate the optimal parameters used in this thesis).

Thus, the spray coating was selected to further explore the MOF integration process in the resonators. On that way, to further improve the spray deposition, the effect of the solvent, concentration of the MOF at the dispersion and the temperature of the target support were analysed. Firstly, solvents with different vapour pressures and viscosities (e.g. acetone, ethanol, isopropanol…) were selected to prepare the MOF suspensions. The MOF spray coated layers were inspected by a binocular microscope after the process. Among them, isopropanol seems to be the best option since it leads to more homogeneous layers, a fact that is probably related to its evaporation rate. Secondly, the concentration of the MOF in the dispersion was varied (from 5 to 15 mg/mL of isopropanol), since it affects its viscosity and therefore the deposition process. In this context, an optimal concentration of 10 mg/mL of isopropanol was estimated after several tests. Moreover, the operation temperature was also adjusted in order to improve the deposited layer homogeneity. Initially, the spray depositions were performed at room temperature, but it was observed that the deposited layer present lot microcracks probably related to the slow evaporation rate of the solvent. For this reason, spraying

was carried out by heating the resonator in a heating plate at different temperatures. It was observed an enhancement of the surface homogeneity related to the solvent evaporation rate. After different tests, 120 °C was selected as the optimal temperature. At these conditions (dispersion concentration = 10mg/L, solvent = isopropanol, temperature = 120 °C), a total MOF mass per surface unit of around 7.5 μg/mm^2 is coated onto the resonator in each deposition cycle. This value of normalized mass per surface unit is 10 times higher than that previously obtained for the direct synthesis method. In conclusion, spray coating allows integrating the MOF as a homogeneous active layer with a high mass per surface unit that can be further augmented in successive spraying cycles as will be explained in the following section.

The UiO-66-NH2@Metglas resonator obtained by spray coating was fully characterized by X-ray diffraction (XRD), Fourier-transform infrared spectroscopy (FTIR), N_2 sorption measurements and Scanning Electron Microscopy (SEM), in order to assure the quality of the active layer; paying particular attention to the layer thickness, mass and structure. Results were compared with that of the bare resonator and the powder MOF. First of all, XRD and FTIR-ATR spectroscopy of the MOF (UiO-66-NH_2), the bare resonator (Metglas) and the functionalized sensor (Sprayed Metglas) are shown in **Figure 3.16**.

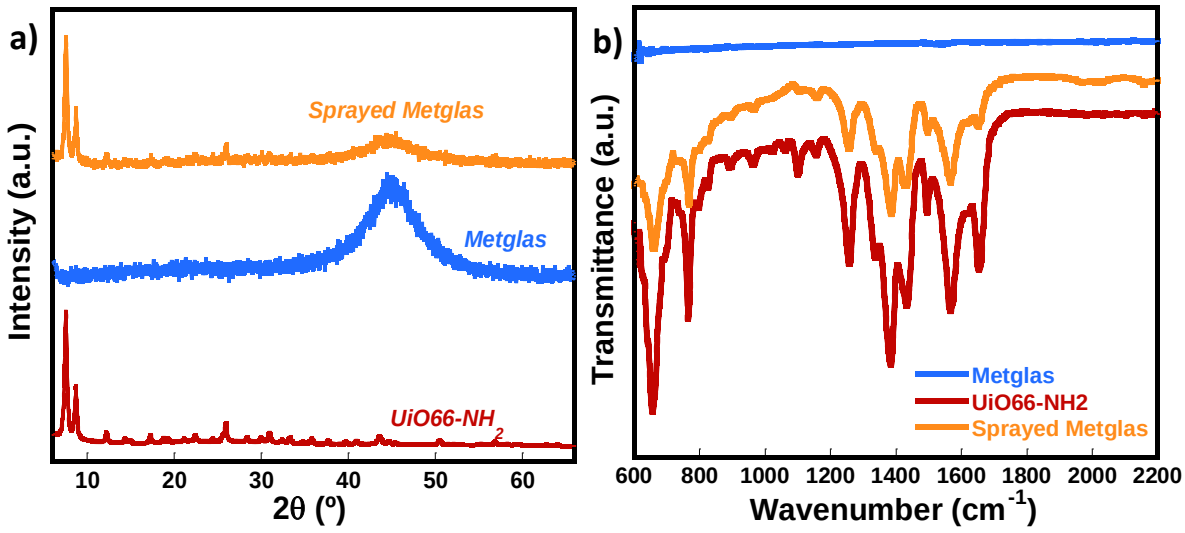

Figure 3.16. (a) XRD patterns and (b) FTIR spectra of the UiO6-NH_2 MOF, the bare Metglas resonator and the sprayed Metglas resonator.

XRD and FTIR measurements confirm the presence and the chemical stability of the MOF material after its deposition on the magnetic resonator. In addition to the characteristic X-ray diffraction maxima ascribed to the UiO-66 material, the XRD pattern (**Figure 3.16**a) of the MOF/Metglas resonator shows the previously described broad diffraction peak at 44.5º related to the amorphous Metglas alloy structure [40]. Moreover, FTIR spectra show the characteristic fingerprint absorption bands of the UiO-66-NH_2 structure, assigned to the longitudinal and transverse modes of the Zr-O_2 (at 745 and 660 cm^{-1}) and asymmetric and symmetric stretching vibrations of the carboxylate groups (1581 and 1389 cm^{-1}) [46]. Besides, the ones attributed to the amino-terephthalic acid linker in the UiO-66-NH_2 samples could be observed at 1261 and 1338 cm^{-1}. It is important to note that the IR absorption band associated to the stretching vibration of C-O bonds (~1650 cm^{-1}) shows a meaningful absorbance decrease when the MOF active material is deposited onto the metallic surface of the resonator. C-O stretching vibrational modes are usually observed in MOF nanoparticles, indicating the presence of an important density of uncoordinated carboxyl (-COOH) moieties at their surface. That reduction of the –COOH density during the UiO-66-NH_2 nanoparticles deposition can be associated to the deprotonation of the carboxyl groups; which can be triggered by their partial chemical bonding to the metal ions of the magnetoelastic resonator (**Figure 3.16**b).

Moreover, the morphology of the UiO-66-NH_2 particles, as well as the MOF layer thickness and structure after its deposition in the Metglas ribbon, were studied by means of surface and transversal scanning electron microscopy (SEM) images (**Figure 3.17**a-c). N_2 adsorption-desorption isotherms at 77 K were measured in the powder MOF and also in the MOF after the spraying process in order to analyse the possibility of an extra meso and macro-porous interconnected void fraction between the MOF particles after their spray coating at the resonator. Results are shown in **Figure 3.17**d-e.

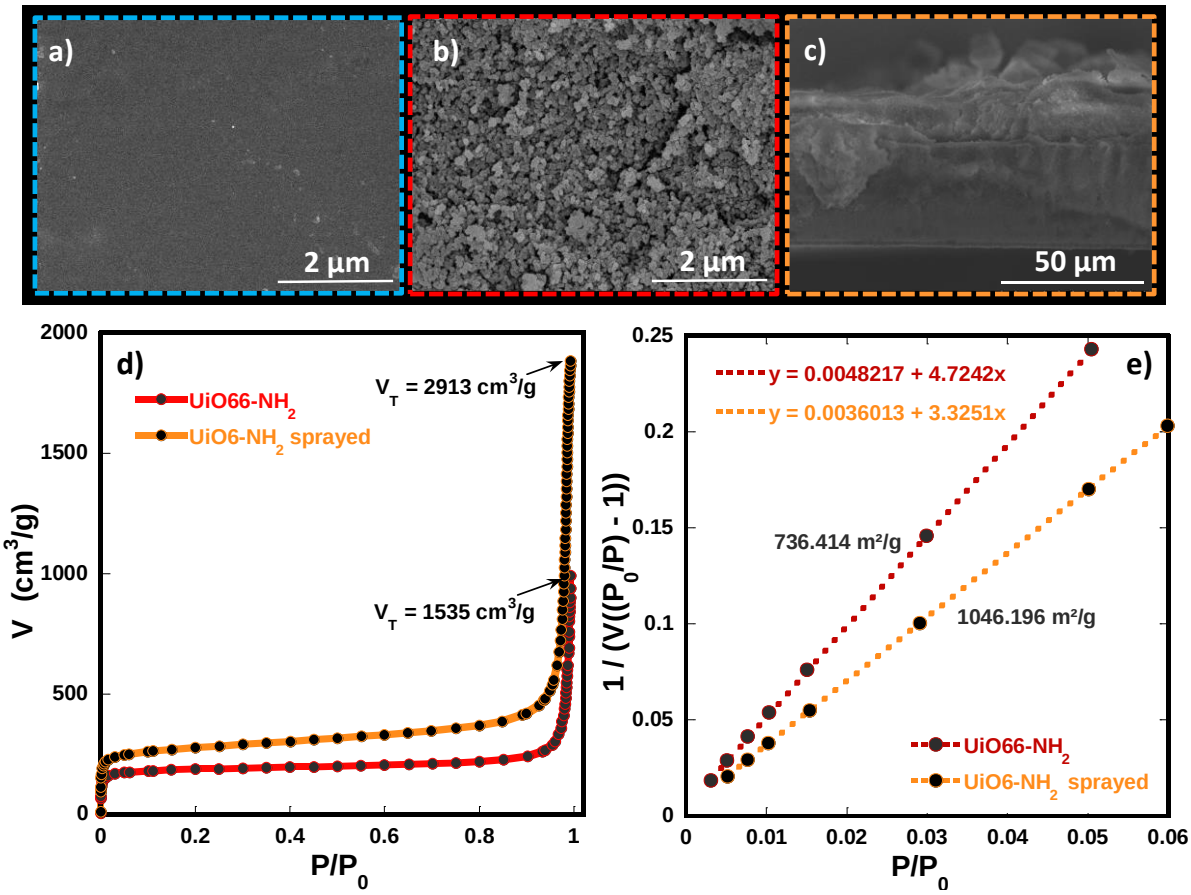

Figure 3.17. (a-c) SEM images of the: (a)Bare Metglas surface, (b) UiO-66-NH_2 MOF layer deposited on the Metglas surface and (c) cross sectional image of the sprayed. (d) N_2 adsorption isotherm measured for the UiO-66-NH_2 and the UiO-66-NH_2 sprayed and (e) Fitting of the N_2 adsorption isotherms with a linearized BET model.

Looking to SEM images, it could be observed that UiO-66-NH_2 crystallizes as nearly spherical particles with an average diameter of 50 nm. The macro-mesoporous structure of the MOF layer is the consequence of the disordered arrangement of the MOF nanoparticles during the spray deposition. A MOF layer thickness of around 15 µm is estimated from the transversal SEM image (**Figure 3.17**c). The percentage of meso and macro-porosity on the active layer can be qualitatively calculated based on its density value. Taking into account the weight of the UiO-66-NH_2 layer (74 µg) in SEMOF-1, and its volume (*i.e. surface of the magnetic ribbon x thickness of the MOF layer determined by SEM*), a density of 0.49 g/cm^3 is estimated, three times lower than the crystallographic density of UiO-66-NH_2 (1.45 g/cm^3). Therefore, the meso and macro-pore volumes on the void fraction between MOF particles represent approximately the 60 % of its volume.

Thus, in addition to the intrinsic micro-porosity of the MOF, the spray deposition methodology endows the layer with an extra meso and macro-porous interconnected void fraction between MOF particles, which it is foreseen to facilitate the target analyte migration though the active sensing area until trapped into the MOF. This was confirmed from the N_2 isotherms measurements after detaching the MOF layer from the Metglas support. The contribution of the external surface area in the MOF-layer after its deposition is three times higher (S_{ext}= 290 m^2/g) than this of the initial material (90m^2/g) (**Table 3.1**).

The Brunauer-Emmett-Teller (BET) surface area of the UiO-66-NH_2 MOF and the sprayed MOF were obtained from the fitting of the linearized part of the N_2 adsorption-desorption isotherm (**Figure 3.17**e), the obtained BET was of 737 m^2/g, which is similar to the reported one for that UiO-66-NH_2 MOF [47]. It is important to note that BET value accounts for the surface area of the micro-pores (S_{micro} = 646 m^2/g) summed the contribution of the meso and macroporous area derived from the MOF particles arrangement (S_{ext}=90 m^2/g). Moreover, the obtained BET for the sprayed MOF was of 1046 m^2/g due to its higher S_{ext} compared with that of the powder MOF. The results obtained from the N_2 adsorption experiments are summarized in **Table 3.1**.

Table 3.1. Parameters obtained from the fitting of the N_2 adsorption isotherms measured for the UiO-66-NH_2 and the sprayed UiO-66-NH_2.

Sample	S_{BET} (m^2/g)	S_{micro} (m^2/g)	S_{ext} (m^2/g)	V_T (cm^3/g)	Average half pore width (Å)
UiO-66-NH_2	736.414	645.974	90.44	1.535	7.097
UiO-66-NH_2 sprayed	1046.196	756.077	290.12	2.913	6.924

Finally, the magnetoelastic resonance frequency curves of the rhombic Metglas resonator before and after the functionalization process were measured in order to confirm that the resonance signal quality of the bare resonator is maintained after the MOF active layer deposition. Results are shown in **Figure 3.18**.

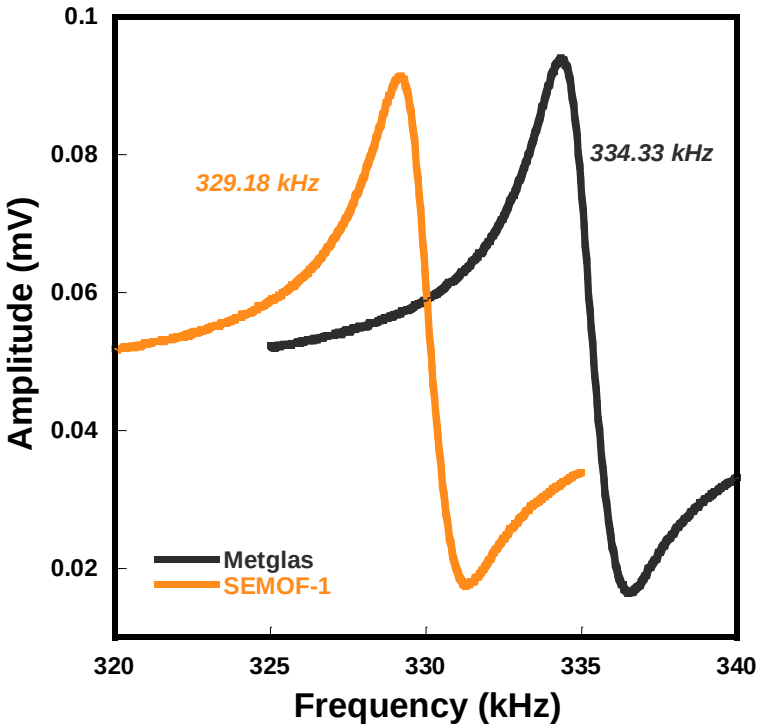

Figure 3.18. Resonance frequency curves measured for the bare Metglas resonator and for the functionalized resonator.

A resonance frequency of 334.34 kHz was measured for the bare Metglas resonator. That value is in accordance with that obtained thought the theoretical equation for the resonance frequency of a freestanding rhombus shaped magnetoelastic resonator (**equation 2.10**). Moreover, a frequency shift of 5.15 kHz is measured after a deposition of 74µg of MOF active layer, again much higher than that previously obtained for the direct synthesis method (200 Hz). This frequency shift under such active layer mass is translated into a mass sensitivity of about 69.6 Hz/µg, which is in concordance with the previously obtained value for a 10 mm rhombic resonator. Moreover, it is worthy to highlight that no significant changes are observed in the resonance frequency curves after the MOF active layer deposition. Indeed the peak quality and the signal intensity are maintained, which is an excellent behaviour since many works report an intensity and quality of the output signal reduction after the magnetoelastic ribbon functionalization process [22,48].

Thus, spray coating is a suitable technique to integrate homogeneous MOF layers at the resonator surface, and also, allows a fast and easy deposition process. The main drawback is that the adhesion of the MOF layer is weak so it should be managed with

care. This technique allows for a high mass deposition per surface unit, maintaining the quality of the resonance curve and resonator properties. In addition, spray coating can be easily adapted for any kind of MOF synthesized so far, which offers outstanding flexibility to access MOF/Metglas resonators with different selectivities and adsorption capacities over target analytes with completely different natures and chemistries. Indeed, spray coating has been successfully applied to integrate the ZIF based MOF with similar results. This technique is especially valuable when the deposition by direct growth on the synthesis media is not possible due to harsh synthesis conditions of the MOFs constructed from acidic metal ions. Moreover, it endows the layer with an extra meso and macro-porous void fraction between MOF particles which facilitates the VOCs migration.

It is clear that the method employed to integrate the MOF active layer into the magnetoelastic resonators can affect both the active layer features as well as its adsorption properties, and therefore the sensing process. Moreover, the type of MOF used as active layer as well as the possible modifications carried out on it are the main factor affecting the adsorption capacity of the active layer and therefore the sensing process (including the sensitivity and selectivity).

On that context, it became necessary to properly choose the MOF material that will be used as the active layer taking into account its adsorption capacity and selectivity to the target compound. In this regard, and considering that any type of MOF can be deposited by spray, MOFs of the UiO-66 family have been selected to further study their performance once integrated at resonator platforms, since starting from the same structural arrangement of the inorganic and organic building blocks, UiO-66 adsorption properties can be easily modulated incorporating specific functionalities within the material. A detailed description of all the UiO-66 MOFs synthesis and characterization of the performed modifications are described on the following.

3.3. Synthesis of UiO-66-R and UiO-66-R-defective MOFs

UiO-66 material has been selected as a porous platform to which different structural and chemical functionalizations can be incorporated by modifying the synthesis conditions. It is worthy to mention that UiO-66 exhibits outstanding chemical and thermal stabilities itself as well as high stability in liquid media which make it ideal for different applications.

In particular, various modifications have been made in the UiO-66 synthesis process to vary the MOFs particle size, linker defects density ("*defect engineering*" - **Figure 3.19**a) and in order to incorporate several functional groups into its structure looking for the best properties regarding its adsorption capacity over gas and aqueous pollutants. The MOF particle size control has been carried out with a water based modulator approach. It is well known that the presence of H_2O in the synthesis media fasten the MOF crystallization kinetics reducing at the same time the MOFs size, while the presence of HCl has the opposite effect, but also modulates the terephthalate linker defect density of the UiO-66 structure. Thus, the optimal addition of H_2O and HCl allows controlling the size and defect chemistry of UiO-66 materials.

Moreover, UiO-66 type framework stands out because of the versatility of the different functional groups that can be incorporated to the terephthalate moiety in order to tune its adsorption capacity and affinity over different adsorbates. In particular, -OH, and $-NH_2$ electron donor functional groups have been used because they can improve the adsorption properties of the UiO-66 framework. The synthesis protocol to incorporate these functional groups within UiO-66 framework is quite simple, since just by replacing the terephthalic acid (BDC) reagent per 2,5-dihydroxyterephthalic acid (doBDC) and 2-aminoterephthalic acid (BDC-NH_2), respectively, the final architecture of the initial compound is usually maintained independently on the used conditions. Thus, by modifying the water and HCl modulators, and incorporating different functional groups at the linker, a scope of linker non-defective samples (UiO-66-R, R= -H, $-NH_2$ and $-(OH)_2$) and linker defective compounds (UiO-66-R-def, R= -H, $-NH_2$ and $-(OH)_2$) were synthesized in order to compare the adsorptive and photo-catalytic properties of the bulk materials and after their integration in the magnetic resonators. A scheme of a defective position in the UiO-66 structure together with the structure of the three employed ligands are shown in **Figure 3.19**a-b.

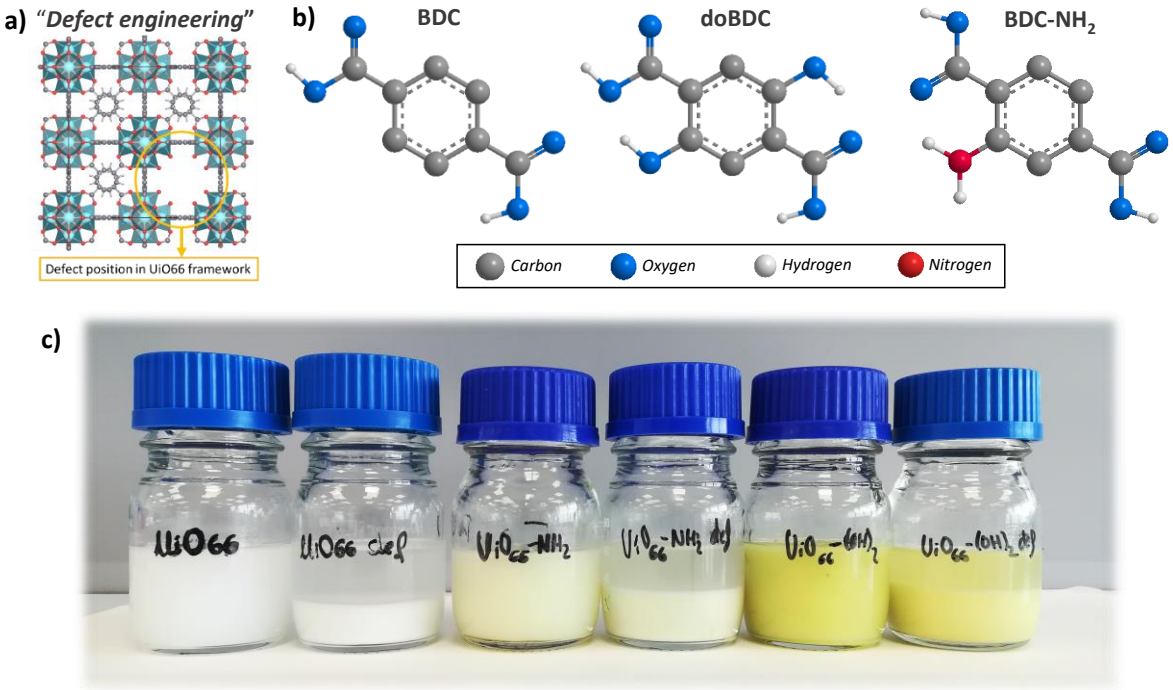

Figure 3.19. (a) Local structure of a linker defect position at UiO-66 MOF structure. (b) Structures of the three used ligands (BDC, doBDC and BDC-NH_2). (c) Image of the UiO-66-R samples and UiO-66-R defective samples after the synthesis process.

Thus, a total of six UiO-66-R samples were prepared through a slightly modified solvothermal synthesis procedure based on the previously reported one by Audu *et. al.* [49]. As a general protocol, $ZrCl_4$ is first dissolved in DMF. Subsequently, the organic ligand (BDC) and HCl (in the case of defective samples) are added to the solution, leading to a white or yellow suspension in the reactors vessel. Finally, water is added as a particle size modulator. The mixture is stirred during 10 min at room temperature, sealed in a 100 mL glass reactor vessel (Pyrex®) and then placed in an oven at 80 °C for 24 h. After the reaction, the vessel is cooled naturally to room temperature in the oven (**Figure 3.19**c). At this point, the difference between the defective and non-defective samples could be appreciated in the decantation degree of the samples with defects, which is probably related to their larger particle size. Moreover, the functional groups endow the material with different light harvesting properties, and hence with different colours.

After that point, the precipitate is centrifuged and then washed with methanol under stirring during 24h, centrifuged at 7000 rpm and dispersed again in fresh methanol. This solvent exchange process was repeated three times in order to remove the unreacted ligand and exchange the residual DMF present at the MOF´s pores. Finally, the washed product is separated from the solvent by centrifugation, dried overnight in an oven set to 80 °C and ground with a mortar and pestle[50,51]. The hydroxylated (UiO-66-$(OH)_2$) and amine (UiO-66-NH_2) analogue materials are obtained applying the same synthesis conditions, but replacing the terephthalic acid reagent per equal molar amounts of 2,5-dihydroxyterephthalic acid (doBDC) and 2-aminoterephthalic acid (BDC-NH_2), respectively. On the other hand, the three analogue linker defective samples (UiO-66-def, UiO-66-$(OH)_2$-def and UiO-66-NH_2-def were synthesised by adding the hydrochloric acid as a modulator in the synthesis media. The amount of product obtained under these conditions is around 0.8 g. A scheme of the synthesis process is represented in **Figure 3.20**, while the amounts and reagents used on the different synthesis are collected in **Table 3.2**.

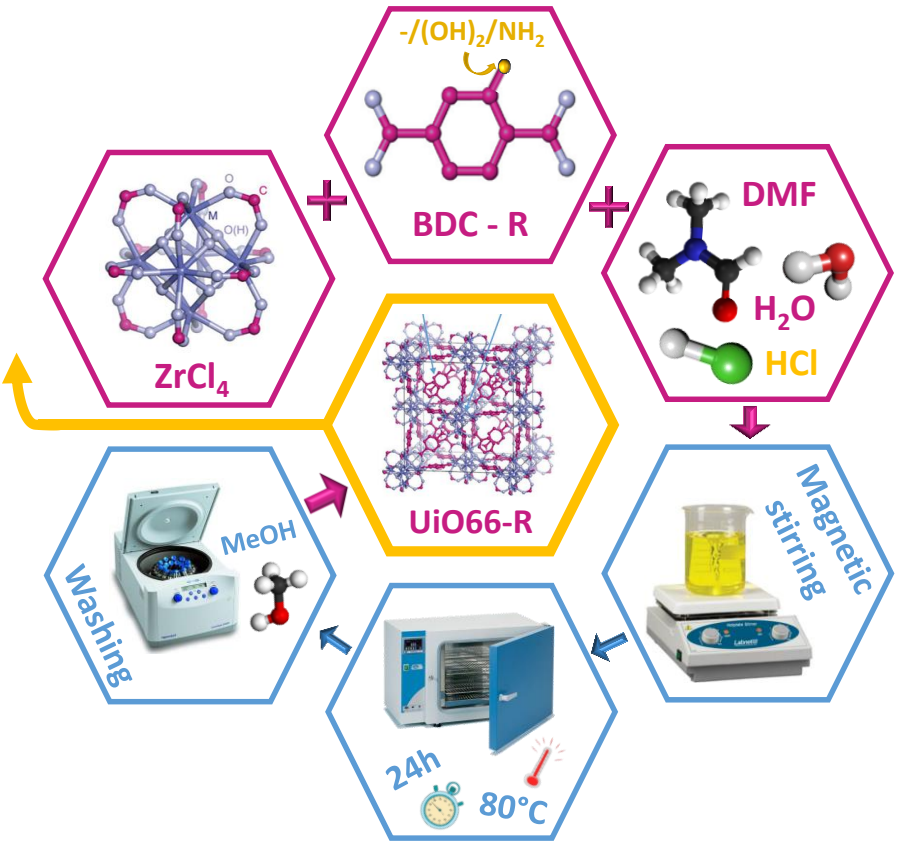

Figure 3.20. Scheme of the synthesis process of UiO-66-R samples.

Table 3.2. Volumes and mass used for the synthesis of the different UiO-66-R MOF samples.

Sample	$ZrCl_4$ (g)	DMF (mL)	Ligand	Ligand (g)	H_2O (mL)	HCl (mL)
UiO-66	0.5418	60	BDC	0.3861	1.5	-
UiO-66 def.						1.5
UiO-66-$(OH)_2$	0.5418	60	doBDC	0.4575	1.5	-
UiO-66-$(OH)_2$ def.						1.5
UiO-66-NH_2	0.5418	60	BDC-NH_2	0.4185	1.5	-
UiO-66-NH_2 def.						1.5

After the synthesis process, the quality of the UiO-66-R MOFs, as well as their defects density, were characterized by applying multiple characterization techniques. In particular, FTIR spectra and X-ray diffraction patterns were first measured in order to determine the crystallinity of the samples as well as the presence of the functional groups in their structure. Results are shown in **Figure 3.21** and **Figure 3.22**.

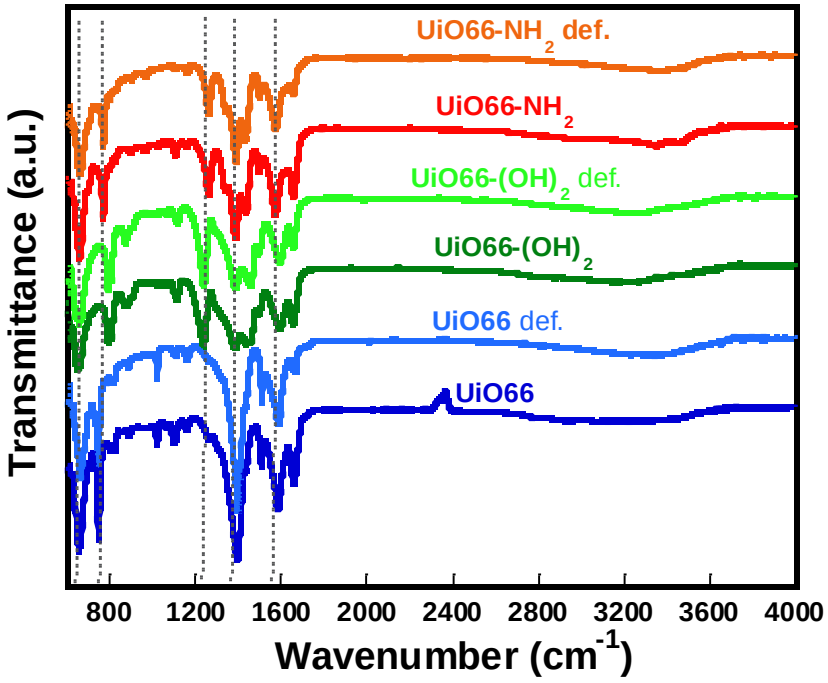

Figure 3.21. FTIR-ATR spectra of the different UiO-66-R samples.

Looking to the FTIR spectra (**Figure 3.21**), the characteristic fingerprint bands of the UiO-66 structure could be observed. These absorption maxima are tentatively assigned to the longitudinal and transverse vibrational modes of the Zr-O bonds (at 745 and 660

cm^{-1}) or/and to the asymmetric and symmetric stretching vibrations of the carboxylate groups (1581 and 1389 cm^{-1}). In addition, phenolic C-OH stretching vibrations (1235 cm^{-1}) [52] and adsorption bands (1258 and 1338 cm^{-1}) related to the vibrational modes of amino groups [46], are also identified for UiO-66-$(OH)_2$/UiO-66-$(OH)_2$-def and UiO-66-NH_2/UiO-66-NH_2-def samples, respectively.

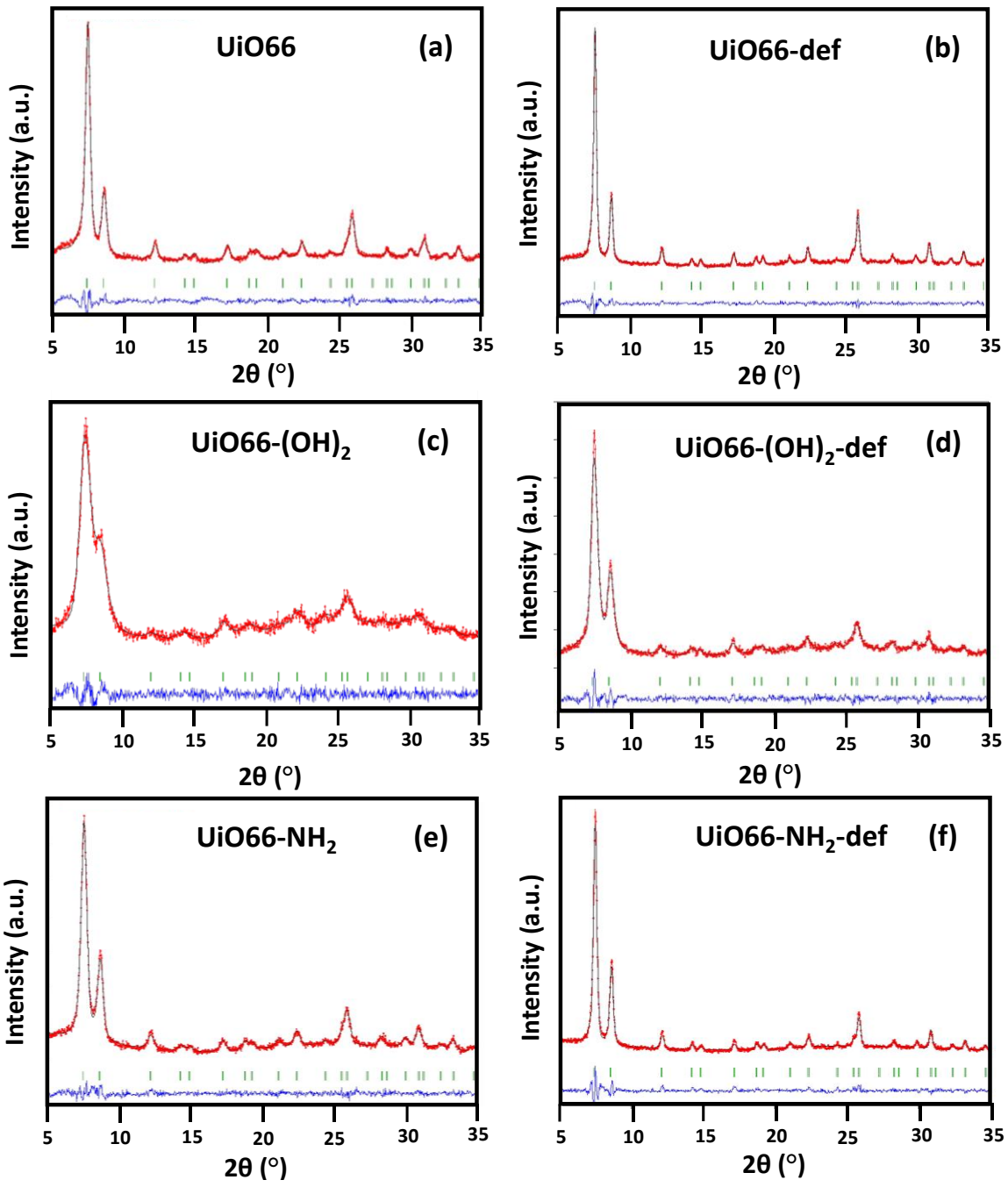

Figure 3.22. Powder X-ray diffraction profile matching analysis of (a)UiO-66, (b)UiO-66-def, (c)UiO-66-$(OH)_2$, (d) UiO-66-$(OH)_2$-def, (e)UiO-66-NH_2 and (f)UiO-66-NH_2-def.

On a similar way, the XRD patterns are fully consistent with the simulated data obtained from the UiO-66 structural model indicating the purity and high crystallinity of the synthesized samples [37]. In general terms, defective samples show more crystalline diffraction patterns, related to the crystal-growth template effect of the HCl incorporation to the synthesis media [49]. Besides, slight broadening of the peak is observed for hydroxylated compounds in comparison to non-functionalized and amino bearing derivatives. Slight differences in the peak width, related to the particle sizes of the samples are also observed. Finally, profile pattern matching analyses confirm no meaningful displacements of the cell parameters due to the organic linkers functionalization and/or defect degree of the compounds (**Figure 3.22**). Cell parameter (a) of around 20.68 Å was obtained for all the samples, in close agreement with previously reported values for UiO-66 compounds (**Table 3.3**).

Table 3.3. Cell parameters obtained from the Le Bail fitting of the XRD patterns of the different MOF samples.

Sample	a parameter (Å)
UiO-66	20.671(3)
UiO-66-def	20.692(2)
UiO-66-NH_2	20.693(3)
UiO-66-NH_2-def	20.698(2)
UiO-66-$(OH)_2$	20.668(9)
UiO-66-$(OH)_2$-def	20.732(5)

For additional bulk characterization, UiO-66-R samples were examined by thermogravimetric analysis (TGA) (**Figure 3.23** a-c) in order to quantify the linker defect density within the structures. In particular, the linker-defects per formula were estimated from the third weight loss in the TGA curve, which is the one associated with the organic linker calcination step [39,53] (**Figure 3.23** d-f).

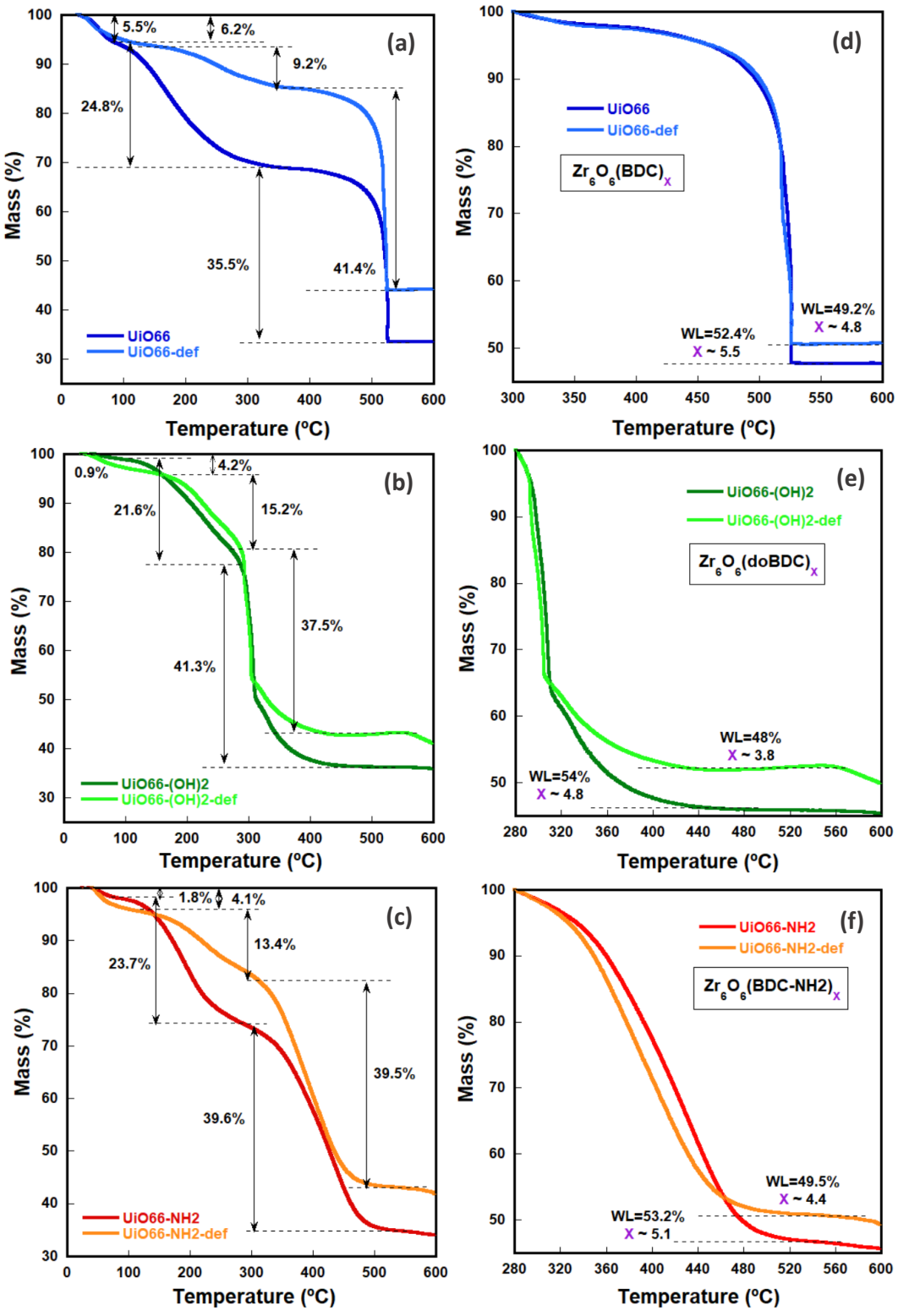

Figure 3.23. (a-c) (a-c) Thermogravimetric curves for UiO-66-R and UiO-66-R-def samples. Weight loss associated with solvent release, coordinative linked species loss (H_2O, OH and DMF) and organic linker calcination has been identified for each of the samples. (d-e) Normalized TGA curves from the last weight lost.

The third experimental weight loss was used to determine the experimental defects per formula by comparing it with a theoretical linear equation obtained from calculated weight losses of samples having different linker-defects per formula unit (**Figure A.12**b). A detailed description of the theory behind this and the calibration curve used to calculate the defect degrees is given in **Annex A**. The defects degree estimated for each sample are summarized in **Table 3.4.** As could be observed, the defect density per formula varies from 0.9-1.1 for "non-defective" samples to 1.1-2.3 in defective ones, a trend that confirms the defect template effect of the HCl addition during the synthesis. It is worth noting that the "non-defective" samples also present some degree of linker missing defects, as derived from TGA results, a common feature broadly described for UiO-66 type compounds in the literature.

Table 3.4. Mass losses and proposed formula unit for each compound estimated from the thermogravimetric curves.

Samples	Mass loss (%)	Formula	Defects
UiO-66	52.4	$Zr_6O_6(BDC)_{5.1}$	0.9/6
UiO-66-(OH)$_2$	54.0	$Zr_6O_6(doBDC)_{4.9}$	1.1/6
UiO-66-NH$_2$	53.2	$Zr_6O_6(BDC\text{-}NH_2)_{5.7}$	0.3/6
UiO-66-def	49.2	$Zr_6O_6(BDC)_{4.5}$	1.5/6
UiO-66-(OH)$_2$-def	48.0	$Zr_6O_6(doBDC)_{3.7}$	2.3/6
UiO-66-NH$_2$-def	49.5	$Zr_6O_6(BDC\text{-}NH_2)_{4.9}$	1.1/6

All these materials have been successfully integrated into magnetoelastic resonators by spray coating. The defect and functional groups decoration of UiO-66 framework is foreseen to modify the adsorptive properties of the material over different pollutant. In the following chapters, the intrinsic characteristics of the UiO-66 samples described here will be taken into account when understanding their adsorptive properties over pollutants from aqueous and air media.

3.4. Summary and conclusions

In this chapter, it has been duly demonstrated the feasibility to integrate MOF active layers at magnetoelastic resonators surface by using different approaches. In particular, spray coating printing stands out as the best choice in term of simplicity, effectiveness and the potential to be broadly transferred to any kind of MOF material synthesized so

far. Spray printing allows depositing controlled, heavy and homogeneous MOF active layers at the resonator surface without altering the quality and intensity of the magnetoelastic resonance signal.

The dispersive solvent for the MOF material (i.e. isopropanol), the concentration of the MOF dispersion (mg mL^{-1}) and the substrate temperature (120 °C) during the printing process have been revealed as key parameters to obtain a homogeneous and cumulative MOF layer deposition within the magnetoelastic platform. The main drawback of spray coating approach is the weak adhesion of the MOF layer to the support.

Moreover, direct growth of the MOF layers into the resonator's surface is adequate to obtain MOF/magnetoelastic resonators with improved layers adhesion, but it is just feasible for the particular cases of MOF materials obtained at soft synthesis conditions that meet the MR chemical stability window.

It can be generally concluded that the stability of the resonator fails when contact acid and redox active metals and organic linker with certain functional groups. Therefore, direct growth approach limits the integration of a broad scope of MOFs at the resonators, and also fails to obtain a MOF layer with a significant mass, in terms of the posterior magnetoelastic shift driven by the mass gain during adsorption.

Taking all these facts into consideration, it can be concluded that spray coating offers much more advantages than direct growth approach, even if direct growth approach gives access to slightly better adhesion of the MOF layer to the resonator.

3.5. References

1. Falcaro, P., Ricco, R., Doherty, C. M., Liang, K., Hill, A. J., & Styles, M. J. MOF positioning technology and device fabrication. *Chem. Soc. Rev.* **43**, 5513–5560 (2014).

2. Liu, J. & Christof, W. Surface-supported metal organic framework thin films: fabrication methods, applications, and challenges. *Chem. Soc. Rev.* **46**, 5730–5770 (2017).

3. Stassen, I., Burtch, N., Talin, A., Falcaro, P., Allendorf, M., & Ameloot, R. An updated roadmap for the integration of metal-organic frameworks with electronic devices and chemical sensors. *Chem. Soc. Rev.* **46**, 3185–3241 (2017).

4. Zacher, D., Shekhah, O., Wöll, C. & Fischer, R. A. Thin films of metal–organic frameworks. *Chem. Soc. Rev.* **38**, 1418–1429 (2009).

5. Gao, J., Wei, W., Yin, Y. Liu, M., Zheng, C., Zhang, Y., & Deng, P. Continuous ultrathin UiO-66-NH2 coatings on a polymeric substrate synthesized by a layer-by-layer method: A kind of promising membrane for oil-water separation. *Nanoscale* **12**, 6658–6663 (2020).

6. Ahrenholtz, S. R., Epley, C. C. & Morris, A. J. Solvothermal preparation of an electrocatalytic metalloporphyrin MOF thin film and its redox hopping charge-transfer mechanism. *J. Am. Chem. Soc.* **136**, 2464–2472 (2014).

7. Shekhah, O., Wang, H., Strunskus, T., Cyganik, P., Zacher, D., Fischer, R., & Wöll, C. Layer-by-layer growth of oriented metal organic polymers on a functionalized organic surface. *Langmuir* **23**, 7440–7442 (2007).

8. Shekhah, O., Wang, H., Kowarik, S., Schreiber, F. Paulus, M., Tolan, M., Sternemann, C., Evers, F., Zacher, D., Fischer, R. A., & Wöll, C. Step-by-step route for the synthesis of metal-organic frameworks. *J. Am. Chem. Soc.* **129**, 15118–15119 (2007).

9. Heinke, L., Tu, M., Wannapaiboon, S., Fischer, R. A. & Wöll, C. Surface-mounted metal-organic frameworks for applications in sensing and separation. *Microporous Mesoporous Mater.* **216**, 200–215 (2014).

10. Zhuang, J., Terfort, A. & Wöll, C. Formation of oriented and patterned films of metal – organic frameworks by liquid phase epitaxy : A review. *Coord. Chem. Rev.* **307**, 391–424 (2016).

11. Stassen, I., De Vos, D. & Ameloot, R. Vapor-phase deposition and modification of Metal–Organic Frameworks: State-of-the-art and future directions. *Chem. - A Eur. J.* **22**, 14452–14460 (2016).

12. Virmani, E., Rotter, J. M., Mähringer, A., Von Zons, T., Godt, A. Bein, T., Wuttke, S., & Medina, D. On-surface synthesis of highly oriented thin metal-organic framework films through vapor-assisted conversion. *J. Am. Chem. Soc.* **140**, 4812–4819 (2018).

13. Demessence, A., Horcajada, P., Serre, C., Boissière, C., Grosso, D., Sanchez, C., & Férey, G. Elaboration and properties of hierarchically structured optical thin films

of MIL-101(Cr). *Chem. Commun.* **101**, 7149–7151 (2009).

14. Kaviyarasu, K., Maria Magdalane, C., Kanimozhi, K. & Kennedy, J., Siddhardha, B., Subba Reddy, E., Rotte, N. K., Sharma, C. S., Thema, F. T., Letsholathebe, D., Mola, G. T., & Maaza, M. Elucidation of photocatalysis, photoluminescence and antibacterial studies of ZnO thin films by spin coating method. *J. Photochem. Photobiol. B Biol.* **173**, 466–475 (2017).

15. Li, P., Huang, T. C., White, K. L., Hawkins, S., Kotaki, M., Nishimura, R., & Sue, H. J. Spray-coated epoxy barrier films containing high aspect ratio functionalized graphene nanosheets. *RSC Adv.* **5**, 102633–102642 (2015).

16. Lu, G. & Hupp, J. T. Metal-organic frameworks as sensors: A ZIF-8 based fabry-pérot device as a selective sensor for chemical vapors and gases. *J. Am. Chem. Soc.* **132**, 7832–7833 (2010).

17. Chernikova, V., Shekhah, O. & Eddaoudi, M. Advanced fabrication method for the preparation of MOF thin films: Liquid-phase epitaxy approach meets spin coating method. *ACS Appl. Mater. Interfaces* **8**, 20459–20464 (2016).

18. Silvestre, M. E., Franzreb, M., Weidler, P. G., Shekhah, O. & Wöll, C. Magnetic cores with porous coatings: Growth of metal-organic frameworks on particles using liquid phase epitaxy. *Adv. Funct. Mater.* **23**, 1210–1213 (2013).

19. Yao, M. S., Tang, W. X., Wang, G. E., Nath, B. & Xu, G. MOF thin film-coated metal oxide nanowire array: Significantly improved chemiresistor sensor performance. *Adv. Mater.* **28**, 5229–5234 (2016).

20. O'Neill, L. D., Zhang, H. & Bradshaw, D. Macro-/microporous MOF composite beads. *J. Mater. Chem.* **20**, 5720–5726 (2010).

21. Liu, F. & Xu, H. Development of a novel polystyrene/metal-organic framework-199 electrospun nanofiber adsorbent for thin film microextraction of aldehydes in human urine. *Talanta* **162**, 261–267 (2017).

22. Atalay, S., Izgi, T., Kolat, V. S., Erdemoglu, S. & Inan, O. O. Magnetoelastic humidity sensors with TiO2 nanotube sensing layers. *Sensors* **20**, 1–12 (2020).

23. Cai, Q. Y., Cammers-goodwin, A. & Grimes, C. A. A wireless, remote query

magnetoelastic CO2 sensor. *J. Environ. Monit.* **2**, 556–560 (2000).

24. Zhang, Z., Pinnaratip, R., Ong, K. G. & Lee, B. P. Correlating the mass and mechanical property changes during the degradation of PEG-based adhesive. *J. Appl. Polym. Sci.* **137**, 1–8 (2020).

25. Sagasti, A., Bouropoulos, N., Kouzoudis, D. Panagiotopoulos, A., Topoglidis, E., & Gutiérrez, J. Nanostructured ZnO in a Metglas/ZnO/hemoglobin modified electrode to detect the oxidation of the hemoglobin simultaneously by cyclic voltammetry and magnetoelastic resonance. *Materials (Basel).* **10**, 1–17 (2017).

26. Zhang, R., Tejedor, M. I., Anderson, M. A., Paulose, M. & Grimes, C. A. Ethylene detection using nanoporous PtTiO2 coatings applied to magnetoelastic thick films. *Sensors* **2**, 331–338 (2002).

27. Baimpos, T., Gora, L., Nikolakis, V. & Kouzoudis, D. Selective detection of hazardous VOCs using zeolite/Metglas composite sensors. *Sensors Actuators, A Phys.* **186**, 21–31 (2012).

28. Tsukala, V. & Kouzoudis, D. Zeolite micromembrane fabrication on magnetoelastic material using electron beam lithography. *Microporous Mesoporous Mater.* **197**, 213–220 (2014).

29. Menti, C., Beltrami, M., Possan, A. L., Martins, S. T., Henriques, J. A.P., Santos, A. D., Missell, F. P., & Roesch-Ely, M. Biocompatibility and degradation of gold-covered magneto-elastic biosensors exposed to cell culture. *Colloids Surfaces B Biointerfaces* **143**, 111–117 (2016).

30. Bouropoulos, N., Kouzoudis, D. & Grimes, C. The real-time, in situ monitoring of calcium oxalate and brushite precipitation using magnetoelastic sensors. *Sensors Actuators, B Chem.* **109**, 227–232 (2005).

31. Guo, X., Sang, S., Guo, J., Jian, A., Duan, Q., Ji, J., Zhang, Q., & Zhang, W. A magnetoelastic biosensor based on E2 glycoprotein for wireless detection of classical swine fever virus E2 antibody. *Sci. Rep.* **7**, 1–8 (2017).

32. Chaemchuen, S., & Verpoort, F. Characterization and properties of Zn/Co zeolitic imidazolate frameworks vs. ZIF-8 and ZIF-67. *J. Mater. Chem. A* **5**, (2017).

33. Feng, X. & Carreon, M. A. Kinetics of transformation on ZIF-67 crystals. *J. Cryst. Growth* **418**, 158–162 (2015).

34. Pan, Y., Liu, Y., Zeng, G., Zhao, L., & Lai, Z. Rapid synthesis of zeolitic imidazolate framework-8 (ZIF-8) nanocrystals in an aqueous system. *Chem. Commun.* **47**, 2071–2073 (2011).

35. Cavka, J. H., Jakobsen, S., Olsbye, U., Guillou, N., Lamberti, C., Bordiga, S., & Lillerud, K. P. A new zirconium inorganic building brick forming metal organic frameworks with exceptional stability. *J. Am. Chem. Soc.* **130**, 13850–13851 (2008).

36. Shearer, G. C., Chavan, S., Ethiraj, J., Vitillo, J. G., Svelle, S., Olsbye, U., Lamberti, C., Bordiga, S., & Lillerud, K. P. Tuned to perfection: Ironing out the defects in metal-organic framework UiO-66. *Chem. Mater.* **26**, 4068–4071 (2014).

37. Shearer, G. C., Chavan, S., Bordiga, S., Svelle, S., Olsbye, U., & Lillerud, K. P. Defect engineering: Tuning the porosity and composition of the metal—organic framework UiO-66 via modulated synthesis. *Chem. Mater.* **28**, 3749–3761 (2016).

38. Muguruza, A. R., Fernandez de Luis, R., Iglesias, N., Bazán, B., Urtiaga, M., K., Larrea, E. S., Fidalgo-Marijuan, A., & Barandika, G. Encapsulation of β-alanine model amino-acid in zirconium(IV) metal organic frameworks: Defect engineering to improve host guest interactions. *J. Inorg. Biochem.* **205**, 110977 (2020).

39. Chavan, S., Vitillo, J. G., Uddin, M. J., Bonino, F., Lamberti, C., Groppo, E., Lillerud K-P., & B. S. Functionalization of UiO-66 metal-organic framework and highly cross-linked polystyrene with Cr(CO)3: In situ formation, stability, and photoreactivity. *Chem. Mater.* **22**, 4602–4611 (2010).

40. Viswan, R., Gray, D., Wang, Y., Li, Y. Berry, D., Li, J., & Viehland, D. Strong magnetoelectric coupling in highly oriented ZnO films deposited on Metglas substrates. *Phys. Status Solidi - Rapid Res. Lett.* **5**, 391–393 (2011).

41. Saliba, D., Ammar, M., Rammal, M., Al-Ghoul, M., & Hmadeh, M. Crystal Growth of ZIF-8, ZIF-67, and Their Mixed-Metal Derivatives. *J. Am. Chem. Soc.* **140**, 1812–1823 (2018).

42. Sagasti, A., Lopes, A. C., Lasheras, A., Palomares, V., Carrizo, J., Gutierrez, J., &

Barandiaran, J. M. Corrosion resistant metallic glasses for biosensing applications. *AIP Adv.* **8**, (2018).

43. Sagasti, A., Palomares, V., Porro, J. M., Orúe, I., Sánchez-Ilárduya, M. B., Lopes, A. C., & & Gutiérrez, J. Magnetic, magnetoelastic and corrosion resistant properties of (Fe-Ni)-based metallic glasses for structural health monitoring applications. *Materials (Basel).* **13**, 1–14 (2020).

44. García-Arribas, A., Gutiérrez, J., Kurlyandskaya, G. V., Barandiarán, J. M., Svalov, A., Fernández, E., Lasheras, A., de Cos, D., & Bravo-Imaz, I. Sensor applications of soft magnetic materials based on magneto-impedance, magneto-elastic resonance and magneto-electricity. *Sensors (Switzerland)* **14**, 7602–7624 (2014).

45. Sagasti, A., Gutiérrez, J., Sebastián, M. S. & Barandiarán, J. M. Magnetoelastic resonators for highly specific chemical and biological detection : A critical study. *IEEE Trans. Magn.* **53**, 10–13 (2017).

46. Ahmed, I. & Jhung, S. H. Effective adsorptive removal of indole from model fuel using a metal-organic framework functionalized with amino groups. *J. Hazard. Mater.* **283**, 544–550 (2015).

47. Chavan, S. M., Shearer, G. C., Svelle, S., Olsbye, U., Bonino, F., Ethiraj, J., Lillerud, K. P., & Bordiga, S. Synthesis and characterization of amine-functionalized mixed-ligand metal−organic frameworks of UiO-66 topology. *Inorg. Chem.* **53**, 9509–9515 (2014).

48. Atalay, S., Kaya, H., Atalay, F. E., Izgi, T. & Kolat, V. S. Formation and detection of magnetic CoNiFe nanowire network using magnetoelastic sensor. *J. Supercond. Nov. Magn.* **32**, 3907–3913 (2019).

49. Audu, C. O. Nguyen, H. G. T., Chang, C. Y., Katz, M. J., Mao, L., Farha, O. K., Hupp, J. T., & Nguyen, S. T. The dual capture of As V and As III by UiO-66 and analogues. *Chem. Sci.* **7**, 6492–6498 (2016).

50. Furukawa, H., Gándara, F., Zhang, Y. B., Jiang, J., Queen, W. L., Hudson, M. R., & Yaghi, O. M. Water adsorption in porous metal-organic frameworks and related materials. *J. Am. Chem. Soc.* **136**, 4369–4381 (2014).

51. Jiang, J., Gándara, F., Zhang, Y. B., Na, K., Yaghi, O. M., & Klemperer, W. G. Superacidity in sulfated metal-organic framework-808. *J. Am. Chem. Soc.* **136**, 12844–12847 (2014).

52. Rada, Z. H., Abid, H. R., Sun, H. & Wang, S. Bifunctionalized metal organic frameworks, UiO-66-NO2-N (N = -NH2, -(OH)2, -(COOH)2), for enhanced adsorption and selectivity of CO2 and N2. *J. Chem. Eng. Data* **60**, 2152–2161 (2015).

53. Valenzano, L., Civalleri, B., Chavan, S., Bordiga, S., Nilsen, M. H., Jakobsen, S., Lillerud, K. P., & Lamberti, C. Disclosing the complex structure of UiO-66 metal organic framework: A synergic combination of experiment and theory. *Chem. Mater.* **23**, 1700–1718 (2011).


Chapter
4

Magnetoelastic/MOF sensors for chromium monitorization

En este capítulo se recogen los resultados relacionados con los experimentos de adsorción, foto-reducción y detección de metales pesados llevados a cabo con los MOF sintetizados y los sensores fabricados. En particular, se presentan diversos experimentos de adsorción y foto-reducción de cromo hexavalente realizados con los MOF de tipo UiO-66-R previamente caracterizados. Por otro lado, los mecanismos de adsorción y la especiación del cromo dentro de estos MOF se han determinado mediante estudios de espectroscopia de resonancia paramagnética electrónica y ultravioleta-visible. Finalmente, se investiga el comportamiento de los resonadores magnetoelásticos basados en estos materiales activos en medios líquidos, y sus limitaciones a la hora de aplicarlos en medios acuosos para la detección de cromo hexavalente y trivalente.

Content

* Publications in which this chapter is based.

Some of the results exposed in this chapter have been published in two indexed scientific publications: 1) **"Chromium speciation in Zr-based Metal-Organic Frameworks for environmental remediation".** *Chemistry - A European Journal (Q1), 2020, DOI:* doi.org/10.1002/chem.202001435*;* and 2) "**Modulation of the bi-functional Cr^{VI} to Cr^{III} photo-reduction and adsorption capacity in Zr^{IV} and Ti^{IV} benchmark Metal-Organic Frameworks".** *Catalysts* (Q2), 2020, *(Under revision);* as well as in some of the conferences presented in Annex C (Results dissemination).

4.1. Introduction

One of the most pervasive problems affecting population health is insufficient access to adequate clean water. A growing number of contaminants are entering water supplies due to the anthropogenic activities, but also as a result of the natural leaching of bedrocks containing high concentrations of hazardous heavy metals and metalloids. The pressure of the human activities on the water natural reservoirs summed to the increasing effects of the global climate change on the access to clean water supplies will grow even more in the coming years [1]. On that context, water monitoring will be a crucial tool to assess in a continuous and remote mode whether the water quality is within the standards established by the water protection bodies, and in parallel, to apply fast and effective mitigation measures in case a risk is detected. In that respect, the development of new techniques for the detection and elimination of those compounds, or the improvement of the existing ones, is a worldwide priority.

In particular, heavy metals (HMs) derived from natural leaching of bedrocks, as well as mining and industrial activities are some of the most common and dangerous pollutants present in water [2–4]. Heavy metals such as Hg^{II}, Cr^{VI}, Pb^{II}, Cd^{II} and metalloids such as As^{V} and As^{III}, are particularly dangerous since even when present at very low concentrations, they are genotoxic, mutagenic, teratogenic and carcinogenic. Apart from their high toxicity, heavy metals are non-biodegradable and present a long-term bio-persistence, which makes their cumulative effects in the long term dangerous even under exposures close or below to the legal limits. If their adverse effects for the human health and the environment are summed to their high mobility and solubility, this increasing environmental and health concern [4–6] is accentuated, since makes that current wastewater treatment plants not completely efficient to retain them.

Most commonly employed techniques for HMs detection are highly selective and sensitive, but they are time-consuming and requires from complex and expensive instrumentation usually managed by specialized technicians [7]. As a consequence, researchers are looking for faster, cheaper and wireless HMs detection technologies [8]. On that way, as it has been explained in previous chapters of this thesis, magnetoelastic sensors could provide an interesting alternative to other sensing devices since they are an already commercialized technology that met low cost and wireless detection

capabilities. Few works have reported the magnetoelastic resonators feasibility for the detection of HMs in liquid media. Just to mention the most relevant ones in this nascent research area, MRs have been employed for the detection of uranium based on its inhibition effect on: i) The catalytic effect of mercury(II) on the precipitation reaction of potassium ferrocyanide in the presence of water [9], and ii) the catalytic hydrolyzation caused by the α-amylase on a starch film deposited on the sensor surface [10]. Moreover, a mercury MR sensor based in the formation of thymine (T)-Hg structures, which lead to the release of complementary DNA on the presence of that heavy metal, has also been reported [11]. In a similar way, the detection of multiple heavy metals (Pb^{2+}, Cd^{2+} and Cu^{2+}) based in the precipitation of bovine serum albumin produced when that protein is in contact with the heavy metal ions has been recently proposed [12].

Nevertheless, there is still a room of improvement in this research area, since novel MRs geometries with improved sensitivities could open the possibility to detect the HMs directly from solution if they are functionalized with the proper active layer. It is worthy to note that in liquid media, there are additional parameters that would affect the performance of the resonators, such as the damping effect caused by liquids as well as their viscosity or density. Moreover, as it can be concluded from the state of the art of MRs applied for heavy metal detection, the recognition process is always coupled to its interaction/precipitation/release triggered by a protein type functionality, but none is based on the adsorption of the HMs on an active layer. Considering the high adsorption capacities of MOFs towards HMs, it is appealing to explore the potentials and limitation of MOF based MRs technology for their direct detection in aqueous media.

Metal-Organic Frameworks are among the most promising adsorbents for heavy metals. In particular, some zirconium-based MOFs stand out for their high water stability, a characteristic that opened the possibility to apply them to adsorption processes in water [13]. The effectiveness of MOFs to remove hazardous metal ions present even at very low concentrations have been widely proved. The hexavalent chromium case is especially appealing since it is quite challenging to adsorb or immobilize this highly soluble and mobile oxyanion. Chromium is usually present as highly soluble and mobile hexavalent chromate ($(Cr^{VI}O_4)^{2-}$) and dichromate ($(Cr_2^{VI}O_7)^{2-}$) oxyanions, which are highly toxic and whose continuous exposure can lead to mutagenesis and carcinogenesis [3]. In the specific case of hexavalent chromium, MOFs have shown remarkable adsorption capacity

exceeding in many cases the 100 mg/g [14,15] (**Figure 4.1**). Nevertheless, when thinking about MOF based MRs application to sense heavy metals at very low concentrations, despite MOF are very effective sorbents, the overall mass gain due to the Cr^{VI} adsorption process could be very low to be detected by the MR platform.

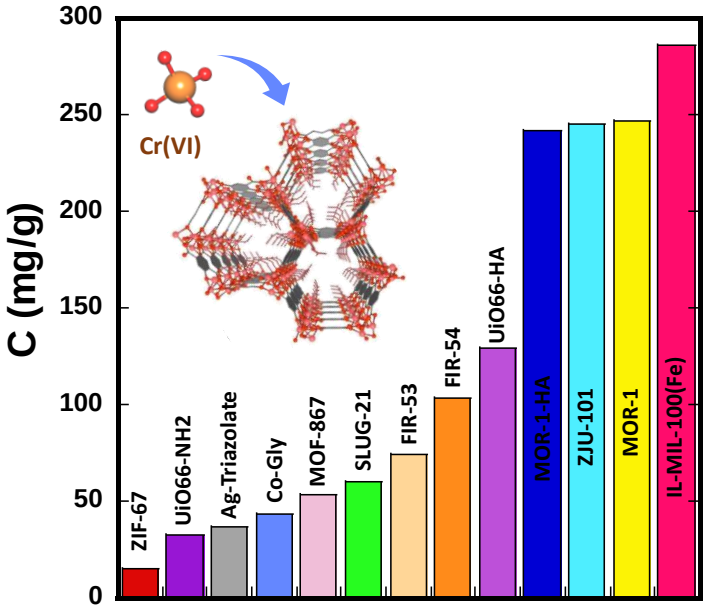

Figure 4.1. Cr^{VI} adsorption capacities measured for different MOFs materials. Results have been represented from the dates collected in [14].

Cr^{VI} can be transformed into other less toxic trivalent specie (Cr^{III}) under specific conditions [16], but it is important to have in mind, that the stabilization of intermediate Cr^{V} pentavalent species need to be avoided during the process since they are even more reactive and dangerous than hexavalent chromium. Here is where bi-functional MOF materials able to photo-reduce Cr^{VI} to Cr^{III}, and at the same time sorb Cr^{III} ions come into play [17–22]. Therefore, by applying this approach, Cr^{VI} could be transformed in other less toxic specie. Moreover, when thinking about HMs sensing with magnetoelastic sensors, the MOF active layer would be able to gain weight even after the Cr^{VI} adsorption equilibrium is reached, since upon illumination the Cr^{VI} still present in the solution will be continuously transformed to Cr^{III} and incorporated to the active layer. Indeed, several photoactive MOF materials have been revealed as very efficient Cr^{VI} to Cr^{III} photo-reducers [23]. Photo-reduction efficiencies and times measured for different MOFs materials are summarized in **Figure 4.2**, it should be noted that different facts affect to these parameters such as the MOF load, the initial Cr^{VI} concentration or the employed light.

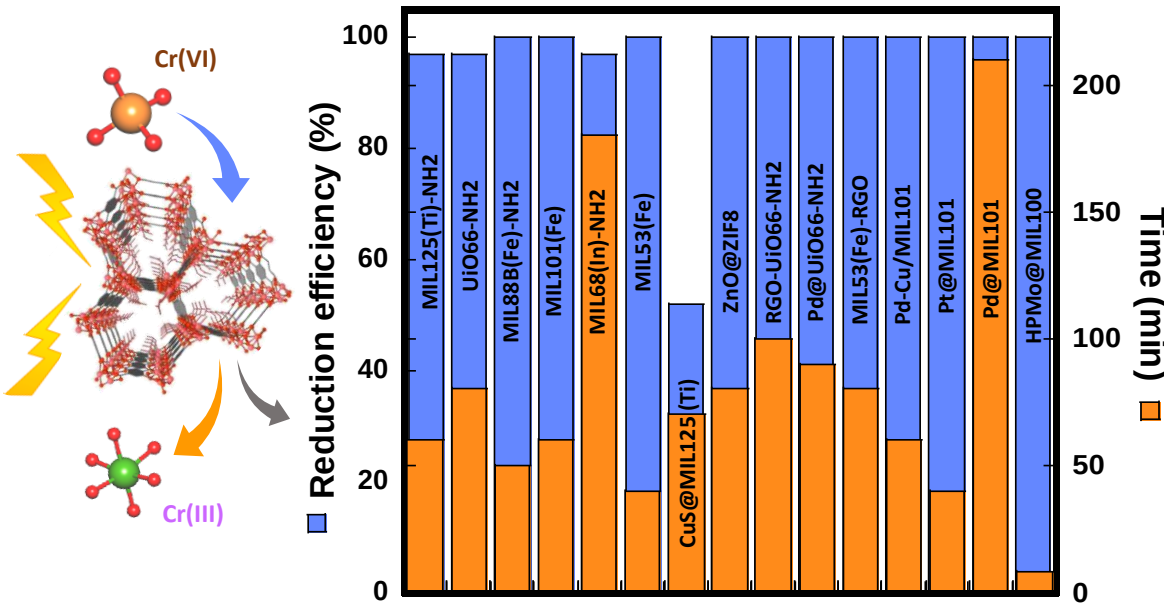

Figure 4.2. Photocatalytic performance of different metal-organic frameworks (or their composites) for the reduction of Cr^{VI}. Graphic represented from the results collected in [23].

But the key question here is, are they able to capture the Cr^{III} photo-reduced species as well? This point has been widely forgotten by the scientific community working of MOF photo-catalysts. It is true that when the photo-degradation process is carried out in neutral or slightly acidic conditions, the Cr^{VI} to Cr^{III} photo-transformation will lead to the precipitation of the Cr^{III} ions as oxides and hydroxides. But at acidic condition, Cr^{III} ions are still soluble, and in this concrete case, the photo-catalyst need both to photo-reduce and at the same time, retain the Cr^{III} photo-transformed ions.

Taking into account the previous factors, the adsorption-chemical reduction and photo-reduction capacity of Cr^{VI} to Cr^{III} species of six Zr-terephthalate (UiO-66 type) MOFs has been deeply studied in this chapter. Moreover, a first-time ultraviolet-visible (UV-Vis) and electron paramagnetic resonance spectroscopy (EPR) combined methodology has been employed to describe the chromium speciation after the adsorption and photo-reduction process in the UiO-66-R frameworks. Secondly, the magnetoelastic response in liquid media of Metglas resonators with different geometries has been investigated. After that, the pros and cons of UiO-66-NH_2 functionalized ME sensors for chromium sensing have been identified.

4.2. Hexavalent chromium adsorption and photo-reduction in Zr-based MOFs

In this section of the chapter, the dual adsorption and ion-reductive capacity of Cr^{VI} and Cr^{III} species in the six different Zr-terephthalate crystal frameworks, previously presented in Chapter 3, has been studied. The linker defect positions in the UiO-66-R structures are expected to be efficient adsorption positions for Cr^{VI}, while the electron donor functionalities (-$(OH)_2$ and -NH_2) encoded within the organic ligands of UiO-66 materials can trigger their Cr^{VI} to Cr^{III} chemical reductive capacity. Obtained results are presented in the following.

4.2.1. Hexavalent and trivalent chromium adsorption capacity

First of all, chromium adsorption isotherms of the UiO-66-R samples were measured and analyzed in order to investigate the combined effect of: *i)* varied linkers defect density and *ii)* the presence of –NH_2 and –$(OH)_2$ electron donor groups, on the adsorption capacity over Cr^{VI} and Cr^{III}. From the adsorbate – adsorbent electrostatic interaction point of view, the absorption process of Cr^{III} and Cr^{VI} species is foreseen to be driven by different mechanisms, since only considering their charge they will be immobilized at different points of the adsorbent structure. This way, hexavalent chromium oxyanions will tend to be immobilized via coordinative bonds at the zirconium oxo-clusters linker defect positions, while Cr^{III} oxo-aquo positively charged species will prompt to interact with the electron donor functionalities placed at the organic linkers of the UiO-66-R frameworks. Adsorption isotherms were measured from batch experiments of chromium solutions (Cr^{III} and Cr^{VI}) with concentrations ranging from 5 to 100 ppm. Chromium concentration before and after the adsorption process was quantified by ICP-AES, and the adsorption capacity of the MOFs was calculated from the chromium concentration variation normalized to the MOF weight. A detailed description of the experimental part along with the non-linear Langmuir [24,25] and Freundlich [24,26] fittings models of the adsorption isotherms are described in **Annex A**. The experimental results and their fittings based on the Langmuir adsorption model are shown in Figure 4.3. Adsorption capacity, adsorption affinity and correlation parameters obtained from the experimental fittings to both models are summarized in **Table *4.1***.

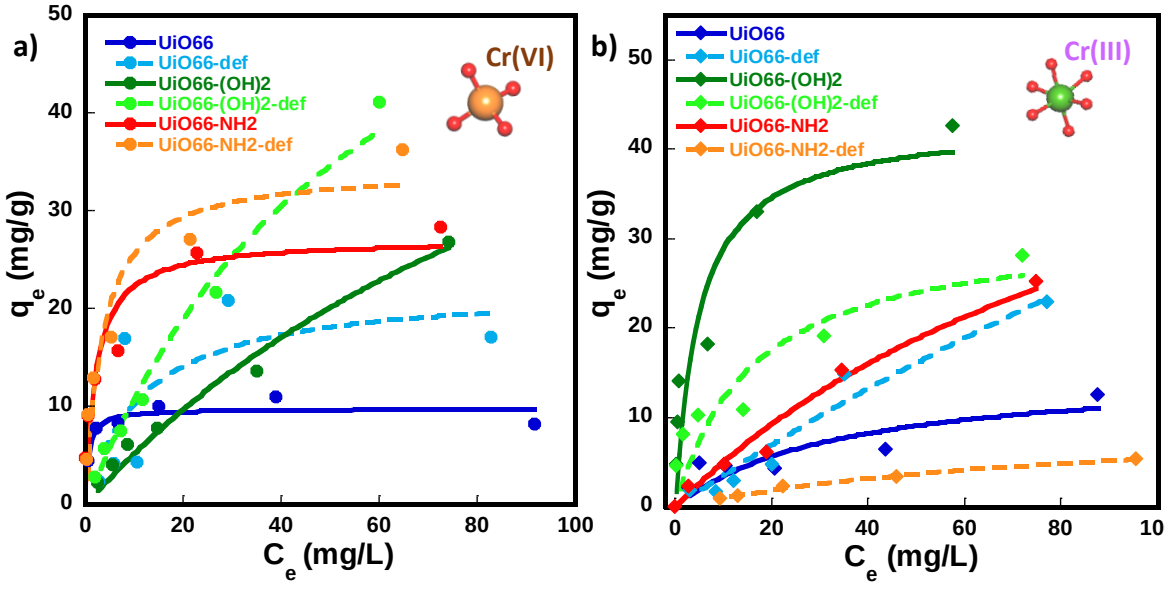

Figure 4.3. Adsorption isotherms for: (a) Cr^{VI} and (b) Cr^{III} measured for UiO-66-R (R= -H, $-NH_2$, $-(OH)_2$, -H-def, $-NH_2$-def, $-(OH)_2$-def) samples. Points: experimental data. Line: Langmuir fitting. Adsorbent concentration 1 $mg \cdot mL^{-1}$, Volume of solution: 10 mL, T: 21 °C, pH= 4, equilibrium time: 24h.

A marked increase in the capacities for chromate adsorption is observed at the isotherms curve saturation region in linker defective samples in comparison with non-defective ones. This experimental evidence confirms the preference of under-coordinated positions at the zirconium oxo-clusters, generated as a consequence of linker defects, as adsorption positions for chromate anions. Moreover, hydroxyl or amine functionalization further boost the chromate uptake capacity of UiO-66-R sorbents, pointing that they also play an important role in the chromate adsorption process. Therefore, in terms of Cr^{VI} adsorption capacity (**Figure 4.3**a), the combination of linker defective network with the presence of electron donor hydroxyl or amine groups is the best combination to reach the highest possible saturation capacity (i.e. ~ 50 $mg \cdot g^{-1}$). It is worth to mention, that although hydroxyl and amine functionalized compounds show similar maximum adsorption capacities (*at 100ppm*), the K_L and n parameters values obtained from the Langmuir and Freundlich fittings suggest that their chemical affinity towards Cr^{VI} differs [28–31]. In fact, at lower chromate concentrations (*≤ 50 ppm*), UiO-66-NH_2 samples show higher adsorption capacity and affinity than the UiO-66-$(OH)_2$ homologue.

Table 4.1. Parameters obtained for the fitting of the Cr^{VI} and Cr^{III} adsorption isotherms of *Figure 4.3* by the non-linear Langmuir and Freundlich models. *The accuracy of the fitting is compromised by the accuracy of the experimental data, especially in these samples with small adsorption capacity values at low concentrations.

	Langmuir			*Freundlich*		
	q_m ($mg\,g^{-1}$)	K_L ($L\,mg^{-1}$)	R^2	K_F ($mg^{1-n}\,L^n\,g^{-1}$)	n	R^2
	Hexavalent Chromium					
UiO-66	8.8(6)	1.6(7)	0.8991	7(1)	10(5)	0.7206
UiO-66-def.	22(8)	0.09(8)*	0.7534	4(3)	3(2)*	0.6828
UiO-66-$(OH)_2$	71(23)	0.008(4)	0.9905	1.0(2)	1.32(7)	0.9964
UiO-66-$(OH)_2$-def.	75(15)	0.017(6)	0.9913	1.6(1)	1.26(3)	0.9994
UiO-66-NH_2	27(3)	0.5(2)	0.9399	10(1)	4.1(5)	0.9803
UiO-66-NH_2-def.	34(4)	0.3(1)	0.9442	10.7(5)	3.4(2)	0.9968
	Trivalent Chromium					
UiO-66	15(6)	0.03(2)*	0.8322	1.3(6)	2.1(5)	0.9153
UiO-66-def.	---*	---*	---*	0.4(2)	1.1(2)	0.9739
UiO-66-$(OH)_2$	43(7)	0.19(13)	0.9301	12(2)	3.1(4)	0.9813
UiO-66-$(OH)_2$-def.	32(8)	0.06(4)	0.8952	5(1)	2.6(4)	0.9743
UiO-66-NH_2	61(20)	0.009(4)	0.9899	0.7(2)	1.2(1)	0.9915
UiO-66-NH_2-def.	10(1)	0.011(2)	0.9963	0.25(4)	1.48(9)	0.9960

As expected, the opposite trend is observed for Cr^{III} adsorption (**Figure 4.3**b), since in this case, the higher the concentration of hydroxyl or amine groups in the UiO-66-R materials, the higher their Cr^{III} adsorption capacity, being the linker-defect generation detrimental. Besides, hydroxyl functionalized compounds (UiO-66-$(OH)_2$ and UiO-66-$(OH)_2$-def) are more effective than amine functionalized analogues (UiO-66-NH_2 and UiO-66-NH_2-def) to adsorb Cr^{III} species. As previously stated, Cr^{VI} is the more toxic and dangerous chromium specie, thus, materials with higher Cr^{VI} adsorption capacities are preferable. In this regard, UiO-66-NH_2 samples are the ones which present the higher

adsorption capacities toward chromate at low concentrations, thus resulting the most interesting for using as active layer in the magnetoelastic resonators.

To further understand the Cr^{III} and Cr^{VI} adsorption process for UiO-66-NH_2 and UiO-66-NH_2-def compounds, their adsorption kinetics over Cr^{III} and Cr^{VI} were also studied. The adsorption kinetic curves were measured over 5 ppm chromium solutions and 0.25 mg/L sorbent loading. The experimental data and their fitting with the Bangham model are shown in **Figure 4.4**.

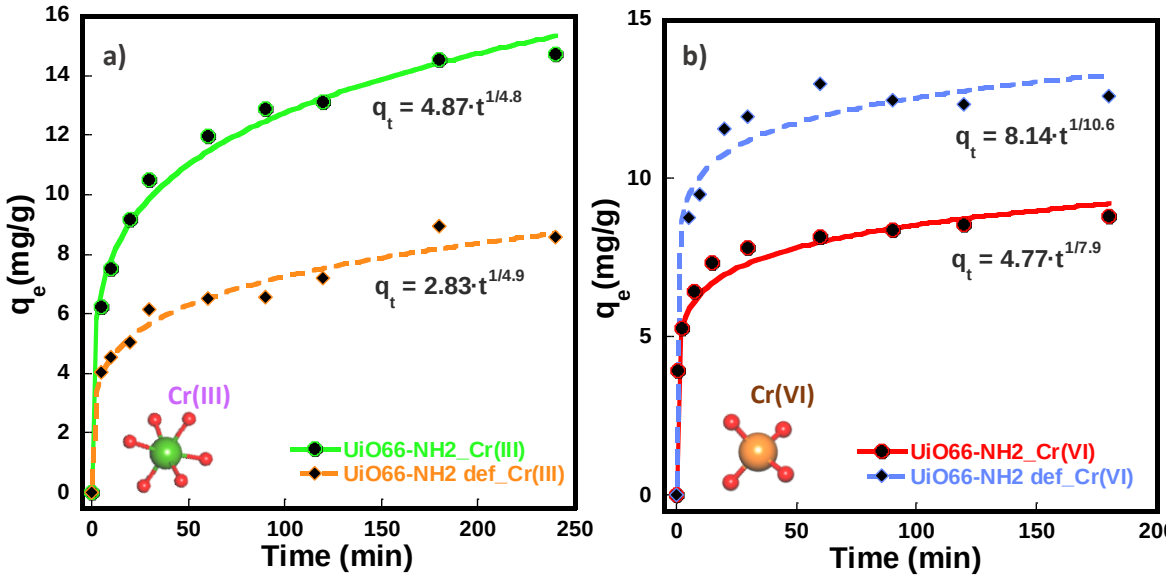

Figure 4.4. Adsorption kinetics for: (a) Cr(III) and (b) Cr(VI) in UiO-66-NH_2 and UiO-66-NH_2-def samples. Points: experimental data. Line: Bangham model fitting. Adsorbent concentration 0.25 mg·mL^{-1}, C=5ppm.

Based on the kinetic profiles shown in **Figure 4.4**, it could be observed that the adsorption kinetics are faster for Cr^{VI} adsorption (saturation point ~ 25 min) in comparison to Cr^{III} (saturation point > 180 min). Following the same tendency observed for the adsorption isotherms, the linker-defective materials show higher uptake capacity over anionic Cr^{VI} species, whilst non-defective UiO-66-NH_2 sorbent shows a better uptake of Cr^{III} cations. Kinetic curves were also fitted to first order and pseudo second order models. The kinetic profiles for both ions are not well modelled with a first order model, a fact that indicates that the adsorption process is not solely governed by the diffusion of the ions into the UiO-66-NH_2 porous crystal structure. Indeed, the kinetic curves are better simulated when pseudo second order and Bangham models are applied, a fact that points that the chromium diffusion is coupled to a posterior chemisorption/reduction

process into the MOF structure. The parameters obtained from the fittings are summarized in **Table 4.2**. It should be noted that the chromate saturation point is reached in a frame of time that is long enough to be followed through the magnetoelastic based sensing process.

Table 4.2. Parameters obtained for the fitting of the Cr^{VI} and Cr^{III} adsorption kinetics of **Figure 4.4** by the Bangham and Pseudo second order models.

	Bangham Model ($q_t = K_T \cdot t^{1/m}$)		
	R	***K_T***	***m***
UiO-66-NH_2_Cr^{III}	0.99562	4.9(3)	4.8(3)
UiO-66-NH_2-def_ Cr^{III}	0.98974	2.8(2)	4.9(4)
UiO-66-NH_2_ Cr^{VI}	0.98816	4.8(3)	8(1)
UiO-66-NH_2-def_Cr^{VI}	0.98626	8.1(6)	11(2)
	Pseudo-second-Order Model ($t/q_t=(1/V_0)+((1/q_e)\cdot t)$)		
	R	***$1/V_0$***	***$1/q_e$***
UiO-66-NH_2_ Cr^{III}	0.99869	0.9(2)	0.065(1)
UiO-66-NH_2-def_ Cr^{III}	0.99163	1.8(6)	0.111(5)
UiO-66-NH_2_Cr^{VI}	0.99971	0.29(6)	0.1137(9)
UiO-66-NH_2-def_Cr^{VI}	0.99974	0.16(6)	0.0786(7)

Considering the results as a whole, it can be concluded that the combination of linker defect positions and the presence of $-NH_2$/-OH groups is the best encoding strategy to adsorb Cr^{VI}, whilst in the case of Cr^{III} immobilization, linker defects are detrimental, being the encoding of hydroxyl functionalities the best approach to adsorb it efficiently (**Figure 4.5**).

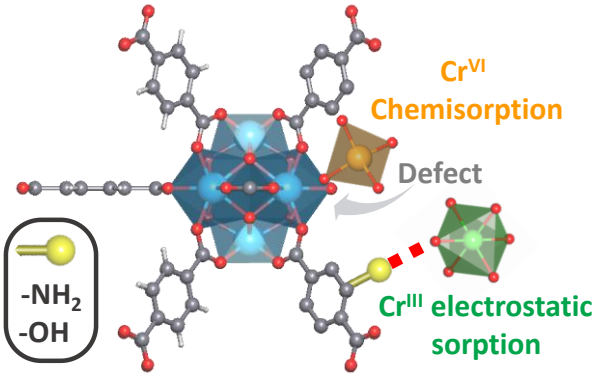

Figure 4.5. Detail of the possible $Cr^{VI}$and Cr^{III} adsorption positions at under-coordinated defect position and organic linkers of zirconium hexa-nuclear local structure.

4.2.2. Coupled chromium photo-reduction and adsorption

The adsorption capacity of UiO-66-R materials over chromium cationic and anionic species have been thoroughly proved. Therefore, it would be highly interesting to investigate whether the capacity of UiO-66-NH_2 samples to photo-reduce Cr^{VI} to Cr^{III} is coupled to the simultaneous adsorption of the photo-generated Cr^{III} ions. Indeed, the main goal of the Cr^{VI} photo-reduction was not only to prove the experimental feasibility of UiO-66-NH_2 samples to photo-transform chromate species, since this has been previously corroborated by several research teams [17,32,33], but to determine to which extent the photo-transformed Cr^{III} species are adsorbed by the photo-catalyst. To this end, photo-reduction experiments were performed under ultraviolet irradiation over a 5 ppm chromate solution with a photo-catalyst loading of 0.25 $g \cdot L^{-1}$. Besides, a specific colorimetric method to quantify the concentration of the hexavalent and trivalent chromium species in the solution was developed. A detailed description of the experimental part and the developed method could be found in **Annex A**. Results are shown in **Figure 4.6**.

As could be observed in **Figure 4.6**, the photocatalysis experiments confirm that all the chromate species have been reduced to Cr^{III} when the material is exposed to UVA radiation. In particular, the photo-reduction process is faster for the defective sample. The photo-reduction kinetic constants were obtained from the linear fitting of the data (**Figure 4.6**c-d), and they indicate a good photocatalytic activity ($k = 0.011$ for the UiO-66-NH_2 and $k=0.027$ for the UiO-66-NH_2-def) when comparing with previous experiments developed with similar materials. Moreover, the quantification of the Cr^{III} content on the solutions confirmed that the Cr^{III} concentration just slightly increases during the photo-reduction, which indirectly points that UiO-66-NH_2 is able to reduce Cr^{VI} to Cr^{III}, and also to immobilize the most of the transformed Cr^{III} species within its structure.

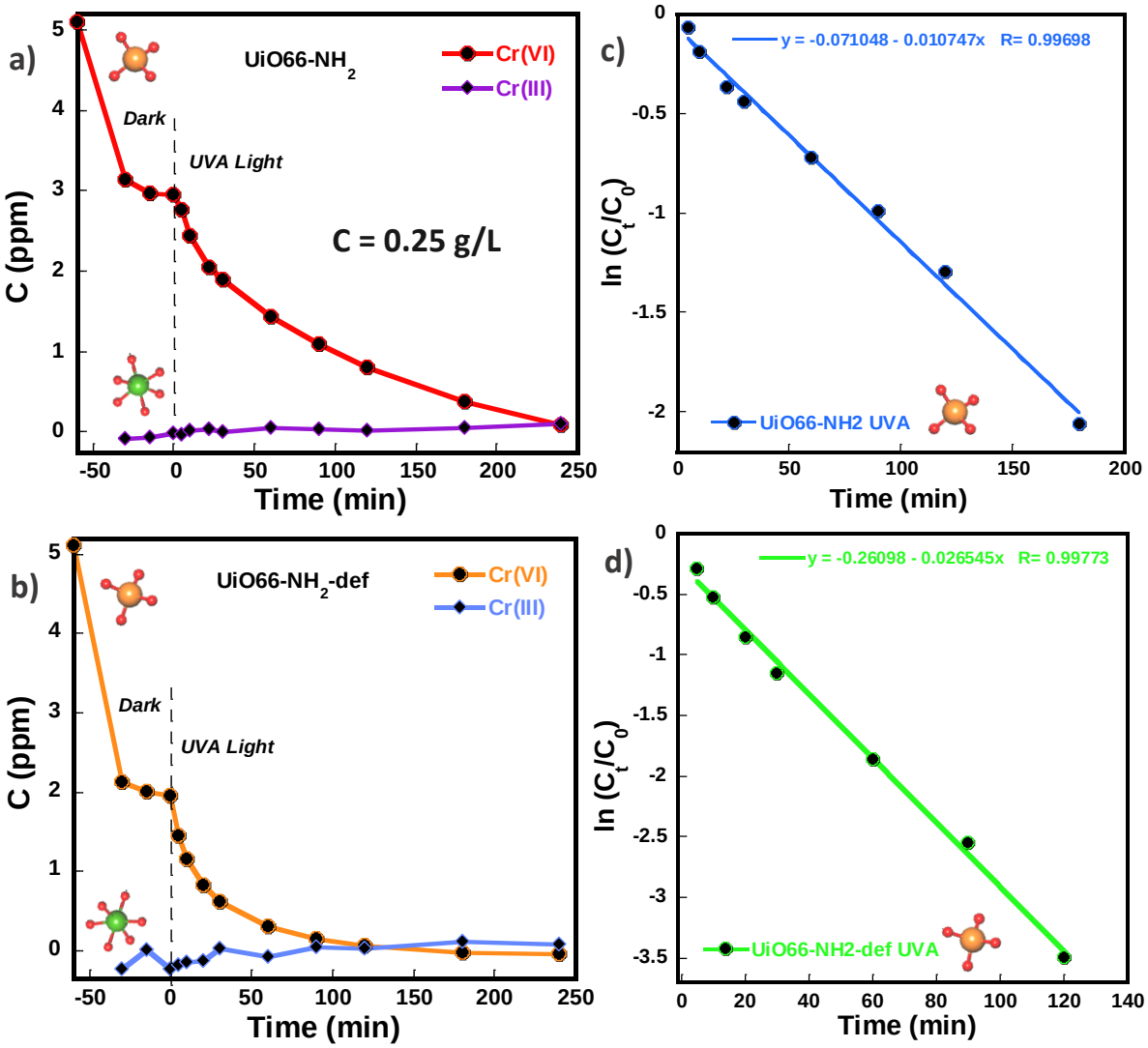

Figure 4.6. Adsorption and photocatalytic reduction under UVA light of Cr^{VI} in: (a) UiO-66-NH_2 and (b) UiO-66-NH_2-def. Adsorbent concentration: 0.25 g·L^{-1}, volume of solution: 200 mL, Ci=5ppm, T = 21°C, pH=4. (c-d)Fitting of the photo-reduction kinetics.

It is worthy to mention that from the chromium sensing perspective, the dual photo-reduction and adsorption capacity of the photo-transformed species is highly beneficial since it would induce an additional mass gain at the active layer of the resonator.

Once confirmed the dual photocatalytic and adsorptive functionality of UiO-66-R materials, and previous to test the chromium detection capacity of UiO-66-NH_2/Metglas resonators, the structural stability and chromium speciation within the MOFs after the adsorption and photo-reduction processes will be investigated.

4.2.3. Chromium speciation after operation: UiO-66-R characterization

Adsorbents were fully characterized by different techniques in order to ensure their stability after operation. First of all, the colour changes after-adsorption is the first visual evidence that indicates that the UiO-66 materials exhibit different degrees of hexavalent chromium adsorption capacities (**Figure 4.7**a).

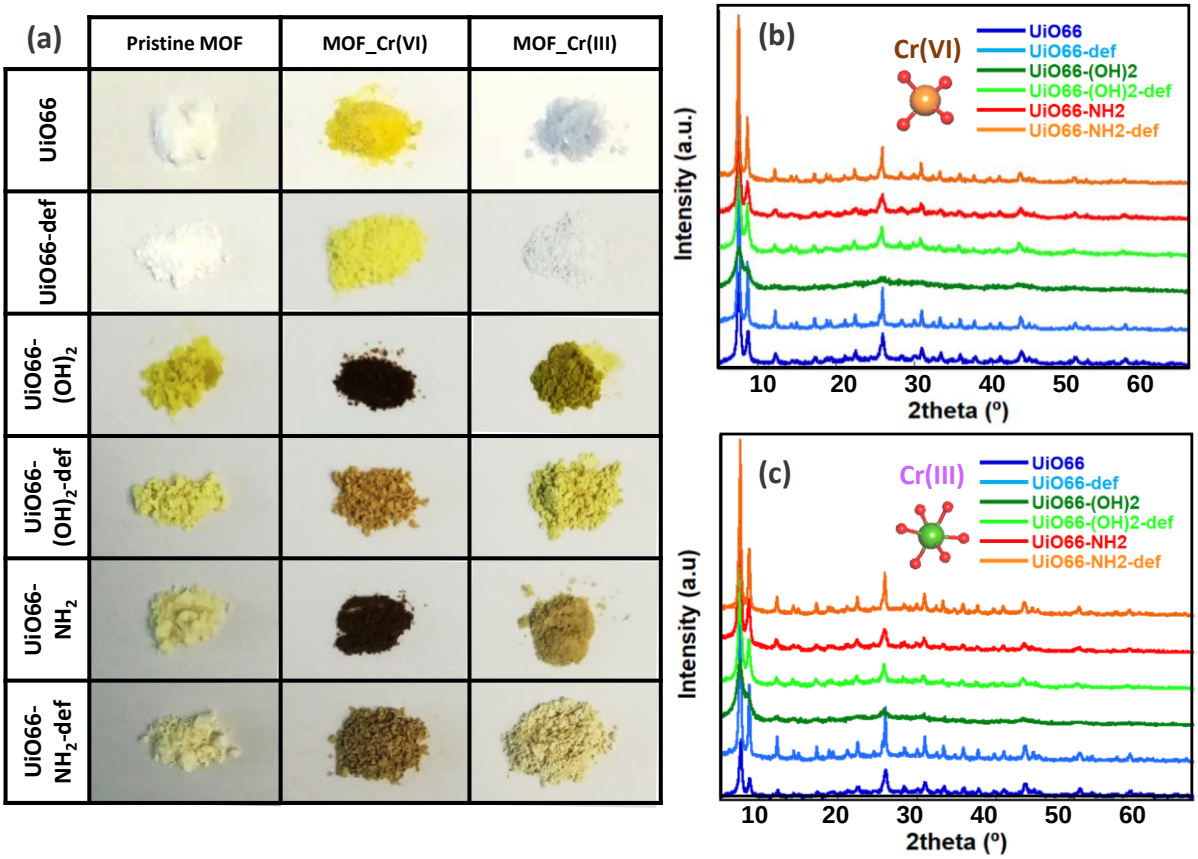

Figure 4.7. (a) Pictures of the different UiO-66-R samples before and after Cr^{VI} and Cr^{III} adsorption experiments, (b-c) XRD patterns of the MOF samples after the adsorption experiments of: (b) Cr^{III} and (c) Cr^{VI}.

UiO-66 and UiO-66-def show a colour change from white to yellow and light grey, respectively. These post-adsorption colours match well with the yellow and light green colours usually found for Cr^{VI} and Cr^{III} species, respectively. The colour variation after the adsorption is further accentuated for hydroxyl and amine decorated samples. After Cr^{VI} adsorption, UiO-66-NH_2 and UiO-66-$(OH)_2$ compounds acquire a dark brown colour which is indicative of an electron transfer process between chromium mixed-valence species. The same tendency has been observed for UiO-66-NH_2 and UiO-66-NH_2 -def samples used for chromium photo-reduction experiments.

It is worth noting that the same compounds after Cr^{III} adsorption show lighter colours than Cr^{VI} loaded materials. In this case, chromium is solely stabilized as Cr^{III} ions, overriding the possibility of electron transfer between chromium species, and hence, the absorbance gain.

Moreover, XRD patterns of UiO-66-R samples after Cr^{III} and Cr^{VI} adsorption and photocatalysis experiments do not show evidences of damage, confirming their structural stability upon prolonged exposition to high concentrated (100 ppm) chromium solutions (**Figure 4.7**b-c). The crystallinity degree and the position and intensity of the diffraction maxima remain unchanged. In addition, no trace of additional phases has been observed by XRD, a fact that discards that the chromium immobilization occurs through its precipitation as chromium oxide, and that further confirms the adsorption process as the main driving mechanism for Cr^{VI} and Cr^{III} retention within the UiO-66-R materials.

The accurate description of the chromium speciation at the sorbent or dual photo-catalyst/sorbent matrixes result key to estimate the chromium adsorption/ reduction/photo-reduction efficiency of these multi-functional porous materials. Nevertheless, experimental approaches unravelling the chromium speciation at MOF sorbents are seldom found [34], and the most of them are based on specific techniques only available at large installation facilities (e.g. X-ray absorption and pair distribution function analyses) [35–38]. Thus, it would be highly desirable to develop a laboratory scale combined characterization protocol that allows: *i)* distinguishing between chromium oxidation state and *ii)* obtaining information about the local structure of low concentrated chromium species immobilized within the sorbent. In this work, chromium speciation within the UiO-66-R adsorbents has been investigated by applying a combined UV-Vis and EPR spectroscopy analyses.

UV-Vis spectra of the of UiO-66-R materials show a typical fingerprint absorption band located around 35000 cm^{-1}, which is attributed to ligand-to-metal charge transfer (LMCT) (**Figure 4.8**). Additional bands located around 27500 cm^{-1} are observed for the functionalized UiO-66-NH_2 and UiO-66-$(OH)_2$ samples, which are associated to the donation of electron density from the hydroxyl and amine groups to the π*-orbitals of the benzene ring.

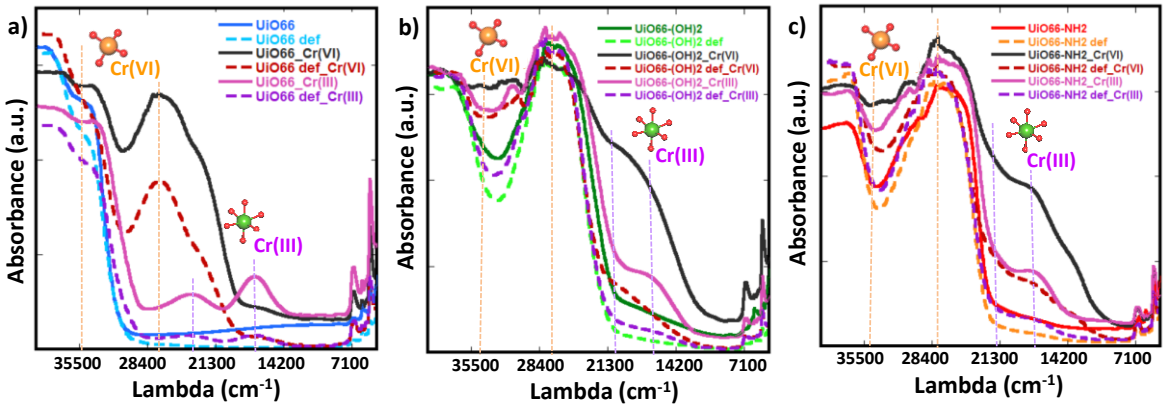

Figure 4.8. UV-Vis spectra for: a) UiO-66, b) UiO-66-$(OH)_2$ and c) UiO-66-NH_2 materials before and after Cr^{III} and Cr^{VI} adsorption processes. Guide for the eye dashed lines have been plotted in the ideal positions for adsorption bands related to Cr^{VI}-O charge transfer processes and octahedral Cr^{III} electronic transitions.

After operation, UV-Vis spectra show additional adsorption bands related to Cr^{VI} and Cr^{III} species. Specifically, Cr^{III} post-adsorption samples exhibit two additional UV-Vis signals commonly associated to a octahedral-coordinated $Cr^{3+}d^7$ spin-allowed d–d transitions, $^4A_{2g}(F) \rightarrow {}^4T_{1g}(F)$ (υ_1 (UiO-66) = 23500 cm^{-1}, υ_1 (UiO-66-def) = 24000 cm^{-1}) and $^4A_{2g}(F) \rightarrow {}^4T_{2g}(F)$ (υ_2 (UiO-66)= 21200 cm^{-1}, υ_2 (UiO-66-def) = 17200 cm^{-1}, υ_2 (UiO-66-NH_2) = 17900 cm^{-1}, υ_2 (UiO-66-NH_2-def) = 17800 cm^{-1}, υ_2 (UiO-66-$(OH)_2$)= 17400 cm^{-1}, υ_2 (UiO-66-$(OH)_2$-def)= 17000 cm^{-1}). It should be noted that in amine and hydroxyl functionalized samples, the absorption band associated to the $^4A_{2g}(F) \rightarrow {}^4T_{1g}(F)$ transition is overlapped with the cluster-ligand charge transfer band. Moreover, the absorbance of the UV-Vis signals related to Cr^{III} are higher for hydroxyl and amine functionalized non-defective materials; in good agreement with the maximum adsorption capacities derived from the chromium adsorption experiments [39].

The UV-Vis spectra of UiO-66-R compounds after Cr^{VI} adsorption show the characteristic fingerprints of Cr^{6+}–O^{2-} charge transfer bands for mono-chromate species at 27500 and 22300 cm^{-1}. Indeed, for the UiO-66 sample, in addition to the above observed signals ascribed to Cr^{VI}, a small absorption peak located around 16500 cm^{-1} confirms also the presence of Cr^{III} species within the sorbent, suggesting that the Cr^{VI} capture is coupled to its partial reduction to Cr^{III} (**Figure 4.8**a). In the case of the amine or hydroxyl functionalized UiO-66 frameworks (**Figure 4.8**b-c), the Cr^{VI} to Cr^{III} reductive capacity is accentuated, as derived from the absorbance values of the Cr^{6+}–O^{2-} charge transfer band observed at around 17500 cm^{-1}.

As it has been previously mentioned, -NH_2 and –OH groups can boost electron transfer processes inducing the chromium reduction. The slight differences observed in the position of the absorption signals can be explained based on varying degrees of distortion of the Cr^{III} coordination environments once stabilized into the UiO-66-R frameworks. Besides the confirmation of the presence of Cr^{III}, the absorbance increases in the 35000 – 30000 cm^{-1} UV-Vis region points to the co-existence of Cr^{VI} and Cr^{III} after operation, indicating that the Cr^{VI} to Cr^{III} reduction is not completely effective. Unsurprisingly, when the adsorption process is coupled to photo-reduction in UiO-66-NH_2 photoactive sample, UV-Vis spectra of UiO-66-NH_2 after operation show even a higher absorbance of the UV-Vis signals related to the Cr^{III} species, a fact that initially suggest that the chromate anions can be further stabilized as Cr^{III} species upon illumination, as can be observed in the **Figure 4.10**a.

Coupled adsorption/reduction/photo-reductions mechanisms in UiO-66-R materials were also studied by means of electron paramagnetic resonance (EPR) spectroscopy (**Figure 4.9** and **Figure 4.10**b). The different signals associated to Cr^{III} and Cr^{V} species observed in the EPR spectra [40] are described in **Annex A**.

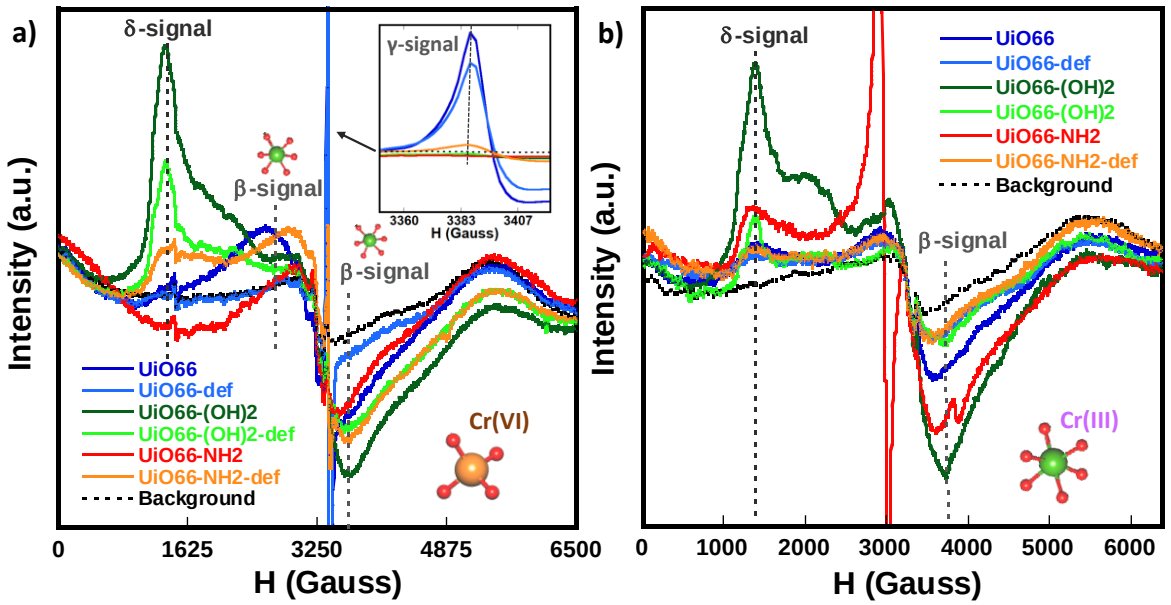

Figure 4.9. (a) EPR spectra of UiO-66-R after Cr^{VI} uptake highlighting the δ and β-signals associated to Cr^{III} species. Inset: Detail of the the 3350 to 3420 Gauss interval of the EPR spectra showing the γ-signal ascribed to Cr^{V} isolated ions. (b) EPR spectra of UiO-66-R after Cr^{III} adsorption.

The results obtained for Cr^{VI} post-adsorption samples are described and depicted in **Figure 4.9**a. It is worthy to note that Cr^{VI} is silent by EPR, but its presence has been previously confirmed by UV-Vis. When comparing the EPR spectra of the samples, it can be confirmed the presence of γ, δ and β signals associated with isolated pentavalent, isolated trivalent and clustered trivalent chromium species. When comparing the absorbance of the EPR signal associated to pentavalent and trivalent chromium, a qualitative estimation of the reduction capacity, dependent on the linker functionalization and/or on the presence of defect points in the crystal structure, can be obtained. UiO-66-NH_2 and UiO-66-$(OH)_2$ compounds exhibit more intense δ-signal and β-signal ascribed to Cr^{III} species, which indicates that the presence of –NH_2 and -OH electron donor groups shifts the post-adsorption chromium equilibrium towards reduced species, such as Cr^{V} and Cr^{III}. Contrarily, EPR spectra of non-functionalized UiO-66 material exhibit only the characteristic γ-signal of transient Cr^{V} ions that, together with the Cr^{VI} species detected by UV-Vis spectroscopy, which indicate a Cr^{VI} and Cr^{V} speciation mixture stabilized within the sorbent after operation. Therefore, the lack of electron donor groups at the UiO-66 framework limits its reductive capacity. In addition, Cr^{VI} to Cr^{III} reduction

is less effective in defective functionalized UiO-66-$(OH)_2$-def and UiO-66-NH_2-def samples, since the absorbance of β and δ-signals ascribed to Cr^{III} is lower.

Moreover, the comparison of EPR spectra of UiO-66-NH_2 after Cr^{VI} adsorption and Cr^{VI} to Cr^{III} photo-reduction experiments, confirms that the concentration of Cr^{V} transient species stabilized within the matrix is significantly reduced after illumination, whilst it is observed an increase of the β and δ-signals associated to Cr^{III} ions. Therefore, upon illumination, the photocatalytic activity of UiO-66-NH_2 displace in more extent the reduction process to Cr^{III} species (**Figure 4.10**b), but still without achieving a complete conversion, since Cr^{V} species are still detected (Inset **Figure 4.10Error! Reference source not found.**b).

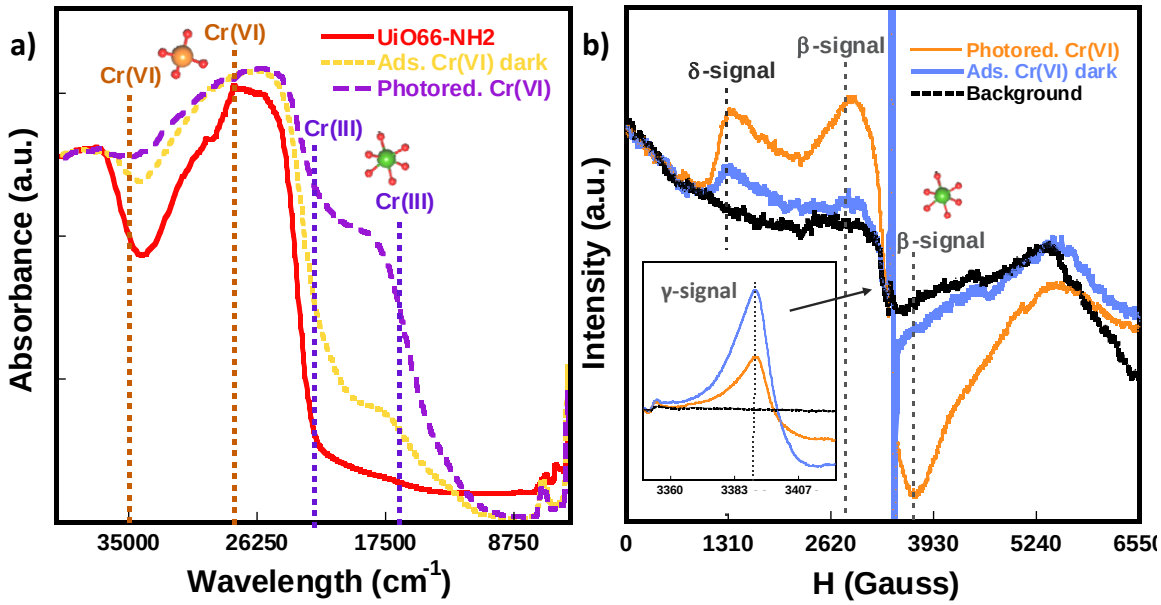

Figure 4.10. (a) UV-Vis spectra of UiO-66-NH_2 before and after Cr^{VI} adsorption and photo-reduction experiments. (b) EPR spectra of UiO-66-NH_2 after Cr^{VI} adsorption and photo-reduction experiments highlighting the δ and β-signals associated to Cr^{III} species. Inset: Detail of the 3200 to 3550 Gauss interval of the EPR spectra showing the γ-signal ascribed to Cr^{V} isolated ions.

4.2.4. Proposed chromium adsorption-reduction coupled mechanisms

As concluded from the results drawn by EPR and UV-Vis, chromate immobilization mechanisms in MOFs go beyond a single adsorption process, since also involve its posterior reduction or photo-reduction to Cr^{III}, together with a last step of Cr^{III} ions clustering. Taking all this into consideration, a simplified model for the adsorption,

chemical reduction and photo-reduction of Cr^{VI} and Cr^{III} species in UiO-66-R materials have been illustrated in **Figure 4.11** and described herein.

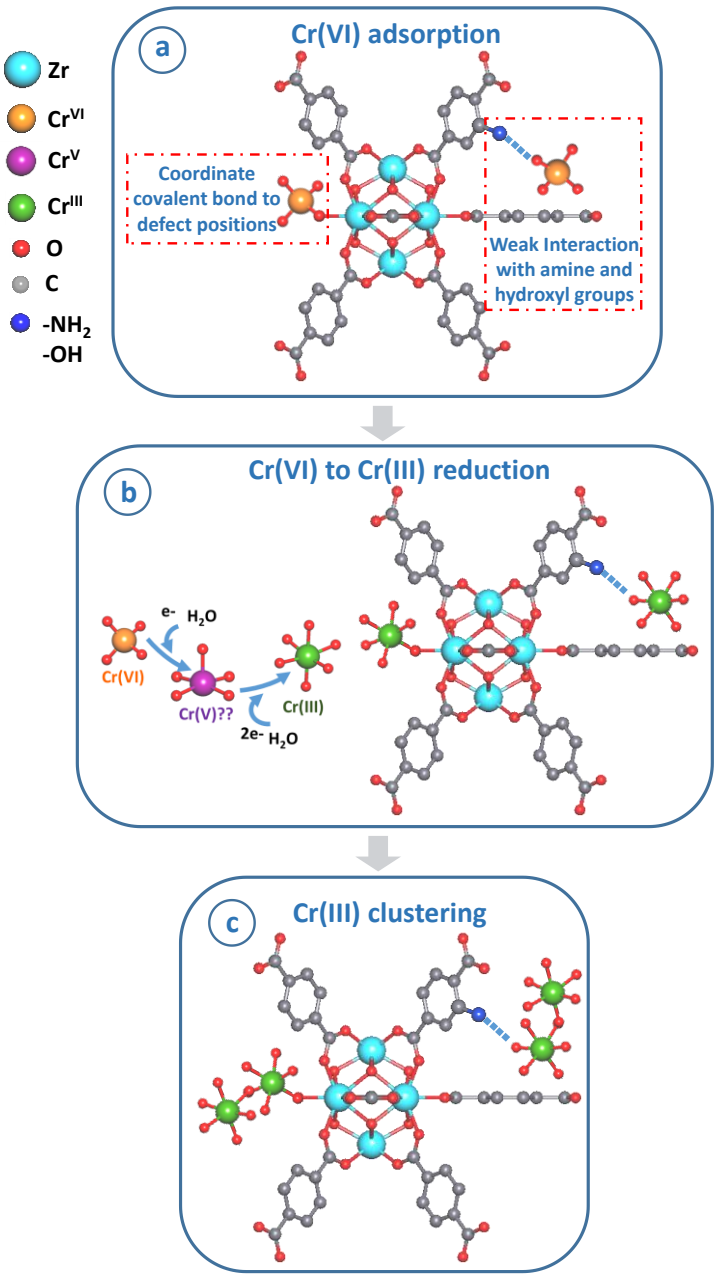

Figure 4.11. Proposed Cr^{VI} adsorption and Cr^{VI} to Cr^{III} reduction mechanisms in UiO-66-R type frameworks, (a) Cr^{VI}→ Cr^{V}→ Cr^{III} reduction at the inorganic clusters, (b) Cr^{VI}→ Cr^{V}→ Cr^{III} reduction at the linkers and (c) Cr^{VI}→ Cr^{V}→ Cr^{III} reduction at the inorganic clusters and the linkers.

Assuming that chromate or dichromate anions establish a coordinate covalent bond with the zirconium clusters after the adsorption stage (**Figure 4.11**a), their posterior transformation to Cr^{V} and Cr^{III} is foreseen to occur through the modification of their coordination sphere (**Figure 4.11**b) [41,42]. Since at acidic conditions (used in this work) a mixture of hydrogen chromate $(HCrO_4)^-$ and dichromate $(Cr_2O_7)^{2-}$ species can be found in similar concentrations, the first chemisorption step can occur indifferently for both species. The possible structural model after the hydrogen chromate chemisorption has been illustrated in **Figure 4.11**a.

Starting from the less complex scenario, in UiO-66 non-functionalized samples, the chromate immobilization it is foreseen to occur through its coordinate covalent bonding to the zirconium clusters (**Figure 4.11**a-left). Afterwards, the Cr^{VI} partial reduction to Cr^{V} transient species can be achieved by an electron transfer process, together with the incorporation of hydroxyl or water molecules to the coordination sphere of chromium pentavalent ions (**Figure 4.11**b). Further, Cr^{V} to Cr^{III} reduction would require from a transformation of the five-coordination environment usually shown by Cr^{V} ions, to a six-coordinated octahedral one usually shown by Cr^{III} oxo-aquo species (**Figure 4.11**b). In the last step, the clustering of Cr^{III} species could occur by a posterior grafting and reduction of chromate species, as it can be observed in the schematic representation in **Figure 4.11**c. Assuming that a dichromate anion is adsorbed at the first stage of the process, its reduction to Cr^{III} would lead also to clustered Cr^{III} ions stabilized within the UiO-66 framework.

Moreover, the presence of hydroxyl or amine electron donor groups at the organic linkers of UiO-66-R materials enhances the chromium adsorption and vary the final Cr^{III} clustering degree. Indeed, it is reasonable to assume that chromate and dichromate adsorption takes place through hydrogen bonding or electrostatic interactions at these positions of the UiO-66-R structures (**Figure 4.11**a-right). Afterwards, chromium reduction would evolve similarly than for the chromate anions chemisorbed at the inorganic clusters (**Figure 4.11**b-c).

Direct adsorption of Cr^{III} ions is foreseen to occur through the establishment of weak host-guess electrostatic and/or hydrogen-bonding interactions. The results drawn by EPR spectroscopy confirm the presence of isolated and clustered Cr^{III} species after the adsorption experiments for all the samples. Nevertheless, the ratio between the isolated and clustered Cr^{III} ions varies depending on the defect degree or functionalization motifs of the UiO-66-R compounds (**Figure 4.9**b). Considering the Cr^{III} speciation equilibrium in solution, it is not surprising that UiO-66-R materials can directly adsorb not only monomeric hexa-aquo cationic species ($(Cr(H_2O)_6)^{3+}$) from solution, but also the dimeric ($(Cr_2(H_2O)_8(OH)_4)^{4+}$) and trimeric ($(Cr_3(H_2O)_9(OH)_4)^{5+}$) clustered species.

4.3. Performance of the magnetoelastic resonators in liquid media

Before performing the HMs sensing experiments, the performance of previously studied resonators in a liquid media should be analyzed. The comparison between the air and water resonant frequency profiles for the rectangular and rhombic Metglas sensors (**Figure *4.12***) clearly states that the damping effect of the water media has a detrimental effect on the quality and intensity of the resonant signal.

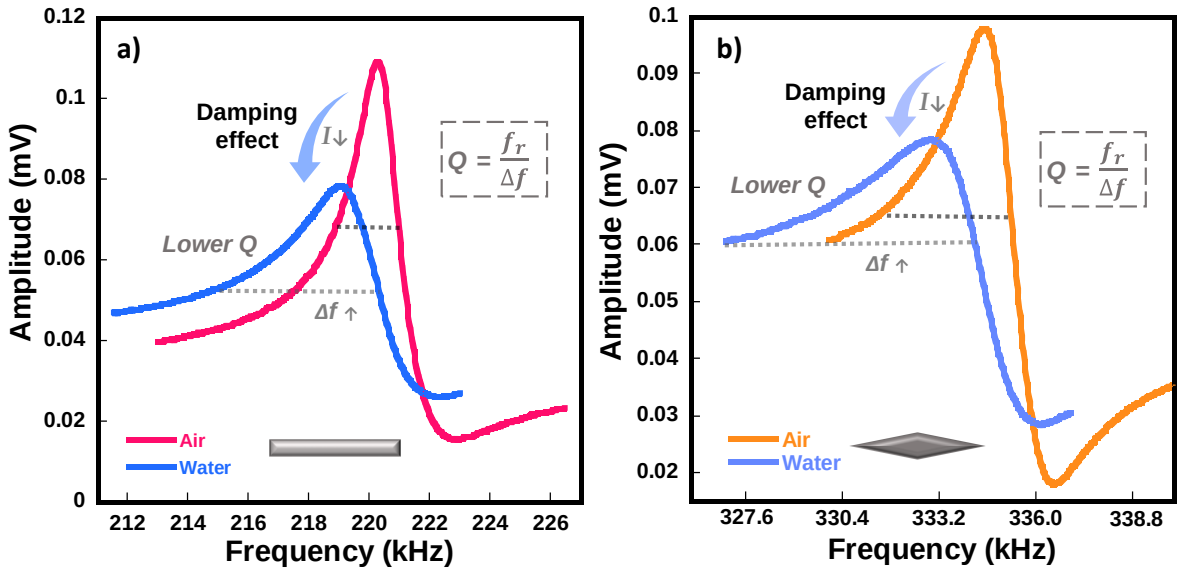

Figure 4.12. Damping effect observed when immersed Metglas magnetoelastic resonators with: (a) Rectangular and (b) rhombic shapes in water.

Further experiments were performed to evaluate the effect of the liquid density and viscosity on the magnetoelastic response of the studied platforms. First of all, the

resonance frequency of the 10mm length rectangular and rhombic shaped resonators of Metglas 2826MB was measured in different water/glycerol mixtures in order to determine the dependence of their resonance frequency with the liquid density/viscosity. Results are shown in **Figure 4.13**.

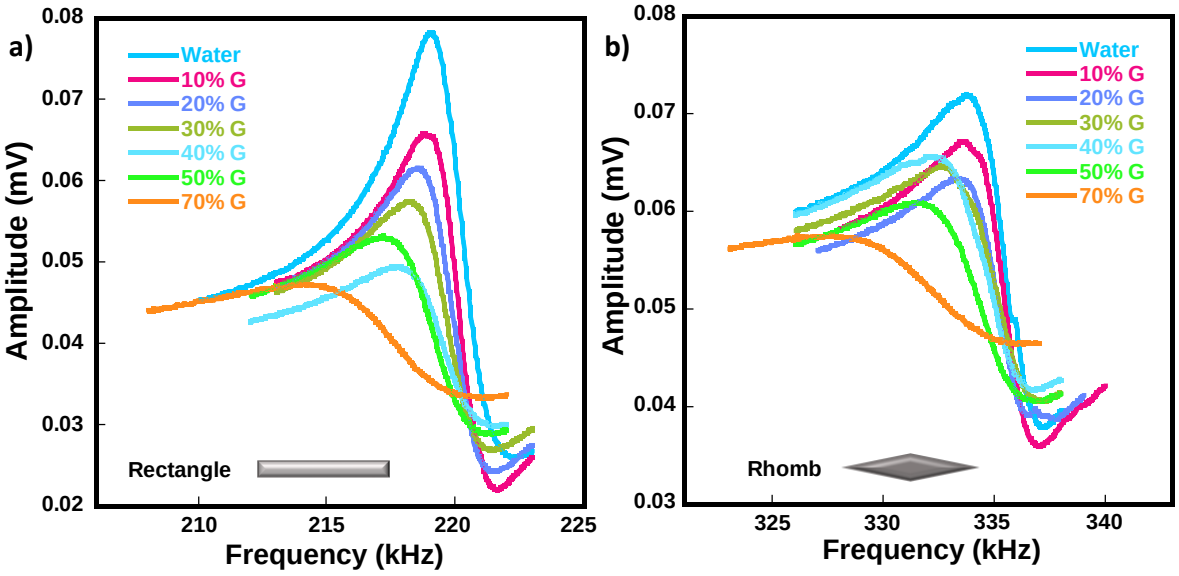

Figure 4.13. Resonance frequency curves measured at different % wt of glycerol in water for the: (a) Rectangular and (b) rhombic Metglas resonators.

As could be observed, there is a significant dependence on the resonance frequency as well as on the signal amplitude with the glycerol percentage, that is, with the increase of the density/viscosity of the media. Indeed, the variation of the normalized frequency shift as a function of the glycerol concentration (**Figure 4.14**) points out that rhombic geometry is also more sensitive to viscosity/density changes.

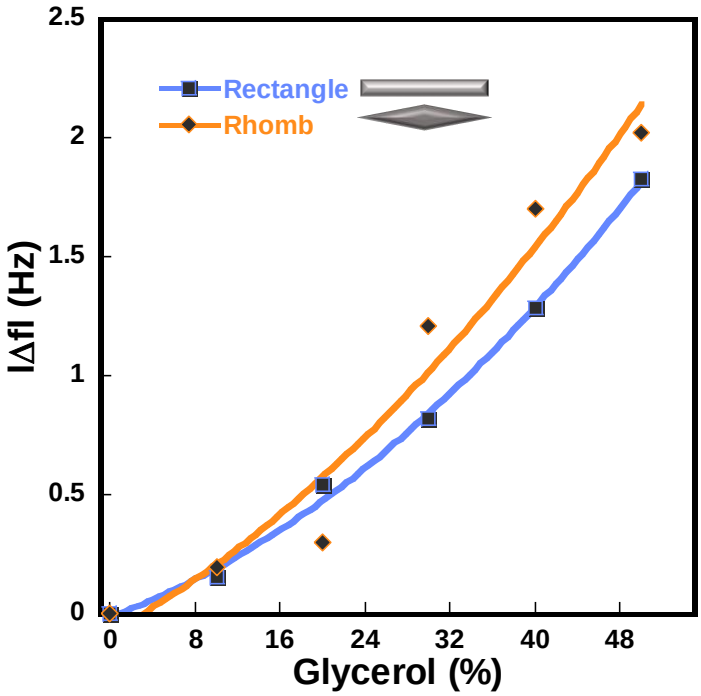

Figure 4.14. Resonance frequency shift measured for the rectangular and rhombic resonators as function of the % wt of glycerol.

The resonator frequency and amplitude dependence on the media characteristics open a key question that needs to be answered in the frame of this thesis work: to which extent the damping effect could reduce the sensitivity of the system against the sensing of pollutants in aqueous media? Taking into account the characteristics of our resonator platforms, rhombic like geometry has been selected as the one to be functionalized and applied in liquid media to detect chromium.

4.4. Heavy metals sensing experiments

As stated before, previously studies working on the detection of HMs with magnetoelastic sensors are based on the precipitation of different compounds in the presence of the target HMs. Nevertheless, there is a gap of research on the detection of HMs by their direct adsorption in the magnetoelastic sensor active layer. Thus, it would be very useful to develop a sensing device which allows for real-time monitoring of HMs adsorption in the active layer.

On that context, the performance of a bare Metglas resonator in chromium and water solutions was first studied in order to evaluate a possible variation of the resonance frequency in the presence of HMs. The resonance frequency curves were measured in

water and in 200 ppm Cr^{VI} and Cr^{III} solutions. Results are shown in **Figure 4.15**. The resonance curve measured in air has also been plotted for sake of comparison.

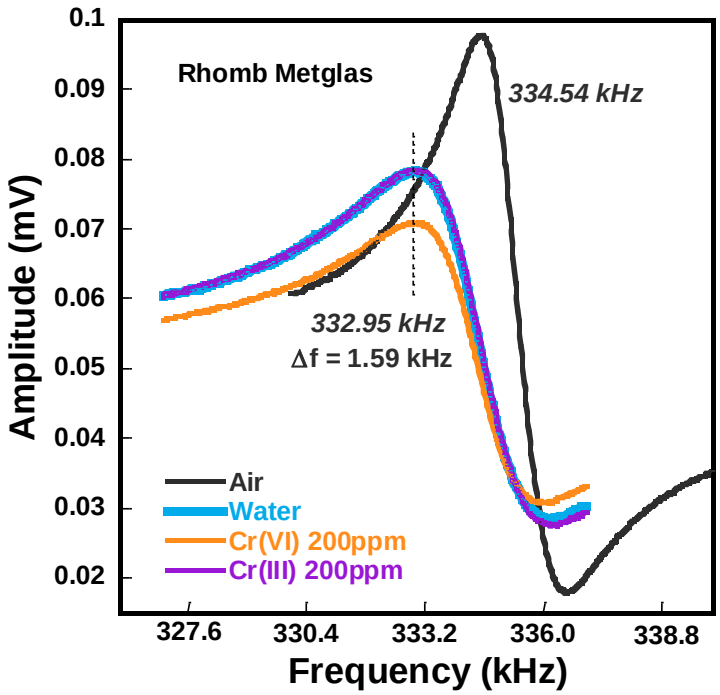

Figure 4.15. Resonance frequency curves measured in water and in Cr^{VI} and Cr^{III} solutions of 200 ppm for a Metglas rhombic resonator of 10 mm in length.

The introduction of the magnetoelastic resonator in water generates a significant decrease on the resonance frequency (of around 1.59 kHz) and also a decrease in the signal amplitude due to the damping effect caused by the liquid media [43]. Moreover, a reduction on the signal quality factor is also observed on the broadening of the resonance peak, which is also a consequence of the damping effect. The comparison between the resonance frequency curves measured in water and in the chromium solutions points that the resonance frequency is not affected by the presence of chromium, and hence, the lack of capacity of the bare resonator to capture or interact with it. The small differences in the signal amplitude are related to the position of the resonator in the vial.

Once analyzed the response of the bare Metglas resonator in water and chromium solutions, the UiO-66-NH_2 material was integrated into the rhombic shaped magnetoelastic resonators by spray coating. This will endow the resonator platform of an active layer prompt to adsorb chromium from water. The mass of the UiO-66-NH_2 active layer was quantified to be 130 micrograms.

Thus, the response of a rhombic Metglas resonator functionalized with the UiO-66-NH_2 MOF by the spraying technique in response to the presence of Cr^{VI} (100 ppm) in a water solution was investigated. The chromium (Cr^{VI}) sensing experiment was performed in static conditions as follows (Scheme **Figure 4.16**a): i) The resonance frequency of the Metglas/UiO-66-NH_2 was initially measured in air, ii) the ribbon was immersed in water and the frequency variation was measured during 20 minutes, iii) the sample was dried in the oven and frequency was measured in air again, iv) the ribbon was immersed in a 100 ppm Cr^{VI} solution during 20 minutes while monitoring the frequency shift of the system, and v) the Metglas/UiO-66-NH_2 system was dried and the frequency remeasured in air. A scheme of the experiment, together with the obtained results, are shown in **Figure 4.16**.

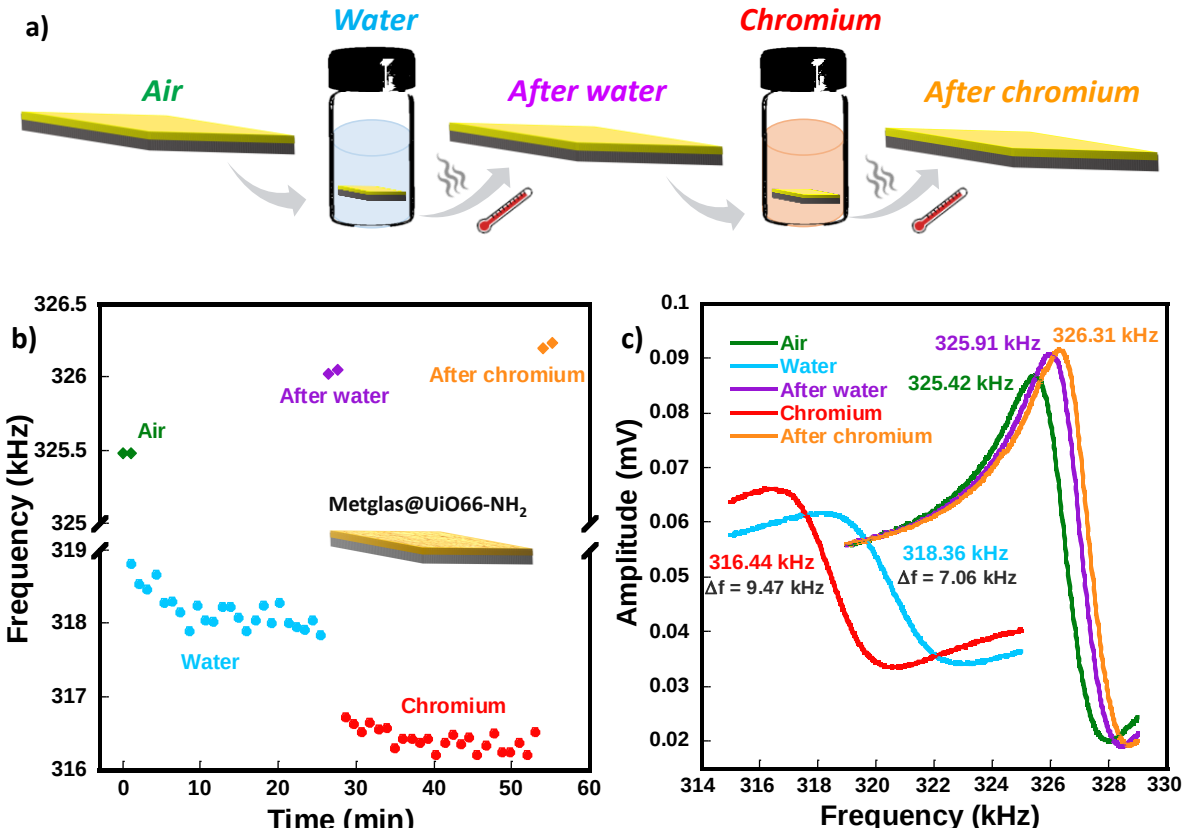

Figure 4.16. (a) Scheme of the points at which the resonance frequency has been measured. (b-c) Chromium sensing experiments performed for a rhombic Metglas resonator functionalized with the UiO-66-NH_2 MOF by the spraying technique. (b) Variation of the resonance frequency as a function of time. (c) Resonance frequency curves measured in the different zones of (b).

Two general conclusions can be drawn from the obtained results. First of all, a reduction in the resonance quality factor is observed on the functionalized resonator (**Figure 4.16**c) if compared with the bare one (**Figure 4.15**). This is related to the added damping effect caused by the MOF active layer. Secondly, a decrease of the resonance frequency when immersed the sensor in water is observed, such as it is observed with the non-functionalized magnetoelastic resonator. However, if the effect of the damping in the bare resonator leads to a shift in the resonance frequency of around 1.6 kHz both for the water and the chromium solutions (**Figure 4.15**), in the case of the functionalized resonator, the frequency shift is four-fold (7 kHz) and six-fold (9.5 kHz) higher when immersed in water and in the Cr^{VI} solution, respectively. It could be also appreciated that when immersed Metglas/UiO-66-NH_2 sensor in water or in the chromium solution, the frequency follows a decreasing trend over time (**Figure 4.16**b). The differences between the frequency shifts measured for the bare resonator and the functionalized resonator are caused by the water Cr^{VI} adsorption processes in the MOF active layer. These adsorption processes result in different mass gains on the resonators system. In fact, the chromium adsorption inside the MOF active layer results in a higher mass gain when compared with the single water adsorption, which in turn results in a higher frequency shift (around 2 kHz). These variations demonstrate the sensitive of Metglas/UiO-66-NH_2 system to the presence of chromate anions.

Some limitation of the Metglas/UiO-66-NH_2 sensor for water pollutant detection can be found, mainly derived from the weak adhesion of the MOF layer. In fact, it is worthy to note that after removing the Metglas/UiO-66-NH_2 sensor from water, the resonant frequency is higher than it was before immersing it in water (around 0.5 kHz higher). Resonance frequency increases even more (another 0.5 kHz) after the second immersion in the Cr^{VI} liquid media. This frequency variation is a result of a lower mass load at the resonator surface, probably related with a MOF peeling of the active layer when immersed the sensor in water.

Thus, there is still a room of improvement in terms of the selectivity and adsorption capacity of the active layer to increase the sensitivity response of Metglas based systems to chromium concentration values closer to the current legal thresholds, as well as in term of integration of MOF active layers on Metglas resonator in order to improve the adhesion between the two components of the system.

4.5. Summary and conclusions

This chapter explores the potentials of UiO-66-R (R= -H, -NH_2, -OH) Metal-Organic Frameworks as active materials to capture, photo/reduce and sensing of Cr^{VI} to Cr^{III} in water environments.

The incorporation of –OH and –NH_2 electron donor functionalities combined with the generation of linker defective positions at UiO-66 framework has resulted the most favourable MOF chemical encoding approach to enhance the capture of chromate anions from water.

In parallel, the presence of amino and hydroxyl groups is also key to enhance the Cr^{III} adsorption capacity of UiO-66 based materials, but, on the contrary to Cr^{VI}, the induction of linker defects within the UiO-66-R frameworks is detrimental in terms of their Cr^{III} adsorption affinity and capacity.

Moreover, a combined UV-Vis and EPR spectroscopy analysis has allowed determining the chromium speciation inside the sorbents after operation. The analysis of the chromium speciation after Cr^{VI} adsorption and photo-reduction experiments points out that UiO-66-R materials are able to couple the capture of Cr^{VI} to its chemical and photo-reduction to Cr^{III} species. Hydroxyl and amine functional groups endow the UiO-66 with the best chemical and photo-reduction capacities in comparison to the non-functionalized framework.

The UV-Vis and EPR combined methodology can be easily extended to other Cr^{VI} MOF sorbents and photo-catalysts in order to quantitatively assess their Cr^{VI} to Cr^{III} reductive or photo-reductive capacity.

Finally, the dependence of the magnetoelastic resonator's response with rectangular and rhombic geometries when immersed in liquid media with different viscosities has been studied. Liquid media induces a significant attenuation of the magnetoelastic signal quality and intensity due to the damping effect, but the resonators, especially the rhombic shaped one, still exhibit a high mass and viscosity sensitivities.

UiO-66-NH_2 /rhombic Metglas resonator has been tested in the wireless detection of 100 ppm chromium solution, demonstrating that it is possible to record a significant frequency variation in response to the presence of chromium. Nevertheless, it is key to

improve the MOF layer attachment to avoid partial MOF peeling from the magnetic resonator surface.

4.6. References

1. Malato, S., Fernández-Ibáñez, P., Maldonado, M. I., Blanco, J., & Gernjak, W. Decontamination and disinfection of water by solar photocatalysis: Recent overview and trends. *Catal. Today* **147**, 1–59 (2009).

2. Azimi, A., Azari, A., Rezakazemi, M. & Ansarpour, M. Removal of heavy metals from industrial wastewaters: A review. *ChemBioEng Rev.* **4**, 37–59 (2017).

3. Sereshti, H., Vasheghani Farahani, M. & Baghdadi, M. Trace determination of chromium(VI) in environmental water samples using innovative thermally reduced graphene (TRG) modified SiO2 adsorbent for solid phase extraction and UV-Vis spectrophotometry. *Talanta* **146**, 662–669 (2016).

4. Saadaoui, E., Ghazel, N., Ben Romdhane, C. & Massoudi, N. Phosphogypsum: potential uses and problems – a review. *Int. J. Environ. Stud.* **74**, 558–567 (2017).

5. Ali, H., Khan, E. & Ilahi, I. Environmental chemistry and ecotoxicology of hazardous heavy metals: Environmental persistence, toxicity, and bioaccumulation. *J. Chem.* **2019**, (2019).

6. Czikkely, M., Neubauer, E., Fekete, I., Ymeri, P. & Fogarassy, C. Review of heavy metal adsorption processes by several organic matters from wastewaters. *Water* **10**, 1–15 (2018).

7. Eddaif, L., Shaban, A. & Telegdi, J. Sensitive detection of heavy metals ions based on the calixarene derivatives-modified piezoelectric resonators: A review. *Int. J. Environ. Anal. Chem.* **99**, 824–853 (2019).

8. Aragay, G., Pons, J.& Merkoçi, A. Recent trends in macro-, micro-, and nanomaterial-based tools and strategies for heavy-metal detection. *Chem. Rev.* **111**, 3433–3458 (2011).

9. Zhao, Z., Liao, L., Xiao, X., Du, N. & Lin, Y. Wireless sensing determination of uranium(IV) based on its inhibitory effect on a catalytic precipitation reaction. *J. Radioanal. Nucl. Chem.* **289**, 893–898 (2011).

10. Zhao, Z., Liao, L., Xiao, X., Du, N. & Lin, Y. Determination of uranium in water based on

enzyme inhibition using a wireless magnetoelastic sensor. *Int. J. Environ. Anal. Chem.* **93**, 613–622 (2013).

11. Huang, Y.Q., Yin, J.C., Wang, Y. S., Xiao, X. L., Zhou, B., Xue, J. H., Tang, X., Wang, X. F., Zhu, Y. F., & Chen, S. H. Streptavidin and gold nanoparticles-based dual signal amplification for sensitive magnetoelastic sensing of mercury using a specific aptamer probe. *Sensors Actuators, B Chem.* **235**, 507–514 (2016).

12. Guo, X., Sang, S., Jian, A., Gao, S., Duan, Q., Ji, J., Zhang, Q., & Zhang, W. A bovine serum albumin-coated magnetoelastic biosensor for the wireless detection of heavy metal ions. *Sensors Actuators, B Chem.* **256**, 318–324 (2018).

13. Buzek, D., Demel, J., & Lang, K. Zirconium metal—organic framework UiO-66: Stability in an aqueous environment and its relevance for organophosphate degradation. *Inorg. Chem.* **57**, 14290–14297 (2018).

14. Feng, M., Zhang, P., Zhou, H. C. & Sharma, V. K. Water-stable metal-organic frameworks for aqueous removal of heavy metals and radionuclides: A review. *Chemosphere* **209**, 783–800 (2018).

15. Paulina A. Kobielska, Ashlee J. Howarth, Omar K. Farha, S. N. Metal–organic frameworks for heavy metal removal from water. *Coord. Chem. Rev.* **358**, 92–107 (2018).

16. Maleki, A., Hayati, B., Naghizadeh, M. & Joo, S. W. Adsorption of hexavalent chromium by metal organic frameworks from aqueous solution. *J. Ind. Eng. Chem.* **28**, 211–216 (2015).

17. Du, X. D., Yi, X. H., Wang, P., Zheng, W., Deng, J., & Wang, C. C. Robust photocatalytic reduction of Cr(VI) on UiO-66-NH2(Zr/Hf) metal-organic framework membrane under sunlight irradiation. *Chem. Eng. J.* **356**, 393–399 (2019).

18. Li, X., Xu, H., Kong, F. & Wang, R. A cationic metal-organic framework consisting of nanoscale cages: Capture, separation, and luminescent probing of Cr2O72- through a single-crystal to single-crystal process. *Angew. Chemie Int. Ed.* **52**, 13769–13773 (2013).

19. Ding, B., Huo, J. Z., Liu, Y. Y., Wang, X., Su, X., Wu, X. X., Zhu, Z. Z., & Xia, J. Triazole based Ag coordination clusters: synthesis, structural diversity and anion exchange properties. *RSC Adv.* **5**, 83415–83426 (2015).

20. Fu, H. R., Xu, Z. X. & Zhang, J. Water-stable metal-organic frameworks for fast and high dichromate trapping via single-crystal-to-single-crystal ion exchange. *Chem. Mater.* **27**, 205–210 (2015).

21. Ding, B., Guo, C., Liu, X., Cheng, Y., Wu, X., & Su, M. A unique multi-functional cationic luminescent metal – organic nanotube for highly sensitive detection of dichromate and selective high capacity adsorption of Congo red. *RSC Adv.* **6**, 33888–33900 (2016).

22. Desai, A. V., Manna, B., Karmakar, A., Sahu, A., & Ghosh, S. K. A water-stable cationic metal–organic framework as a dual adsorbent of oxoanion pollutants. *Angew. Chemie* **128**, 7811–7815 (2016).

23. Wang, C. C., Du, X. D., Li, J., Guo, X. X., Wang, P., & Zhang, J. Photocatalytic Cr(VI) reduction in metal-organic frameworks: A mini-review. *Appl. Catal. B Environ.* **193**, 198–216 (2016).

24. Allen, S. J., Mckay, G. & Porter, J. F. Adsorption isotherm models for basic dye adsorption by peat in single and binary component systems. *J. Colloid Interface Sci.* **280**, 322–333 (2004).

25. State, K., State, E. & State, K. Langmuir, Freundlich, Temkin and Dubinin – Radushkevich isotherms studies of equilibrium sorption of Zn^{2+} unto phosphoric acid modified rice husk. **3**, 38–45 (2012).

26. Chowdhury, S., Mishra, R., Saha, P. & Kushwaha, P. Adsorption thermodynamics, kinetics and isosteric heat of adsorption of malachite green onto chemically modified rice husk. *Desalination* **265**, 159–168 (2011).

27. Li, J., Wang, X., Zhao, G., Chen, C., Chai, Z., Alsaedi, A., Hayat, T., & Wang, X. Metal-organic framework-based materials: Superior adsorbents for the capture of toxic and radioactive metal ions. *Chem. Soc. Rev.* **47**, 2322–2356 (2018).

28. González, J. A., Villanueva, M. E., Piehl, L. L. & Copello, G. J. Development of a chitin/graphene oxide hybrid composite for the removal of pollutant dyes: Adsorption and desorption study. *Chem. Eng. J.* **280**, 41–48 (2015).

29. Torres, D. I., Lazaro-Martínez, J. M., Copello, G. J. & dall Orto, V. C. Single step synthesis of a polyhydroxy ether and its optimization to adsorption of a textile dye. *J. Environ. Chem. Eng.* 103416 (2019). doi:10.1016/j.jece.2019.103416

30. González, J. A., Villanueva, M. E., Peralta Ramos, M. L., Pérez, C. J., Piehl, L. L., & Copello, G. J. Chitin based hybrid composites reinforced with graphene derivatives: A nanoscale study. *RSC Adv.* **5**, 63813–63820 (2015).

31. Peralta Ramos, M. L., González, J. A., Albornoz, S. G., Pérez, C. J., Villanueva, M. E., Giorgieri, S. A., & Copello, G. J. Chitin hydrogel reinforced with TiO2 nanoparticles as an arsenic sorbent. *Chem. Eng. J.* **285**, 581–587 (2016).

32. Bibi, R., Shen, Q., Wei, L., Hao, D., Li, N., & Zhou, J. Hybrid BiOBr/UiO-66-NH2 composite with enhanced visible-light driven photocatalytic activity toward RhB dye degradation. *RSC Adv.* **8**, 2048–2058 (2018).

33. Feng, Y., Chen, Q., Cao, M., Ling, N. & Yao, J. Defect-tailoring and titanium substitution in metal-organic framework UiO-66-NH2 for the photocatalytic degradation of Cr(VI) to Cr(III). *ACS Appl. Nano Mater.* **2**, 5973–5980 (2019).

34. Zhu, K., Chen, C., Xu, H., Gao, Y., Tan, X., Alsaedi, A., & Hayat, T. Cr(VI) reduction and immobilization by core-double-shell structured magnetic polydopamine@zeolitic idazolate frameworks-8 microspheres. *ACS Sustain. Chem. Eng.* **5**, 6795–6802 (2017).

35. Jaber, M., Ribot, F., Binet, L., Briois, V., Cassaignon, S., Rao, K. J., Livage, J. & Steunou, N. Ex situ X-ray diffraction, X-ray absorption near edge structure, electron spin resonance, and transmission electron microscopy study of the hydrothermal crystallization of vanadium oxide nanotubes: An insight into the mechanism of formation. *J. Phys. Chem. C* **116**, 25126–25136 (2012).

36. Valenzano, L., Civalleri, B., Chavan, S., Bordiga, S., Nilsen, M. H., Jakobsen, S., Lillerud, K. P., & Lamberti, C. Disclosing the complex structure of UiO-66 metal organic framework: A synergic combination of experiment and theory. *Chem. Mater.* **23**, 1700–1718 (2011).

37. Chen, L., Bai, Z., Zhu, L., Zhang, L., Cai, Y., Li, Y., Liu, W., Wang, Y., Chen, L., Diwu, J., Wang, J., Chai, Z., & Wang, S. Ultrafast and efficient extraction of uranium from seawater using an amidoxime appended metal-organic framework. *ACS Appl. Mater. Interfaces* **9**, 32446–32451 (2017).

38. Chavan, S., Vitillo, J. G., Uddin, M. J., Bonino, F., Lamberti, C., Groppo, E., Lillerud K-P., & B. S. Functionalization of UiO-66 metal-organic framework and highly cross-linked polystyrene with $Cr(CO)_3$: In situ formation, stability, and photoreactivity. *Chem. Mater.* **22**, 4602–4611 (2010).

39. Węgrzyniak, A., Rokicińska, A., Hędrzak, E., Michorczyk, B., Zeńczak-Tomera, K., Kuśtrowski, P., & Michorczyk, P. High-performance Cr-Zr-O and Cr-Zr-K-O catalysts prepared by nanocasting for dehydrogenation of propane to propene. *Catal. Sci. Technol.* **7**, 6059–6068 (2017).

40. Weckhuysen, B. M., Schoonheydt, R. A., Mabbs, F. E. & Collison, D. Electron paramagnetic resonance of heterogeneous chromium catalysts. *J. Chem. Soc. - Faraday Trans.* **92**, 2431–2436 (1996).

41. Rai, D., Sass, B. M. & Moore, D. A. Chromium(III) hydrolysis constants and solubility of chromium(III) hydroxide. *Inorg. Chem.* **26**, 345–349 (1987).

42. Weckhuysen, B. M., Ramachandra Rao, R., Pelgrims, J., Schoonheydt, R. A., Bodart, P., Debras, G., Collart, O., Van Der Voort, P. & Vansant, E. F. Synthesis, spectroscopy and catalysis of [Cr(acac)3] complexes grafted onto MCM-41 materials: Formation of polyethylene nanofibres within mesoporous crystalline aluminosilicates. *Chem. - A Eur. J.* **6**, 2960–2970 (2000).

43. Stoyanov, P. G., & Grimes, C. A. A remote query magnetostrictive viscosity sensor. *Sensors Actuators, A Phys.* **80**, 8–14 (2000).


chapter
5

Magnetoelastic/MOF sensors for toluene detection

Este capítulo recoge la adsorción y detección de compuestos orgánicos volátiles (VOCs) mediante el uso de sensores magnetoelásticos funcionalizados con MOFs. Inicialmente, se describe el montaje de un sistema de circulación continua de gases con concentración controlada de VOCs, necesario para realizar los experimentos de detección de los mismos mediante los sensores fabricados. Por otro lado, se recogen los experimentos de detección de tolueno realizados con resonadores romboédricos funcionalizados con UiO-66-NH_2, mediante la técnica de sprayado. En particular, una vez determinadas la sensibilidad, velocidad de detección y ciclabilidad del sensor, se ha investigado, en mayor profundidad, el efecto de la masa de capa activa de MOF en las propiedades de detección de tolueno del sistema. Finalmente, la selectividad del sensor frente a diferentes gases también se analiza.

Content

*** Publications in which this chapter is based.**

Some of the results exposed in this chapter have been published in an indexed scientific publication: **"Rhombic-magnetoelastic/metal-organic framework functionalized resonators for high sensitive toluene detection"**, *Journal of Materials Chemistry C (Q1), 2020, DOI:* doi.org/10.1039/D0TC02612C *;* as well as in some of the conferences presented in Annex C (Results dissemination).

5.1. Introduction

Air pollution is one of the most concerning environmental issues of the XXI century society. A growing number of contaminants derived from anthropogenic industrial activities are ejected into the atmosphere every day causing a broad environmental impact and the consequences global warming or health derived problems, just to mention two of the most important effects of altering the atmospheric composition. Within the complex problematic of atmospheric pollution, the presence of significant levels of Volatile Organic Compounds (VOCs) in the atmosphere is particularly alarming, since VOCs combine their volatility with high toxicity and deep health hazards (e.g. *respiratory diseases or cancer*) even upon short expositions to them at very low concentrations [1,2]. Despite their potential health effects, VOCs are usually found at outdoor and indoor environments as a result of their emission from industrial processes, paints, building materials or natural events (*e.g. volcanic eruptions*), among others [3–6]. In particular, toluene is among the most dangerous VOCs. Despite the well-known adverse and strong effects of exposition to toluene on the nervous system (*e.g. brain function disorder, vision or hearing disfunction*) [7], its use as raw material in the manufacturing industry is broadly extended. Thus, it is critical first to limit VOCs emissions, and second, to develop monitoring systems able to track their concentration in a continuous and wireless way in order to implement mitigation measures if VOCs concentration exceeds the legal limits.

Traditional experimental methodologies employed for VOCs detection or quantification are based on complex, high cost and time-consuming techniques, such as gas chromatography or adsorption spectroscopies [8,9]. In addition to this, it is usually required highly specialized staff to manage all the VOC monitoring process, from the gas sampling, its treatment and conditioning, and the later quantification. For those reasons, the scientific community has paid special attention to the development of miniaturized devices able to provide an easy applicable VOCs sensing technology, that could exhibit a faster response at a lower cost than classic procedures [10–12]. In this regard, magnetoelastic sensors based on zeolites and polymers type active layers have been already employed for the wireless detection of different VOCs but, as far as we know, none of them has been applied for the specific case of toluene. Among these studies, the Metglas/zeolites-based resonator for VOCs detection is of particular interest. Different zeolites with varied pore window and chemistry (FAU, LTA, MFI and b-oriented MFI

types) were directly grown on the magnetoelastic resonators surface, and afterwards, the sensor's response was tested over six different but similar aromatic VOCs (such benzene or xylene) [13]. Results showed that the sensitivity is highly dependent on the zeolite type, the oriented or random disposition of the zeolite´s crystals at the resonator surface, as well as on the sensed VOC. Indeed, randomly oriented MFI zeolite active layer presents the highest sensitivity to n-hexane, and FAU zeolite-based resonators exhibit the lower detection limit for o-xylene.

The sensing response of magnetoelastic resonators functionalized with Bayhydrol-110 polymer as the recognition layer of VOCs (e.g. hexane or benzene) has also been reported [14]. Metglas/Bayhydrol-110 sensor was tested for eight different VOCs at varied concentrations in order to analyze the sensor sensitivity and crossed selectivity. This polymeric based resonator shows very low response to hexane and higher sensitivity to xylene (at least 10 times higher than for the other VOCs).

Considering the few works dealing with VOCs sensing based on magnetoelastic resonators technology reported up to date, it seems clear that the adsorption capacity of the active layer over the target analyte is key to improve the sensing response of the system. In this regard, zeolites and polymers exhibit a limited porosity, total surface area and chemical specificity to selectively adsorb a significant amount of a specific VOC when it is present at very low concentrations. These weaknesses of polymer and zeolites-based resonators ultimately limits the mass gain in the magnetoelastic sensor, reducing its sensitivity threshold.

In this context, Metal-Organic Frameworks (MOFs) result highly appealing materials to be integrated into magnetoelastic resonators systems as active layers, because of their appreciably higher adsorption capacity and selectivity over VOCs than traditional sorbents [15]. As described in deep at the introduction chapter of this thesis work, MOFs have been already and widely investigated for the adsorption of VOCs and their mass, optic and electric based sensing, with very promising results [16,17]. Different factors can shape the VOC adsorption capacity of MOFs, such as the MOF crystal structure, pore size/window, hydrophobicity, or the presence of functional groups at the MOF framework prompt to interact with VOC molecules. In particular, several studies has investigated the capacity, affinity and adsorption/desorption stability in continuous flux mode over VOCs of some of the most iconic MOFs reported so far. In this part, only the

toluene adsorption performance of MOFs in continuous flux mode has been considered at the time to select the best of the reported MOFs to later develop the Metglas/MOF resonator systems. Other investigations have also determined the maximum vapour adsorption capacity for different MOFs over toluene, but the experimental conditions of these static adsorption experiments (*i.e. closed chamber, high VOCs relative vapour pressures*) differ significantly of these that are applied in sensing experiments (*i.e. open circuit, air flux with low VOCs concentration*). The obtained adsorption capacities for the different tested samples are shown in **Figure 5.1**. The first conclusion drawn from the data summarized in **Figure 5.1**, is that the toluene adsorption capacity obtained from continuous flux experiments is not directly related with the surface area of the MOF, but with its pore's characteristics (i.e. size and functionality). Indeed, MOFs with moderate surface areas and pores of small to medium sizes, such as UiO-66 and ZIF-67 exceeded by much the toluene adsorption capacity of mesoporous MIL-101 or zinc terephthalate MOF-5. Functional groups decorating the pore surface of the MOFs also play a key role within the adsorption process, as revealed by the significant increase on the toluene adsorption capacity of amino functionalized UiO-66-NH_2 in comparison to UiO-66. Indeed, UiO-66-NH_2 presents the highest toluene adsorption capacity (252 mg·g^{-1}) among all the tested materials, which supposes an overperformance of more than an 820% compared with the traditionally used 4A zeolite (*30.7 mg·g^{-1}*) [18]. UiO-66-NH_2 also showed the most stable toluene adsorption capacity over cycling, contrary to other MOFs that exhibit a marked decrease on their performance after the first cycle. Moreover, a recent study has demonstrated that the modulation of the linkers defects density in UiO-66-NH_2 structure is also beneficial to further enhance its toluene adsorption capacity [19]. Thus, all the obtained results point that the UiO-66-NH_2 is the most promising material for high toluene adsorption, but more importantly, that the toluene adsorption, when the toluene

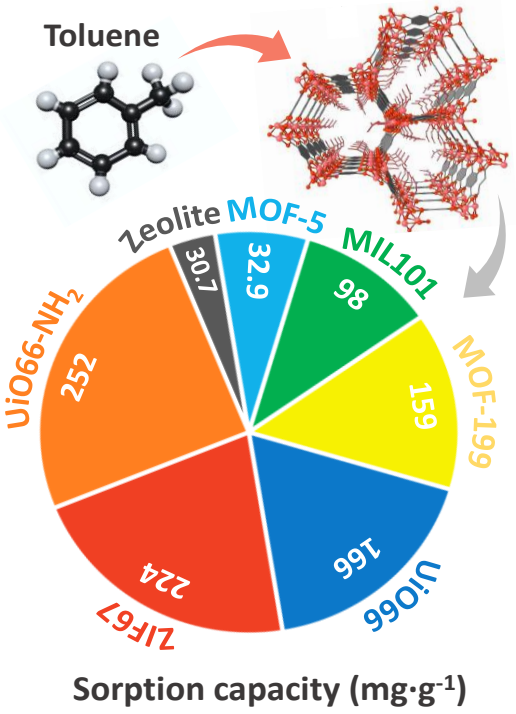

Figure 5.1. Toluene adsorption capacities measured for different MOF samples [18].

is diluted in a continuously flowing air matrix, is mainly governed by the MOF to toluene association affinity and not by the total volumetric capacity that the MOF has to storage toluene at high vapour pressure conditions.

Bearing all these considerations in mind, the general purpose of this chapter is to test the performance of highly sensitive rhombic magnetoelastic resonators functionalized with UiO-66-NH_2 for toluene sensing, as a case study to identify the strengths and weaknesses of magnetoelastic MOF based sensors to monitor hazardous gaseous chemicals The sensitivity, cyclability, reproducibility and detection limits of the Metglas/UiO-66-NH_2 sensing system over toluene were evaluated. In particular, sensors with different masses of the UiO-66-NH_2 active layer have been fabricated by spray coating in order to evaluate the effect of this parameter on the toluene sensing response of our system. Finally, and based on the obtained results, some future perspectives to further improve the Metglas/MOF technology have been proposed.

5.2. VOCs chamber set-up

In order to perform the VOCs sensing experiments, the design and assembly of a new gas chamber system able to control the circulation of a VOCs air flux with a known concentration is necessary. The assembly of the VOCs circulation system has been key, not only to achieve the objectives marked by this thesis, but to open the possibility within the BCMaterials to study and implement other gas sensing systems beyond the magnetoelastic technology. This is the case of the work developed by E. Fernández and co-workers on capacitive sensor based on Metal-Organic Framework/Ionic Liquids composites for VOCs detection [20]. A scheme of the home-made set up designed for the VOCs sensing experiments is shown in **Figure 5.2**. The initial point of the system starts in a nitrogen gas pressurized cylinder followed by two flow controllers. The first flow-controller (FC2) allows the variation of the N_2 flux that passes through a glass bubbler filled with the VOC *(i.e. toluene*), while the second one (FC1) modifies the toluene free N_2 flow. In a second step, both gas streams converge and the gas mixture passes through a glass chamber in which the fabricated sensor is located. This is surrounded by the coils of the magnetoelastic system described in **Annex A**. Finally, a gas trap collects toluene from the output flow. A computer is used for automatic data acquisition. The modification of the N_2 and VOC/N_2 fluxes allow controlling the VOC concentration. This way, the higher the N_2 and the lower the toluene-N_2 fluxes, respectively, the lower the final toluene output

concentration. A detailed description of the system design and of its components is given in the following.

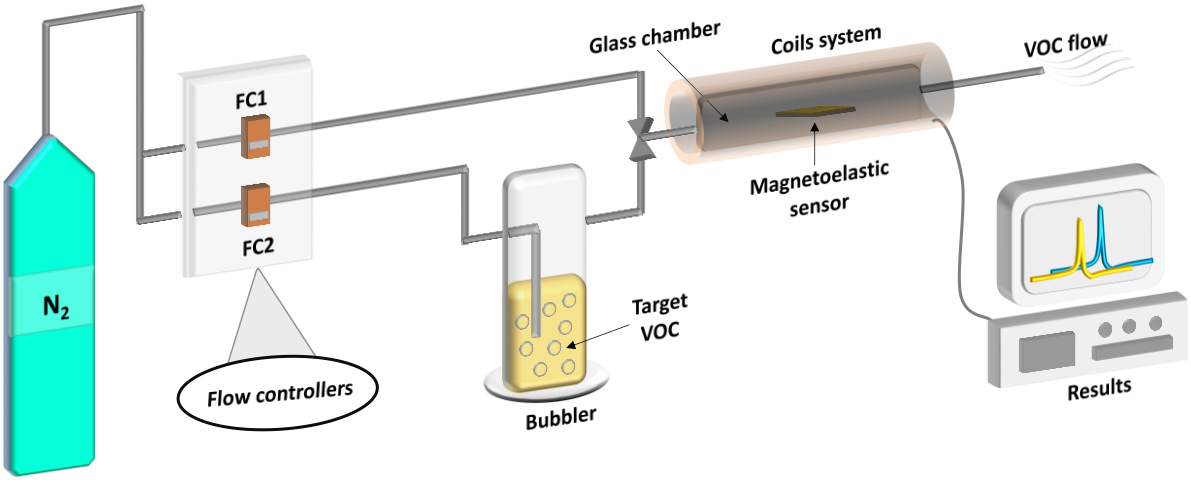

Figure 5.2. Scheme of the experimental set-up used for the VOCs sensing experiments.

Once designed the system and acquired all the necessary elements (**Figure *5.3***), the experimental set-up was assembled. The glass bubbler (SIMAX-250mL, **Figure *5.3***a), the polyamide tube (Legris, 6x4mmø) together with the necessary connections, the analogic flow controllers (Brooks Instruments, 0.05 to 0.5 l/min) and the pressurized nitrogen container (Alphagaz high purity > 99.999%) were purchased and connected. Moreover, the bubbler and the flow controllers supports were made by 3D printing. The 3D printer was found to be an excellent tool for quickly create different components for the system.

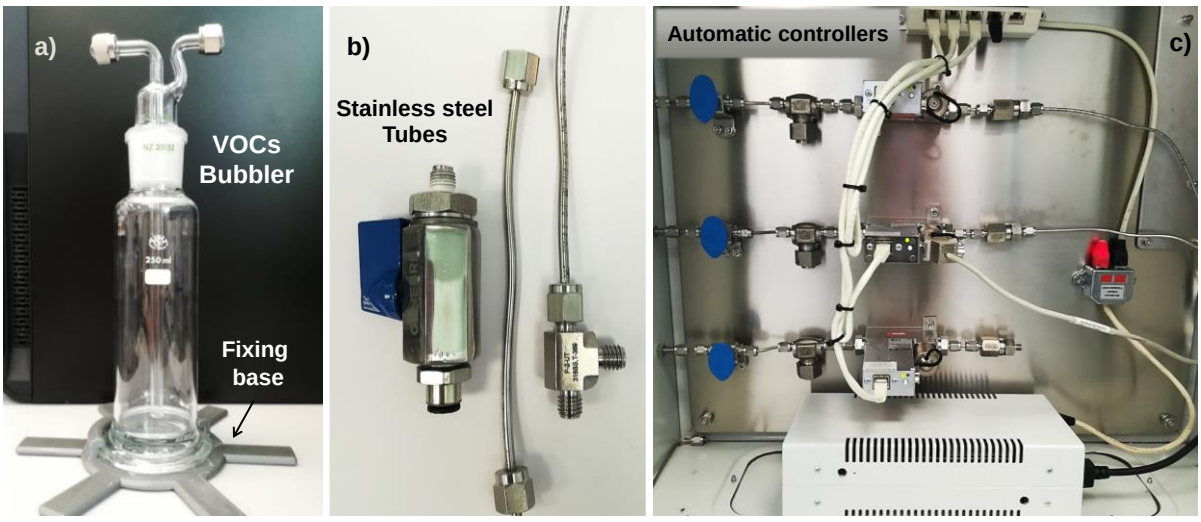

Figure 5.3. (a) Glass bubbler with the 3D printed base, (b) stainless steel tubes (316/316L, 1/8) and (c) automatic flow controllers box.

Some implementations of the initial system were developed after its first assembly. First, the existing pick-up coils had smaller diameter than the glass tube where the sensor is placed and through which the VOC passes. Thus, a new pick-up coil, and the respective air compensated pick-up coil, were designed and fabricated. The coils´ support (diameter of 10.5 mm) was designed and 3D printed (**Figure 5.4**a). The total number of turns of each coil was 500. The fabricated coils are shown in **Figure 5.4**b together with the big coils of the magnetoelastic system (for DC and AC magnetic fields). A detailed description of the magnetoelastic system itself could be found in **Annex A** (Section A.1.3).

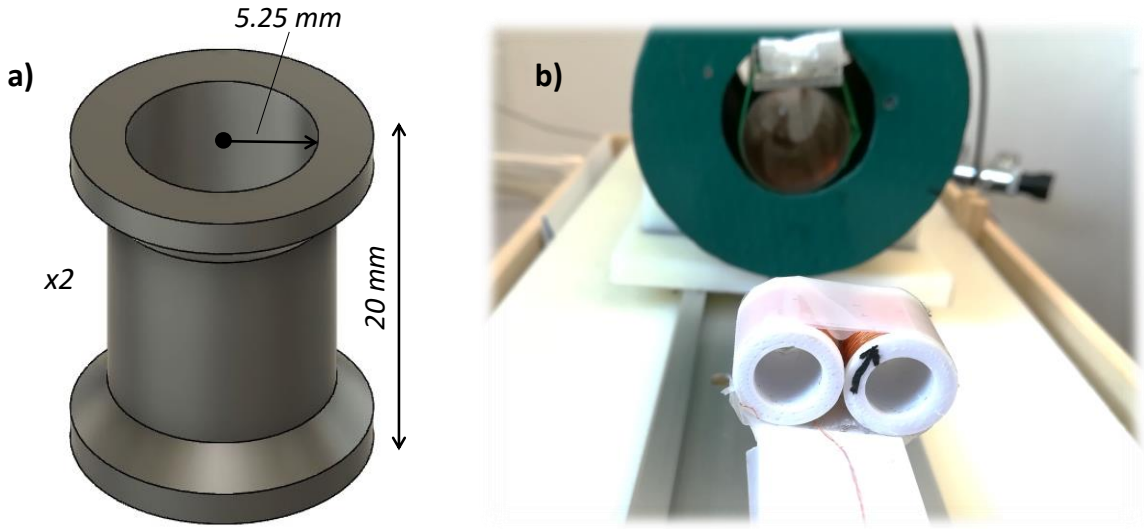

Figure 5.4. (a) Scheme of the pick-up coil base design and (b) pick up coils placed in the magnetoelastic system.

Furthermore, the diameter of the tube system was reduced and polyamide tubes were replaced for stainless still in order to minimize the gas leakages and prevent flux decays. In fact, polyamide tubes were quite unyielding due to their stiffness, and so, the control of their position in the system was difficult. Besides, a polymer tube can be degraded by the solvent vapours, which will shorten the life cycle of the set-up [21]. Moreover, the stainless-steel connections result in a significant reduction of gas losses (possible gas leakages were tested with a solution of water with soap). The stainless-steel tube (Swagelok, 316/316L, 1/8) together with some connections used in the set-up are shown in **Figure 5.3**b. That stainless-steel tube circuit that carries the N_2/VOC final mixture connects to a chamber (glass tube) in which the magnetoelastic sensors is located. Glass was chosen for the measuring chamber in order to gain visibility when the sensor is placed and centred between the pick-up coil.

Moreover, an oven was integrated on the system, allowing to perform experiments at different temperatures and implement activation protocols for the sensor without taking it out from the gas circuit. An image of the final set-up with a tubular oven and the stainless steel tubes connected to the glass chamber is shown in **Figure 5.5**.

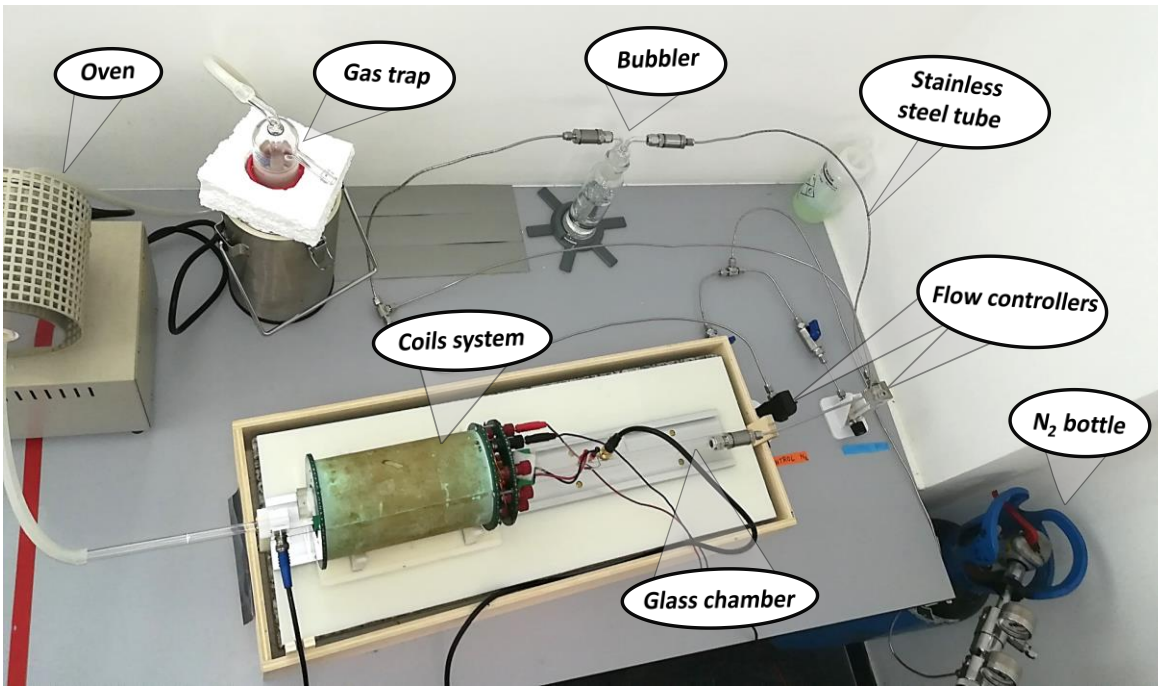

Figure 5.5. Image of the mounted VOCs system with the analogic flow controllers.

Finally, it was found that the range of fluxes accessible through analogic flow controllers do not allow an accurate tuning of the final VOC concentration. Thus, the analogic flow controllers were replaced by digital analogues (from Iberfluid), which allow a specific flow control between 0 to 200 sccm (*standard cubic centimetres per minute*). **Figure *5.3*c** shows the connection of the system through the digital flow controllers. It is important to specify that from the three flow controllers shown in the **Figure 5.3**c, just two of them are used in the set-up described herein. The third one could be used if two or more VOCs want to be mixed.

Different LabVIEW programs were developed to control in an automatic and remote mode the digital flow meters and the data acquisition process. In particular, a programme to monitor the resonance frequency as a function of the time was designed. This programme allows measuring the resonance frequency curve at a given magnetic field as function of the time, as well as selecting the measuring resonance frequency interval and

the period between measurements. An image of the main control panel of the programme along with all the configurable parameters is shown in **Figure 5.6**.

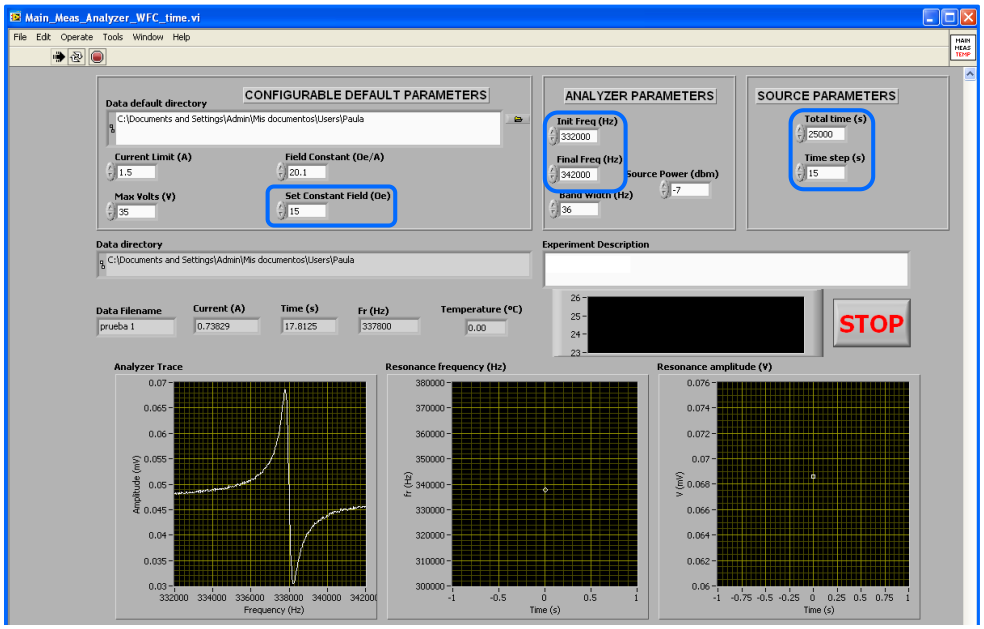

Figure 5.6. Screen of the LabVIEW programme implemented to measure the resonance frequency curve as function of the time.

The remote control of the gas flux through the two flow meters was achieved by the implementation of a second LabVIEW programme. This one allows setting the flux value (*in sccm*) of both flow controllers. Though a function implemented in the program, it was possible to vary the VOC flux automatically as function of time. An image of the control screen is shown in **Figure *5.7***.

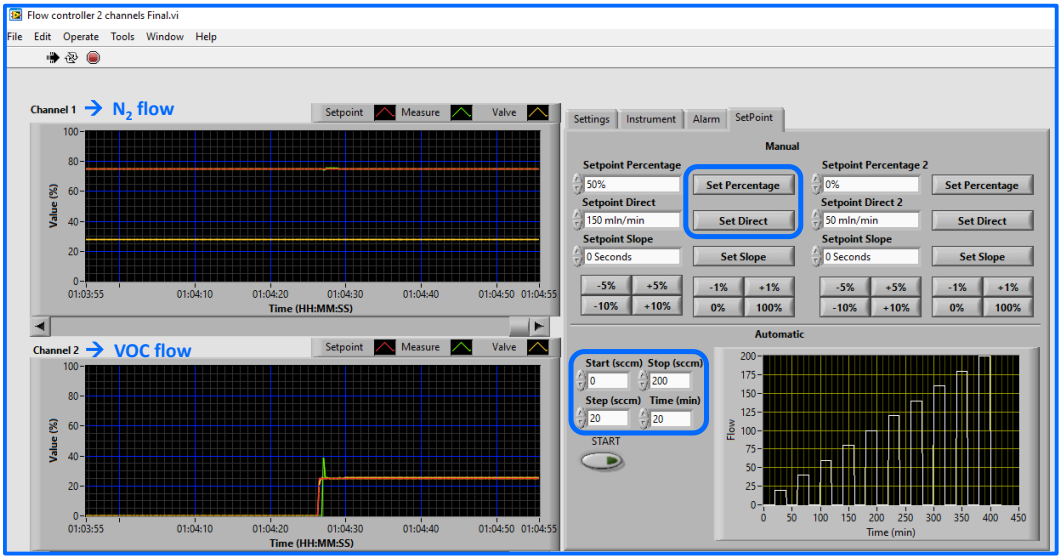

Figure 5.7. Screen of the LabVIEW programme used to control the flow meters.

As previously stated, the modification of the N_2 and the VOC/N_2 fluxes allow varying the final VOC concentration that reaches the sensor. The VOC concentration (in parts per million-ppm) obtained as function of the flux rate could be calculated using the following equation:

$$C = \frac{P^*_{voc} \cdot \upsilon_{voc}}{P_0 \cdot (\upsilon_{voc} + \upsilon_{N2})} \quad (5.1)$$

where υ_{N2} is the applied nitrogen flux, υ_{voc} the applied nitrogen flux going through the saturator with the VOC, P_0 the atmospheric pressure ($101\ kPa$) and P^*_{voc} the vapour pressure of the VOC at room temperature which is calculated as:

$$P^*_{voc} = \exp(C_1 + \frac{C_2}{T} + C_3 \cdot \ln T + C_4 \cdot T^{C_5}) \quad (5.2)$$

where T is the temperature and C_i are constant values for each VOC which are given in Perry's Chem. Eng. Handbook [22]. C_i constant of the VOCs used in this work together with the corresponding calculated vapor pressures (P^*_{voc}) are given in **Table *5.1***.

Table 5.1. Constant values employed to calculate the vapour pressure of the different VOCs used along this chapter.

C_i	Toluene	Acetone	Ethanol	Water
C_1	80.877	69.006	74.475	73.649
C_2	-6902.400	-5599.600	-7164.300	-7258.2
C_3	-8.7761	-7.0985	-7.3270	-7.3037
C_4	0.00000580	0.00000622	0.00000313	0.0000042
C_5	2	2	2	2
P^*_{voc} (kPa)	2.8864	24.5466	5.8482	2.3176

From that constants and considering the previous equations, the VOC concentrations were obtained. A calibration table of the VOC concentration as a function of the flux in both flow controllers was developed for different VOCs. In particular, the variation of the toluene concentration (*in ppm*) calculated as function of the VOC and nitrogen fluxes (*in sccm*) is represented in **Figure 5.8** as an illustrative example. Similar results have been obtained for the other VOCs but using their corresponding vapour pressures.

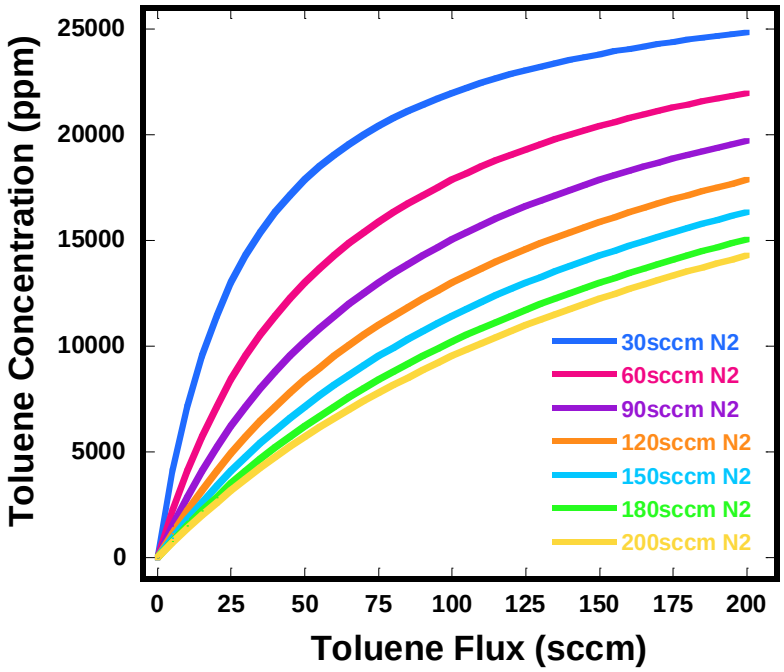

Figure 5.8. Toluene concentration (in ppm) as function of the VOC flux at different nitrogen fluxes (in sccm).

5.3. VOCs sensing experiments

Once the VOC continuous flux system was assembled and implemented, VOCs sensing experiments were carried out with rhombic Metglas 2826MB resonators functionalized with UiO-66-NH_2 MOF layers. It is worthy to note that other MOF based magnetoelastic resonator systems based on ZIF-8 or MIL-125 MOFs were also studied for VOCs sensing purposes but these were assembled after identifying the key parameters governing the sensing process during the main research developed with the Metlglas/UiO-66-NH_2 systems studied in this section. The performance of the Metglas/UiO-66-NH_2 sensor has been deeply analyzed in terms of recovery time, cyclability and selectivity. In fact, the effect of the MOF active layer mass of the resonator system in all these parameters has also been investigated. All the obtained results are shown and described in the following.

5.3.1. Magnetoelastic sensor fabrication and characterization

The UiO-66-NH_2 powdered sample, previously characterized in Chapter 3, was integrated onto the surface of a rhombic Metglas 2826MB resonator (10 mm x 2 mm) by the spray printing technique, following the protocols described in deep in the same chapter. The mass and thickness of the UiO-66-NH_2 active layer were controlled by the

cumulative spraying of the MOF dispersion. In particular, two UiO-66-NH_2/Metglas sensors were assembled varying the mass of the MOF active layer deposited onto the magnetoelastic ribbon, here and after identified as SEMOF-1 (74 µg of UiO-66-NH_2 active layer) and SEMOF-2 (130 µg of UiO-66-NH_2 active layer). The mass gain after each deposition process was thoroughly determined with a microbalance, as well as further related to the magnetoelastic frequency shift induced in the resonator. The functionalized Metglas resonator was fully characterized (results described in Chapter 3) by X-ray diffraction (XRD), Fourier-transform infrared spectroscopy (FTIR), N_2 adsorption isotherms and Scanning Electron Microscopy (SEM). All these complementary characterization techniques allow assuring the quality of the active layer; and particularly determining the layer thickness, mass and structure. A scheme of the analyzed sensors together with the mass of their MOF active layer is shown in **Figure 5.9**.

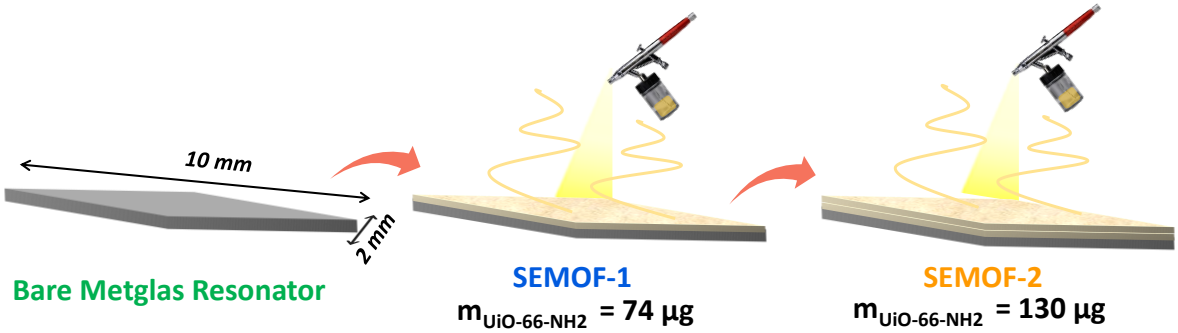

Figure 5.9. Scheme of the magnetoelastic samples characterized along this part.

The ability of the separate components, the bare resonator, the UiO-66-NH_2 layer the functionalized Metglas/MOF sensors, to adsorb toluene was assessed in static conditions by means of headspace solid-phase microextractions. This assembly was designed as it was not possible to measure the VOCs adsorption capacity of MOFs with a specific set-up for it. A detailed description of this methodology can be found in **Annex A**. The results clearly point out the lack of capacity of the bare resonator to adsorb toluene, while UiO-66-NH_2 powder, as well as the Metglas/MOF functionalized resonators do it properly. This observation confirms the great importance of functionalizing the resonator with a proper active layer to endow it of the adsorptive capacity over the target gas analyte. The toluene adsorption capacity of UiO-66-NH_2 was determined by performing Multiple Headspace solid-phase microextractions after exposing the sample to a toluene saturated atmosphere during 1day (**Figure 5.10**a). The cumulative addition of the toluene

concentrations obtained from the successive extraction cycles from the MOF allowed to quantifying its toluene adsorption capacity on 91.3 mg/g (**Figure 5.10**b). This value is lower than the previously reported ones obtained from continuous flow breakthrough experiments (161-252 mg/g) [18], but still demonstrating the high toluene adsorption capacity of the UiO-66-NH_2 in experimental conditions close to the ones used in the sensing experiments. The toluene concentration monitoring by gas chromatography for one microextraction cycle and the experimental fitting of successive extractions to quantify the toluene adsorption capacity of UiO-66-NH_2 are represented in **Figure 5.10**.

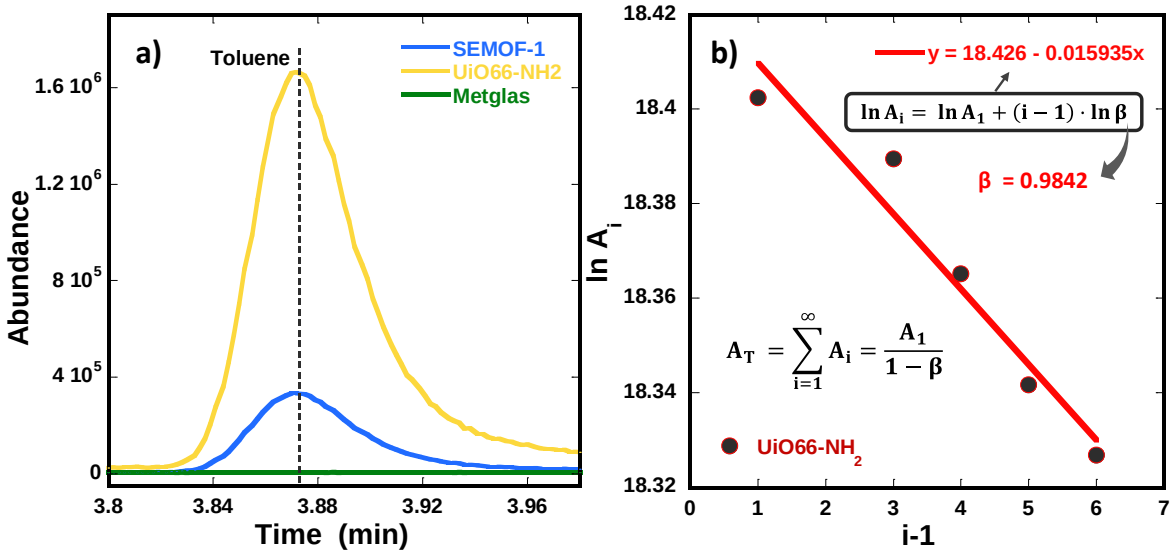

Figure 5.10. (a) Toluene abundance measured in a bare Metglas resonator, the UiO-66-NH_2 powder and the UiO-66-NH_2/Metglas sensor and (b) Calculation of the UiO-66-NH_2 toluene adsorption capacity from the Multiple Headspace solid-phase

The magnetoelastic resonance frequency curves of bare Metglas, SEMOF-1 and SEMOF-2 resonators were measured to confirm that the resonance signal quality is maintained after the MOF active layer deposition. The resonant frequency curves for the studies samples are shown in **Figure 5.11**. As determined in Chapter 2, the optimal applied magnetic field (Hk max) for such a rhombic resonator of 10 mm in length is 14.9 Oe. Thus, in order to maintain the best resonance signal, all the magnetoelastic measurements have been performed at this bias magnetic field.

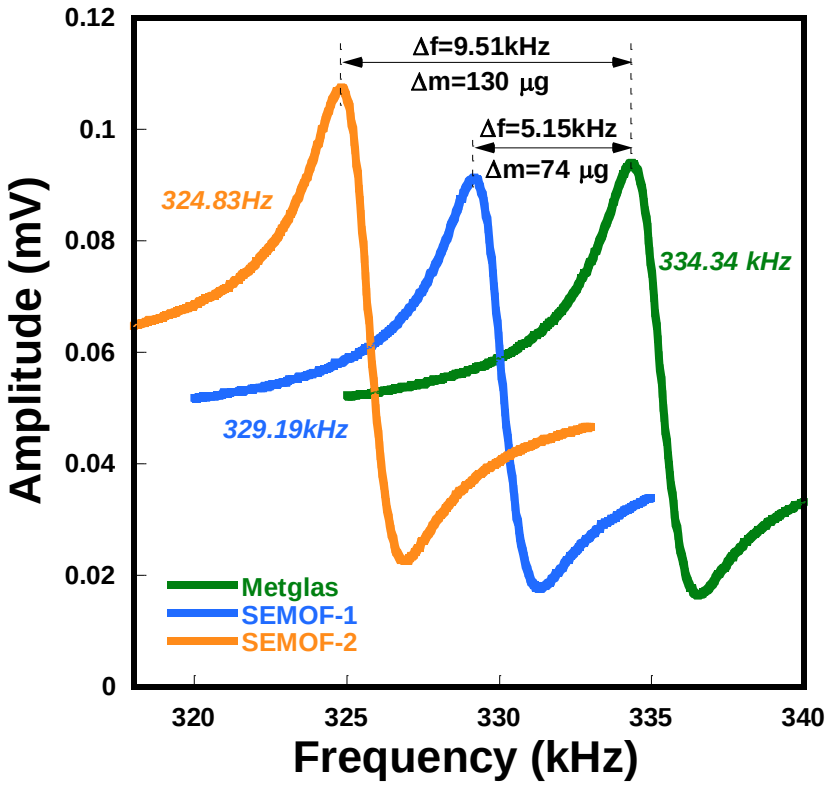

Figure 5.11. Resonance frequency curves of the bare Metglas resonator and of the functionalized resonator after one MOF layer deposition (SEMOF-1) and after the second layer deposition (SEMOF-2).

A resonance frequency of 334.34 kHz is measured for the bare Metglas resonator. That value is in accordance with the obtained through the theoretical equation for the resonance frequency of a freestanding rhombus shaped magnetoelastic resonator (**Equation 2.10**). The first UiO-66-NH_2 layer deposition at the rhombic shaped ribbon (SEMOF-1) add 74 μg of active sorbent layer and a subsequent frequency shift of 5.15 kHz. The second UiO-66-NH_2 deposition (SEMOF-2) increments the active layer mass to 130 μg, leading to a total resonance frequency displacement of 9.51 kHz. These frequency shifts after the MOF layer depositions are translated into a mass sensitivity of about 71 ± 2 Hz/μg. Moreover, it is worthy to highlight that peak quality and the signal intensity of the resonance frequency curves are maintained after the first and second MOF depositions. Actually, this is an excellent result, since many investigations have reported a reduction in the peak intensity and the signal quality after the magnetoelastic ribbon functionalization [23,24].

5.3.2. Toluene sensing experiments

Finally, the UiO-66-NH_2/Metglas sensors (SEMOF-1 and SEMOF-2), as well as the bare resonator, were applied in real-time detection experiments of toluene volatile organic compound. By using the previously described home-made set-up, the sensors were exposed to flux with increasing toluene concentration. The frequency shift induced by the mass gain due to the toluene adsorption in the MOF active layer was continuously monitored. Besides, the sensor selectivity was investigated by measuring its response to other atmospheres (water, ethanol and acetone). Finally, the toluene sensitivity and detection limits as function of the active layer mass were determined. A scheme of the detection process is collected in **Figure *5.12***.

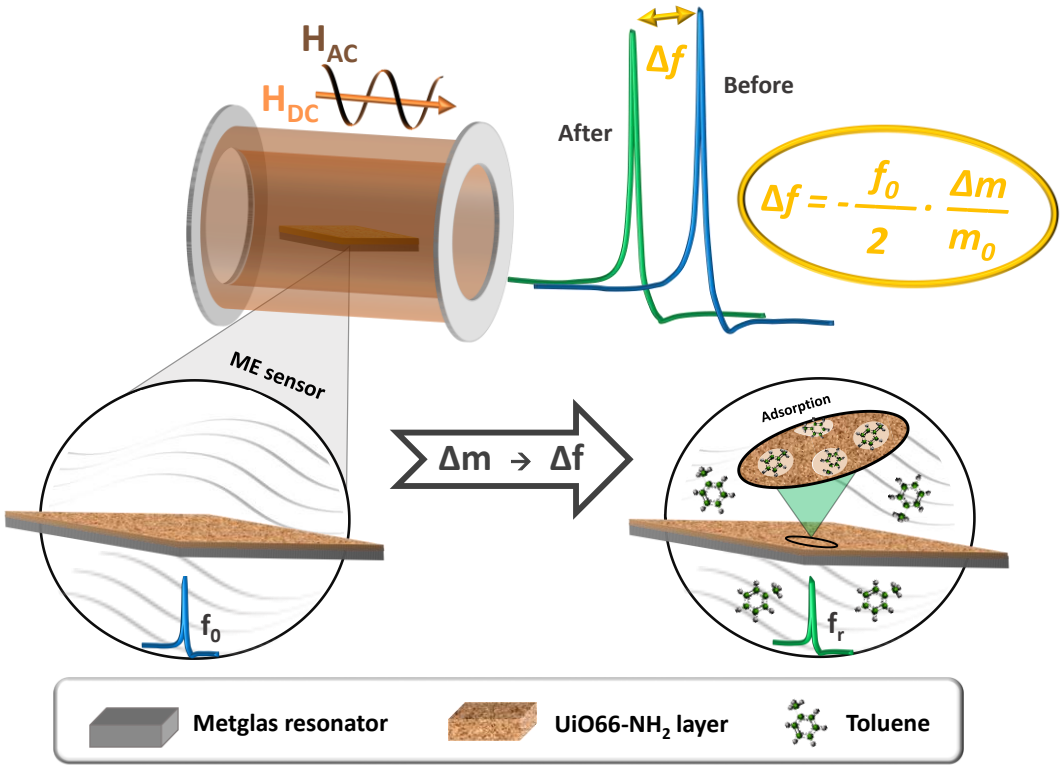

Figure 5.12. Scheme of the toluene sensing process with the rhombic Metglas resonators functionalized with the UiO66-NH_2 MOF.

First, the magnetoelastic resonance frequency of the bare Metglas resonator was measured under different toluene concentrations (**Figure 5.13**a), confirming that no meaningful frequency shift is observed in the absence of an active layer.

Afterwards, the MOF functionalized sensors, SEMOF-1 and SEMOF-2, were tested under the same conditions, giving rise to a fast and recoverable significant frequency shift, between 0.7 and 1.3 kHz, as a consequence of the toluene presence (**Figure 5.13**b).

For SEMOF-1 and SEMOF-2 magnetoelastic sensors, the resonance frequency shift increase as the toluene concentration does, which is a consequence of the mass gain at the MOF active material induced by the toluene adsorption equilibrium established with the surroundings. Nevertheless, the frequency shift tends to stabilize at high toluene concentrations, a fact that suggests that the MOF layer is reaching the toluene adsorption saturation.

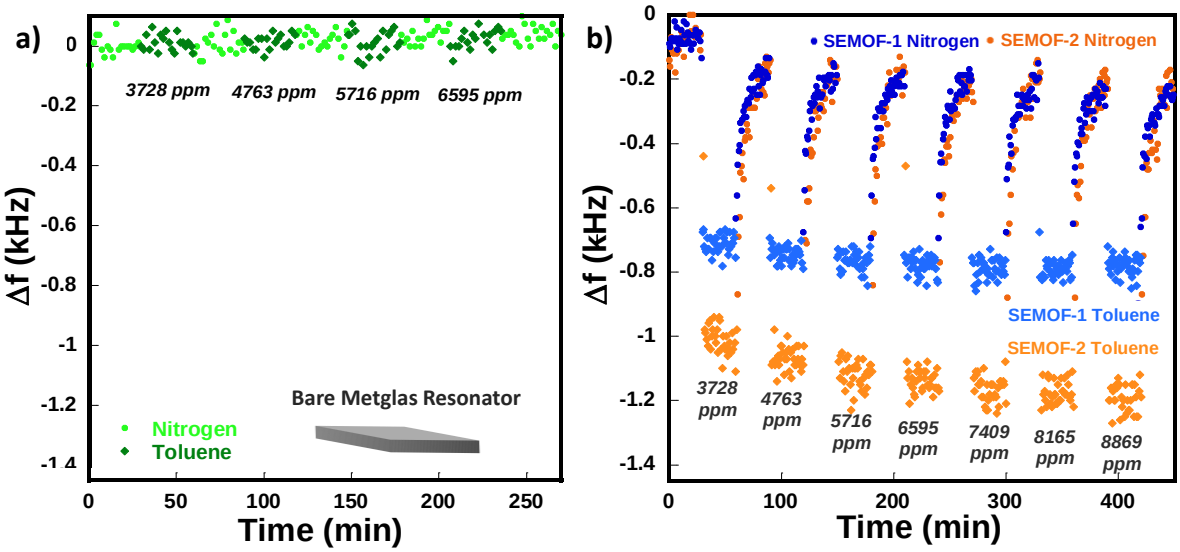

Figure 5.13. Toluene sensing experiments performed for: (a) the bare Metglas resonator and (b) the Metglas resonator functionalized with a first MOF layer (SEMOF-1) and a second MOF layer (SEMOF-2). Toluene flux varies from 30 to 90 sccm with a step size of 10 sccm every 30 minutes. N_2 flux is maintained at 200 sccm.

A clear advantage of the Metglas/UiO-66-NH_2 sensor is its fast toluene adsorption kinetics. Independently on the toluene concentration, the maximum frequency shift is reached in less than one minute, which hinders measuring intermediate points during the toluene detection process. This is in concordance with fast toluene adsorption kinetics previously reported for that kind of MOF [18]. Otherwise, the desorption process turns out to have slower kinetics, and even it is not yet completed after 30 minutes under the pure nitrogen flux exposure of the sensor. This is related to the host guess interactions established between the MOF material and the toluene guest molecules [25]. Previous researches point that toluene hydrogen bonding to NH_2 groups present in the structure stabilizes the guest molecules once adsorbed within the porous structure of UiO-66-NH_2 sorbent[18]. Therefore, even when very fast toluene uptake is driven by these MOF-toluene

interactions, its desorption requires of an input of energy into the system that can detach the toluene molecules from their binding points within the inner pore structure of UiO-66-NH_2 material. In this regard, the MOF/Metglas sensors exhibit an anisotropic adsorption/desorption response that is similar to the previously reported ones for toluene vapour isotherms of MOFs presenting hysteresis between the adsorption and desorption stages.

In view of these results, repeated response-recovery measurements were performed in order to quantify the degree of resonance frequency recovery per adsorption/desorption cycle, its kinetics, and the overall reproducibility of the sensing process after six cycles. To perform this experiment, the sensing device was repeatedly exposed 1 hour to a pure nitrogen flux and 5 minutes to a nitrogen/toluene mixture flux for several cycles. Results are represented in **Figure 5.14**.

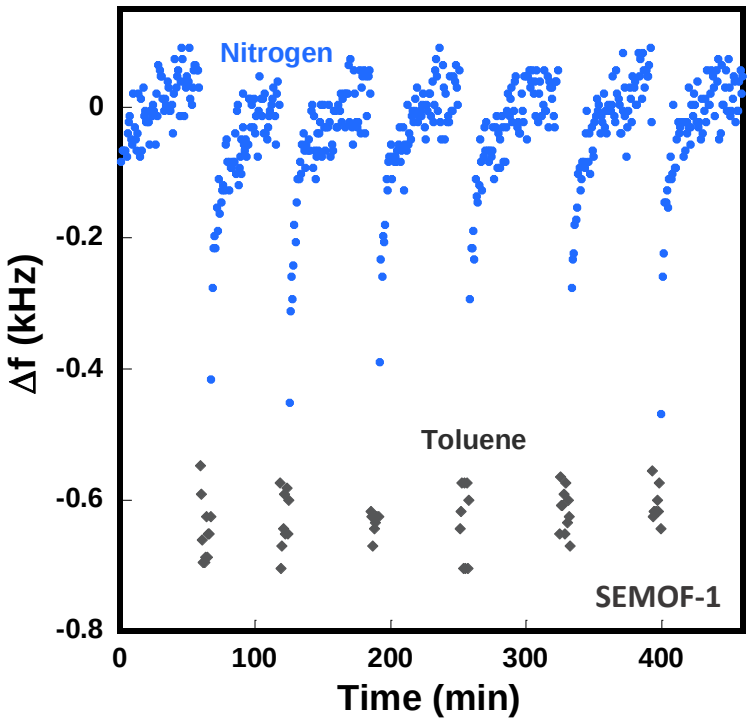

Figure 5.14. Response-recovery curve measured for the SEMOF-1 sensor. 1 hour of pure nitrogen flux and 5 minutes of toluene/nitrogen flux have been alternated.

As could be observed, after the toluene adsorption stage, when the MOF active layer is exposed to the pure nitrogen flux, the sensor recovers repeatedly its initial resonance frequency value, that is, the toluene is completely desorbed from the UiO-66-NH_2 pores.

Nevertheless, and as it was previously mentioned, while the response times of the sensor upon exposition to toluene are so fast (less than 1 minute), the recovery process requires more time (about 50 minutes). Toluene desorption could be accelerated by applying temperature to the system, but it is not definitively necessary to re-activate the sensor. Finally, it could be observed that this recovery process is maintained even after several cycles which demonstrate the excellent cyclability of the Metglas/UiO-66-NH_2 system.

5.3.3. Evaluation of the sensor selectivity

The SEMOF-1 selectivity was evaluated through the analysis of its magnetoelastic response upon its exposition to N_2 atmospheres of water, acetone and ethanol. The responses of the sensor over different gases were quantitatively compared in **Figure 5.15**. Water was selected as competitor specie of toluene due to its ubiquitous presence in the atmosphere. The sensor response over acetone and ethanol was also studied because they are very common polar VOCs present also in the indoor environment. In addition, the selection of target gas analytes with so different relative polarities ([1] $r.p.^2_{Toluene} = 0.099$, $r.p.^2_{Acetone} = 0.355$, $r.p.^2_{Ethanol} = 0.654$, $r.p.^2_{Water} = 1.000$) allows estimating the response of the SEMOF-1, and consequently, of the UiO-66-NH_2 active layer over the adsorption of polar (*i.e. water, ethanol*), intermediate (*i.e. acetone*) and non-polar (*i.e. toluene*) substances.

The experiments were performed at a VOC concentration of around 8000 ppm. Cyclability and stability of the sensor were also studied inducing the desorption of the gas analyte by exposing the sensor to a nitrogen flux. The response of the sensor to the different compounds (resonance frequency variation over time) is shown in **Figure 5.15**.

[1] r.p.2= square relative polarity. Values for relative polarity have been extracted from: Christian Reichardt, *Solvents and Solvent Effects in Organic Chemistry*, Wiley-VCH Publishers, 3rd ed., **2003**. Chemical polarity is defined as a separation of electric charge leading to a molecule or its chemical groups having an electric dipole moment, with a negatively charged end and a positively charged end.

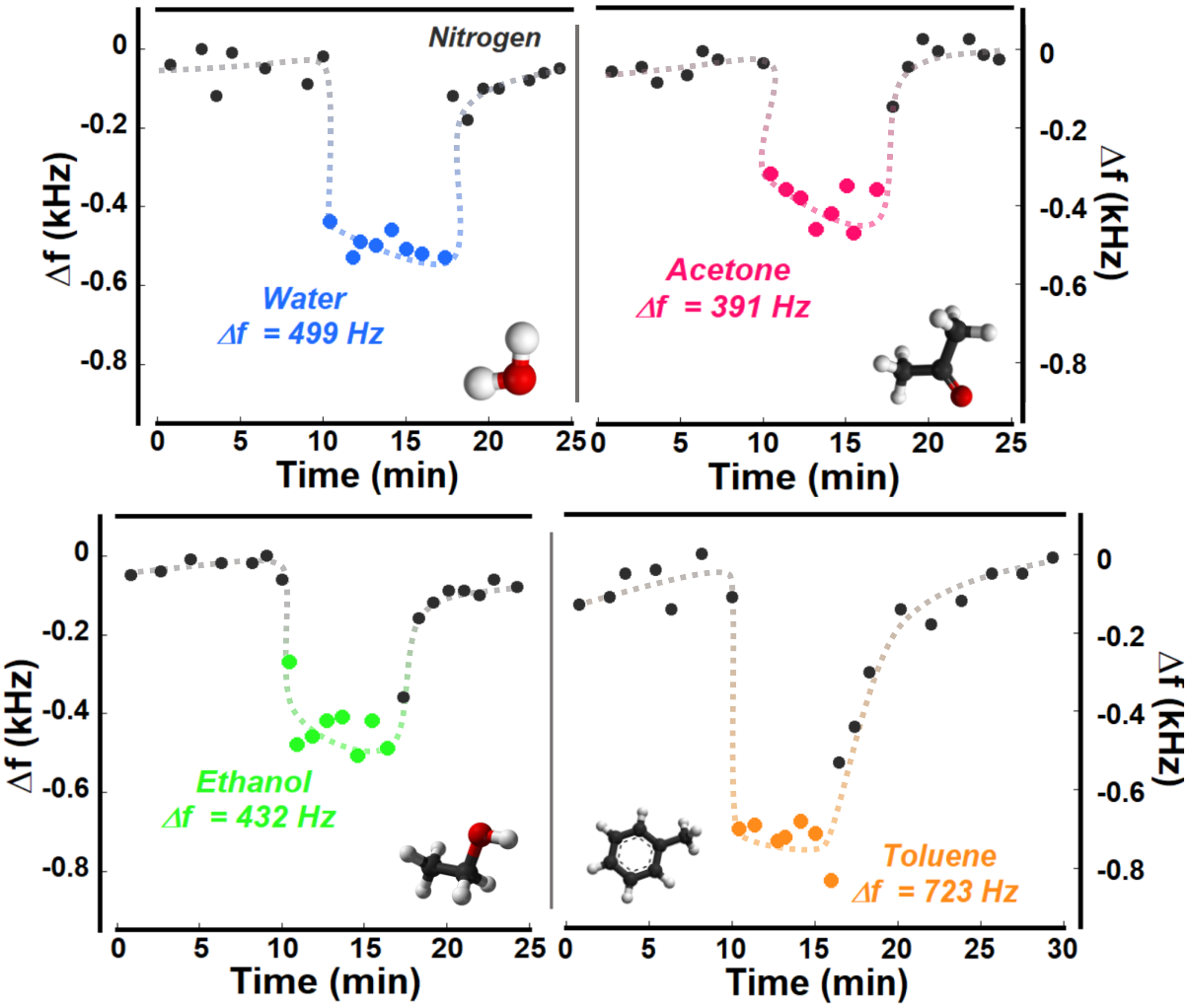

Figure 5.15. Selectivity experiments performed in the SEMOF-1 sensor under water, acetone, ethanol and toluene at a concentration of 8000 ppm.

The SEMOF-1 sensor exhibits a fast response after its exposition to the different target gas. The reactivation times once the loaded sensor is exposed to the nitrogen flux are slightly longer, but still below the 30 seconds. The measured frequency shift under a concentration of 8000 ppm of each target compound is summarized in **Figure 5.16**. As could be observed in **Figure 5.16**, the response of the sensor clearly depends on the target compound. In particular, the selective response of the sensor towards toluene could be clearly observed by the higher frequency shift (723 Hz) measured for this analyte. A lower response is measured for water (499 Hz), followed by ethanol (432 Hz) and by acetone (391 Hz).

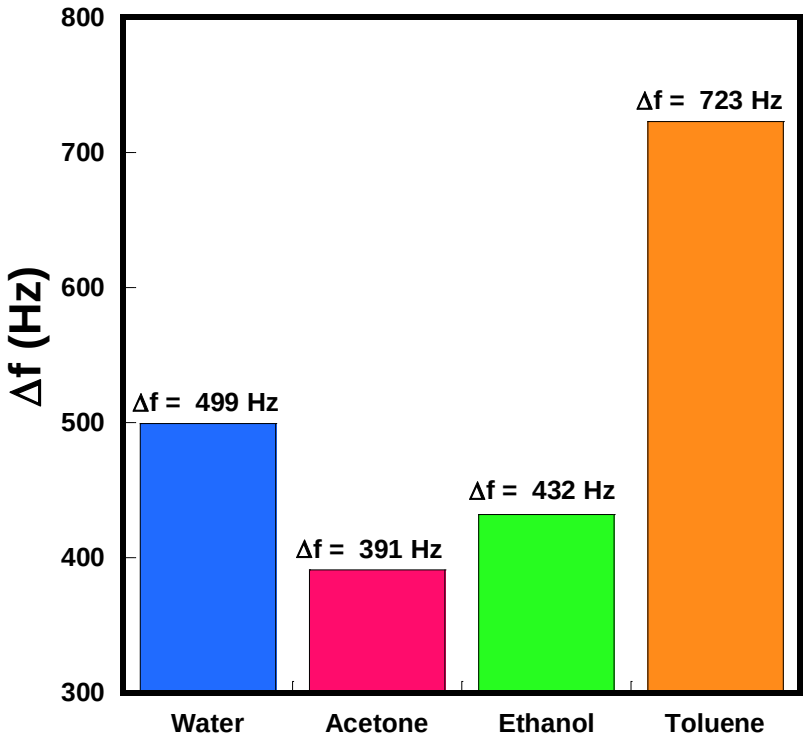

Figure 5.16. Mean resonance frequency shift measured for the SEMOF-1 under the different atmospheres (water, acetone, ethanol and toluene) at 8000 ppm.

Moreover, in **Figure 5.15** it could be also observed that the desorption kinetics differs slightly depending on the gas nature. Indeed, after translating the frequency shift in weigh units of the adsorbed gas (mg), and normalizing it per grams of UiO-66-NH_2 layer involved in the adsorption, the adsorption capacity (mg/g) could be obtained, and the desorption profile can be roughly fitted to a Langmuir kinetic desorption model (**Figure 5.17**). The conversion between the frequency shift and mg of adsorbed gas has been done considering the sensitivity value of 70 Hz/µg previously obtained.

Thus, the adsorption capacity and affinity of the UiO-66-NH_2 can be derived from the translation of the frequency shift to mg/g units of adsorption, as well as from the Langmuir kinetic rate parameter obtained from the fitting of the desorption cycle for each target analyte. First, the adsorption capacity of the UiO-66-NH_2 active layer has been estimated from the experimental frequency shift in: Q_{water}= 96 mg/g, $Q_{acetone}$ = 76 mg/g, $Q_{ethanol}$= 85 mg/g and $Q_{toluene}$= 140 mg/g. Obtained toluene adsorption capacity is slightly lower than the previously reported ones for vapour and breakthrough adsorption experiments with UiO-66-NH_2 compound [18,19], but it has to be taken into account that the experimental conditions differ significantly in the dynamic and static gas adsorption

measurements. Even though the different absolute values obtained from static and dynamic breakthrough experiments, the adsorption capacity tendency: Toluene > Water > Ethanol > Acetone, could be suggested.

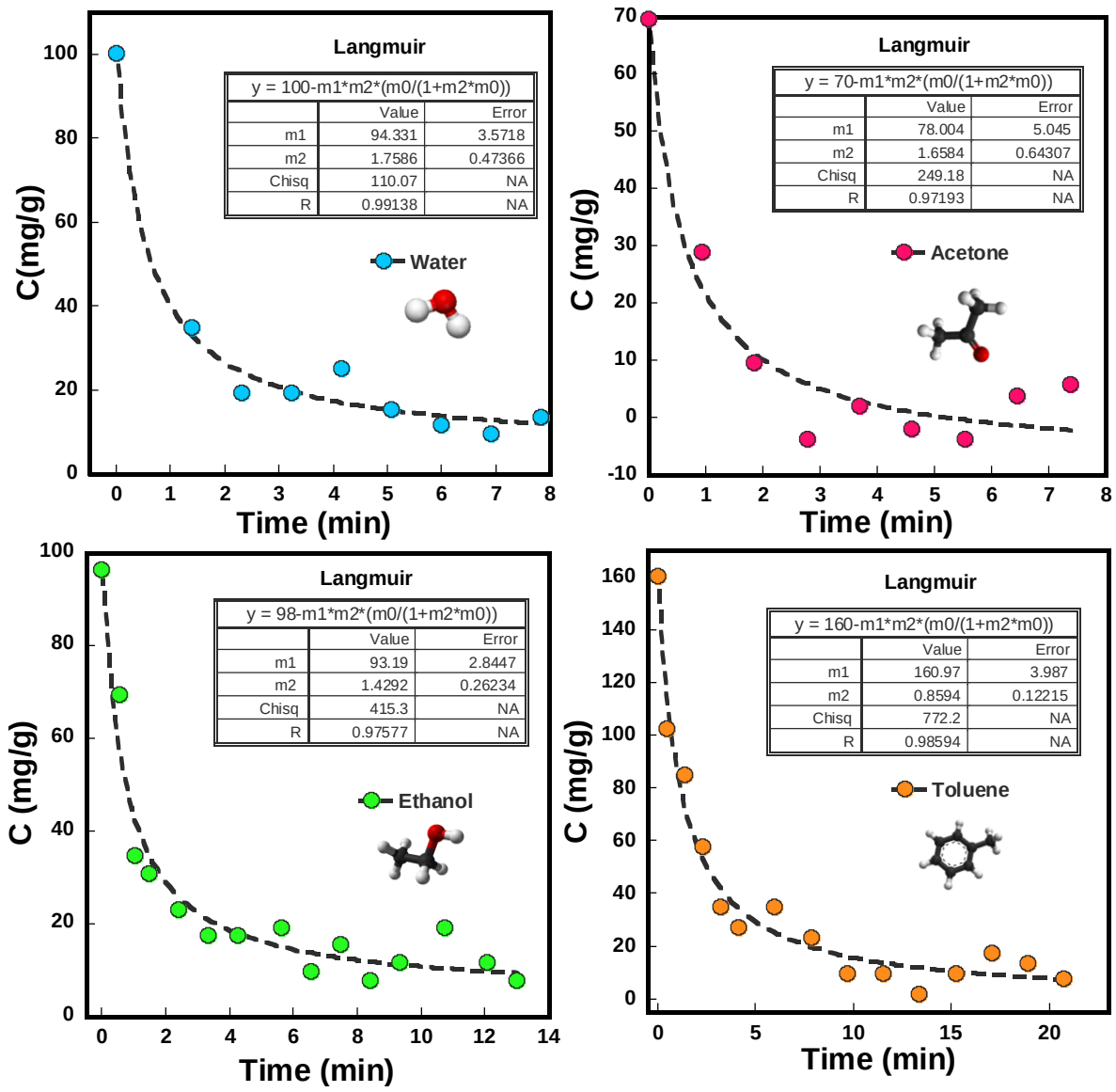

Figure 5.17. Desorption isotherms measured by the magnetoelastic/MOF device adjusted by the Langmuir model.

Moreover, when the experimental adsorption capacity of UiO-66-NH_2 over the studied gases is plotted versus their square chemical polarity very interesting linear trend emerges for the more polar water, ethanol and acetone compounds, as can be observed in the ***Figure 5.18***. Opposite, toluene deviates appreciably from the main data group. Despite the data is quite reduced in terms of number of studied gas molecules with

different chemistries, and hence, potential binding interactions with the host, it seems that the linear tendency observed for polar gas molecules is related to the strength of the hydrogen bonding bridges between the adsorbent and the adsorbate, that is, the higher the polarity the stronger the hydrogen interaction with the host. In the specific case of toluene, its adsorption is foreseen to be governed by weak interactions far from hydrogen bonding, such as π – π or NH_2 – π, so the polarizability index is not so relevant to explain the adsorption capacity of the active material.

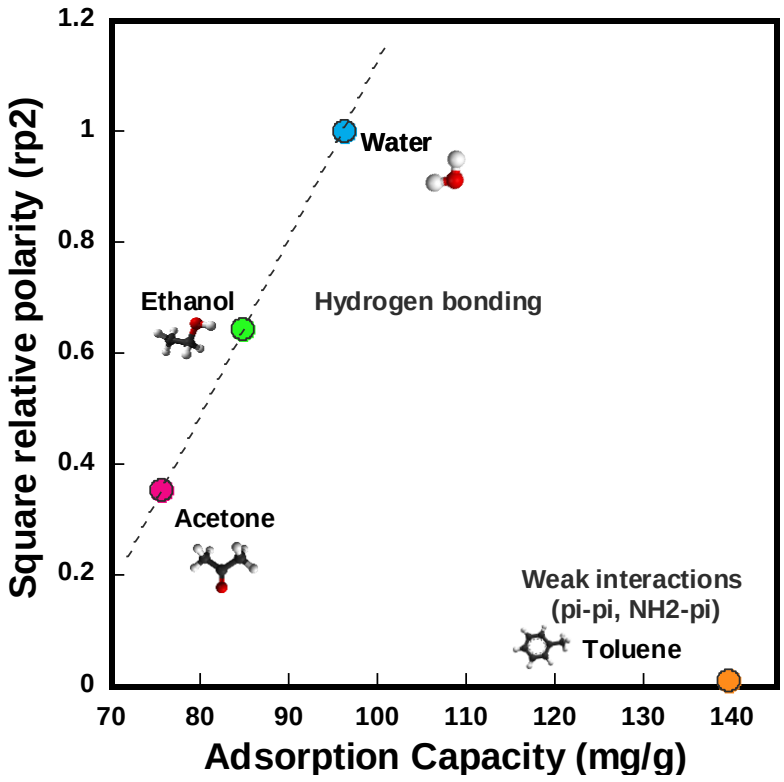

Figure 5.18. Relation of the square relative polarity (rp2) with the adsorption capacity estimated from the magnetoelastic resonance frequency shift.

Regarding the Langmuir kinetic parameter (k_L) obtained from the fitting of the desorption steps of the sensing experiments, its value stands for the strength of the host-guest interaction between the UiO-66-NH_2 and the target gas. Indeed, the lower the value of the k_L parameter, the slower the desorption and the stronger the interaction established between the host and the guest. First, it is worthy to note that the obtained values have to be considered qualitatively since even if the desorption process is slower than adsorption, in some cases, such as water sensing experiments, few experimental points could be acquired. Indeed, water seem to be sorbate that establish the weaker

interaction with the host (k_L = 1.8(5)), followed by far for acetone (k_L =1.6(6)), ethanol (k_L =1.4(3)) and toluene (k_L =0.86(12)).

In terms of selectivity over toluene, the significant response of the sensor, explained by the high hydrophilicity of UiO-66-NH_2, hinders its application in real conditions since the presence of water vapour is ubiquitous, and exceeded by far the VOC concentrations even in the worst scenarios. Thus, further modification on the MOF active layer itself could be explored in the future to endow it of a hydrophobic character that blocks the water adsorption from the surrounding. This could be achieved by the introduction of hydrophobic groups into the MOF structure or by include cooperative adsorption points within the MOF´s pore space through multivariate chemistry, among others.

5.3.4. Sensitivity dependence with the MOF active layer mass

Finally, the dependence of the sensor response and the mass of the active layer in SEMOF-1 and SEMOF-2 has been analyzed. As it is observed in **Figure 5.13**b, there is a direct relationship between the mass of the MOF active layer and the variation of the resonant frequency, as expected. Such as an example, under a flux of 3728 ppm of toluene, the resonance frequency variations of SEMOF-1 and SEMOF-2 are 710 and 1010 Hz, respectively. This direct relation between the active layer mass and the frequency shift is related to the higher surface area of SEMOF-2, and consequently with its higher capacity to adsorb toluene. In addition, the sample with the highest MOF active layer mass (SEMOF-2) exhibits slower kinetics and higher toluene concentration to reach the saturation. Thus, the final part of this study concerns the analysis of the influence of the MOF active layer mass on the sensor sensibility. **Figure 5.19**a shows the resonance frequency shift as a function of the toluene concentration (calibration curves), whilst **Figure 5.19**b depicts the sensitivity values as a function of the toluene concentration calculated on the following basis: $S = frequency\ shift/toluene\ concentration = \Delta f/C$.

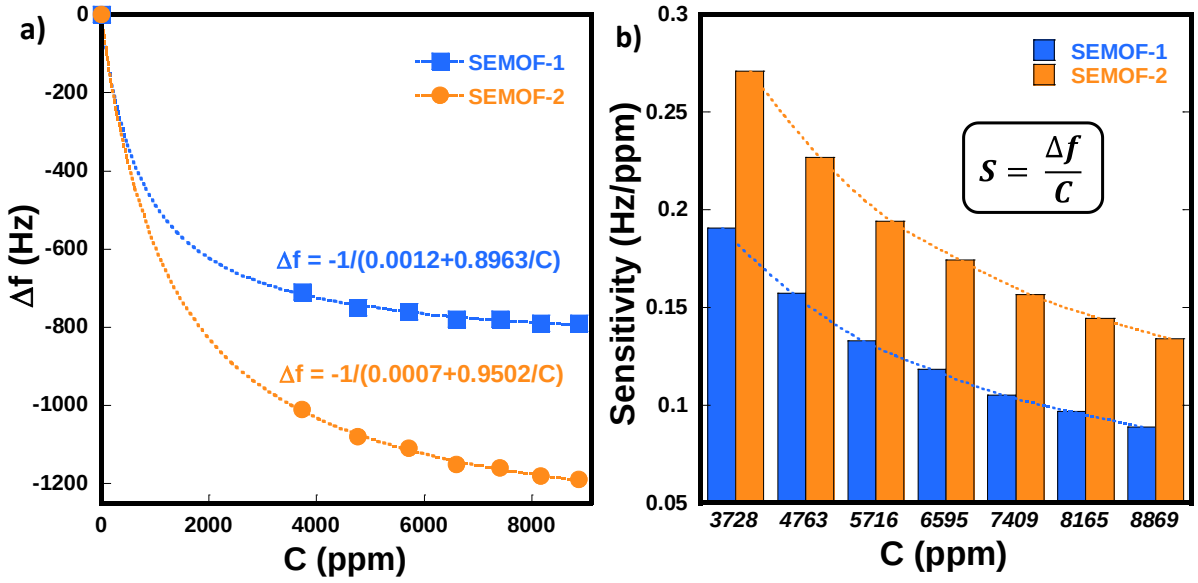

Figure 5.19. (a) Resonance frequency shift as function of the toluene concentration (dashed lines indicate the fits obtained from the equation reported previously [26]) and (b) toluene derived sensitivities for the sensors with one MOF layer (SEMOF-1) and with two MOF layers (SEMOF-2). Dashed lines are a guide to the eyes.

Looking to the frequency shift and sensitivity trends observed in **Figure 5.19**, the experimental findings clearly point out that:

1) The sensor response as a function of the toluene concentration is not linear, since it tends to saturation at high toluene concentrations. This tendency has also been reported for other sensors [26], and is related to the slowdown of the toluene diffusion through the MOF active layers whilst the pore filling of the UiO-66-NH_2 materials increases. Indeed, if the frequency shift values are translated in mg/g adsorption capacities, the profile is similar to the one of a gas adsorption isotherm and can be easily fitted to theoretical models developed for gas adsorption.
2) The bigger the weight of the deposited MOF active layer (SEMOF-2 sensor) the higher the toluene saturation concentration, since the maximum amount of toluene adsorbed is proportional to the MOF active layer mass. There are clear differences between the responses of both sensors upon exposure to the same toluene concentration. In fact, SEMOF-1 reach the saturation at about 6595 ppm while SEMOF-2 sensor has not yet reached saturation for the maximum toluene concentration measured (8869 ppm).
3) It is not possible to give just a unique sensitivity value since the dependence of the resonance frequency shift with the toluene concentration is not linear, as is observed

in **Figure 5.19**b for both sensors. Independently on the toluene concentration, the SEMOF-2 sensitivity is higher than this of SEMOF-1, an observation that again is directly related to its higher MOF active layer mass. In particular, a maximum toluene sensitivity of 0.19 Hz/ppm for the SEMOF-1 and of 0.27 Hz/ppm for the SEMOF-2 have been obtained at the lower toluene concentration value (3730 ppm).

4) By using the fitting equations obtained from **Figure 5.19**a, the sensitivity of the sensors at different toluene concentrations could be estimated. As an example, the toluene sensitivity at 1000 ppm is calculated to be of 0.48 Hz/ppm and 0.61 Hz/ppm, for the SEMOF-1 and SEMOF-2, respectively. That is, at least a value twice the maximum sensitivities obtained in this work.
5) In addition, the lower limit of sensitivity of the device can be roughly estimated by considering the set-up RBW. The sensor presents a sensitivity of 70 Hz/μg which means that a frequency variation of around 35 Hz is related to a mass increment of 0.5 μg. Relating this with the formula of **Figure 5.19** fittings, a frequency shift of 35 Hz is expected under a concentration of 34 ppm. Thus, the detection limit of the fabricated sensor is around 33 ppm. This value is similar for both SEMOF-1 and SEMOF-2, which indicate that at low concentrations the increase of the active layer mass is not a critical aspect. Thus, improve the affinity of the MOF layer at low concentrations as well as the selectivity are the key parameters that should be improved in order to obtain a lower sensitivity threshold. The reduction of the sensor length is another fact that could be improved to increase that threshold since the mass sensitivity will increase when reducing the size.
6) An estimation of the toluene adsorption capacity of the MOF active layer deposited on the resonator could be obtained from the measured resonance frequency shift considering also the active layer mass and the estimated mass sensitivity of the resonator. This estimation has been calculated for the SEMOF-2 sample, which is the one that has reached the saturation. The maximum frequency shift (Δf) for SEMOF-2 is of 1190 Hz, considering the resonator mass sensitivity (S=70 Hz/ μg) the total toluene mass adsorbed is calculated to be 17 μg ($\Delta m = \Delta f/S$). Taking into account that the total MOF active layer in the SEMOF-2 sample is of 74 μg, a toluene adsorption capacity or around 131 mg/g is estimated, just slightly below the values obtained from breakthrough experiments (from 160 mg/g to 260 mg/g) [18,19] and very similar to that previously estimated for SEMOF1. It is difficult to compare the absolute values

since they depend a lot on factors such as the synthesis parameters, particle size or final linker defect degree of the UiO-66-NH_2 material. Besides, the comparison of the capacity values obtained from two different experimental set-ups is not straightforward. Nevertheless, it could be highly interesting to perform both experiments with a UiO-66-NH_2 material obtained in the same experimental conditions and try to correlate the final data. Toluene adsorption measurement (vapour isotherms or columns breakthrough experiments) are time-consuming, whilst a MOF/resonator-based adsorption capacity estimation could be done in less than one hour once implemented the system.

7) Finally, normalizing the sensitivity to the mass of the active layer, it is possible to compare results obtained in this work with the ones obtained in previous studies. A maximum VOCs sensitivities of around 0.0591 $Hz \cdot ppm^{-1}/mg_{active\text{-}layer}$ and of 0.04 $Hz \cdot ppm^{-1}/mg_{active\text{-}layer}$ have been estimated when using respectively polymers and zeolites as active layers, on magnetoelastic sensors [13,14]. In the present study, a normalized sensitivity of 2.56 $Hz \cdot ppm^{-1}/ mg_{active\text{-}layer}$ has been obtained, which is more than 43 times higher than the sensitivity values reported previously. This mass normalized sensitivity values encourage us to describe our system as a highly sensitive device.

5.4. Summary and conclusions

In this chapter, the feasibility of magnetoelastic sensors functionalized with metal-organic frameworks (MOFs) for the wireless detection of volatile organic compounds (VOCs) has been duly demonstrated.

It has been concluded that the integration of MOF sorbent layer having a high and specific adsorption capacity over the desired VOC at highly sensitive rhombic magnetoelastic resonator is a feasible approach to detect VOCs in a fast, reproducible and highly sensitive manner.

MOF/magnetoelastic devices exhibit repeatable and stable cyclability over toluene. Sensitivity of the UiO-66-NH_2/Metglas system (S_{max} = 0.27 Hz/ppm) depends on parameters such as the toluene concentration and the mass of the MOF layer deposited at the resonator. Certain selectivity towards toluene has been observed when comparing

the performance of the studied system over other gases such as acetone, ethanol and water.

Moreover, the MOF/Metglas system allows determining the VOC adsorption capacity of the UiO66-NH_2 active layer if measured frequency shifts are translated on mass of gas adsorbed per mass unit of adsorbent. Indeed, obtained adsorption capacity values are in good agreement with the previously reported ones from VOCs static vapour adsorption and breakthrough experiments. The results open the possibility to study the potentials of a cheap home-made set-up to investigate VOCs adsorption capacities of different MOFs and traditional sorbents after their integration in resonant platforms.

The minimum sensitivity threshold of the best MOF/magnetoelastic device toward toluene has been estimated to be around 34 ppm. The improvement of the MOF layer affinity and selectivity over toluene at low concentrations as well as the sensor geometry and miniaturization are key parameters to reduce the sensitivity threshold to lower toluene concentrations usually found in air polluted media. Moreover, it is a must to improve the experimental set-up developed for the VOCs in order to get access to lower VOC concentration in the system.

In general, the comparison of the proposed systems with previous researches for similar systems reveals that the MOF/magnetoelastic resonator combination result a very promising approach for future VOCs detection systems.

5.5. References

1. Guo, H., Lee, S. C., Chan, L. Y. & Li, W. M. Risk assessment of exposure to volatile organic compounds in different indoor environments. *Environ. Res.* **94**, 57–66 (2004).

2. Wieslander, G., Norbäck, D., Björnsson, E., Janson, C. & Boman, G. Asthma and the indoor environment: The significance of emission of formaldehyde and volatile organic compounds from newly painted indoor surfaces. *Int. Arch. Occup. Environ. Health* **69**, 115–124 (1996).

3. Çankaya, S., Pekey, H., Pekey, B. & Özerkan Aydın, B. Volatile organic compound concentrations and their health risks in various workplace microenvironments. *Hum. Ecol. Risk Assess.* **26**, 822–842 (2018).

4. Nabizadeh, R., Sorooshian, A., Delikhoon, M., Baghani, A. N., Golbaz, S., Aghaei M., &

Barkhordari, A. Characteristics and health effects of volatile organic compound emissions during paper and cardboard recycling. *Sustain. Cities Soc.* **56**, (2020).

5. Son, Y. S., Lim, B. A., Park, H. J. & Kim, J. C. Characteristics of volatile organic compounds (VOCs) emitted from building materials to improve indoor air quality: Focused on natural VOCs. *Air Qual Atmos Heal.* **6**, 737–746 (2013).

6. Peñuelas, J. & Llusià, J. Plant VOC emissions: Making use of the unavoidable. *Trends Ecol. Evol.* **19**, 402–404 (2004).

7. Filley, C. M., Halliday, W., & Kleinschmidt-DeMasters, B. K. The effects of toluene on the central nervous system. *J. Neuropathol. Exp. Neurol.* **63**, 1–12 (2004).

8. Spinelle, L., Gerboles, M., Kok, G., Persijn, S. & Sauerwald, T. Review of portable and low-cost sensors for the ambient air monitoring of benzene and other volatile organic compounds. *Sensors* **17**, 1–30 (2017).

9. Schnelle Jr, K. B., Dunn, R. F., & Ternes, M. E. *Air pollution control technology handbook*. (CRC press, 2015).

10. Viespe C., & Miu, D. Characteristics of surface acoustic wave sensors with nanoparticles embedded in polymer sensitive layers for VOC detection. *Sensors* **18**, 1–9 (2018).

11. Silva, L.I.B., M-Costa, A., Freitas, A. A., Rocha-Santos, T. A. P., & Duarte, A. C. Polymeric nanofilm-coated optical fibre sensor for speciation of aromatic compounds. *Int. J. Environ. Anal. Chem.* **89**, 183–197 (2014).

12. Wen, Z. & Tian-mo, L. Gas-sensing properties of SnO_2 – TiO_2 -based sensor for volatile organic compound gas and its sensing mechanism. *Phys. B Phys. Condens. Matter* **405**, 1345–1348 (2010).

13. Baimpos, T., Gora, L., Nikolakis, V. & Kouzoudis, D. Selective detection of hazardous VOCs using zeolite/Metglas composite sensors. *Sensors Actuators, A Phys.* **186**, 21–31 (2012).

14. Baimpos, T., Boutikos, P., Nikolakis, V. & Kouzoudis, D. A polymer-Metglas sensor used to detect volatile organic compounds. *Sensors Actuators, A Phys.* **158**, 249–253 (2010).

15. Vellingiri, K., Kumar, P. & Kim, K. Coordination polymers : Challenges and future scenarios for capture and degradation of volatile organic compounds. *Nano Res.* **9**, 3181–3208 (2016).

16. Li, Y., Xiao, A., Zou, B., Zhang, H., Yan, K., & Lin, Y. Advances of metal – organic frameworks for gas sensing. *Polyhedron* **154**, 83–97 (2018).

17. Li, H. Y., Zhao, S. N., Zang, S. Q. & Li, J. Functional metal-organic frameworks as effective sensors of gases and volatile compounds. *Chem. Soc. Rev.* **49**, 6364–6401 (2020).

18. Vellingiri, K., Kumar, P., Deep, A. & Kim, K. H. Metal-organic frameworks for the adsorption of gaseous toluene under ambient temperature and pressure. *Chem. Eng. J.* **307**, 1116–1126 (2017).

19. Shi, X., Zhang, X., Bi, F., Zheng, Z. Sheng, L., Xu, J., Wang, Z., & Yang, Y. Effective toluene adsorption over defective UiO-66-NH2 : An experimental and computational exploration. *J. Mol. Liq.* **316**, 113812 (2020).

20. Fernandez, E., G. Saiz, P., Perinka, N., & Fernandez, de Luis, R. Metal-Organic Framework based printed capacitive sensor for Volatile Organic Compounds detection. *Adv. Funct. Mater.* (Under review)

21. Gotrik, K. W. Flow controlled solvent vapor annealing of block copolymers for lithographic applications. (2013).

22. Perry's Chemical Engineers Handbook, McGraw-Hill, 1999.

23. Atalay, S., Kaya, H., Atalay, F. E., Izgi, T. & Kolat, V. S. Formation and detection of magnetic CoNiFe nanowire network using magnetoelastic sensor. *J. Supercond. Nov. Magn.* **32**, 3907–3913 (2019).

24. Atalay, S., Izgi, T., Kolat, V. S., Erdemoglu, S. & Inan, O. O. Magnetoelastic humidity sensors with TiO2 nanotube sensing layers. *Sensors* **20**, 1–12 (2020).

25. Zheng, X., Liu, S., Rehman, S., Li, Z. & Zhang, P. Highly improved adsorption performance of metal-organic frameworks CAU-1 for trace toluene in humid air via sequential internal and external surface modification. *Chem. Eng. J.* **389**, (2020).

26. Qin, N., Xiang, Q., Zhao, H., Zhang, J. & Xu, J. Evolution of ZnO microstructures from hexagonal disk to prismoid, prism and pyramid and their crystal facet-dependent gas sensing properties. *CrystEngComm* **16**, 7062–7073 (2014).


Chapter
6

Conclusions and open perspectives

Finalmente, en este último capítulo se resumen los resultados obtenidos a lo largo de esta investigación así como las conclusiones más importantes derivadas de los mismos: Desde el efecto de la geometría del resonador en las propiedades magnéticas y magnetoelásticas de los resonadores magnetoelásticos hasta la aplicación de los sensores magnetoelásticos, funcionalizados con MOFs, para la detección de compuestos orgánicos volátiles y metales pesados. Pasando por la síntesis de dichos MOF así como por los métodos de funcionalización empleados junto con sus ventajas y desventajas. Por otro lado, los frentes abiertos de este trabajo así como los posibles pasos a seguir en el futuro se describen también.

Content

6.1. General conclusions

The main conclusions derived from this thesis are collected on the following. More detailed conclusions can be found at the end of each chapter. In general, the initially proposed key objectives of this thesis have been satisfactorily fulfilled, opening new research possibilities to be explored in the future.

- ✓ It has been duly proved that the magnetoelastic response of the resonators, and more concretely their mass sensitivity, can be significantly improved by shaping them in geometries having sharp edges. Moreover, that sensitivity can be further enhanced by reducing the resonator length or by performing partial coatings at the tips of the magnetoelastic resonant platform. An analysis of the magnetic microstructure confirms that the presence of smaller magnetic domains at these regions/geometries is one of the factors that governs the improved sensitivity response of the novel resonator platforms.

- ✓ MOFs have been successfully integrated as active layers in Metglas 2826MB magnetoelastic resonators. Spray coating has proven to be the most optimal methodology to obtain heavy and homogeneous MOF active layers in a fast, easy and repetitive way. Moreover, the synthesis of the MOF active layer at the resonator's surface is an optimal method to directly grow MOFs layers with better adhesion to the MR supports, but is restricted to soft MOF synthesis conditions that do not alter the ferromagnetic resonator.

- ✓ The generation of linker defects and the addition of functional groups in the UiO-66 framework improves its chromium adsorption/reduction capacity. The sensitivity of the MR platforms to the viscosity of the liquid media is also higher when using rhombic resonator instead of rectangular ones. Finally, it has been demonstrated that wireless chromium detection in liquid media by using MOF/magnetoelastic devices is feasible, but MOF attachment to the MR should be improved in order to prevent its detachment when introduced into liquid solutions

- ✓ Magnetoelastic resonators functionalized with MOFs active layers were successfully applied on the selective wireless detection of a specific VOC (toluene). It was proved that the mass of the MOF active layer plays a very important role in the overall sensor response since, the higher MOF active layer mass, the higher the frequency shift and

henceforth, the more accurate the quantification of smaller VOCs concentration in the environment. A 10 mm rhombic sensor functionalized with the UiO66-NH_2 MOF presented a sensitivity of 0.27 Hz/ppm to the presence of toluene. Furthermore, an enhanced selectivity towards toluene has been observed when comparing with other gases such as acetone, ethanol and water.

6.2. Open perspectives and future work

The advances made throughout this work have opened a room of new perspectives for the future improvement of the magnetoelastic wireless sensors performance. In particular, it would be interesting to focus the future work in the different research points detailed below:

- The analysis of the different parameters affecting the sensitivity of magnetoelastic platforms and the exploration of new geometries leading to magnetic microstructures with smaller magnetic domains located at specific regions of the resonator.
- Look for new magnetoelastic compositions with improved properties such: higher quality factor or enhanced corrosion resistant.
- Post annealing treatments together with their thickness reduction would be very interesting approaches to further improve their magnetoelastic response.
- Improve the adhesion between the MOF active layers and the MR platforms by exploring new functionalization techniques, such as electrochemical growth of MOFs or their blending with polymeric binders.
- Improve the detection process of heavy metals using magnetoelastic sensors. Set up a system for continuous water flow with variable HMs concentration and try to study the in-situ photoreduction process of HMs in MOF/Metglas platforms.
- Improve the VOCs flux set-up in order to reduce the accessible VOC concentration at the flux below 1 ppm or integrate more than 2 gas types in the same flux. This type of experimental set-up will open the possibility to test the performance of the multiple sensors.

- Explore the possibility to adapt the full experimental set-up as an equipment to determine the gas/vapour adsorption capacity of porous/sorbent materials supported on MR.
- Explore alternative applications of MOF/Metglas systems, such as selective quantification of temperature, viscosity or concentration of specific vapours on high concentrated gas industrial streams.

Annex A

Experimental techniques

Content

A.1. Magnetoelastic resonant platforms fabrication and characterization

A.1.1. Magnetoelastic materials – Metglas 2826MB alloy

Magnetoelastic sensor platforms are commonly based on amorphous ferromagnetic alloys, usually metallic glasses, with high mechanical tensile strength, high magnetostriction and high magnetoelastic coupling, which allow for an efficient conversion between elastic and magnetic energies. Magnetoelastic ribbons are usually fabricated by the melt spinning technique or by sputtering deposition techniques [1,2].

Commonly used magnetoelastic materials for sensing applications include several iron-rich alloys combined mostly with nickel or cobalt as well as with other metals in smaller proportions (such as boron, molybdenum or silicon). In particular, Metglas 2826MB amorphous ferromagnetic alloy is the most employed material for magnetoelastic sensing applications due to its good magnetic and magnetoelastic properties. Other magnetoelastic alloys, both commercially available as well as home-fabricated, have also been reported. Some commercial alloys employed for magnetoelastic sensing applications include other Metglas alloys [3] such Metglas 2605SA1 ($Fe_{90}Si_5B_5$), Metglas 2828CO ($Fe_{67}Co_{18}B_{14}Si_1$) or Metglas 2605S3A ($Fe_{77}Cr_2Si_5B_{16}$) as well as Vitrovac alloys [4] such Vitrovac 4040 ($Fe_{39}Ni_{39}Mo_4Si_6B_{12}$) or Vitovac 7600 ($Fe_{64.5}Co_{18}B_{16}Si_1C_{0.5}$). In addition, different home-made alloys has been employed for magnetoelastic sensing applications such: $Fe_{77.5}Si_{7.5}B_{15}$ [5], $Fe_{79}B_{21}$ [6], $Fe_{83}Ga_{17}$ [7] or $Fe_{64}Co_{17}Si_{6.6}B_{12.4}$ [8] alloys, among others. As could be observed, all of them consist on iron rich alloys.

Throughout this thesis, Metglas 2826MB amorphous ferromagnetic alloy has been mainly used as the magnetoelastic platform materials due to its good magnetic and magnetoelastic properties such as high magnetoelastic coupling *(0.98)*, high saturation magnetostriction *(12 ppm)* and high saturation magnetization *(0.88 T).* Besides, this alloy shows high corrosion resistance which makes it ideal to be used in harsh environment sensing applications. All these properties, as well as its low cost, makes this alloy perfect to be used for different biological or chemical sensing applications.

The most important physical and magnetic properties of Metglas 2826MB alloy obtained from the Metglas technical bulletin together with the material composition obtained from the material safety datasheet are collected in **Table A.1** [9].

Table A.1. Physical and magnetic properties and compositional information of Metglas 2826MB alloy.

Magnetic and Physical Properties		Composition	
Saturation Induction (T)	0.88	**Ingredient name**	**Weight (%)**
Saturation Magnetostriction (ppm)	12	Boron	1-5
Curie Temperature (ºC)	353	Iron	40-50
Crystallization Temperature (ºC)	410	Molybdenum	5-10
Density (g/cm^3)	7.90	Nickel	40-50
Elastic Modulus (GPa)	100-110	Cobalt (trace impurity)	0.3 (max)

As could be observed, the exact composition of the Metglas 2826MB alloy is not given (just wt% interval). Moreover, when consulting other articles to give an exact composition, it is found that different articles present different compositions for the Metglas 2826MB. For that reason, the real composition of the Metglas 2826MB alloy used in that work was analyzed by means of EDX. The obtained wt% composition was: $Fe_{41}Ni_{48}Mo_7B_4$, what is between the range displayed by the Metglas datasheet. Thus, the composition of the Metglas 2826MB ribbons in atomic percentage is $Fe_{37}Ni_{42}Mo_4B_{17}$.

Metglas alloy was obtained commercially from Metglas®, Inc in the form of a long strip roll with 30 μm of thickness and 6mm in width. Then, the magnetoelastic resonators were cut in the desired shape by using a picosecond pulsed laser. This technique is described in the following.

A.1.2. Picosecond pulsed laser

Commonly used methods for magnetoelastic sensors shaping include micro-dicing saw, polishing, direct scissor cuts, pulsed laser ablation or Computer Numerical Control (CNC) milling. Other times, resonators are directly fabricated in the desired shape by using techniques of microelectronics fabrication (*eg. sputtering+lift-off*). In this work, cutting of the magnetoelastic resonators with different sizes and shapes was carried out

by using a picosecond pulsed laser. A detailed description of the employed equipment is presented below. The use of this technique has result crucial in order to obtain repeatability and avoid edge defects that are usually obtained when using other methods such as scissors or the micro dicing saw.

Picosecond pulsed laser ablation technology is a very common and versatile technique used for micropatterning or surface texturing of different types of materials, such polymers, ceramics, glass or metals [10]. With this technique, any desired pattern in the micro and nano levels can be developed by adjusting the pulses energy, frequency and overlapping distance.

The equipment employed in this thesis is property of Tekniker foundation (Guipúzcoa, Spain). It consists on a picosecond pulsed Nd:YVO_4 laser (RAPID: Lumera Laser, Germany) integrated in a micromachining workstation (3D Micromac, microStruct). The laser is able to deliver 10 ps pulses at different wavelengths (1064, 532 and 355 nm) and with a repetition rate ranging from 4 to 1000 Hz. The spot diameter is less than 50 µm. Laser position can be adjusted with a X-Y-Z stage system with a high resolution in the µm range. Images of the equipment used are shown in **Figure A.1**.

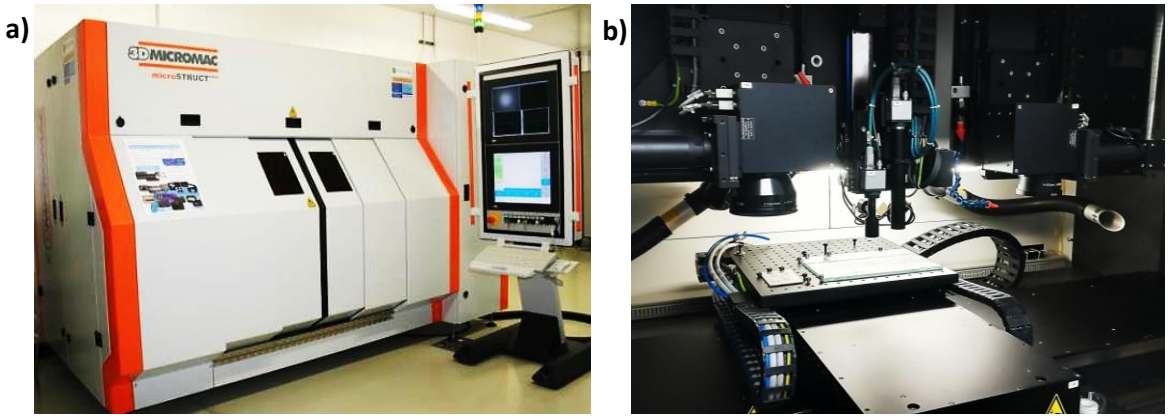

Figure A.1. (a) 3D Micromac microStruct workstation and (b) laser source and cutting place located inside the workstation.

Using this equipment, long magnetoelastic ribbons were laser-irradiated in order to cut them in different geometries and sizes. After the laser treatment, a complete analysis was performed to analyze the repeatability of this technique and if the amorphous character of the ribbons is maintained after laser heating. As far as we know, no studies have been performed about the effect of that kind of lasers in magnetoelastic alloys such

Metglas. However, in other materials (such as sapphire [11]) it has been shown that while slow milliseconds pulsed laser excitation produces thermal melting, nanosecond or picoseconds pulses ablate via electron sputtering and no produce thermal melting. Anyway, in order to confirm the inexistence of grain nucleation or crystallization, SEM and XRD analysis were performed both at the centre and at the edges of the laser-cut samples. Looking at the SEM images (**Figure A.2**a), it could be observed that the edge is not affected by the pulsed laser. Just 3 μm of the edge looks some change. In the same way, the XRD measurements were performed at the centre and the edge of the cut sample and in the non-processed ribbon (**Figure A.2**b). As can be observed the results are similar for all the samples and just the common Metglas peak present at around 45° is observed for all the samples which clearly indicate the absence of any crystallization as a consequence of the laser irradiation.

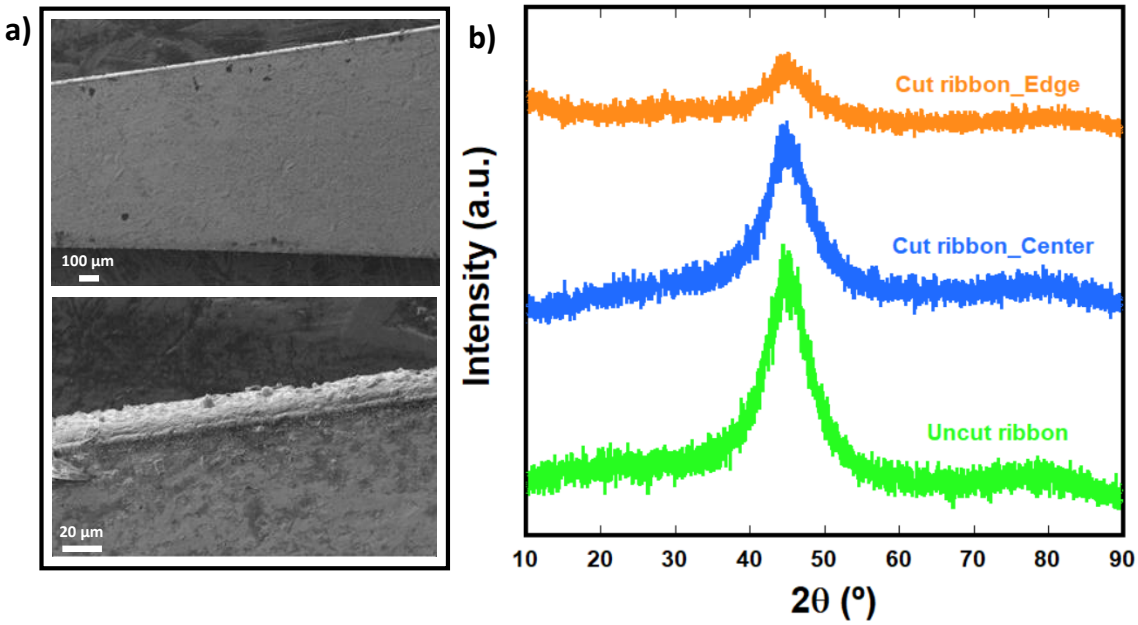

Figure A.2. (a) SEM images of a laser cut magnetoelastic ribbon. (b) XRD patterns of the centre and the edge of a laser cut ribbon and of an uncut ribbon.

A.1.3. Magnetoelastic characterization

The magnetoelastic resonance behaviour of the different sensor platforms, as well as the derived parameters, were characterized with the magnetoelastic resonance detection system located at BCMaterials. The system consists on 2 coaxial solenoids, where the external solenoid generates a DC magnetic field (or bias) of 138.2 Oe/A for amplification

of the signal through an HP 6653A DC power supply and the inner solenoid (primary coil) applies the AC magnetic field of small amplitude (36.9 Oe/A) which drives the sample to the resonance. Then, the induced signal in the sample is measured through an air compensated pick-up coil (secondary coil) placed within the two coaxial solenoids, and is then displayed in an HP3589A spectrum analyzer. This spectrum analyzer allows to observe the induced signal in a wide frequency range (between 10 Hz and 150 MHz) and also provides the AC voltage to excite the resonator magnetically via the primary coil. The whole process is fully automatized and data is recorded in the computer. Two programs in the computer are assigned to the measurements system, one for measuring the resonance frequency as a function of the applied DC magnetic field and the other to measure the resonance frequency as a function of the time at a fix DC magnetic field. A scheme of the experimental set-up, together with the real system, is shown in **Figure A.3**.

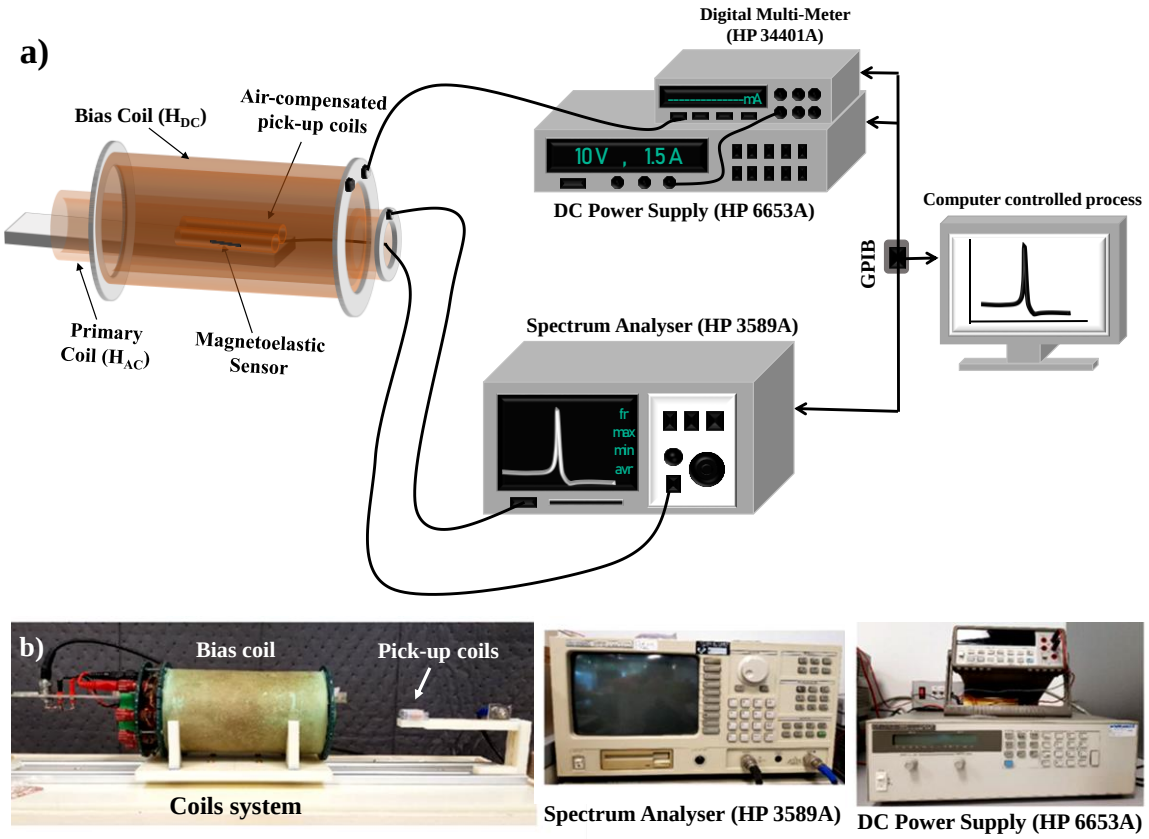

Figure A.3. Scheme of the experimental set-up used for the magnetoelastic characterization measurements.

The magnetoelastic resonance frequency of the magnetoelastic ribbons as a function of the applied magnetic field can be measured using this set-up. A common representative curve of the dependence of the magnetoelastic resonance frequency with the magnetic

field (measured for a 25mm x 5mm x 30μm rectangular Metglas resonator) is shown in **Figure A.4**a as an example. This curve is represented with five different points marked, which correspond with five characteristic fields. In particular, the most characteristic field in that curve are the minimum applied field which is almost 0 (H_0), the applied field at the minimum of the curve which is related with the anisotropy field (H_k) and the magnetic field at the magnetic saturation (H_s). Then the H_d and H_u fields are random values between the other fields which study is also important. The magnetoelastic resonance frequency curves measured at all these magnetic fields are represented in **Figure A.4**b.

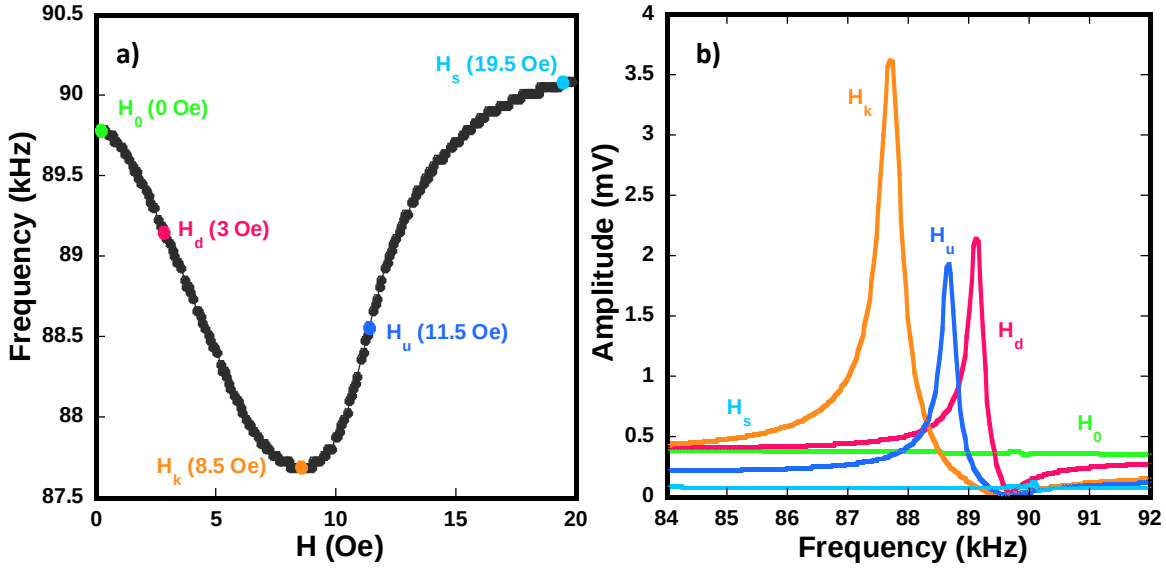

Figure A.4. (a) Dependence of the magnetoelastic resonance frequency with the applied magnetic field, (b) Resonance frequency curves measured at the different magnetic fields marked in (a).

As could be observed, the bias magnetic field affects clearly to the resonance frequency value as well as to the signal intensity and quality. This is related with the dependence of the sample elasticity (Young modulus) with the applied magnetic field (the so-called ΔE effect). In particular, the amplitude of the resonance depends on the applied magnetic field being it maximum at a value which corresponds to the anisotropy field of the sensor (H_k) and minimum at the saturation field (H_s). This is the reason why all the performed measurements in that work have been measured at this anisotropy field at which the signal amplitude is maximum.

Besides, the main magnetoelastic parameters of the sample can be derived from the magnetoelastic resonance frequency curve and its dependence with the applied field. In particular, the Young modulus (and the derived ΔE effect) and the magnetoelastic coupling coefficient of the previous sample could be obtained from **Figure A.4**a by using equations (A.1) and (A.2), respectively [12,13]:

$$E(H) = \rho(1-v)(2Lf_r)^2 \tag{A.1}$$

$$k^2 = \frac{\pi^2}{8}\left[1-\left(\frac{f_r}{f_a}\right)^2\right] \tag{A.2}$$

where E is the Young modulus, ρ is the density, v is the Poisson coefficient, L is the length and f_r and f_a are the resonance and antiresonance frequencies of the magnetoelastic resonator, respectively. The dependence of these magnetoelastic parameters with the applied magnetic field for the previous sample are represented in **Figure A.5**.

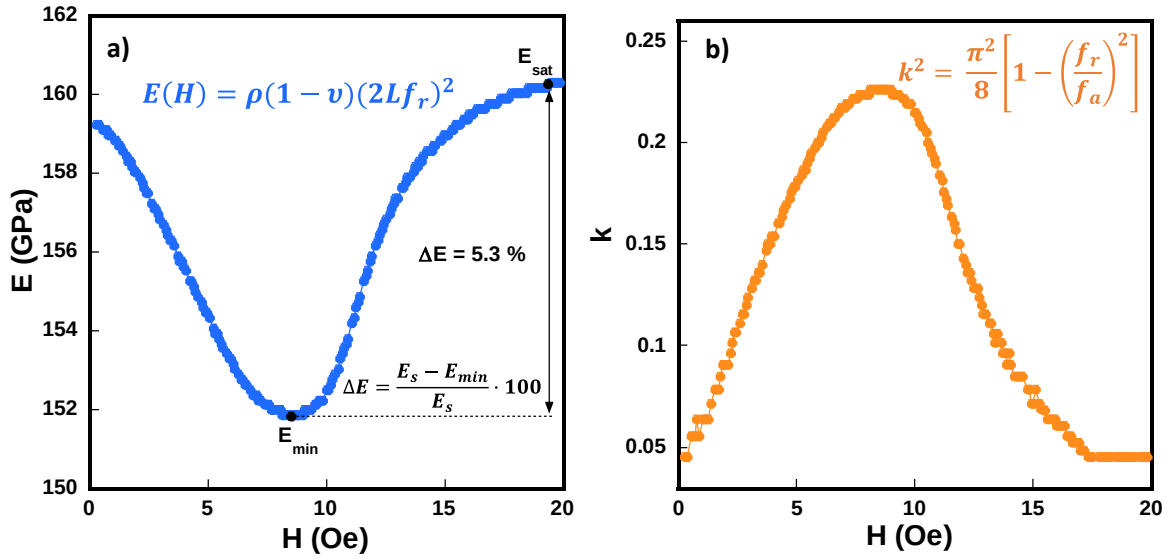

Figure A.5. Dependence with the magnetic field of the: (a) Young modulus and (b) Magnetoelastic coupling coefficient in a 25 mm x 5 mm rectangular Metglas resonator.

As could be observed the young module of a magnetoelastic resonator depends a lot of the applied magnetic field having that the minimum value is found at the anisotropy field (H_k). That dependence of the young modulus with the magnetic field is related with the

so-called ΔE effect which could be derived from the maximum and minimum values of the Young modulus by using the equation showed in **Figure A.5**a. This ΔE effect depends on factors such as the length to width relation, the geometry or the composition of the magnetoelastic ribbons. Respect to the magnetoelastic coupling, it could be observed that the tendency of this parameters is inverse to that of the Young's modulus having that the maximum magnetoelastic coupling coefficient is found at the anisotropy field (H_k), which is the field of maximum resonance amplitude.

Finally, the resonance quality factor *(Q)* is the parameter that quantifies the energy losses of the resonator and is related with the sharpness of the measured resonance frequency curve. In particular, a higher Q value is related with low energy losses and is translated into a narrower and sharper resonance curve while a small Q value is related with a higher rate of energy losses which is translated into a wider resonance curve. Quality factor is usually calculated from the resonance curve as [14]:

$$Q = \frac{f_r}{\Delta f} \tag{A.3}$$

where f_r is the resonance frequency and Δf the full width at half maximum intensity.

A.1.4. Magnetic characterization

The magnetic properties of the magnetoelastic samples were also analyzed by measuring their macroscopic and microscopic hysteresis loops and also their magnetic domains structure. In particular, the magnetic microstructure of the magnetoelastic samples has been investigated by means of magneto-optic Kerr effect (MOKE) microscopy imaging [15]. This technique is based on the magneto-optic Kerr effect, which is related to the changes on the polarization of a reflected light from a magnetic surface. In particular, the observed changes on the light polarization from the magnetic surface will depend on the magnetization state of the sample, which therefore allow for a direct examination of its magnetic microstructure or magnetic domains [16]. This technique allows for measuring local microscopic hysteresis loops but, it should be noted that just the qualitative comparison between coercive fields in different samples could be performed and extrapolated to the macroscopic behaviour but this is not valid for the saturating fields as these depend on the local magnetism of the sample an hence will vary a lot from one zone to other. Moreover, the magnetic domains could be observed by this

technique and their size could be also indicative of the magnetic properties of the sample. In particular, smaller magnetic domains accumulate less (exchange) energy in the domain boundaries and thus smaller applied magnetic field are needed to flip these domains toward saturation which is directly related to lower saturation and coercive fields while bigger domains need higher magnetic fields to flip the domains.

In this work, an Evico–Zeiss Magneto-Optical Kerr Microscope has been employed for the microscopic hysteresis loops measurements. An image of that system is shown in **Figure A.6**a. Moreover, the macroscopic hysteresis loops of the samples have been measured by using a classical inductive hysteresis loop tracer. In this set-up the magnetic field is generated by a pair of Helmholtz coils driven by a KEPCO BOP 20-20M bipolar power supply at a given frequency. A pick-up coil where the sample is placed together with a compensation coil, are located between the big coils. An image of this set-up is shown in **Figure A.6**b.

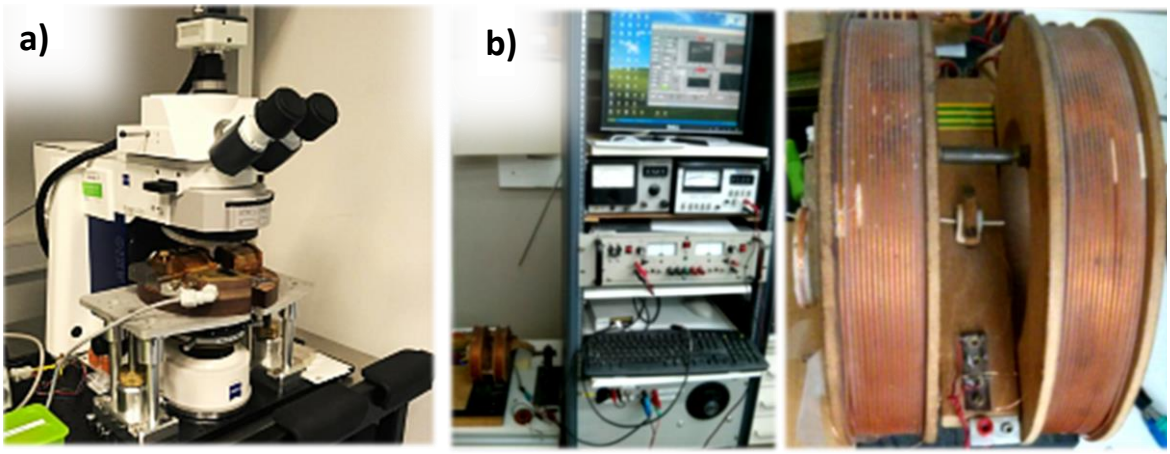

Figure A.6. (a) Evico–Zeiss Magneto-Optical Kerr Microscope, (b) Inductive hysteresis loop tracer system (left) and detail of the Helmholtz coils (right).

A.1.5. COMSOL simulations

Theoretical simulations of the characteristic resonance frequencies of different sensor platform analyzed along this thesis, as well as simulations of the gold mass loadings into the resonator's surface have been carried out by using Finite Element Analysis (FEM). The purpose of those simulations is to obtain the characteristic resonance frequency of the pure longitudinal vibration for the different samples. This task was performed through an eigenfrequency study in COMSOL Multiphysics. In this way, it must be noted

that just pure elastic waves spreading along the different geometries have been considered.

First of all, the 3-D solid structures of the different geometries were defined. These built structures are free to move in any direction, without any constraint. A fine tetrahedral mesh was used for the simulations. Then, the elastic parameters of the Metglas® 2826MB previously defined (Young's modulus (E) ranging between 151 and 154 GPa depending on the sample, density (ρ) of 7900 kg/m^3 and Poisson's ratio (ν) of 0.33 [17]) were introduced and the simulated resonance frequencies were obtained. In order to obtain the longitudinal resonance frequency of each sample iterative simulations were performed until a convergence solution with a precision of 10e^{-6} was achieved. Finally, in order to simulate the frequency shift under a mass load and the derived mass sensitivities, a new layer was defined on the resonator surface with the elastic parameters of the gold given in the COMSOL materials library (Young's modulus (E) of 70 GPa, density (ρ) of 19300 kg/m^3 and Poisson's ratio (ν) of 0.44) and the theoretical resonance frequency after the gold deposition, and hence the frequency shift, were obtained. An image of the COMSOL working panel during the simulations performance is shown in **Figure A.7**.

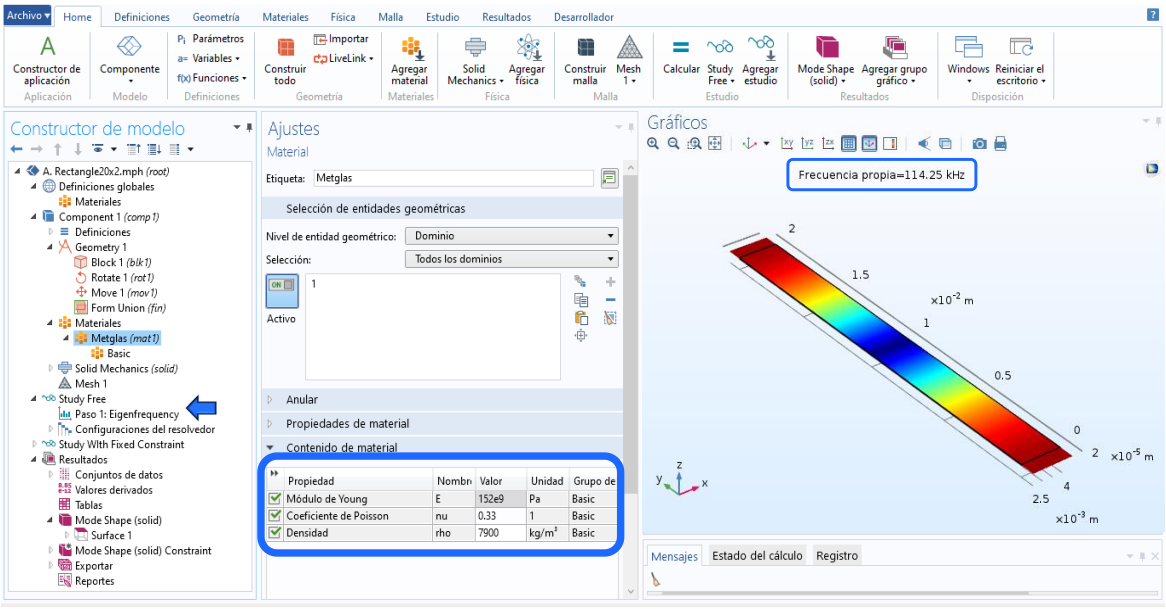

Figure A.7. COMSOL working panel during the simulations performance for a rectangular Metglas resonator of 20 mm in length.

A.1.6. Gold Sputtering for constant mass deposition

The effect of mass deposition and subsequent analysis of the corresponding sensitivity was studied by sputtering a gold layer on the surface of the cleaned ribbons using a Quorum Q150TS turbo pumped coater. That equipment is shown in **Figure *A.8***a. In order to determine the Au deposition rate (as mass/cm^2), a calibration curve was performed by using a high precision balance (0.1 μg sensitivity) after each deposition cycle. The calibration curve measured is shown in **Figure *A.8***b together with an optical microscope image of a rectangular resonator sample after the gold deposition (**Figure *A.8***b). The mass loading deposition rate obtained with the employed conditions (30 mA, 30 s) was 16 ± 0.5 μg/cm^2. It should be noted that the Metglas® 2826MB strips have one rough and one smooth side, due to their fabrication process. In order to keep systematic measurements, the Au mass deposition was always carried out in the smooth side of the ribbons. Resonance frequency shift was measured after each gold deposition in order to estimate the mass sensitivities of the resonators. Different masks were fabricated for the partial coatings.

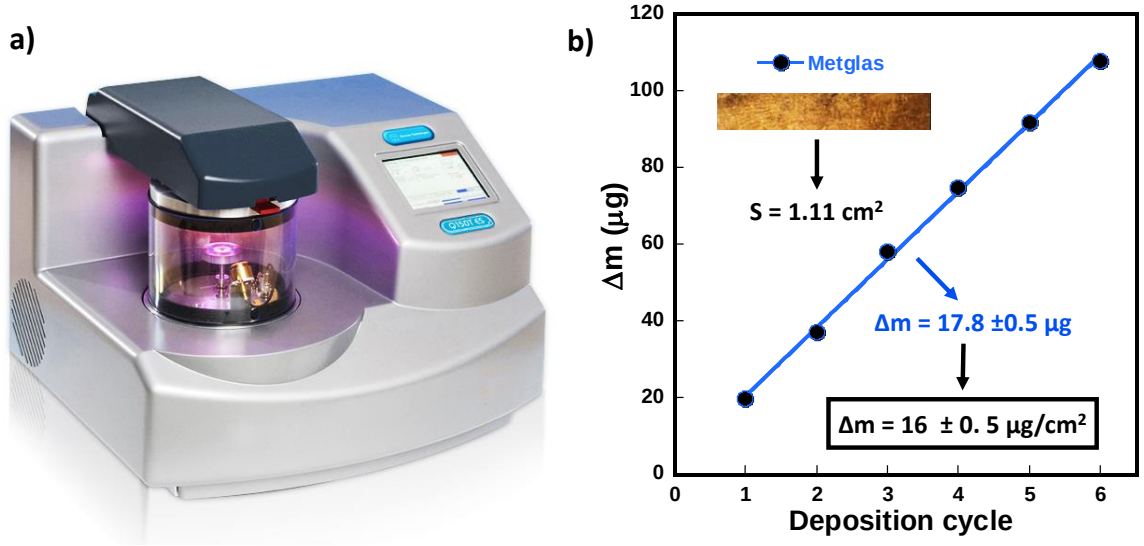

Figure A.8. (a) Quorum Q150TS turbo pumped coater from BCMaterials, (b) Calibration curve measured for the successive gold depositions in a Metglas ribbon of 1.11 cm^2.

A.2. MOFs synthesis and characterization

A.2.1. MOFs synthesis

- *Chemicals*

Along this thesis, different MOFs with different modifications have been synthesized in order to improve their VOCs or HMs adsorption capacities. The synthesis process of these MOFs as well as all the modifications carried out are described in detail in Chapter 3. A list of all the reagents employed for the MOFs synthesis is collected herein.

Zirconium (IV) chloride (98%, Alfa Aesar, Germany), Terephthalic acid (BDC) (97%), 2,5-Dihydroxyterephthalic acid (doBDC) (98%) and 2-Aminoterephthalic acid (BDC-NH2) (99%) from Sigma Aldrich, were used for the UiO-66-R MOFs synthesis. Zinc acetate dihydrate (99%, Sigma-Aldrich) and cobalt acetate tetrahydrate (98%, Sigma-Aldrich) were used as the metal source and 2-methylimidazole (99%, Sigma Aldrich) was used as the linker in the ZIF8 and ZIF67 MOFs synthesis. In general, Methanol (Labkem 99.9%, Germany) and N,N-dimethylformamide (DMF) (99.8%, Sigma Aldrich) were used as solvents and hydrochloric acid (37%, PanReac), acetic acid (99%, Fisher) and distilled water as modulators. All chemicals were used as provided.

- *ZIF8 and ZIF67 synthesis*

The synthesis of ZIF based MOFs have been so easy since it is performed in water and at room temperature[18]. For the ZIF8 synthesis, zinc acetate or zinc nitrate are usually used as the metal source while for the ZIF67 synthesis, cobalt acetate or cobalt nitrate are employed. Moreover, the organic ligand employed consist on 2-Methylimidazole (mIM). In the synthesis process, 0.45g of the metal salt is dissolved in 3 mL of water and 2g of the organic ligand are dissolved separately in 20 mL of water. Once dissolved, the metal solution is added to the 2-methylimidazole solution and the mixture is left under magnetic stirring for 24 hours at room temperature. After that, the precipitate is centrifuged and washed with methanol. The solvent exchange process is repeated three times in order to remove all the unreacted products. Finally, the washed MOF is separated from the solvent by centrifugation, dried overnight in an oven at 80 °C and ground with a mortar and pestle.

- *UiO-66-R synthesis*

As explained in Chapter 3, the synthesis conditions applied to obtain the UiO-66-R and UiO-66-R-def materials has been directed to i) generation of linker defective positions within the UiO-66 type crystal framework by adding HCl in the synthesis process, and ii) to incorporate $-NH_2$ and –OH electron donor functional groups in the structure by modifying the ligand reagent. UiO-66-R samples were prepared through a slightly modified solvothermal synthesis [19,20]. As a general protocol, $ZrCl_4$ is first dissolved in DMF. Subsequently, the organic ligand and HCl (in the case of defective samples) are added to the solution, leading to a white or yellow suspension in the reactors vessel. Finally, water is added as a particle size modulator. The mixture is stirred during 10 min at room temperature, sealed in a 100 mL glass reactor vessel (Pyrex®) and then placed in an oven at 80 °C for 24 h. After the reaction, the vessel is cooled naturally to room temperature in the oven. The precipitate is centrifuged and washed with methanol three times. Subsequently, the obtained precipitate is dried at 80 °C [21,22]. All the reactive amounts used on the different synthesis carried out are summarized in **Table 3.2**.

A.2.2. X-ray diffraction (XRD)

X-ray diffraction is one of the most important experimental techniques in the field of crystalline materials characterization. X-ray diffraction allows, among other facts, to analyze the crystalline structure of the materials, since the X-rays radiation wavelength (λ) is in the magnitude order of the interatomic distance. The operation of X-ray diffraction is based on the fact that when the X-rays reach the material atoms, they are scattered. The radiation emitted by each atom expands as a wave and interferes with that created by the surrounding atoms. These interferences can be destructive or constructive. The constructive ones occur at certain angles (θ) that satisfy the Bragg's law [23]:

$$n \cdot \lambda = 2\, d_{hkl} \cdot \operatorname{sen}\, \theta \qquad \text{(A.4)}$$

where λ is the wavelength of the incident X-rays (1.5406 Å for the kα Cu line), n is the diffraction order, d_{hkl} is the interplanar distance (with h, k and l the Miller indices) and θ is the angle which forms the refracted angle with the normal. X-ray diffraction process is schematically illustrated in **Figure A.9**.

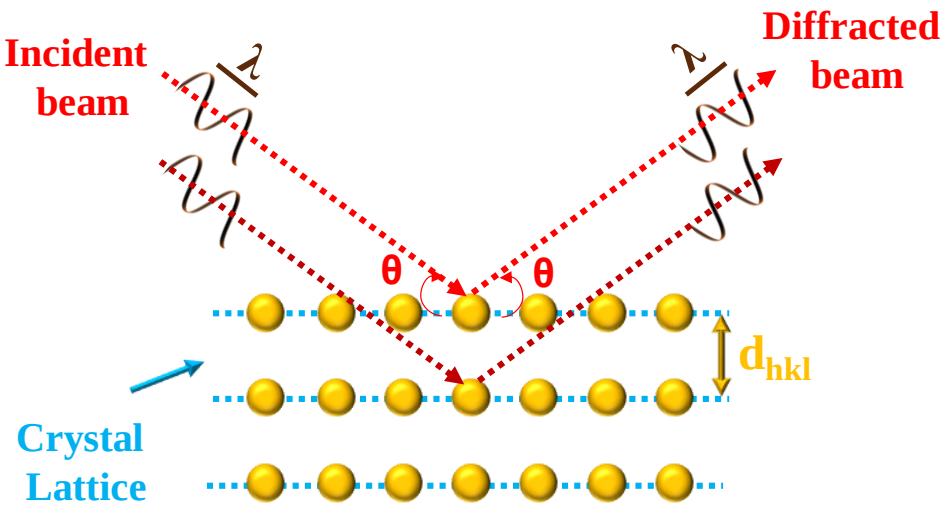

Figure A.9. Scheme of the X-ray diffraction process.

Diffractometers allow to accurately determine the direction in which that diffraction occurs. X-ray diffraction patterns presented along this work have been measured in a Panalytical X´pert PRO diffractometer with CuK$_\alpha$ radiation (λ=1.5406Å) in the range of 5<2θ<70° with a step size of 0.05° and an exposure time of 10 s at room temperature. Panalytical X´pert is a polycrystalline sample diffractometer with theta-theta geometry, a programmable slit, secondary graphite monochromator adjusted to a copper radiation and fast solid state PixCel detector adjusted to a 3.347° active length in 2θ(°). The equipment allows to perform quality measurements for the subsequent data processing, at the level of full profile adjustments without/with a structural model. Image of that system is shown in **Figure A.10**a.

Moreover, X-ray diffraction temperature dependence patterns have been measured using a Bruker D8 Advance Vantec diffractometer with also CuK$_\alpha$ radiation (λ=1.5406Å) equipped with a variable-temperature stage HTK2000. The evolution of the peaks position and intensity with the temperature is usually analyzed in order to study the stability of the compound. Diffractograms were recorded from 30 to 600°C each 10°C in the range of 6<2θ<38° with a step size of 0.03° and an exposure of 10 s per step. Image of that system is shown in **Figure A.10**b. Both diffractometers belong to the General Research Services (SGIker) of the UPV/EHU.

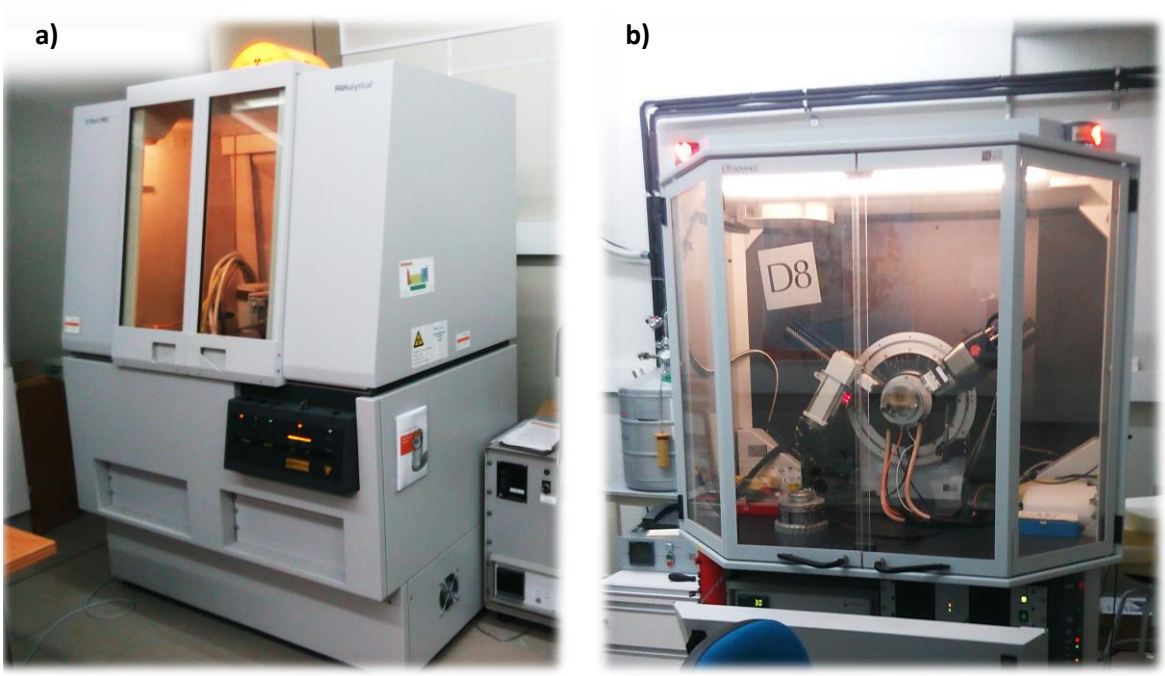

Figure A.10. (a) Panalytical X´pert PRO diffractometer and (b) Bruker D8 Advance Vantec diffractometer from the General Research Services (SGIker) of the UPV/EHU.

The X-ray diffraction results are collected on a diffractogram representing the intensity of the diffracted radiation that reaches the detector as a function of the 2θ angle. In this diffractogram, a series of peaks that occur for those values of θ that comply with Bragg's law (**Equation A.4**) could be observed. Each crystalline solid presents a characteristic diffractogram, as if it were its fingerprint. In order to obtain information from the diffractograms, it is necessary to make an analysis of them taking into account the position of the diffraction maxima, their profile and their intensity. Among the information that can be obtained from the X-ray diffractograms are the space group and the network parameters or the average size of the particles.

To obtain that parameters the results are commonly analyzed by using different programs, such as FullProf or TOPAS, and are compared with those present in a database in order to study the crystalline structure of the sample by using a refinement method, such as the Rietveld method. The Rietveld method consists on a theoretical least squares adjustment of the full diffraction pattern to a profile calculated for a structural model in order to refine the crystal structures and obtain the structural and profile parameters. Along this thesis, full peak fit profile matching of the samples has been performed in order to confirm the absence of impurities and analyze the structure of the samples.

A.2.3. Fourier-transform infrared spectroscopy (FTIR)

Another important technique widely used in both organic and inorganic materials characterization is the Fourier-transform Infrared Spectroscopy (FTIR). This technique allows measuring the infrared spectrum of a solid, liquid or gas in order to identify specific functional groups or organic molecules present in the material. In this technique, the sample is irradiated with infrared radiation in a wavelength range and the molecules absorb the frequencies that are characteristic of their structure [24]. That is, absorption bands occur when the absorbed radiation matches the vibrational frequency of the molecules.

In order to absorb in the infrared range, the molecules must undergo a change in the dipole moment as a consequence of its vibrating or rotating movement. In particular, the radiation can interact with the molecule and cause changes in the amplitude of some of its movements. If the frequency of the radiation matches the natural vibration frequency of the molecule, a net transfer of energy takes place, causing a change in the amplitude of the molecular vibration and the infrared absorption as a consequence.

Two basic types of vibrations can be distinguished: stretching and bending. A stretching vibration implies a continuous change in the interatomic distance along the axis of the bond while the bending vibrations are characterized by a change in the angle between two bonds. A scheme of that vibration modes is collected in **Figure A.11**a.

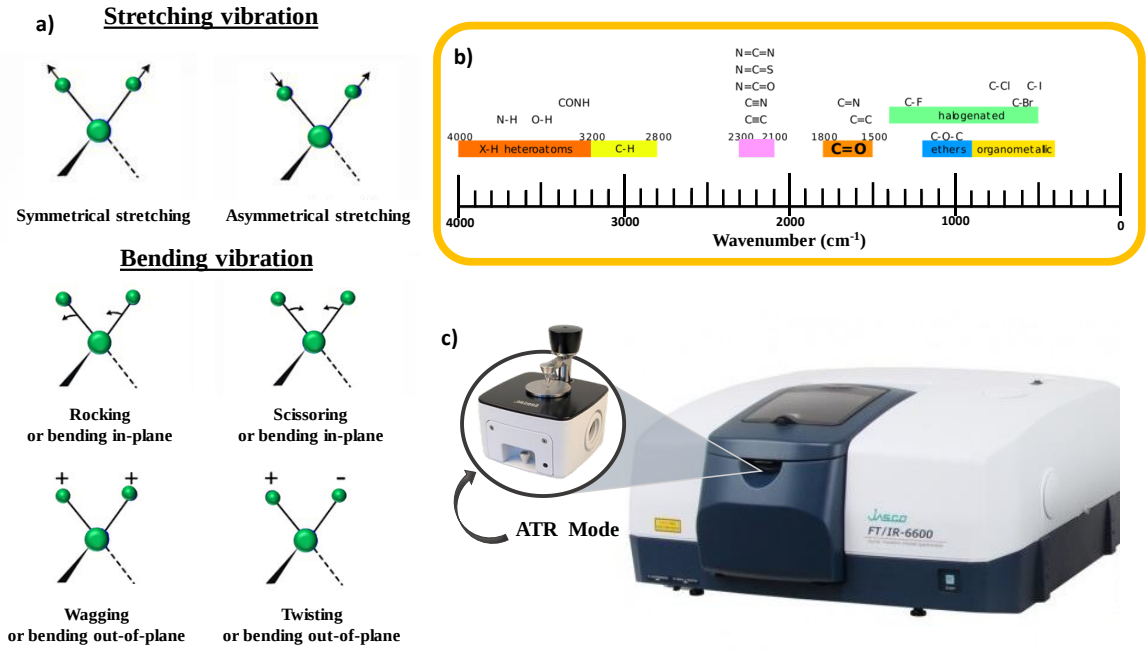

Figure A.11. (a) Vibrations modes (+ indicates upward movement and - indicates downward movement), (b) examples of links assigned to the different areas of the IR spectrum and (c) Jasco FT/IR-6100 spectrometer with the ATR accessory.

The signal resulting from the Fourier-transform Infrared Spectroscopy measurement is a spectrum that represents the molecular "footprint" of the sample which is characteristic of its chemical structure. Thus, by analyzing the wavelengths at which a compound absorbs in the infrared zone, information about the molecules present in the material can be obtained. The spectrum is usually interpreted in two regions; i) The functional groups region which is found in the medium infrared zone (between 4000 and 1300 cm^{-1}) where a series of bands assigned to the vibration of just two atoms of the molecule appear and ii) the so-called fingerprint region which is found in the far infrared (between 1300 and 400 cm^{-1}) where the assignment of the absorption bands to molecular vibrations is more complicated since each one is generated by individual absorptions. The positions of these bands and the vibrations assigned to them are usually collected in different tables. A scheme of the range in which some of the most important bands appear is represented in **Figure A.11**b.

Along this work, Fourier-transform infrared spectroscopy (FTIR) spectra have been measured using a Jasco FT/IR-6100 spectrometer in Attenuated Total Reflectance mode (FTIR-ATR). Each spectrum was recorded from 600 to 4000 cm^{-1} with a 1 cm^{-1} resolution.

64 scans were measured and averaged to obtain the final spectra. The use of this technique has been very useful for identifying the existence of the functionalization groups introduced in the different MOFs. An image of the equipment is shown in **Figure A.11**c.

A.2.4. Thermogravimetric analysis (TGA)

Thermal analysis techniques are techniques of great importance in the characterization of materials since they allow to analyze the dependence of the physical and chemical properties of the sample with the temperature. Among these techniques, thermogravimetric analysis (TGA) stands out for MOFs characterization since it allows to determine the variation in the sample mass as a function of the temperature and, therefore, to study the sample degradation processes (decomposition, oxidation or other processes such as vaporization or desorption).

A thermogravimetric analysis consists of the continuous measurement of the mass of a sample while it is subjected to a temperature programme in a controlled atmosphere. The mass variation as a function of temperature is collected in a curve known as a thermogram. This curve provides information on the processes that the sample undergoes during heating. This technique is usually used in combination with other techniques such as the Differential Scanning Calorimetry (DSC) in order to obtain complementary information on the kind of processes (endothermic or exothermic) that occur in the sample during the temperature change.

Thermogravimetric analysis (TGA) presented in this work has been performed under synthetic air (25 mL/min) with a NETZSCH STA 449F3 DSC–TGA thermobalance instrument. This equipment allows adjusting the heating rate, controlling the measurement atmosphere and selecting the temperature program. Measurements have been performed by heating an alumina crucible containing the powder sample at 5 °C/min in the temperature range of 30–700 °C under synthetic ait (25 mL/min). The used equipment is shown in **Figure A.12**a.

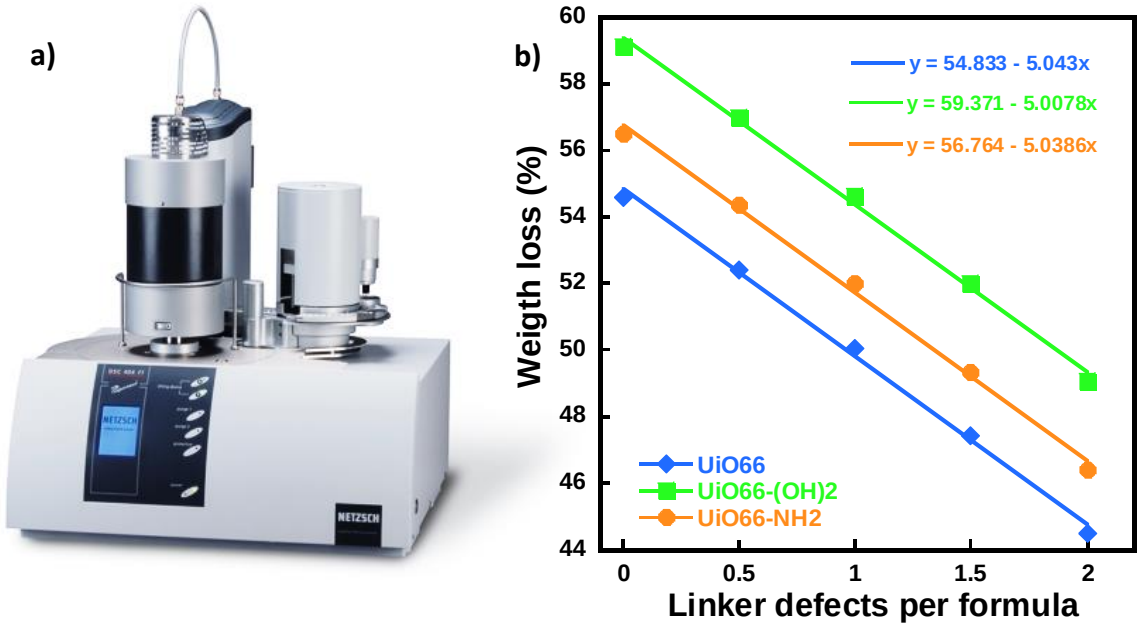

Figure A.12. (a) NETZSCH STA 449F3 thermobalance from the IMaCris group (UPV/EHU), (b) Theoretically calculated weight loss associated to linker defects in UiO-66-R (R=-H, NH_2, $(OH)_2$ compounds.

Thermogravimetric analysis has been especially useful to quantify the defect degree within the UiO-66-R MOFs structure. The linker-defect positions average per formula was estimated from the weight loss associated with the organic linker calcination step (at an approximately temperature of 300 °C) [25] observed in the TGA curve. The TGA curves exhibit three important weight loss steps. The first one (in the temperature range between 30 to 100 °C) is related to the release of the solvent trapped within the porous framework. The second one (from 100 to 300 °C) is related to the de-hydroxylation and de-hydration of the Zr-hexanuclear clusters. Finally, the third step is ascribed to the previously mentioned calcination of the organic linkers, which induces the collapse of the crystal framework [26,27].

Assuming that the complete dehydration of the zirconium hexanuclear clusters of the UiO-66-R MOFs occurs before the organic linker calcination step, the theoretical weight loss associated to the linker release can be calculated based on the **Equation A.5**.

$$Zr_6O_{6+x}(Linker)_{6-x} \rightarrow Zr_6O_{12} \qquad (A.5)$$

where x is the defect degree. The theoretical % weight losses assigned to the different samples formula are collected in **Table *A.2***. The calculated weight losses as a function of the ligands number for the different UiO-66-R samples are represented in **Figure A.12**b. From those curves, the experimental defects per formula in the UiO-66-R samples have been determined from the experimental weight losses.

Table A.2. Theoretical weight loss assigned to the organic linker calcination in UiO-66-R samples (UiO-66, UiO-66-NH_2 and UiO-66-$(OH)_2$) calculated for different defects degrees.

	Defects degree	Formula	Molecular Weight Formula	Molecular Weight (Zr_6O_{12})	Weight Diff	% Diff
UiO-66	0	$Zr_6O_{6,0}(BDC)_{6,0}$	1628,03016		888,693	54,587
	0,5	$Zr_6O_{6,5}(BDC)_{5,5}$	1553,97238		814,635	52,423
	1	$Zr_6O_{7,0}(BDC)_{5,0}$	1479,9146	739,337	740,578	50,042
	1,5	$Zr_6O_{7,5}(BDC)_{4,5}$	1405,85682		666,520	47,410
	2	$Zr_6O_{8,0}(BDC)_{4,0}$	1331,79904		592,462	44,486
UiO6-NH_2	0	$Zr_6O_{6,0}(BDC\text{-}NH2)_{6,0}$	1699,98		960,643	56,509
	0,5	$Zr_6O_{6,5}(BDC\text{-}NH2)_{5,5}$	1619,92		880,583	54,359
	1	$Zr_6O_{7,0}(BDC\text{-}NH2)_{5,0}$	1539,86	739,337	800,523	51,987
	1,5	$Zr_6O_{7,5}(BDC\text{-}NH2)_{4,5}$	1459,81		720,473	49,354
	2	$Zr_6O_{8,0}(BDC\text{-}NH2)_{4,0}$	1379,76		640,423	46,415
UiO-66-$(OH)_2$	0	$Zr_6O_{6,0}(BDC\text{-}(OH)2)_{6,0}$	1807,92		1068,583	59,106
	0,5	$Zr_6O_{6,5}(BDC\text{-}(OH)2)_{5,5}$	1718,87		979,533	56,987
	1	$Zr_6O_{7,0}(BDC\text{-}(OH)2)_{5,0}$	1629,82	739,337	890,483	54,637
	1,5	$Zr_6O_{7,5}(BDC\text{-}(OH)2)_{4,5}$	1540,78		801,443	52,015
	2	$Zr_6O_{8,0}(BDC\text{-}(OH)2)_{4,0}$	1451,73		712,393	49,072

A.2.5. Scanning and transmission electron microscopies (SEM/TEM)

Scanning electron microscopy (SEM) as well as transmission electron microscopy (TEM) have been used to study the morphology and composition of the samples used throughout this work as well as the MOF active layers. Electron microscopy techniques allow to obtain morphological, topological and compositional information of a sample and also producing high-resolution images of the same from the interaction of an electron beam with the sample.

Electron microscopy is based on the use of an electron beam instead of a light beam to form an image [28]. A scheme of the components of a SEM and a TEM compared with a light microscope is shown in **Figure A.13**a. Thus, electron microscopy techniques are based on the analysis of the effects produced by the interaction of the sample with the electron beams, in which different absorption and emission processes are produced. In particular, the scanning electron microscope produces images of a sample by scanning the surface of the sample with the electron beam while in the transmission electron microscope some of the electrons pass through the sample and form the image. Both are very powerful magnification techniques that can provide much information about the sample, from the morphological properties to the composition. Also, it is very useful to analyze fractures, surface contamination or layer thicknesses among many others.

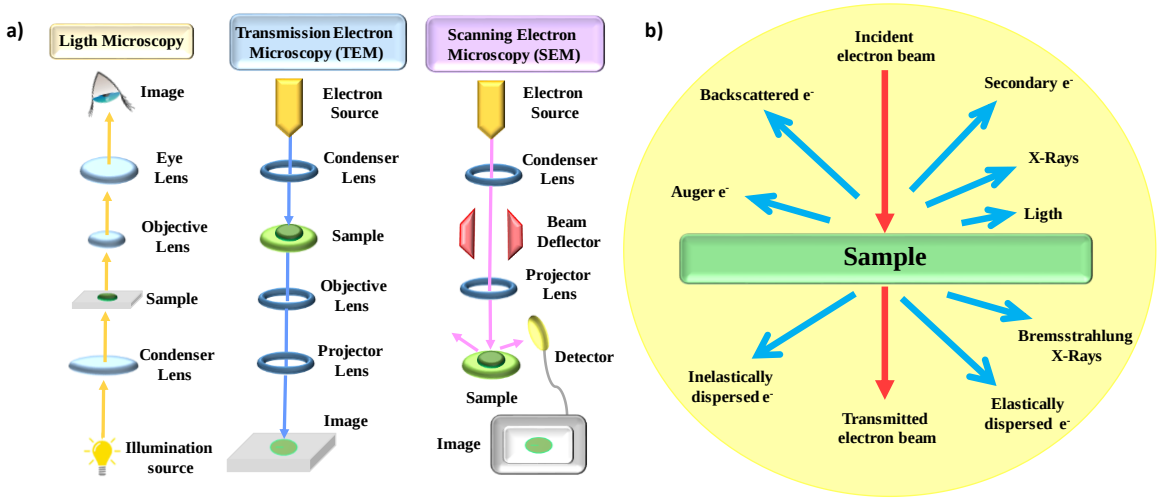

Figure A.13. (a) Scheme of the principal components of a light microscope, a transmission electron microscope (TEM) and a scanning electron microscope (SEM). (b) Effects produced on a sample when irradiated with an electron beam.

The interaction of the electron beam with the sample produces different signals that are amplified by the lens and detected by a series of detectors that form the image. The different signals produced when the electron beam interacts with the sample are collected in **Figure A.13**b. Scanning Electron Microscopy (SEM) analyses secondary and backscattered electrons, while Transmission Electron Microscopy (TEM) analyses scattered electrons (passing through the sample). In addition, these devices usually include an energy dispersive X-rays (EDX) detector, which allows to analyse the sample composition.

Along this thesis, the morphologies of the samples as well as the properties of the active layer have been investigated using two different scanning electron microscopes, a SEM (JEOL JSM-7000F) with an accelerating voltage of 5 kV from the SGIker and a SEM-EDX (Hitachi TM3000) with less resolution from the Science and Technology Faculty (UPV/EHU). Prior to analysis, samples were coated with a gold layer of 15 nm using the Quorum Q150TS turbo pumped coater previously described. Moreover, the transmission electron employed has been a Philips Supertwin CM200 TEM, also from the SGIker. This TEM operate at 200 kV and is equipped with a LaB_6 filament and EDAX-DX-4 microanalysis system. The equipment incorporates double tilting sample holder, a Megaview III rapid acquisition camera, and a high resolution (4k x 4k) and high sensitivity digital camera. The three instruments used are shown in **Figure A.14**.

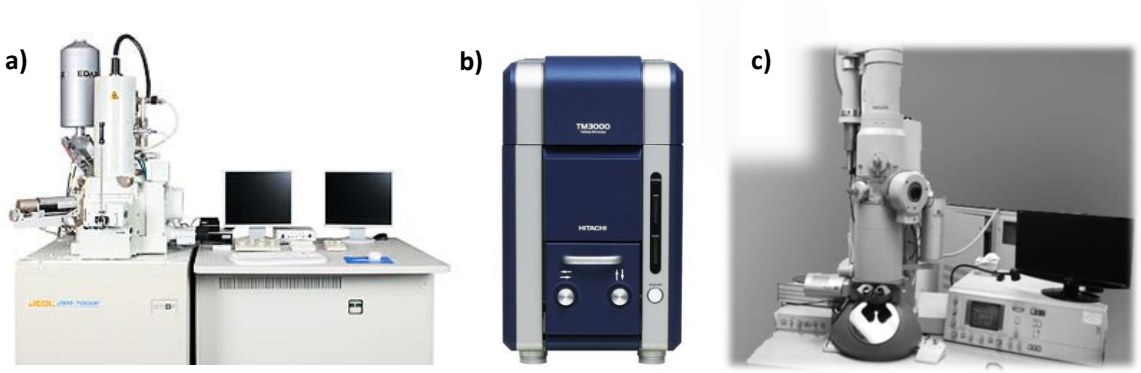

Figure A.14. Scanning and Transmission Electron Microscopies used: (a) JEOL JSM-7000F SEM, (b) Hitachi TM3000 SEM and (c) Philips Supertwin CM200.

In addition, SEM-EDX (Hitachi TM3000) was also employed for analyze the magnetoelastic sample's composition with the X-ray energy dispersive (EDX) analyzer which includes. Dispersive X-rays are other important emission resulting from the interaction of the electron beam with the sample. The analysis of these X-rays by EDX spectroscopy allows investigating the sample composition since the energy and wavelength of these rays is characteristic of the elements present in the sample.

The EDX analysis process consists on stimulate the emission of this X-rays from the sample with a high-energy electron beam. This incident beam excites an electron in an inner shell of the sample, and eject it from the shell while creating an electron-hole which is then filled by an electron from an outer shell. This jump involves the release of energy,

in the form of X-rays, which is characteristic of the atomic structure of the emitting element. So, the number and energy of this dispersed X-rays are measured by the EDX detector allowing to figure out the elemental composition of the sample.

A.2.6. N_2 adsorption-desorption isotherms

Gas adsorption isotherms measurement is one of the most important techniques for the characterization of MOF materials since it offers information about the surface area and the porosity distribution (pores size and volume) in these materials. These measurements are based on the analysis of the amount of gas physically adsorbed in the material surface and how it adsorbs it.

Adsorption is defined as a process in which atoms, ions, or molecules of gases or liquids are trapped or held in the surface of a solid material. The amount of gas adsorbed on a material depends on parameters such as the interaction energy between the gas and the solid, the temperature or the pressure. It should be noted that the estimation of the "surface area" parameter is highly important in the characterization of this type of materials since it gives an idea of the material adsorption capacity. This parameter includes the outer surface of the particles plus the available surface inside the pores. Commonly used gases for that purpose are nitrogen or carbon dioxide.

The total surface area is usually calculated from the isotherm curve measured for the compound. There are five different isotherms types which are related to different adsorption modes [29]. A type II isotherm very common in MOF type materials is represented in **Figure A.15**a as an example. As could be observed, different adsorption process occurs in the sample. The Brunauer-Emmett-Teller (BET) surface area of the samples is obtained by analyzing the monolayer adsorption zone [30] (marked in **Figure A.15**a).

Along this work, N_2 adsorption-desorption isotherms have been measured using an iSorb HP1 high-pressure gas sorption Quantachrome instrument (**Figure A.15**b). Approximately 10-20 mg of the MOF sample were employed in each experiment. Prior to the measurement, samples were degassed at 120°C in high vacuum for at least 12 h. The surface area values were obtained by fitting the adsorption data to a linearized form of the BET model [31]. The correlation coefficient was higher than 0.999 for all samples. These

measurements give an idea of the adsorption capacity of the samples (in relation to their surface area) and allow analyzing the different modifications carried out in the MOFs.

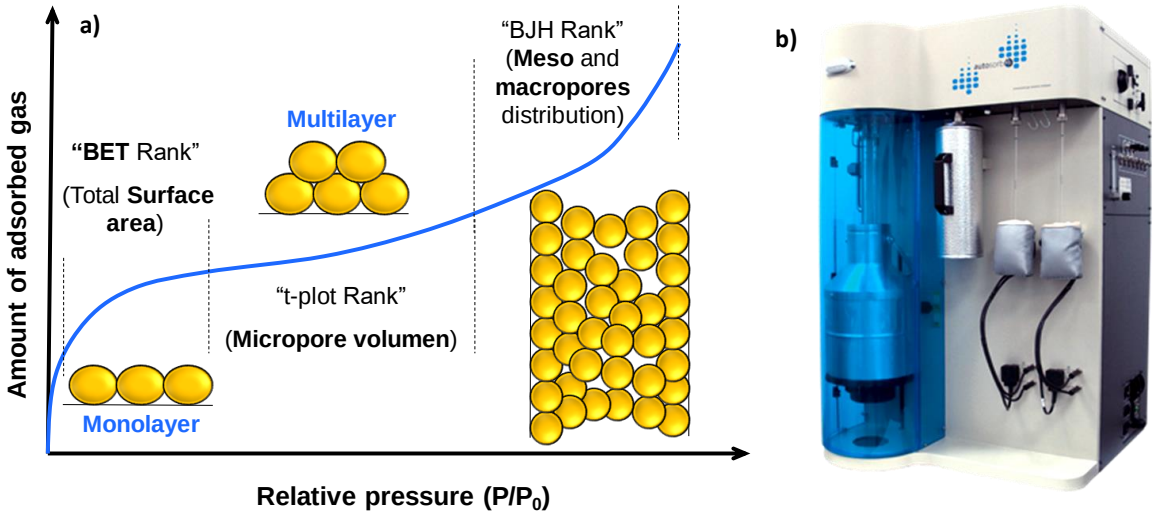

Figure A.15. (a) Type II adsorption isotherm with the most important zones marked (monolayer and multilayer adsorption) and (b) iSorb HP1 high-pressure gas sorption Quantachrome instrument from the UPV/EHU.

A.2.7. Multiple headspace solid-phase microextraction (MHS-SPME)

Multiple headspace solid-phase microextractions (MHS-SPME) were employed in order to analyze the VOCs adsorption capacity of the powder MOFs as well as of the functionalized sensors. This technique is ideal for the quantitative and qualitative analysis of samples with volatile or semi-volatile organic compounds.

Headspace solid-phase microextraction has proven to be very useful in the determination of different compounds. However, it should be kept in mind that the results of this measurement depend largely on the matrix, especially in solid samples. For this reason, multiple extractions born as a solution to improve this problem since the effect of the matrix is eliminated at a large extent when making several continuous extractions. In that context, it could be considered that the sum of infinite successive extractions gives the total area of the analyte, allowing to estimate the analyte amount present in the sample [32]. This can be reduced to a finite number of extractions having that the total analyte are (A_T) is given by [33]:

$$A_T = \sum_{i=1}^{\infty} A_i = \frac{A_1}{1-\beta} \quad \text{(A.6)}$$

where i is the extraction number, A_1 is the area of the first extraction peak and β is a constant calculated from the linear regression of the individual peaks areas. This constant is obtained by representing the logarithm of the i-th extraction area ($\ln A_i$) as a function of the (i-1) value, having that:

$$\ln A_i = \ln A_1 + (i-1) \cdot \ln \beta \quad \text{(A.7)}$$

Thus, the β factor is obtained from the slope ($ln\,\beta$) of the linear adjustment. Then, the total area (A_T) could be estimated from β allowing to obtain the analyte mass adsorbed in the sample ($m_{analyte}$) by using a calibration reference taking into account that:

$$m_{analyte} = \frac{\sum A_{T\,analyte}}{\sum A_{T\,reference}} \cdot m_{reference} \quad \text{(A.8)}$$

where $m_{reference}$ is the known reference mass, $A_{T\,reference}$ is the total area estimated for the calibration reference sample and $A_{T\,analyte}$ is the total area estimated for the analyte sample.

In order to perform these measurements and Agilent HP 6890 Gas Chromatograph coupled to an Agilent HP5973 Mass Spectrometer with a COMBI PAL injector (CTC Analytics) has been used. The injector worked in split mode (split ratio 1:100). An image of the equipment property of the SGIker (UPV/EHU) is shown in **Figure *A.16***a. Prior to the experiment, samples were exposed to a VOC rich atmosphere for 60 minutes. As the concentration of the target VOC used during the static adsorption stage is high, it is foreseen that obtained adsorption capacity values during desorption will be near the maximum adsorption capacity of the MOF material. Afterwards, seven successive extractions were performed in order to determine the VOC adsorption capacity of the MOFs while just one extraction was performed in order to determine the ability of the functionalized sensors to adsorb VOCs.

Since the MOF was an unknow matrix for us, several experiments were performed in order to tune this technique. Initially, the experiments were with a sample mass of 0.02g and with a desorption temperature of 70 °C during 20 minutes. After the first experiments different things were observed: i) The amount of MOF is so high, the signal should be diluted, so the sample mass could be much less, ii) A higher desorption temperature improve the desorption process on the sample and iii)10 minutes under desorption are

enough. So, the final experiment conditions were adjusted to: A desorption temperature of 150 °C during ten minutes and a sample mass of about 2 mg. Thus, successive desorption cycles in the MOF samples with the adsorbed VOC were performed, quantifying the peak area at each microextraction cycle. In addition, the calibration process was carried out in the same experimental conditions, but with a known volume of the VOC (toluene) which is translated into a known VOC mass ($m_{reference}$) for a given total area *(A_T)*. The calibration process was carried out by performing the experiment in the same experimental conditions with a known amount of the target VOC (toluene). In particular, 0.2 µL of toluene (which are translated into 173.4 µg) were used to measure the calibration curve. This calibration curve is shown in **Figure *A.16***b.

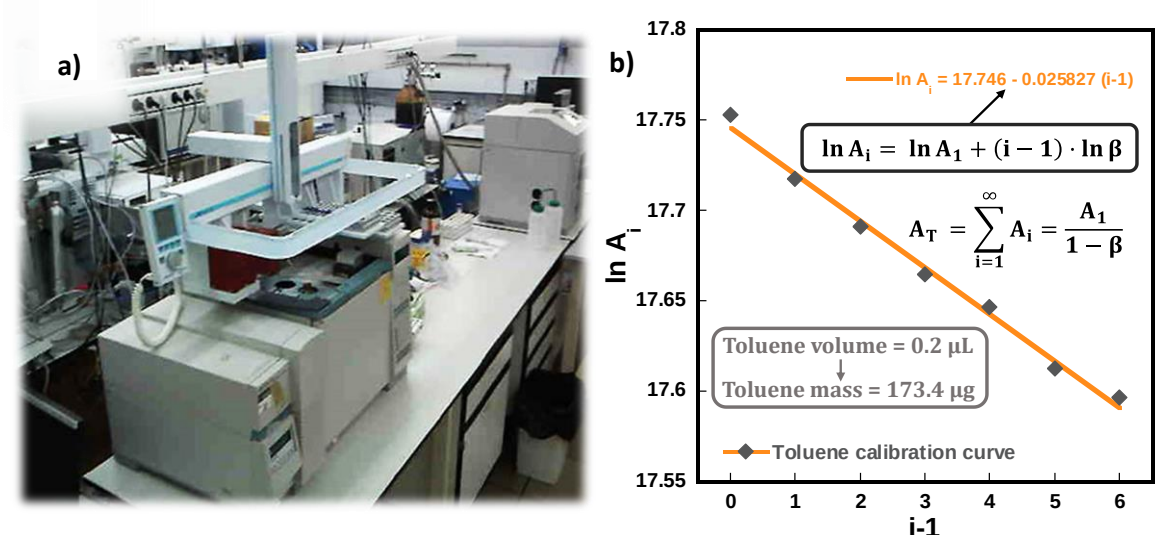

Figure A.16. (a) Agilent HP 6890 gas chromatograph coupled to an Agilent HP5973 mass spectrometer from the SGIker (UPV/EHU) and (b) Calibration curve obtained for a toluene volume of 0.2 µL.

A.2.8. Heavy metals adsorption experiments

In order to carry out the heavy metals (HMs) adsorption experiments, solutions with different concentrations were obtained by diluting the 200 ppm stock solutions of potassium dichromate ($K_2Cr_2O_7$) and chromium chloride ($CrCl_3$) with deionized water. pH of the chromium solutions was kept below 3.5 to prevent chromium oxide precipitation. The absence of chromium oxide precipitation was confirmed experimentally by monitoring the Cr^{III} concentration on the Cr^{III} stock solution over a period of two months, which remained constant. In order to measure the isotherms and

the kinetics curves, the adsorbent concentration was fixed to 1g/L for the adsorption isotherms and 0.25g/L for the kinetics. All the studies were conducted stirring at 400 rpm at room temperature. Kinetics curves were measured by adding 100 mg of MOF in 100 mL of chromium solution and taking samples at different times (0, 5, 10, 15, 30, 60 and 120 minutes). Isotherm curves were obtained by measuring six different concentrations points (5, 10, 15, 25, 50 and 100 ppm). For that, 10 mg of the MOF were added to 10mL of the chromium solutions and left in agitation for 24 hours. Obtained samples were filtered using a PTFE syringe filter with a pore size of 0.22 µm and then acidified with nitric acid. Adsorbents were dried and collected for future characterization after the adsorption kinetics experiments. A scheme of the adsorption experiments performed is shown in **Figure A.17**.

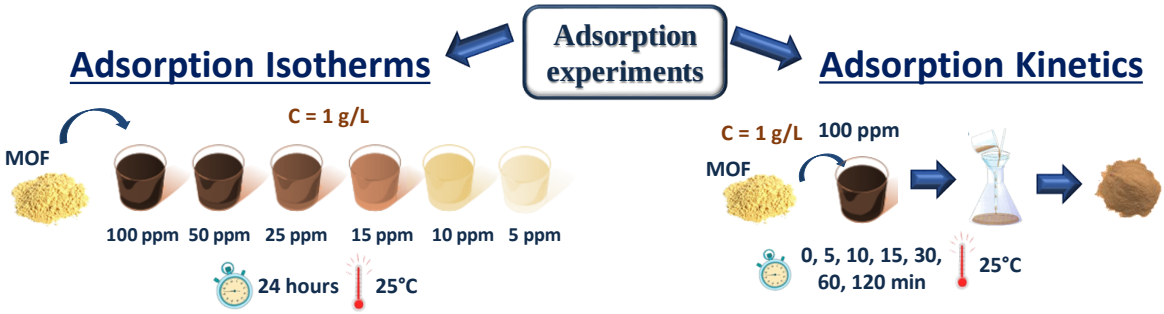

Figure A.17. Scheme of the heavy metals adsorption experiments carried out.

The final concentration of the Heavy Metals solutions was determined by means of atomic emission spectroscopy (ICP-AES), described in section A.2.12. Finally, different adsorption models were used to fit the adsorption isotherms and adsorption kinetics data. The correlation of the experimental adsorption data with that theoretical models is crucial for understanding the adsorption process in the sample. The employed models to fit the experimental results are described below.

The Langmuir model is widely employed to fit adsorption isotherms and determine the isotherm parameters. This model is given by [34]:

$$q_e = q_m K_L \frac{C_e}{1+K_L C_e} \quad \text{(A.9)}$$

where q_e is the adsorption capacity (mg·g^{-1}) at equilibrium conditions, q_m is the maximum adsorption capacity, C_e is the equilibrium concentration and K_L is the Langmuir constant.

The Freundlich model has also been employed to fit the isotherms data and compared with the Langmuir model. This model is given by [34]:

$$q_e = K_F C_e^{1/n} \quad \text{(A.10)}$$

where again q_e is the adsorption capacity (mg·g^{-1}) at equilibrium conditions, q_m is the maximum adsorption capacity, C_e is the equilibrium concentration and K_L and n are constants for a given adsorbate and adsorbent at a particular temperature.

The Bangham's Model has been used to fit the kinetics data. This model is given by [35]:

$$q_t = k_t \cdot t^{1/m} \quad \text{(A.11)}$$

where q_t is the amount of adsorbate adsorbed at a time t, 1/m provides an idea of the kinetics order of the system and k_t is the constant rate of the adsorption process.

The Pseudo First Order and the Pseudo Second Order Model were also employed to fit the adsorption kinetics results. These models are given by **equations A.12 and A.13**, respectively [35].

$$\frac{dq_t}{dt} = k_1(q_e - q_t) \quad \text{(A.12)}$$

$$\frac{dq_t}{dt} = k_2(q_e - q_t)^2 \quad \text{(A.13)}$$

where k_1 (min^{-1}) is the pseudo first order constant rate and k_2 (min·g·mg^{-1}) is the pseudo second order constant rate.

A.2.9. Photoreduction experiments

Photocatalysis is a highly employed process for the removal of heavy metals. In that work, photo-reduction experiments have been conducted in 5 ppm Cr^{VI} solution under UVA light. MOF concentration was fixed to 0.25 g/L. Thus, 50 mg of the MOF were immersed in 200 mL of a 5 ppm Cr^{VI} solution under stirring in dark. Once adsorption equilibrium conditions are achieved (after 1 hour), light is turned on and 5 mL aliquots are taken at different times under illuminated conditions. LuzChem LZC-4V photoreactor equipped with 14 lamps emitting in the ultraviolet range was used for the photo-reduction experiments. This equipment belongs to the University of Chile. A picture of the

photoreactor (inside and outside) during a photoreduction experiment under UVA light is shown in **Figure A.18.**

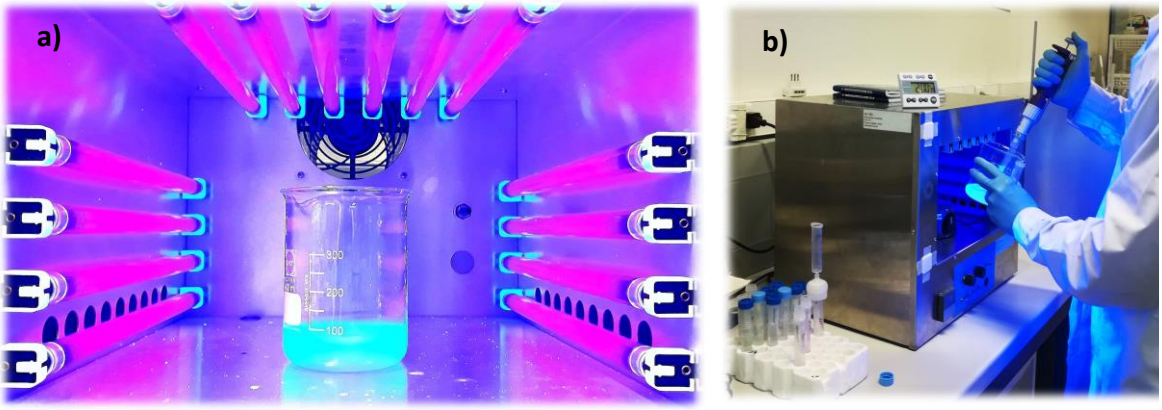

Figure A.18. LuzChem LZC-4V photoreactor (a) Inside and (b) outside during a photoreduction experiment with UVA light.

A.2.10. Electron paramagnetic resonance (EPR)

Coupled adsorption-reduction mechanisms in UiO-66-R materials after heavy metals adsorption were studied by means of electron paramagnetic resonance (EPR) spectroscopy. EPR spectroscopy is a very useful technique for characterizing materials with unpaired electrons. Thus, this technique is widely used in materials science to identify and quantify radicals or to study transition metal ions. Furthermore, EPR analysis provides information on the geometry of the environment of paramagnetic ions, as well as on the existence of possible magnetic interactions between them.

The physical principles of this technique are similar to those of nuclear magnetic resonance (NMR), but in the case of the EPR spectroscopy electronic spins are excited instead of nuclear. Thus, in this technique, the sample is irradiated with microwave radiation with a fixed frequency and the field is tuning in an interval. At certain field resonance occurs, the field at which this resonance occurs as well as the resonance profile are characteristic of the number of unpaired electrons as well as of the interactions of the unpair electrons with their environment. This technique is based on the Zeeman effect, that is, on the fact that in the presence of an external magnetic field the spin of an electron (or its magnetic moment) can adopt two orientations along the direction of that field (parallel or antiparallel) which gives rise to an energy difference between these two levels (**Figure A.19**a). Then, a fixed microwave irradiation frequency is used to induce

transitions between the energy levels and the energy absorption on these transitions is recorded on the spectrometer.

For the particular case of the chromium species investigated in this thesis, it should be noted that Cr^{VI} is silent by EPR. On the contrary, three different EPR signals are associated with Cr^{III} or Cr^{V} species [36]:

- *γ-signal:* This axially symmetric intense and sharp adsorption band located around 3400 G is ascribed to an isolated Cr^{5+}, which usually presents a highly distorted octahedral or pseudo-pyramidal coordination environment. γ-signals exhibit a characteristic sharp g_x and a weak somewhat diffuse g_{II} line.
- *δ-signal:* This dispersed adsorption band located about 1300 G is related to Cr^{III} isolated species.
- *β-signal:* This broad isotropic absorption band is related with the Cr^{III} magnetically coupled systems, which g value strongly depends on the size and shape of the chromium clusters. The presence of this EPR characteristic fingerprint indicates that Cr^{III} ions are immobilized within the UiO-66 matrix close enough to establish magnetic interactions, which in terms of local structure can be explained as the presence of Cr^{III}-O-Cr^{III} or Cr^{III}-OH···O-Cr^{III} bridges within the pores of the MOF framework.

Electronic paramagnetic resonance (EPR) spectra of the MOF samples were recorded at room temperature using a Bruker ELEXSYS 500 spectrometer (X band) equipped with a superhigh-Q resonator ER-4123-SHQ. Samples were placed in quartz tubes with approximately the same amount of sample and packing degree in order to establish a qualitative comparison. The magnetic field was calibrated by a nuclear magnetic resonance (NMR) probe and the frequency inside the cavity (~9.395 GHz) was determined with an integrated Hewlett-Packard 5352B microwave frequency counter. A picture of this equipment is shown in **Figure A.19**b.

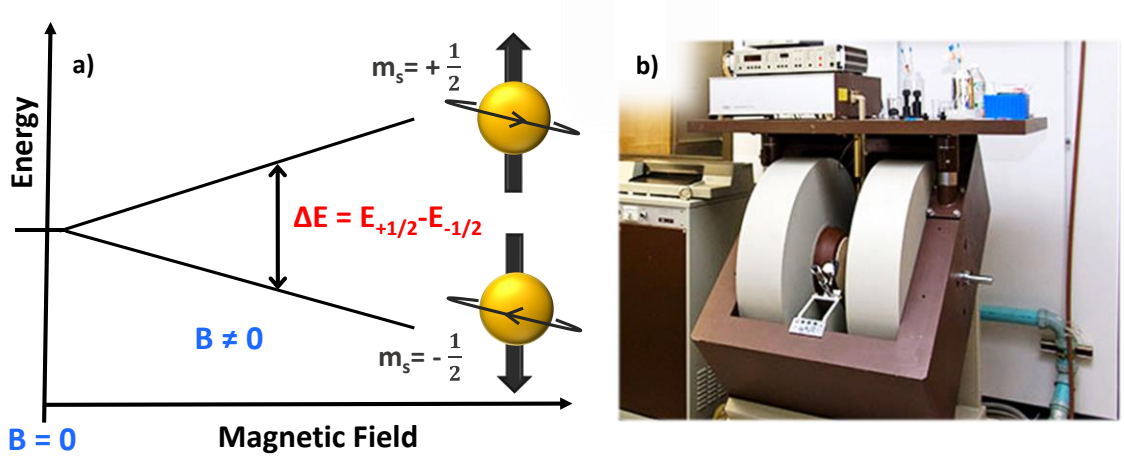

Figure A.19. (a) Scheme of the Zeeman effect in which the EPR spectroscopy is based and (b) Bruker ELEXSYS 500 spectrometer.

A.2.11. UV-Vis (in solid and liquid samples) and the colorimetry method

UV-Vis spectroscopy is a characterization technique widely used to identify certain functional groups as well as to determine and quantify the presence of certain substances. UV-Vis absorption spectroscopy consists on measure the light that a sample absorbs at different wavelengths (in the UV-Vis range). This absorption depends on the molecules' structures and is characteristic of the substance, so the spectra measurement allows obtaining information on the structure and binding of the compounds.

UV-Vis absorption spectroscopy has been used along this work in order to characterize the functionalizations on the MOFs as well as their HMs adsorption capacities and the HMs speciation once after adsorption. Thus, UV/VIS spectroscopy has been measured both in solid and in liquid samples. The laser absorptivity of the powder samples has been measured using Diffuse Reflectance Spectroscopy (DRS). DRS has been carried out in the 200-2200 nm wavelength range with 1 nm spectral resolution using an ultraviolet visible near-infrared (UV-Vis-NIR) V-770 Jasco spectrophotometer (**Figure A.20**a) from the SGIker (UPV/EHU) equipped with a 150 mm diameter integrating sphere coated with Spectralon. A Spectralon reference was used to measure the 100% reflectance and internal attenuators were used to determine zero reflectance in order to remove background and noise. The powders were placed in a quartz cuvette, sealed, and mounted on a Teflon sample holder for the measurement. The measured reflectance spectra are converted to Kubelka-Munk (K-M) absorption factors to evaluate the absorption spectra

of the powders. These measurements were performed in order to analyze the functionalization of the MOF as well as the chromium species adsorbed on it.

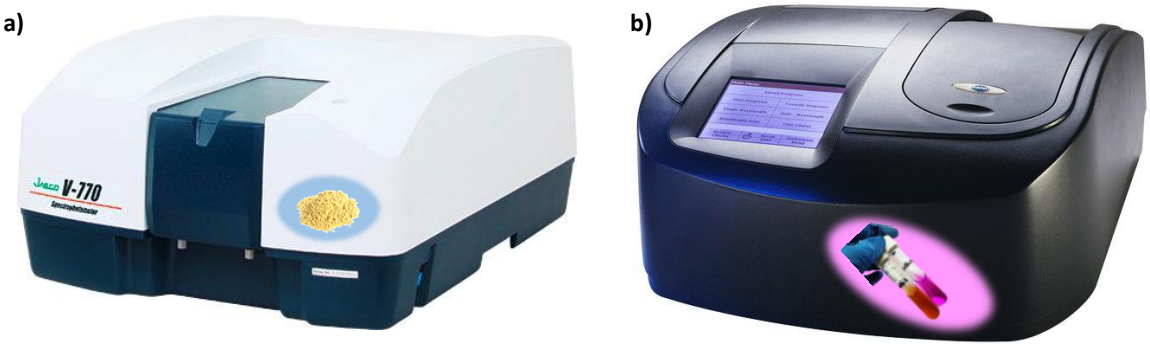

Figure A.20. (a) V-770 UV/VIS Jasco spectrophotometer used for the powder samples characterization and (b) DR 5000 UV-VIS – HUALIX spectrophotometer used for the liquid samples characterization.

On the other hand, measurements in liquid samples have been performed in order to measure the concentration of chromium in solution. UV-Vis spectra measurements on liquid samples were performed in the University of Chile using a DR 5000 UV-VIS – HUALIX spectrophotometer. An image of that system is shown in **Figure A.20**b. For Cr^{VI} quantification, a simplified methodology based on the previously reported one for 1,5-Diphenylcarbazide was used [37,38]. Absorbance at a single wavelength at the maximum of the absorbance fingerprint peak of the chromate Cr^{VI} ($\lambda_{max} = 540$ nm) was recorded. In order to measure the calibration curve, a concentrated Cr^{VI} stock solution was prepared and several solutions of lower concentrations were obtained by diluting. The different samples used to measure the calibration curve are shown in **Figure A.21**a. Moreover, in order to quantify the concentration of Cr^{III} by the diphenylcarbacide method, its oxidation to Cr^{VI} was previously performed using a 22.6 mM potassium permanganate solution and under heating. An image of several Cr^{III} samples with the potassium permanganate before and after the oxidation from Cr^{III} to Cr^{VI} is shown in **Figure A.21**b.

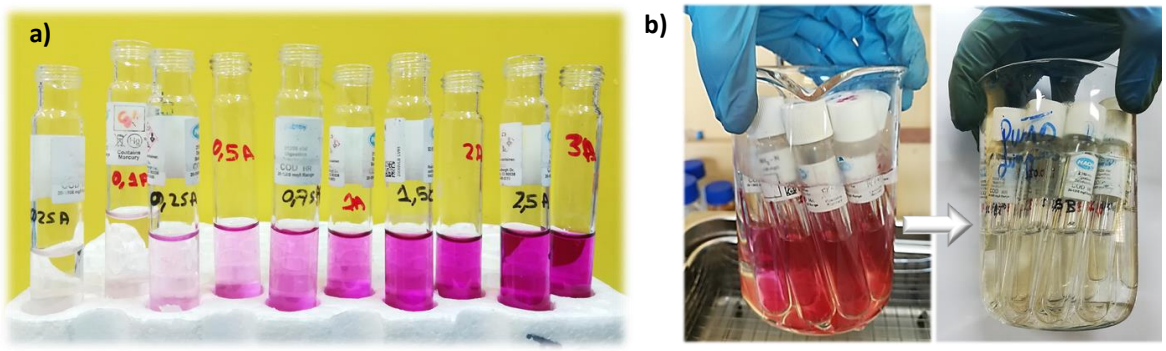

Figure A.21. (a) Image of the Cr^{VI} solution with different concentrations employed for the Cr^{VI} calibration curve measurement and (b) oxidation process from Cr^{III} to Cr^{VI} after potassium permanganate treatment and heating.

A.2.12. Inductively coupled plasma atomic emission spectroscopy (ICP-AES)

Inductively coupled plasma atomic emission spectroscopy (ICP-AES) has been employed for measuring the heavy metals concentration in solution. This technique is an analytical technique highly employed in different areas for the detection of chemical elements. ICP-AES is a type of emission spectroscopy based on the employment of inductively coupled plasma to excites atoms and ions which emit electromagnetic radiation at characteristics wavelengths of the element.

An Horiba Jobin Yvon Activa atomic emission spectrophotometer with inductively-coupled plasma (ICP-AES) has been used to quantify the HMs concentration. This system is equipped with a glass and Teflon nebulizer system, which enables samples from acidic digestion to be determined using HF. The equipment is controlled by a computer with Activa Analyst 5.4 software. It allows sequential multi-elemental analysis as well as numerous analytical requirements. Due to the large linear interval that characterizes this technique it also allows to determine very low concentrations of HMs (in the ppb order). For the experiments, samples were diluted until the detection limits of the equipment and triplicate measurements were performed in order to reduce the experimental error. An image of the instrument property of the SGIker (UPV/EHU) is shown in **Figure A.22.**

Figure A.22. Horiba Jobin Yvon Activa atomic emission spectrophotometer with inductively-coupled plasma (ICP-AES) from the SGIker (UPV/EHU).

A.3. References

1. Thang, P. D., Duong, H. H. & Nghi, N. H. Magnetic and sensitive magnetoelastic properties of Finemet nanostructured ribbon. *J. Phys. Conf. Ser.* **187**, (2009).

2. Johnson, M. L., LeVar, O., Yoon, S. H., Park, J. H., Huang, S., Kim, D. J., Cheng, Z., & Chin, B. A. Dual-cathode method for sputtering magnetoelastic iron-boron films. *Vacuum* **83**, 958–964 (2009).

3. Atalay, S., Kolat, V. S., Atalay, F. E., Bayri, N., Kaya, H., & Izgi, T. Magnetoelastic sensor for magnetic nanoparticle detection. *J. Magn. Magn. Mater.* **465**, 151–155 (2018).

4. Bravo, I., Arnaiz, A. & Garcia-Arribas, A. Damping of magnetoelastic resonance for oil viscosity sensing. *IEEE Trans. Magn.* **55**, (2019).

5. Atalay, S., Kolat, V. S., Bayri, N. & Izgi, T. Magnetoelastic sensor studies on amorphous magnetic FeSiB wire and the application in viscosity measurement. *J. Supercond. Nov. Magn.* **29**, (2016).

6. Johnson, M. L., Wan, J., Huang, S., Cheng, Z., Petrenko, V. A., Kim, D. J., Barbaree, J.M., Hong J. W., & Chin, B. A. A wireless biosensor using microfabricated phage-interfaced magnetoelastic particles. *Sensors Actuators, A Phys.* **144**, 38–47 (2008).

7. Sang, S., Cheng, P. Zhang, W. Li, P. Hu, J. Li, G., & Jian, A. Investigation on a new Fe83Ga17 wire-based magnetoelastic resonance biosensor. *J. Intell. Mater. Syst. Struct.* **26**, 980–

987 (2015).

8. Sagasti, A., Gutierrez, J., San Sebastian, M. & Barandiaran, J. M. Magnetoelastic resonators for highly specific chemical and biological detection: A critical study. *IEEE Trans. Magn.* **53**, (2017).

9. Metglas® 2826MB. Available at: www.metglas.com. (Accessed: 9th September 2020)

10. Pacharra, S., Ortiz, R., Mcmahon, S., Wang, W. Viebahn, R., Salber, J., & Quintana, I. Surface patterning of a novel PEG-functionalized poly- L -lactide polymer to improve its biocompatibility : Applications to bioresorbable vascular stents. *J. bioomedical Mater. Res. B* **107**, 624–634 (2018).

11. Woerner, P., Blood, D., Mills, D. Sheplak, M., & Oates, W. S. Quantifying the uncertainty of picosecond pulsed laser ablation in sapphire. *J. Manuf. Process.* **35**, 687–699 (2018).

12. Liang, C., Morshed, S., & Prorok, B. C. Correction for longitudinal mode vibration in thin slender beams. *Appl. Phys. Lett.* **90**, 221912 (2007).

13. Marín, P., Marcos, M. & Hernando, A. High magnetomechanical coupling on magnetic microwire for sensors with biological applications. *Appl. Phys. Lett.* **96**, 1–4 (2010).

14. Petersan, P. J. & Anlage, S. M. Measurement of resonant frequency and quality factor of microwave resonators: Comparison of methods. *J. Appl. Phys.* **84**, 3392–3402 (1998).

15. Qiu, Z. Q. & Bader, S. D. Surface magneto-optic Kerr effect. *Review of Scientific Instruments* **71**, 1243–1255 (2000).

16. Schäfer, R. Investigation of domains and dynamics of domain walls by the magneto-optical Kerr-effect. *Handb. Magn. Adv. Magn. Mater.* (2007).

17. Grimes, C. A., Roy, S. C., Rani, S. & Cai, Q. Theory, instrumentation and applications of magnetoelastic resonance sensors: A review. *Sensors* **11**, 2809–2844 (2011).

18. Pan, Y., Liu, Y., Zeng, G., Zhao, L., & Lai, Z. Rapid synthesis of zeolitic imidazolate framework-8 (ZIF-8) nanocrystals in an aqueous system. *Chem. Commun.* **47**, 2071–2073 (2011).

19. Shearer, G. C., Chavan, S., Bordiga, S., Svelle, S., Olsbye, U., & Lillerud, K. P. Defect engineering: Tuning the porosity and composition of the metal−organic framework UiO-66 via modulated synthesis. *Chem. Mater.* **28**, 3749–3761 (2016).

20. Øien, S., Wragg, D., Reinsch, H. , Svelle, S., Bordiga, S., Lamberti, C., & Lillerud, K. P. Detailed structure analysis of atomic positions and defects in zirconium metal-organic frameworks. *Cryst. Growth Des.* **14**, 5370–5372 (2014).

21. Furukawa, H., Gándara, F., Zhang, Y. B., Jiang, J., Queen, W. L., Hudson, M. R., & Yaghi, O. M. Water adsorption in porous metal-organic frameworks and related materials. *J. Am. Chem. Soc.* **136**, 4369–4381 (2014).

22. Jiang, J., Gándara, F., Zhang, Y. B., Na, K., Yaghi, O. M., & Klemperer, W. G. Superacidity in sulfated metal-organic framework-808. *J. Am. Chem. Soc.* **136**, 12844–12847 (2014).

23. Guinier, A. *X-ray diffraction in crystals, imperfect crystals, and amorphous bodies*. (Courier Corporation, 1994).

24. Smith, B. C. *Fundamentals of Fourier transform infrared spectroscopy*. (CRC press, 2011).

25. Audu, C. O. Nguyen, H. G. T., Chang, C. Y., Katz, M. J., Mao, L., Farha, O. K., Hupp, J. T., & Nguyen, S. T. The dual capture of AsV and AsIII by UiO-66 and analogues. *Chem. Sci.* **7**, 6492–6498 (2016).

26. Valenzano, L., Civalleri, B., Chavan, S., Bordiga, S., Nilsen, M. H., Jakobsen, S., Lillerud, K. P., & Lamberti, C. Disclosing the complex structure of UiO-66 metal organic framework: A synergic combination of experiment and theory. *Chem. Mater.* **23**, 1700–1718 (2011).

27. Chavan, S., Vitillo, J. G., Uddin, M. J., Bonino, F., Lamberti, C., Groppo, E., Lillerud K-P., & B. S. Functionalization of UiO-66 metal-organic framework and highly cross-linked polystyrene with Cr(CO)3: In situ formation, stability, and photoreactivity. *Chem. Mater.* **22**, 4602–4611 (2010).

28. Egerton, R. F. *Physical principles of electron microscopy*. (New York: Springer, 2005).

29. Chiou, C. T. *Partition and adsorption of organic contaminants in environmental systems - Chapter 4*. (John Wiley & Sons, 2003).

30. Walton, K. S., & Snurr, R. Q. Applicability of the BET method for determining surface areas of microporous metal-organic frameworks. *J. Am. Chem. Soc.* **129**, 8552–8556 (2007).

31. Chul, K., Yoon, T. & Bae, Y. Applicability of using CO2 adsorption isotherms to

determine BET surface areas of microporous materials. *Microporous Mesoporous Mater.* **224**, 294–301 (2016).

32. Kolb, B. Multiple headspace extraction-A procedure for eliminating the influence of the sample matrix in quantitative headspace gas chromatography. *Chromatographia* **15**, 587–594 (1982).

33. Rincón, A. A., Pino, V., Ayala, J. H. & Afonso, A. M. Multiple headspace solid-phase microextraction for quantifying volatile free fatty acids in cheeses. *Talanta* **129**, 183–190 (2014).

34. Chen, X. Modeling of experimental adsorption isotherm data. *Information* **6**, 14–22 (2015).

35. Rodriguez, A., Ovejero, G., Mestanza, M., & Garcia, J. Removal of dyes from wastewaters by adsorption on pillared clays. *Ind. Eng. Chem. Res.* **49**, 3207–3216 (2010).

36. Weckhuysen, B. M., Schoonheydt, R. A., Mabbs, F. E. & Collison, D. Electron paramagnetic resonance of heterogeneous chromium catalysts. *J. Chem. Soc. - Faraday Trans.* **92**, 2431–2436 (1996).

37. Sereshti, H., Vasheghani Farahani, M. & Baghdadi, M. Trace determination of chromium(VI) in environmental water samples using innovative thermally reduced graphene (TRG) modified SiO2 adsorbent for solid phase extraction and UV-Vis spectrophotometry. *Talanta* **146**, 662–669 (2016).

38. Rai, D., Sass, B. M. & Moore, D. A. Chromium(III) hydrolysis constants and solubility of chromium(III) hydroxide. *Inorg. Chem.* **26**, 345–349 (1987).

Annex B

Analytical calculations

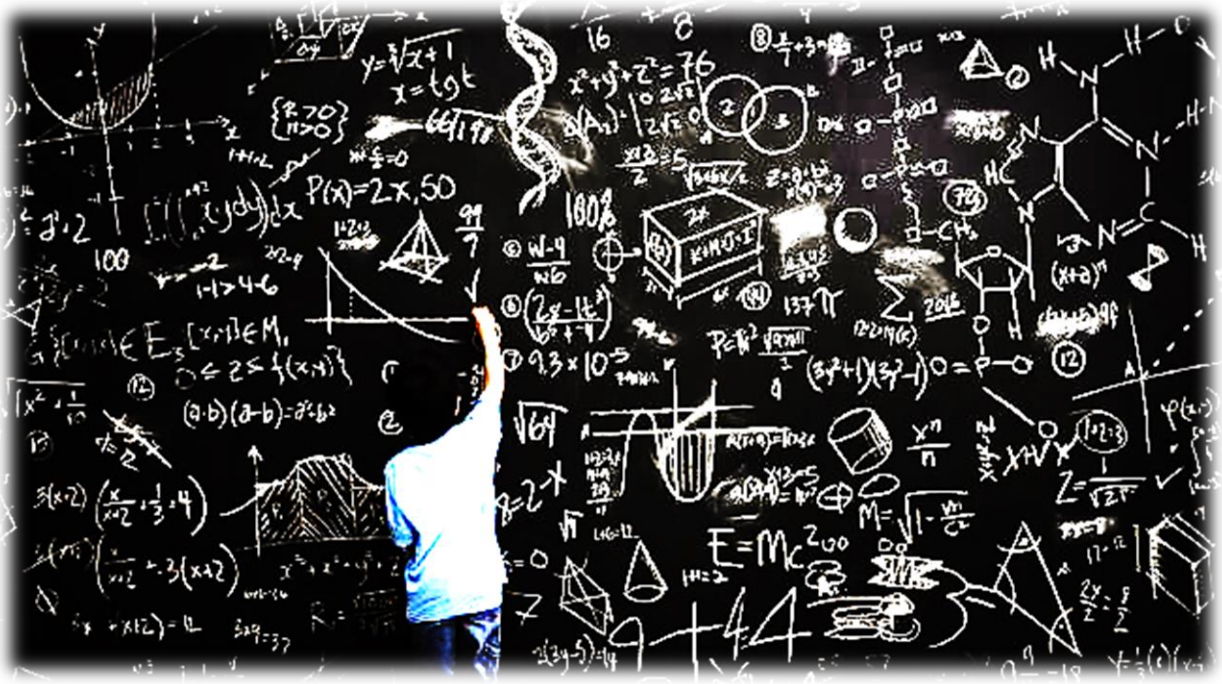

Content

B.1. Theoretical resonance frequency for the rhombic geometry

The classically used rectangular shaped magnetoelastic resonator is a very well-known system already well reported in the literature [1]. Several studies describe its resonance frequency corresponding equations or its mass sensitivity behaviour [2]. Instead, everything remains to be studied for non-rectangular ME resonators geometries. The equation for the resonance frequency in a rectangular magnetoelastic resonator is obtained by solving a series of equations for the displacement function ($u(x,t)$) of a longitudinal elastic wave [3]. It is well known that the displacement function ($u(x,t)$) of a longitudinal elastic wave propagating along the length direction (in the following, supposed to be the x axis) of a ME resonator of length L is given by [4]:

$$u(x,t) = u_o \cos\left(\frac{n\pi}{L}x\right) e^{i2\pi f_n t} = u(x)e^{i2\pi f_n t} \qquad \text{(B.1)}$$

where u_0 is a constant and f_n is the resonance frequency of the n-th harmonic mode. So, all points in the sensor material oscillate at the same frequency but with different amplitudes, since these depend on the distance from the ends, being maximum at the ends and null at the resonator centre (blind point). This behaviour is equal for the rectangle and the rhomb due to their symmetric shape. The displacement amplitude as a function of the length position for both a rectangular or a rhombic geometry of length L is represented in **Figure B.1**.

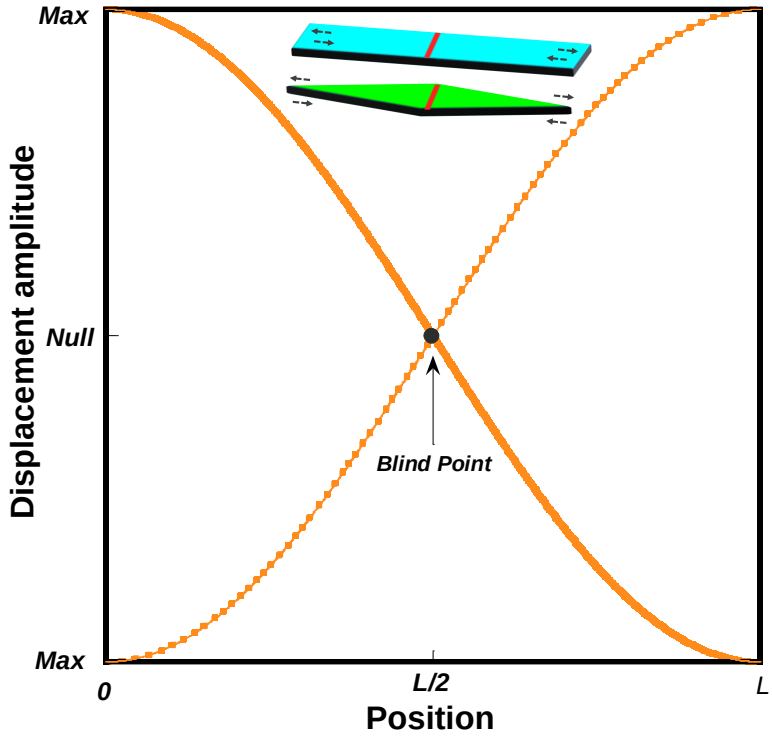

Figure B.1. Displacement amplitude at different length points of a rectangular and a rhombic resonator of length L. Blind point (point with null displacement) is marked by a red line in the figures.

In addition, the kinetic energy *(T)* and the potential energy *(V)* of a freestanding ME resonator vibrating along the x-axis are given by [5]:

$$T = \frac{1}{2}\int_0^L \rho \cdot A_s \cdot \left(\frac{\partial u(x,t)}{\partial t}\right)^2 dx \tag{B.2}$$

$$V = \frac{1}{2}\int_0^L \frac{E}{1-\upsilon} \cdot A_s \cdot \left(\frac{\partial u(x,t)}{\partial x}\right)^2 dx \tag{B.3}$$

where ρ, E and ν are the density, Young's modulus and Poisson's ratio of the bare ME resonator and A_s is its cross-sectional area. This cross-section is constant for rectangular shaped materials, so solving the above equations is easy for that geometry since A_s does not depend on x. Nevertheless, in the case of the rhombus shaped sensor, its width is variable *(W(x))* and so its cross-section is also variable (**Figure B.2**).

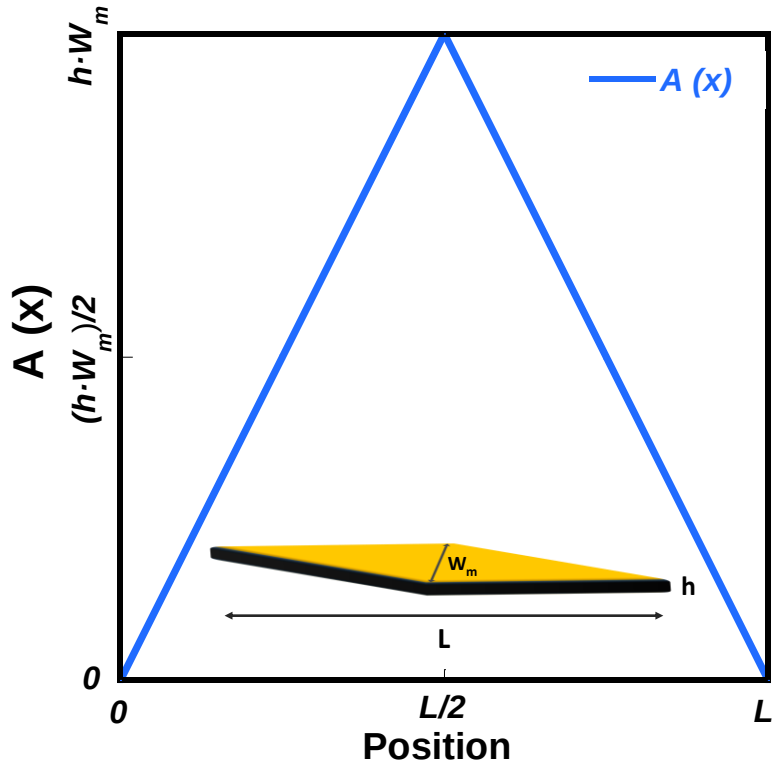

Figure B.2. Cross-sectional area dependence (A(X)) for a rhombic resonator.

This variable cross-section *(A(x))* can be analytically expressed as:

$$A(x) = \begin{cases} \frac{xhw_m}{L/2} & (0 \le x \le L/2) \\ (L-x)\cdot\frac{2hw_m}{L} & (L/2 \le x \le L) \end{cases} \quad \text{(B.4)}$$

where w_m is the maximum width of the rhombus (width at its longitudinal centre), h is the height and L is the length of the ribbon. Solving the above equations (for the first resonance mode, n=1) and equalling the maximum kinetic and potential energies[6], the theoretical equation for the first mode resonance frequency of a freestanding rhombus shaped magnetoelastic resonator of length L can be obtained:

- For T (**equation B.2**):

$$*\left(\frac{\partial u(x,t)}{\partial t}\right) = u_o \cos\left(\frac{\pi}{L}x\right) e^{i2\pi ft}\cdot i2\pi f \rightarrow \left(\frac{\partial u(x,t)}{\partial t}\right)^2 = u_0^2\cdot 4\pi^2 f^2 \cdot cos^2\left(\frac{\pi x}{L}\right) e^{i4\pi ft} \quad \text{(B.5)}$$

$$T = \frac{1}{2}\int_0^L \rho \cdot A_s \cdot \left(\frac{\partial u(x,t)}{\partial t}\right)^2 dx =$$

$$\frac{\rho}{2}\, u_0^2 e^{i4\pi ft} 4\pi^2 f^2 \int_0^L A(x) \cdot cos^2\left(\frac{\pi x}{L}\right)\mathrm{dx} =$$

$$\frac{\rho}{2}\, u_0^2 e^{i4\pi ft} 4\pi^2 f^2 \left(\int_0^{L/2} \frac{xhw_m}{L/2} cos^2\left(\frac{\pi x}{L}\right)\mathrm{dx} + \int_{L/2}^{L}(L-x)\cdot \right.$$

$$\left.\frac{2hw_m}{L} cos^2\left(\frac{\pi x}{L}\right)\mathrm{dx}\right) = \frac{\rho}{2}\, u_0^2 e^{i4\pi ft} 4\pi^2 f^2 hw_m L\left(\frac{1}{4} - \frac{1}{\pi^2}\right) \quad \text{(B.6)}$$

- For V (**equation B.3**):

$$* \left(\frac{\partial u(x,t)}{\partial x}\right) = u_o \,\mathrm{sen}\left(\frac{\pi}{L}x\right) e^{i2\pi ft}.\frac{\pi}{L} \rightarrow \left(\frac{\partial u(x,t)}{\partial x}\right)^2 = u_0^2 \cdot sen^2\left(\frac{\pi x}{L}\right) e^{i4\pi ft}.\frac{\pi^2}{L^2} \quad \text{(B.7)}$$

$$\mathrm{V} = \frac{1}{2}\int_0^L \frac{E}{1-\upsilon} \cdot A_s \cdot \left(\frac{\partial u(x,t)}{\partial x}\right)^2 dx =$$

$$\frac{E}{2(1-\upsilon)}\, u_0^2 \cdot e^{i4\pi ft}.\frac{\pi^2}{L^2}\int_0^L A(x) \cdot sen^2\left(\frac{\pi x}{L}\right) dx =$$

$$\frac{E}{2(1-\upsilon)} u_0^2 e^{i4\pi ft}.\frac{\pi^2}{L^2}\left(\int_0^{L/2} \frac{xhw_m}{L/2} sen^2\left(\frac{\pi x}{L}\right)\mathrm{dx} + \int_{L/2}^{L}(L-x)\cdot \right. \quad \text{(B.8)}$$

$$\left.\frac{2hw_m}{L} sen^2\left(\frac{\pi x}{L}\right)\mathrm{dx}\right) = \frac{E}{2(1-\upsilon)} u_0^2 e^{i4\pi ft}\, \frac{\pi^2}{L^2} hw_m L\left(\frac{1}{4} + \frac{1}{\pi^2}\right)$$

And equalling the previous results the resonance frequency of a rhombic resonator could be obtained:

$$\frac{\rho}{2}\, u_0^2 e^{i4\pi ft} 4\pi^2 f^2 hw_m L\left(\frac{1}{4} - \frac{1}{\pi^2}\right) = \frac{E}{2(1-\upsilon)} u_0^2 e^{i4\pi ft}\, \frac{\pi^2}{L^2} hw_m L\left(\frac{1}{4} + \frac{1}{\pi^2}\right) \quad \text{(B.9)}$$

Which by simplifying and clearing the f value lead to the resonance frequency of the rhombic geometry (f_r^{rh}):

$$f_r^{rh} = \sqrt{\frac{\pi^2+4}{\pi^2-4}} \cdot \left(\frac{1}{2L} \cdot \sqrt{\frac{E}{\rho(1-\upsilon)}}\right) \quad \text{(B.10)}$$

where again E is the Young modulus, ρ is the density and ν is the Poisson coefficient of the sensing material. This obtained frequency could be related with that of a rectangular ME resonator of the same length which is given by [7]:

$$f_r^{rec} = \frac{1}{2L} \cdot \sqrt{\frac{E}{\rho(1-\upsilon)}} \tag{B.11}$$

By direct comparison of the equation obtained for the rhombic resonator with this last one, when the Young's modulus of both samples is the same, the relationship between the resonance frequency of the rhombus and the rectangular shaped resonators is given by:

$$f_r^{rh} = \sqrt{\frac{\pi^2+4}{\pi^2-4}} \cdot f_r^{rec} \approx 1.53 \cdot f_r^{rec} \tag{B.12}$$

Which mean that the resonance frequency of a rhombic resonator with respect to the resonance frequency of a rectangular resonator with the same length will we always higher (by a factor of 1.53).

B.2. References

1. Grimes, C. A., Roy, S. C., Rani, S. & Cai, Q. Theory, instrumentation and applications of magnetoelastic resonance sensors: A review. *Sensors* **11**, 2809–2844 (2011).

2. Zhang, K., Zhang, L., Fu, L., Li, S., Chen, H., & Cheng, Z. Y. Magnetostrictive resonators as sensors and actuators. *Sensors Actuators, A Phys.* **200**, 2–10 (2013).

3. Grimes, C. A., Mungle, C. S., Zeng, K., Jain, M. K., Dreschel, W. R. Paulose, M., & Ong, K. G. Wireless magnetoelastic resonance sensors : A critical review. *Sensors* **2**, 294–313 (2002).

4. Li, S. & Cheng, Z. Y. Nonuniform mass detection using magnetostrictive biosensors operating under multiple harmonic resonance modes. *J. Appl. Phys.* **107**, (2010).

5. Zhang, K., Zhang, K. & Chai, Y. Study of 'blind point' and mass sensitivity of a magnetostrictive biosensor with asymmetric mass loading. *AIP Adv.* **4**, (2014).

6. Hosseini, R. & Hamedi, M. An investigation into resonant frequency of triangular V-shaped cantilever piezoelectric vibration energy harvester. *J. Solid Mech.* **8**, 560–567 (2016).

7. Zhang, R., Tejedor-Tejedor, M. I., Grimes, C. A. & Anderson, M. A. Measuring the mass of thin films and adsorbates using magnetoelastic techniques. *Anal. Chem.* **79**, 7078–7086 (2007).

Annex C

Results dissemination

Content

This appendix includes the scientific works published/accepted or presented throughout this thesis, both from the thesis work itself and from other collaborations of the group. Moreover, it collect other R&D activities, training courses and research stays carried out during the PhD stage.

C.1. Contributions related to the thesis research work

- ### Publications

1. Paula G. Saiz, David Gandia, Andoni Lasheras, Iban Quintana, Jon Gutiérrez, María Isabel Arriortua, Ana Catarina Lopes. "Enhanced mass sensitivity in novel magnetoelastic resonator geometries for advanced detection systems". *Sensors and Actuators B,* 296, 126612 (2019), doi.org/10.1016/j.snb.2019.05.089 [D1 (2/64), Impact factor = 7.100].
2. Paula G. Saiz, Jon Gutiérrez, María Isabel Arriortua, Ana Catarina Lopes. "Theoretical and Experimental analysis of novel rhombus shaped magnetoelastic sensors with enhanced mass sensitivity". *IEEE Sensors* (2020), doi.org/10.1109/JSEN.2020.3006379 [Q1 (13/61), Impact factor = 3.076].
3. Paula G. Saiz, Naroa Iglesias, Bárbara González Navarrete, Maibelin Rosales, Yurieth Marcela Quintero, Ander Reizabal, Joseba Orive, Arkaitz Fidalgo Marijuan, Edurne S. Larrea, Catarina Lopes, Luis Lezama, Andreina García, Senentxu Lanceros-Mendez, María Isabel Arriortua, Roberto Fernández de Luis. "Chromium speciation in Zr-based Metal-Organic Frameworks for environmental remediation". *Chemistry - A European Journal (2020),* doi.org/10.1002/chem.202001435 [Q1 (37/172) Impact factor = 5.160].
4. Paula G. Saiz, Roberto Fernández de Luis, Luis Bartolome, Jon Gutiérrez, María Isabel Arriortua, Ana Catarina Lopes. "Rhombic-magnetoelastic/metal-organic framework functionalized resonators for high sensitive toluene detection". *Journal of Materials Chemistry C (2020),* doi.org/10.1039/D0TC02612C [Q1 (21/154), Impact factor = 7.059].
5. Paula G. Saiz, Jose Maria Porro, Andoni Lasheras, Roberto Fernández de Luis, Maria Isabel Arriortua, Ana Catarina Lopes. "Influence of the magnetic domain structure in the mass sensitivity of magnetoelastic sensors with different geometries". *Journal of alloys and compounds* [Q1 (8/79), Impact factor = 4.650, *Under revision*].

6. Paula G Saiz, Ainara Valverde, Bárbara Gonzalez-Navarrete, Maibelin Rosales, Yurieth Marcela Quintero, Arkaitz Fidalgo-Marijuan, Joseba Orive, Ander Reizabal, Edurne Serrano, María Isabel Arriortua, Senentxu Lanceros-Méndez, Andreina García, Roberto Fernández de Luis "Modulation of the bi-functional Cr^{VI} to Cr^{III} photo-reduction and adsorption capacity in Zr^{IV} and Ti^{IV} benchmark Metal-Organic Frameworks. *Catalysts* [Q2, (65/159), Impact factor = 3.520, *Under revision*]

- **Conference contributions**

1. *Porous structures as key enabling materials for advanced technologies* (Bilbao (Spain), 20/11/2018). Paula G. Saiz, David Gandia, Andoni Lasheras, Iban Quintana, María Luisa Fdez-Gubieda, Jon Gutiérrez, María Isabel Arriortua, Ana Catarina Lopes. "Increasing the sensitivity of magnetoelastic sensors by playing with the geometry" (Poster + flash presentation).
2. *7th International Conference on Materials and Applications for Sensors and Transducers* (Bratislava (Eslovaquia), 24-27/9/2018). Paula G. Saiz, Andoni Lasheras, Ariane Sagasti, Iban Quintana, Jon Gutiérrez, María Isabel Arriortua, Ana Catarina Lopes. "Increasing the sensitivity of magnetoelastic sensors by modifying the geometry" (Oral presentation).
3. *American Physical Society March Meeting* (Boston (EE.UU.), 4-8/3/2019). Paula G. Saiz, David Gandia, Andoni Lasheras, Iban Quintana, Jon Gutiérrez, María Isabel Arriortua, Ana Catarina Lopes. "Increase the sensitivity of magnetoelastic sensors by modifying the sensor geometry". (Oral presentation).
4. *XXXVII Reunión Bienal de la Real Sociedad Española de Química* (San Sebastián (Spain), 26-30/5/2019). Paula G. Saiz, Roberto Fernandez de Luis, Luis Lezama, Naroa Iglesias, Arkaitz Fidalgo, Edurne S. Larrea, Ana Catarina Lopes, María Isabel Arriortua. "A deeper EPR spectroscopy insight of Cr(VI) and Cr(III) species capture/reduction by Zr-MOFs". (Poster).
5. *IEEE Magnetics Summer School* (Virginia (EE.UU), 2-7/6/2019). Paula G. Saiz, David Gandia, Andoni Lasheras, Iban Quintana, Jon Gutiérrez, María Isabel Arriortua, Ana Catarina Lopes. "Increase the sensitivity of magnetoelastic sensors by modifying the sensor geometry". (Poster).

6. *MOFschool* (Como (Italy), 17-21/7/2019). Paula G. Saiz, Ana Catarina Lopes, Roberto Fernández de Luis, Jon Gutiérrez, María Isabel Arriortua. "Magnetoelastic resonators@MOFs for advanced selective and sensitive detection systems". (Poster).
7. *Jornadas doctorales UPV/EHU* (Bilbao (Spain), 3/7/2019). Paula G. Saiz. "Magnetoelastic resonators functionalized with MOFs for advanced selective and sensitive Volatile Organic Compounds detection systems". (Poster).
8. *RSCPoster Twitter Conference* (Twitter, 3/3/2020). Paula G. Saiz. "Towards a new generation of gas sensors: Magnetoelastic resonators functionalized with MOFs for Volatile Organic Compounds detection". (Poster).
9. *LatinXChem Twitter Conference* (Twitter, 8/9/2020). Paula G. Saiz, Naroa Iglesias, Barbara González Navarrete, Ander Reizabal, Ana Catarina Lopes, Luis Lezama, Andreina Garcia, María Isabel Arriortua and Roberto Fernández de Luis. "A deeper analysis insight chromium speciation in Zr-based Metal-Organic Frameworks for environmental remediation". (Poster).

C.2. Contributions related to other collaborations

- **Publications**

1. Paula G. Saiz, Ana Catarina Lopes, Simone Eizagirre, Roberto Fernández de Luis, María Isabel Arriortua. "Ionic liquids for the control of the morphology in poly(vinylidene fluoride-co-hexafluoropropylene) membranes". *Journal of Materials & Design*, 155, 325-333 (2018), doi.org/10.1016/j.matdes.2018.06.013 [Q1 (50/293), Impact factor = 5.770].
2. Andoni Lasheras, Paula G. Saiz, Jon Gutiérrez, Ana Catarina Lopes. "Development of novel piezo-ionic/magnetostrictive composites for energy generation systems". *Smart Materials and Structures,* 29(8), 085041 (2020), doi.org/10.1088/1361-665X/ab9f4b [Q1 (10/64), Impact factor = 3.613].
3. Ander Reizabal, Carlos Miguel Costa, Paula G. Saiz, Barbara Gonzalez, Leyre Pérez-Álvarez, Roberto Fernandez, Andreina Garcia, Jose L. Vilas, Senentxu Lanceros-Mendez. "Processing Strategies to Obtain Highly Porous Silk Fibroin Membranes with Tailored Microstructure and Molecular Characteristics and Their Applicability in Heavy-Metal Water Remediation". *Journal of Hazardous Materials, 403, 23675*

(2020), doi.org/10.1016/j.jhazmat.2020.123675 [D1 (8/265), Impact factor = 9.038].

4. Eduardo Fernández, Paula G. Saiz, Nikola Peřinka, Roberto Fernández de Luis. "MOF based printed capacitive sensor for Volatile Organic Compounds detection" *[Under preparation].*
5. Roberto Fernández de Luis, Edurne Serrano Larrea, Arkaitz Fidalgo, Paula G. Saiz, Ander Reizabal-Para, Ainara Valverde, Gabriel Tovar, Guillermo Copello, Barbara Rodriguez, Marcela Quintero, Maibelin Rosales, Andreina García, María Isabel Arriortua. "Porous lightweight materials: Environment and energy sustainability", *[Book Chapter - Advanced Lightweight Multifunctional Materials], Elsevier* (2020).

- **Conference contributions**

1. *Nanomaterials applied to life science* (Gijon (Spain), 13-15/12/2017). Paula G. Saiz, Ana Catarina Lopes, Simone Eizagirre, Roberto Fernández de Luis, Edurne S. Larrea, Arkaitz Fidalgo-Marijuan , Maria Isabel Arriortua. "Ionic liquids in the control of the poly(vinylidene fluoride-co-hexafluoropropylene) membranes morphology". (Oral presentation).
2. *A new neutron source for a new generation of advanced materials* (Leioa (Spain), 27/10/2017). Paula G. Saiz, Ana Catarina Lopes, Simone Eizagirre, Roberto Fernández de Luis, Edurne S. Larrea, Arkaitz Fidalgo-Marijuan , Maria Isabel Arriortua. "Ionic liquids in the control of the poly(vinylidene fluoride-co-hexafluoropropylene) membranes morphology". (Poster presentation).
3. *E-MRS Fall meeting* (Varsovia (Poland), 16-19/9/2018). Ana Catarina Lopes, Paula G. Saiz, Andoni Lasheras, Ariane Sagasti, Jon Gutiérrez. "Variation of Magnetoelastic resonant sensors shape in the basis of the increase sensitivity". (Oral presentation).
4. *MMM Intermag Conference (Washington (EE.UU.), 14-18/1/2019).* Andoni Lasheras, Jon Gutiérrez, Iñaki Orue, Iban Quintana, Paula G. Saiz and Ana Catarina Lopes. "Magnetoelectric response of different geometries of metallic glasses/PVDF laminates". (Oral presentation).
5. *MMM Intermag Conference (Washington (EE.UU.), 14-18/1/2019).* Ana Catarina Lopes, Paula G. Saiz; Andoni Lasheras; Alicia Muela; Jon Gutiérrez. "Non-rectangular shaped Magnetoelastic Ribbons for the accurate detection of pathogen Agents". (Oral presentation).

6. *New Technologies for a Sustainable Future Symposium* (Santiago de Chile (Chile), 14/6/2019). Roberto Fernández de Luis, Guillermo Copello, Andreina García, Paula G. Saiz, Gabriel Tovar, D. Torres, Ainara Valverde, Marcela Quintero, Maibelin Rosales, Barbara González, Edurne Serrano-Larrea, Arkaitz Fidalgo-Marijuan, Luis Lezama, María Isabel Arriortua. "Metal Organic Framework advanced adsorbents for metal ions recovery from polluted water sources". (Oral presentation).
7. *Goldschmidt2019* (Barcelona (Spain), 18-23/8/2019). Roberto Fernández de Luis, Guillermo Copello, Andreina García, Paula G. Saiz, Gabriel Tovar, Dimas Torres, Ainara Valverde, Marcela Quintero, Edurne Serrano-Larrea, Arkaitz Fidalgo-Marijuan, María Isabel Arriortua."Metal Organic Framework advanced adsorbents to revalorize metal ions from mining and industrial wastewater sources". (Oral presentation).
8. *New Materials for a Better Life!: Advanced devices and Materials as Key Enabling Technologies for Sustainable Environment.* (Leioa (Spain), 27/11/2019). Roberto Fernández de Luis, Bárbara Rodríguez, Paula Gonzalez, Ander Reizabal-Para, Maibelin Rosales, Edurne Serrano, Maribel Arriortua, Senentxu Lanceros, Andreina García. "Arsenic remediation with photoactive MOFs" (Oral presentation).

C.3. Grants (2017-2020)

1. **IEEE Magnetics Society** (June 2019): Travel grant to attend the IEEE MagSoc Summer School 2019 (Virginia, USA).
2. **RSEQ- Real Sociedad Española de Química** (May 2019): Scholarship to attend the RSEQ biennal congress (San Sebastián, Spain).
3. **APS- American Physical Society** (March 2019): Travel grant to attend the APS March meeting (Boston, USA).
4. **IEEE Magnetics Society** (December 2017): Travel grant for the NALS2017 conference (Gijon, Spain).
5. **BCMaterials** (October 2017): Grant to carry out the doctoral thesis at BCMaterials (Bizkaia, Spain).

C.4. Organization and participation in R & D activities

1. **Science week.** Universidad del País Vasco (UPV/EHU) (2017-2020)
2. **International day of women and girls in science events.** 11 February Initiative (2018-2020)
3. **Talks EGIN ETA EKIN program.** Diputación foral de Bizkaia, at BCMaterials (2018-2020)
4. **VI research days of the Faculty of Science and Technology, UPV/EHU.** University of the Basque Country (UPV/EHU) (14-15/3/2018)
5. **Workshop: Porous Structures as Key Enabling Materials for Advanced Technologies.** Organization staff. BCMaterials (20/11/2018)
6. **Organization of fortnightly seminars at BCMaterials research center.** (2018-2019).
7. **Member of LOGOS Elkartea (scientific divulgation association).** (2019-Actually).
8. **Zientziaz Blai event organization**. Barrio de San Francisco, Bilbao. (23-30/05/2019).
9. **Talk at the "science and society" session of the Zientziaz Blai event.** Barrio de San Francisco, Bilbao (25/05/2019)
10. **Sentsore magnetoelastikoak: kanpo-agenteak detektatzeko metodoa.** Elhuyar (14/05/2020)
11. **Fotciencia17.** Participation with three photographs.
12. **OnZientzia 2020**. Participation with: “Biomateriales, una solución para el futuro”.
13. **Science week Unican 2020**. Participation with three scientific photographs.
14. **BCMaterials calendar**. Images selected to appear in the 2019 and 2020 editions of the company calendar.

C.5. Research stays

1. **Advanced Mining Technology Center (AMTC),** Santiago de Chile, Chile (23/10/2019-5/2/2020): 14 weeks
2. **Universidad de Patras**, Patras, Grecia (1-4/4/2019): 1 week.

C.6. Training courses

1. **"First International School on Advanced Porous Materials (MOFSchool)",** *Como, Italy (17-21/June/2019 – 40 hours).*
2. **"IEEE Magnetics Summer School", Virginia**, *EEUU (2-7/June/2019 – 40 hours).*
3. **"Neutrons for the Biotech Industry",** *Universidad de Zaragoza, España (28-29/March/2019 – 8 hours).*
4. **Buenas prácticas en el laboratorio (II): residuos.** *(February-March/2019 - 25 hours).*
5. **Bases y Aplicaciones de la difracción de polvo: Análisis cuantitativo, microestructural y método Rietveld***". CSIC/IACT, Granada (16-20/September/2018 - 25 hours).*
6. **Seminario de análisis térmico.** *TA Instruments, UPV/EHU (7/June/2018 – 9 hours).*
7. **Difracción de Rayos X. Especialidad en muestra policristalina.** *SGIker, UPV/EHU (7-16/May/2018 – 30 hours).*
8. **PhDing by Design: Designing and Preparing a Research Publication.** *Tim Smithers, UPV/EHU (April-May/2018 – 24 hours).*
9. **Rietveld refinement for X-Rays powder diffraction data analysis.** *Cristina Echevarria, BCMaterials (12-15/January/2018 – 10 hours).*
10. **Scanning Electron Microscopy.** *Dimitris Kouzoudis, UPV/EHU (15-16/February/2017 – 10 hours).*
11. **Herramientas para una gestión eficaz de la Investigación.** *SGIker, UPV/EHU (1/ February /2017 – 5 hours).*